Impedance-Based Stability Analysis in Power Systems with Multiple STATCOMs in Proximity

Chi Li

Dissertation submitted to the faculty of the Virginia Polytechnic Institute and State University in partial fulfillment of the requirements for the degree of

Doctor of Philosophy

In

Electrical Engineering

Rolando Burgos, Chair

Dushan Boroyevich

Robert P. Broadwater

Virgilio A. Centeno

Steve C. Southward

Keywords: power system, STATCOM, small-signal stability, impedance-based stability criterion

July 23rd, 2018
Blacksburg, Virginia

Impedance-Based Stability Analysis in Power Systems with Multiple STATCOMs in Proximity

Chi Li

Abstract

Multiple STATCOM units in proximity have been adopted in power transmission systems in order to obtain better voltage regulation and share burdens. Throughout stability assessment in this dissertation, it is shown, for the first time, that STATCOMs could interact with each other in a negative way in the small-signal sense due to their control, causing voltage instability, while loads and transmission lines showed small effects. Since this voltage stability problem is induced by STATCOMs, d-q frame impedance-based stability analysis was used, for the first time, to explore the inherent power system instability problem with presence of STATCOMs as it provides an accurate understanding of the root cause of instability within the STATCOM control system.

This dissertation first proposes the impedance model in d-q frame for STATCOMs, including dynamics from synchronization, current and voltage loops and reveals the significant features compared to other types of grid-tied converters that 1) impedance matrix strongly coupled in d and q channel due to nearly zero power factor, 2) different behaviors of impedances at low frequency due to inversed direction of reactive power and 3) coupled small-signal propagation paths on the voltage at point of common coupling from synchronization and ac voltage regulation.

Using the proposed impedance model, this dissertation identifies the frequency range of interactions in a viewpoint of d-q frame impedances and pinpointed that the ac voltage regulation was the main reason of instability, masking the effects of PLL in power transmission systems. Due to the high impedance of STATCOMs compared to that of transmission lines around the frequency

range of interactions, STATCOMs were seen to interact with each other through the transmission lines. A scaled-down 2-STATCOM power grid was built to verify the conclusions experimentally.

Impedance-Based Stability Analysis in Power Systems with Multiple STATCOMs in Proximity

Chi Li

General Audience Abstract

STATCOMs have been proven a type of effective power electronics device for reactive power compensations and people are trying to install multiple STATCOMs in proximity in power systems in order to have better performances. This dissertation, for the first time, evaluates the operation of multiple STATCOMs in proximity and finds out that they could interact with each other in a negative way in the small-signal sense due to their control, causing voltage instability, while loads and transmission lines showed small effects. Since this voltage stability problem is induced by STATCOMs, d-q frame impedance-based stability analysis was used, for the first time, to explore the inherent power system instability problem with presence of STATCOMs as it provides an accurate understanding of the root cause of instability within the STATCOM control system. To this end, an impedance model of STATCOMs is proposed, which accurately explains the terminal behaviors of STATCOMs. Using the model, this dissertation identifies the frequency range of interactions in a viewpoint of d-q frame impedances and pinpointed that the ac voltage regulation was the main reason of instability, masking the effects of PLL in power transmission systems. All the above is validated experimentally in a scaled-down 2-STATCOM power system.

ACKNOWLEDGEMENTS

First, I would like to express my sincere gratitude to my advisor, Dr. Rolando Burgos, for his guidance, help and encouragement. I will not be able to achieve all these without his patience in leading me and experience in power electronics. I am always encouraged by him technically and emotionally when I feel down and can hardly proceed productively.

I would also like to thank Dr. Dushan Boroyevich, whose foresight often inspires me to think deeper and further rather than being confined to a specific technical issue. His challenging questions can always reveal something I ignore and impel me to find answers out of the box.

In addition to my advisors, I would like to thank the rest of my committee, Dr. Robert Broadwater, Dr. Virgilio A. Centeno and Dr. Steve Southward, for giving me valuable advice and insightful suggestions from different technical perspectives. It has been wonderful to have them on my advisory committee.

I would like to thank the support from the Center for Power Electronics Systems (CPES) Wide Bandgap High Power Converters and Systems (WBG-HPCS) Mini-consortium and Dominion Energy.

The great CPES staff have made it easy for me to focus on my progress and I would like to thank them all: Ms. Marianne Hawthorne, Ms. Teresa Shaw, Ms. Teresa Rose, Ms. Linda Long, Mr. David Gilham, and Ms. Lauren Shutt.

Many senior students have offered me great help during these years, especially Dr. Zhiyu Shen, for his help in guidance in experiments, Dr. Xuning Zhang for his advice in debugging my hardware, Dr. Igor Cvetkovic for the cooperation and work on experimental set-ups and Dr. Bo Wen for his enlightenment for some breakthroughs in my research.

It is a pleasure to work with the talented colleagues in the Wide Bandgap High Power Converters and Systems (WBG-HPCS) mini-consortium who offered me help and support. I would like to thank Dr. Marko Jaksic especially for his hardware, Dr. Yang Jiao, Dr. Jun Wang, Dr. Sizhao Lu, Mr. Wei Zhang, Dr. Fang Chen, Mr. Shishuo Zhao, Mr. Yadong Lv, Dr. Zeng Liu, Dr. Alinaghi Marzoughi, Ms. Ye Tang, Mr. Jianghui Yu, Mr. Zhengrong Huang and Mr. Yi-Hsun Hsieh.

I also would like to thank all my friends at CPES who made my life enjoyable and beautiful: Dr. Qiong Wang, Ms. Bingyao Sun, Dr. Ming Lv, Dr. Chao Fei, Mr. Zhongsheng Cao, Mr. Xuebing Chen, Dr, Yincan Mao, Dr. Lingxiao Xue, Mr. Bo Zhou, Dr. Shuilin Tian, Dr. Xiucheng Huang, Dr. Zhemin Zhang, Dr. Zhengyang Liu, Dr. Yuchen Yang, Mr. Yin Wang, Mr. Zhengrong Huang, Mr. Junjie Feng, Mr. Lujie Zhang, Mr. Vahid Najmi, Mr. Ruiyang Qin, Mr. Chen Li, Mr. Alex Chu, Dr. Syed Bari, Dr. Niloofar Rashidi, Mr. Chien-An Chen, Mr. Junjie Feng, Dr. Ting Ge, Ms. Jiewen Hu, Mr. Joseph Kozak, Mr. Bin Li, Mr. Bo Li, Ms. Qian Li, Ms. Virginia Li, Dr. Zichen Miao, Mr. Slavko Mocevic, Ms. Emma Raszmann, Ms. Rebecca Rye, Mr. Keyao Sun, Mr. Victor Turriate, Ms. Le Wang, Ms. Grace Watt, Ms. Christina DiMarino, Mr. Sungjae Ohn, Mr. Tam K.T. Nguyen and Mr. Yue Xu.

I am also very grateful to have my friends in Blacksburg who had so much fun together and so many memories: Dr. Jingren Deng, Dr. Yi Liu, Dr. Qinghui Mu, Dr. Qian Cao, Mr. Zhongnan Jin, Dr. Danni Lu, Mr. Qizhi Qin, Ms. Cen Zhong, Ms. Weizhen Sun, Ms. Yudong Xu, Mr. Yu Lin, Dr. Nan Chen, Dr. Duotong Yang, Dr. Shaohua Lei, Mr. Kaisen Lin and Ms. Xin Ning.

Finally but most importantly, I would like to thank my parents, Mr. Yang Li and Dr. Suping Huang for their love, encouragement and support from all respects since I was born. I feel blessed to have them in my life.

TABLE OF CONTENTS

LIST OF FIGURES

LIST OF TABLES

Chapter 1. INTRODUCTION

1.1 Overview of power systems with STATCOMs

1.1.1 Basic operations of STATCOMs

Static synchronous compensators (STATCOMs) are based on converters composed of force-commutated power electronic devices and topology, first proposed by Gyugyi in 1979 [1]. Although the DC source of STATCOM can be both current and voltage, the most practical and used one is voltage source converter (VSC), shown in Figure 1-1, along with its basic operation mode.

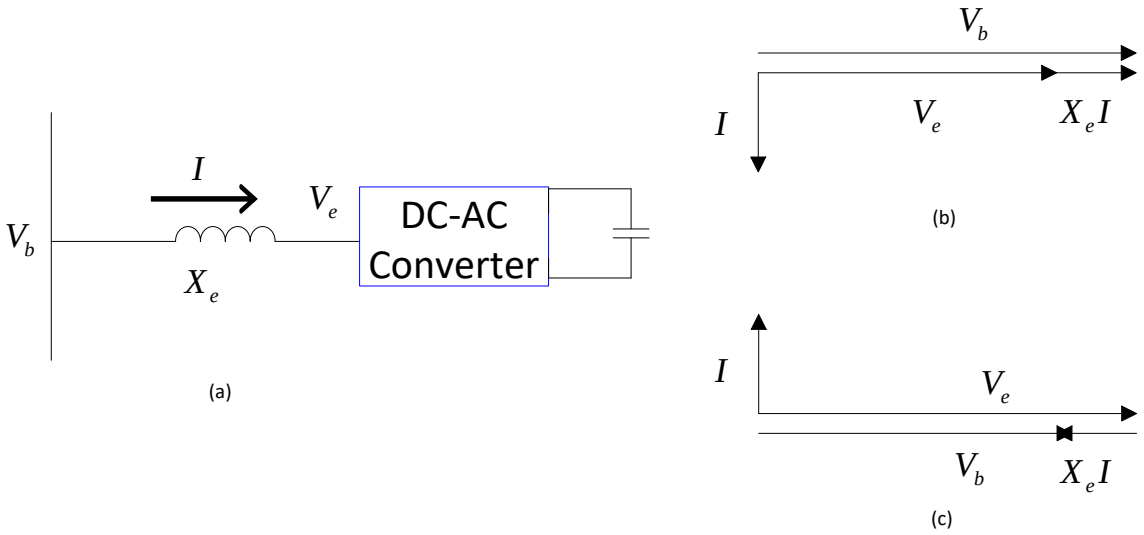

Figure 1-1 Basic concept of STATCOM

(a) basic topology of STATCOM; (b) inductive mode; (c) capacitive mode

The VSC-STATCOM generates an AC voltage V_e $V_e$and shunt connects to the bus with the voltage V_b V_b via an equivalent inductance $X_e$$X_e$, which is often the leakage inductance of a

transformer, where all the values are reflected to the primary side of a transformer. By controlling the output voltage of the converter by either firing angles or DC link voltage, it is easy to obtain a continuously controllable V_e $V_e$to control the compensating current and thus the reactive power compensation. The capacitor at DC side can be regarded as a reactive power source in a STATCOM. In practical applications, the losses of a STATCOM are compensated by the power system, that is, the STATCOM will draw a little active power from the grid, which results in a small phase lag of the output voltage $V_e$$V_e$. If we only consider the line-frequency components, the phasor diagrams in Figure 1-1 show how the STATCOM provide or absorb reactive power by adjusting its output voltage magnitude. When its output voltage is less than the bus voltage, the voltage drop in the inductance creates a lagging current and the STATCOM is absorbing reactive power, which is inductive mode. If the output voltage is higher than the bus voltage, the current will flip in polarity and be leading the voltages. At this time, the STATCOM is providing reactive power and in capacitive mode.

Figure 1-2 shows how a STATCOM works to compensate by adjusting its output voltage dynamically. The solid lines describe the V-I characteristics of the STATCOM with the output voltage V_{e1} $V_{e1}$and the grid, where the intersection shows the operating point at the present with the bus voltage $V_1$$V_1$. If the system voltage drops suddenly and therefore the bus voltage decreases to V_2 V_2', the STATCOM will be controlled to increase its output voltage to V_{e2} V_{e2} and obtain a new V-I characteristic to reach a new operating point with the bus voltage V_2. As Figure 1-2 shows, V_2 is greater than V_2' and could be even greater than V_1 based on the compensation capability of the STATCOM and the system condition. In such way, the bus voltage change is compensated.

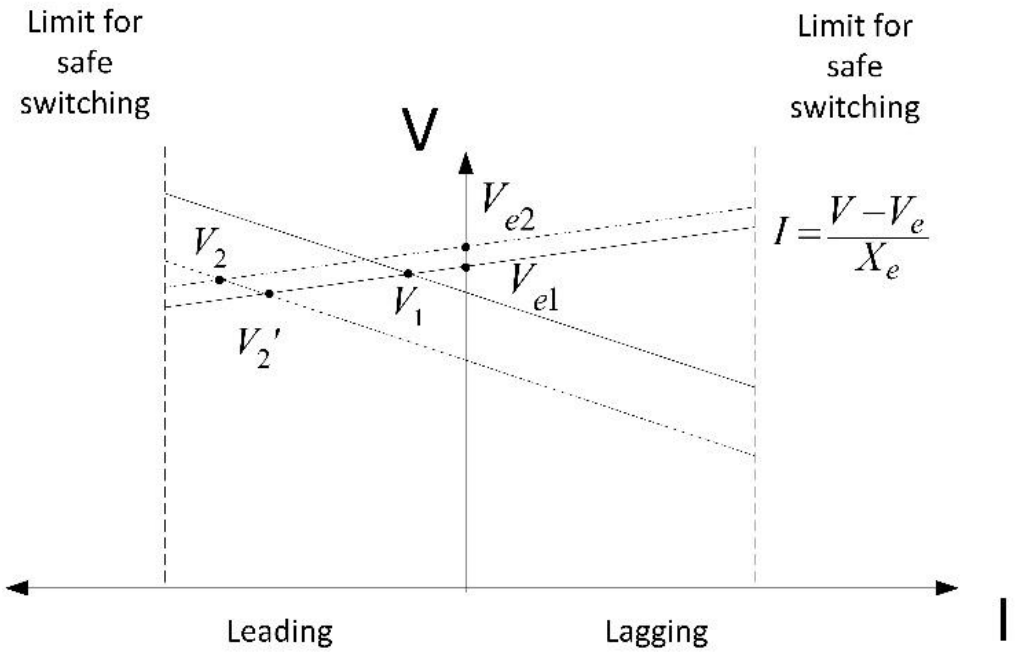

Figure 1-2 Operating characteristics of STATCOM

1.1.2 STATCOM operation in power systems

On top of reactive power compensation, there are several purposes to install a STATCOM in power systems: steady state voltage regulations including active power transfer capability enhancement, oscillation damping and transient improvement after contingencies. The voltage regulation studied the steady state of STATCOM operation, mainly focused on optimization problems with respect to algebraic power flow calculation. The oscillation damping is about how power systems behave in the small-signal sense around a given operating point, which relies on linear system theory. The transient improvement is to explore how power systems operate after a large change, e.g. fault, where the studied subject is no longer linear and requires nonlinear system theory.

Voltage regulation is to maintain voltages within acceptable ranges to ensure proper working conditions for grid-tied components. Control over some specific bus offers the possibility to

change power flow of power systems for economic considerations, for example, lessening the power flows through the heavily loaded lines and maintaining the critical buses voltage to enhance the stability margin. The term total transfer capability (TTC) is to define the amount of power that is available to transfer between interconnected transmission systems in a reliable manner and is determined by system's thermal and voltage limits and stability margins [2]. This is usually done by power injection model (PIM) [3-5] that studies the terminal power flow injection of FACTS devices and makes corresponding modifications to the original power flow equations. After applying the PIM into the conventional power flow program, there are some mathematical methods to compute TTC [2, 6, 7], which intrinsically are to solve a set of optimization problems, typically maximizing the load in the sink area, with large amounts of non-linear equality and inequality constraints. The optimization has to be repeated if the topology and any source or load changes.

The second main purpose of STATCOMs is to damp oscillations. Power system oscillation damping is referred to the damping of inter-area oscillations with frequency 0.2 Hz to 2.0 Hz due to the development of interconnection of large power systems, which may cause stability problems. With faster responses than major electric power plants, the capability of STATCOM to suppress power system oscillations and thus to increase system stability has been explored in many aspects. The small-signal model is often a state-space model linearized around a given operating point and the damping is achieved by a FACTS device stabilizer (FDS) which is installed as a higher level local controller to control the effective active or reactive power output according to the command of a grid level global or local controller [8-23]. Chong Han etc. [24] conducted an impact study of a STATCOM in a 12-bus power system with two large wind farms connected and from the PV and VQ curves obtained from the simulation the article discussed the size and location of the STATCOM to ensure enough stability margin. The results showed that the STATCOM is

minimized in size without losing its controllability when it is located right at the PCC, which is found out to be a common place to install the STATCOM. Nadarajah Mithulananthan [21] looked into the typical electromechanical oscillations and used Hopf bifurcation theory to study the influence of different controllers, locations and control signals. The PCCs of renewable energies are often shown to be the critical point to maintain the voltage profile of the whole power system, which demonstrates Chong Han's results to some extent, although the choice of the placement still needs carefully investigating case by case [25, 26]. To simplify the problems as for local small-signal stability analysis where the part without renewable energies of the grid is simplified as a voltage source with a reactance, the impact of the STATCOM was studied with more detailed models of both the renewable energy and STATCOM. In [27], Pranesh Rao derived the state-space model of the STATCOM in the D-Q frame and compared various state feedback controllers where all the variables are local and thus accessible, lending background to many following papers. Woei-Luen Chen etc. and Li Wang etc. both used modal control theory to place the eigenvalues of the state models of the local system they derived to achieve desired damping effects with state feedback control [28-30]. After designing the structure of the control loops, the eigenvalues of the state model with respect to the parameters of the controller are placed using a state feedback controller according to the pole placement method or the eigen-structure assignment method to get the maximum damping according to the preset optimum functions and objectives. After acquiring the state-space equations, there are many controllers to implement to manipulate the transfer functions [10, 12, 14] and thus to improve the steady-state and dynamic responses. Some advanced controllers which have been studied in some other STATCOM applications [31-35] e.g. hybrid fuzzy control [13], H_∞ control [16], robust control [17], etc. are possible to be adopted in the small-signal stability analysis in order to grant a more robust characteristics.

Another purpose is less common but still important, the low voltage ride through (LVRT) capability, concerning the stability of the wind generators interacted with the voltage variance at the PCC [36-38]. This falls into the large-signal stability field. During the system faults, the PCC voltage will collapse and there will be not enough reactive power for magnetic excitation for the generators, generating less electromagnetic torque. If the input source is kept constant, the generator will accelerate according to the mechanic equations and finally has to be disconnected to the grid for the safety consideration. Then it may trigger a chain reaction of disconnection of the generators due to the less input power to the grid and eventually result in the whole system collapse. Therefore the reactive power support during and after power system contingency is a critical issue. However, this is very challenging because the small-signal model fails during faults with the system highly nonlinear. Typically energy function methods are analytical but complex to obtain and solve while the numerical simulation is more common but takes more time with different cases [29, 38-42]. M. H. Haque [20] started from the equal area criterion to propose a control strategy thanks to continuously control capability of the STATCOM to improve the first swing stability limit by adjusting the equivalent damping torque for the generators. On the other hand in [41, 42], Marta Molinas etc. started from the quasi-stationary torque-speed curves of the wind generator to get the similar results.

1.2 Small-signal analysis in electric power systems

1.2.1 Traditional state-space modeling and limitations

The small-signal stability in power systems has been usually analyzed using eigenvalues, which are computed from the full system state-space equations [43]. The state-space equations include the complete information about any responses at any time intervals with given initial

conditions while this approach requires every detail of all the components in the system, from load to source, from passive elements to controlled power converters and generators, from circuit topology to unit configurations.

Specifically, there are quite a bit researches for power systems with STATCOMs in the small-signal sense, studying on how a STATCOM can damp power system oscillations [19, 21, 22, 44-54] or help integrate renewable energy like wind [24, 28, 29, 37, 38]. Again, all these papers based on state-space equations with prerequisites that the control details are known to power system operators which are often the opposite in reality.

As power systems get complicated, the state-space equations will be tremendous and whenever a new unit is connected and state-space equations are updated, the assessment of stability often needs to be repeated from the beginning and therefore is of great computation burden. Moreover, this method depends on the full knowledge over the power grid, which may not always be accessible, as some components in the grid, especially newly adopted power electronics based converters, are practically like black boxes to the system operators. It is either because of lack of model details due to the sharing of proprietary information from venders or due to inability to model with satisfactory accuracy [51]. In this case, absence of the model details leads to difficulties in conducting eigenvalues analysis and further controller design [52].

1.2.1 Impedance-based stability methods

As a more promising and practical alternative, the impedance-based stability analysis, has been shown a great success in dc systems for a long time [55] based on Nyquist stability criterion. In three-phase ac systems, sinusoidal variables can be translated into dc values in d-q frame using the Park transformation and generalized Nyquist stability criterion (GNC) was proposed for

analysis [56-60]. Impedances are also studied in abc frame [61, 62] or α-β domain [63]. There are also similar researches [64, 65] in power system area, which used the term "frequency scan" that was equivalent in principle and was actually modeling impedances in abc frame. Recently equivalency between modeling in abc and d-q frame has been shown [66, 67], with power converters creating complexity of coupling and more definitions added to bridge modeling in different frames.

For three-phase ac systems, dc equilibrium operating points can be created using Park transformation and d-q frame circuits with dc values are then available for linearization to study small-signal stability. Consider a three-phase balanced ac system as in Figure 1-3 where every variable is in its matrix form with d-q values as (1.1) shows. The return ratio matrix defined in (1.2) can be used as small-signal stability index. GNC shows that the closed-loop system is stable if and only if the net sum of anticlockwise encirclements of the critical point (-1, *j*0) by the set of characteristic loci of the open loop transfer function $\mathbf{L}(s)$ equals to the total numbers of right-half plane poles of $\mathbf{Z}_s(s)$ and $\mathbf{Z}_l^{-1}(s)$. Thus in the ac systems, it is necessary to compute all the eigenvalues of $\mathbf{L}(s)$, $\lambda_1(s)$ and $\lambda_2(s)$, and plot them in the complex plan to check the encirclements of the critical point.

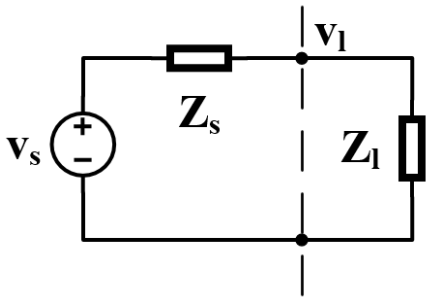

Figure 1-3 Small-signal circuit of a three-phase balanced ac system in d-q frame

$$\mathbf{v_s}(s)=\begin{bmatrix} v_{sd}(s) \\ v_{sq}(s) \end{bmatrix}, \mathbf{v_l}=\begin{bmatrix} v_{ld}(s) \\ v_{lq}(s) \end{bmatrix},$$
$$\mathbf{Z_s}(s)=\begin{bmatrix} Z_{sdd}(s) & Z_{sdq}(s) \\ Z_{sqd}(s) & Z_{sqq}(s) \end{bmatrix}, \mathbf{Z_l}(s)=\begin{bmatrix} Z_{ldd}(s) & Z_{ldq}(s) \\ Z_{lqd}(s) & Z_{lqq}(s) \end{bmatrix} \quad (1.1)$$

$$\mathbf{L}(s)=\mathbf{Z_s}(s)\mathbf{Z_l^{-1}}(s) \quad (1.2)$$

Stability analysis based on impedances has been explored, covering many applications including interactions between power grid and HVDC [68-71], between wind farm and HVDC [72-74] and integration of generic inverters [75-77] and electric vehicles [78]. Some papers based on abc frame are theoretically wrong because the frequency coupling effects found in [66, 79] were ignored due to the presence of power electronics converters and corresponding d-q frame control. The impedance of a three-phase converter under balanced voltage should be described by a 2×2 matrix instead of a single element [66, 67], no matter in abc or d-q frame. That is where some researcher made mistakes when they modeled the impedance in abc frame and assumed that there were only positive sequence component in power systems at all frequencies in the small-signal sense. As a result, the negative sequence component existed because of the frequency coupling effects but was neglected. Although the used impedance models were wrong in the above analysis, some conclusions still held true, either because the frequency coupling effects could be masked under unity power factor case or as the main reason of instability was in the positive sequence and captured in a large portion of cases [80].

Some people investigated how to shape the impedance of a specific converter in the desired frequency range. Current loop was modified with more robust compensators [81-85] or with additional damping controller [76, 86-88] to handle undamped harmonics in the presence of weak grids. The modification of impedance is limited with practically simple compensators used in

digital controllers. It is hard to shape impedance to be whatever one desires in every channel but it is possible to provide additional damping of resonance and to increase or decrease the magnitude within a given frequency range. For current harmonics due to weak power grids, impedance-shaping techniques were very effective [82-84] because the possible interactions between impedances were relatively simple to locate the origins in frequency range above 100 Hz. Nevertheless, the definition of a "good" impedance is yet unclear without knowing the crucial cause of instability for each situation, especially at about a few tens of Hertz – so-called sub- and super-synchronous harmonics, because many control loops and power system dynamics are in this frequency range. The actual root of instability was rarely mentioned and pinpointed until [56, 57] pointed out different instability reasons for constant power loads and synchronization, and [89] showed how to apply passivity theory to impedance analysis. Therefore, this weakens many reported impedance-shaping methods because they were not really targeting the main cause.

The biggest benefit from the impedance-based method is the accessibility of the information needed, where measurements at terminals are enough to determine the small-signal stability at the given operating points. Since the terminal impedances intrinsically include all the circuit behind with its control, this approach offers us confidence to assess the stability and evaluate stability margins without knowing every detail inside. Besides analysis in simulation with computers, this approach is practical in real systems as long as there is a power electronics based converter capable of injecting perturbations in the d-q frame. Without additional efforts, the voltage and current measurements at the converter terminal are enough to compute the small-signal impedances for stability analysis. As such, the assessment of small-signal stability can be done online [90]. Compared to the traditional eigenvalue-based stability method, impedance-based approach only needs terminal impedance measurements to obtain small-signal stability information. In such way,

the converter manufacturers may not need to provide its detailed model and control to the system integrator or vice versa to investigate the stability. All that matters are the terminal impedance information based on different operating points, which can be measured by the manufacturers and provided along with the manuals and products. On the other hand, the measurements of the grid side impedance can be done by the connected converter by injecting small amount of perturbation, sweeping the frequency range of interest, and reading the voltage and current measurements at its own terminal in d and q channel respectively. Usually the process only takes a few minutes and no interruption would happen during the perturbation. Another benefit is that it is easy to set a certain impedance requirement for newcomers to be allowed to connect to the power grid, although possibly over-conservative sometimes. If a new unit does not meet the requirements of stability with respect to its impedance, its owner can tune its control parameters to follow the grid code, instead of the system operators calculating all the eigenvalues of the whole power system. However, it should be noted that integration of impedance models of each single unit to a power grid needs careful inspection when applying GNC to make sure sufficient conditions are met [91-95].

Admittedly, state-space equations can provide the full information of the system, which can be used to analyze participation factors and to design power system stabilizers (PSSs) while the impedance-based method has no capability to do so since it only detects the terminal information. In summary, the impedance-based stability criterion is a fast and convenient approach for small-signal stability without additional efforts with the presence of power electronics converters but it provides less information to conduct comprehensive study and global control of the power grids. [96-130]

1.3 Motivations and objectives

There are two aspects, on which this dissertation is trying to focus, one being the operation of multiple STATCOMs in proximity in a small-signal sense and the other being the analysis to address stability issues based on impedance-based stability criterion.

As mentioned before, there are few literatures talking about the stability problems in power systems with multiple STATCOMs in presence. Therefore, the first objective is to evaluate and find out how STATCOMs can interact with each other or with power grids in the small-signal sense. To analyze small-signal stability problems induced by STATCOMs in the evaluation, impedance-based stability criterion is selected for the drawbacks in the traditional state-space modeling method. However, there are no well-formed impedance models for STATCOMs to tackle. Hence, the second objective is to derive an impedance model and to use it in order to solve the small-signal stability problems. Whether there is a new type of instability pattern in addition to previous works and what is the crucial reason behind are also targets of this dissertation.

1.4 Proposed dissertation outline

The dissertation is organized as follows.

Chapter II will introduce the power transmission grid with four STATCOMs. Evaluation of this system will be given with respect to different possible factors, including STATCOM control and power system parameters. In order to simplify analysis, a 2-STATCOM power system will be then introduced, trying to search similar potential instability as in the full system. Starting from the 2-STATCOM power system, a scaled-down experimental set-up was built accordingly for verification.

In Chapter III, a dq-frame small-signal impedance model of STATCOMs including all control loops will be derived systematically, with detailed analytical expressions. Some key features are discussed in different frequency ranges, which distinguishes this dissertation from previous works. The impedance model will be validated in the above scaled-down set-up too, using impedance measurement unit (IMU).

Once the impedance model is ready, Chapter IV will use this tool to analyze the potential instability found in Chapter III, but in the simplified 2-STATCOM system. The significant factors that affect the stability will be analyzed in details and a new type of instability pattern, ac voltage regulation, will be pointed out. Discussions on the reasons of this pattern will be provided too. The IMU was used again to verify the analysis in this chapter experimentally.

Chapter V extends the previous conclusions in Chapter IV back to the full system with four STATCOMs. The conclusions are first re-checked to see if they are still valid and then some new issues that only appear in the full system are discussed.

Finally, Chapter VI concludes the whole dissertation and a possible future road map is proposed.

Chapter 2. ASSESSMENT OF POWER SYSTEMS WITH MULTIPLE STATCOMS IN PROXIMITY

2.1 Introduction and novelty

STATCOMs, as a common type of FACTS devices, have been widely adopted in modern power systems to offer reactive power compensation and enhance stability performances [131, 132]. It is a common practice to install a STATCOM at the bus either where it can regulate bus voltages over the grid to the best, or where some renewable energy is connected. However, this single-STATCOM approach may not be the best solution in every power system, because 1) reactive power cannot be delivered through long distances and a single STATCOM may not be able to maintain all the bus voltages; 2) possibly more than one STATCOM can achieve better oscillation damping; 3) several STATCOMs small in power rating could be more economic than a large one. Due to the above considerations, there is a power transmission grid from Dominion Energy with four STATCOMs installed in physical proximity in about tens of miles away. To generalize the analysis on interactions between STATCOMs, an IEEE 14-bus system test bed was selected with four STATCOMs placed nearby in Figure 2-1. By having multiple STATCOMs, a better voltage profile over the grid can be obtained and the STATCOMs are able to share the burden so that a smaller power rating can do the job for each STATCOM. Additionally, flexibility of operation is available to facilitate maintenance.

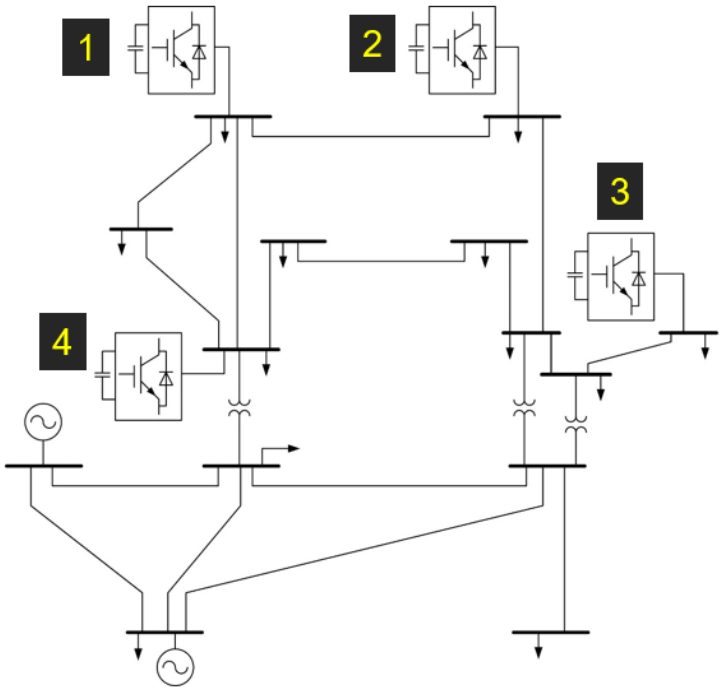

Figure 2-1 IEEE 14-bus system with four STATCOMs

Researchers have been studying the influences of a single STATCOM connected to a given power grid, including steady state, small-signal and large-signal stability. Because there are not many power systems with multiple STATCOMs running in proximity, little has been done regarding multiple STATCOMs, not even to mention possible interactions between them in the small-signal sense. The existing papers on multiple STATCOMs are mostly focused on steady state analysis, for example, allocation and sizing [133-136] and coordinated secondary voltage regulation [50, 51, 137-140]. This section will try to fill the blanks in small-signal stability, starting from the assessment of a power system with multiple STATCOMs in proximity to see how multiple STATCOMs could interact and whether the system would be possibly unstable in the presence of STATCOMs.

2.2 Modeling and control of STATCOM

STATCOMs have been introduced since 1970s, composed of thyristors. As power semiconductor technologies advances, present practical STATCOM configuration is dominant by multilevel structure to build up high voltages using silicon IGBTs due to flexibility and scalability. For example, Figure 2-2 shows a Siemens product configuration called SVC Plus where H-bridge modules using Si devices are stacked for high voltages, e.g. 30 kV for each phase and then a step-up transformer is used to interface transmission power systems at the PCC point v_{PCC}.

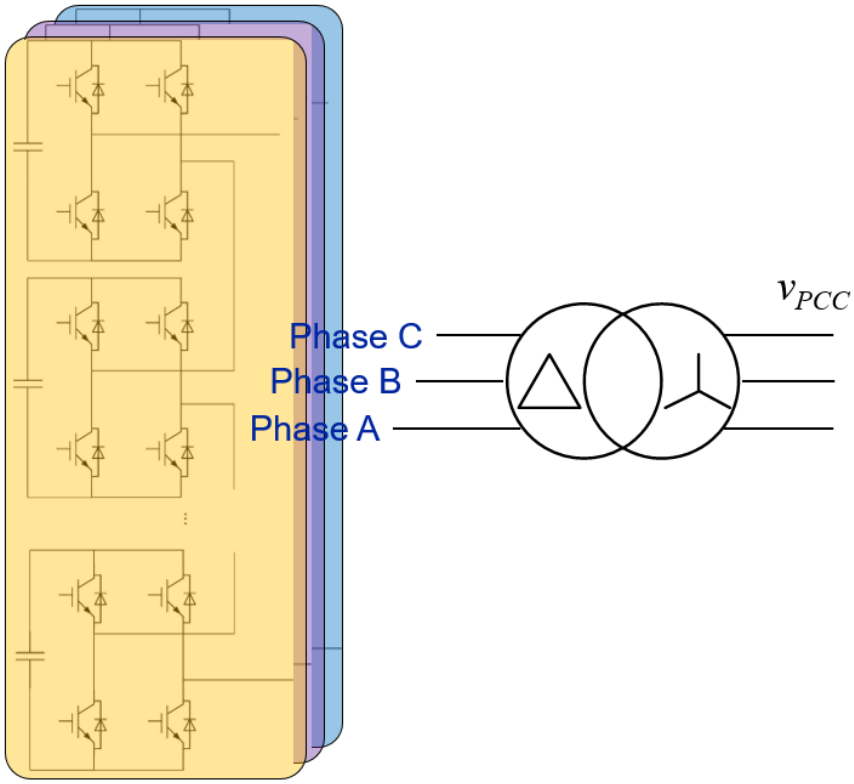

Figure 2-2 Multilevel STATCOM configuration from Siemens

According to [141], from the system level control point of view, which means dynamics below several kilo Hertz within the fastest current control loop, STATCOMs with multilevel structure show no difference between a simple 2-level voltage source converter. Therefore, STATCOM

topology and its control are shown in Figure 2-3. The controller of the STATCOMs is the commonly implemented cascaded controller with inner current loops and outer voltage loops oriented by a phase-locked loop (PLL) in dq-frame. Figure 2-4 shows the details where variables with * are the references; subscript *d* means variables in d-channel and subscript *q* means variables in q-channel. The inner current loop is controlled in d-q frame with decoupling to generate duty cycles for PWM to drive the power electronic devices, with the d-channel compensator G_{cid} and the q-channel compensator G_{ciq}. The d-channel current reference is provided to maintain the dc bus voltage using dc voltage compensator G_{cvdc} and the q-channel current reference is given to regulate the ac bus voltage magnitude via ac voltage compensator G_{cvac}. Outside the ac voltage loop, there is an optional QV droop to allow the PCC voltage vary in an acceptable range in order to lessen the burden of STATCOM, as shown in Figure 2-5 where K represents the slope and v_{PCCd0} is the set point when the STATCOM outputs zero reactive power. The PLL is a synchronous reference frame PLL that regulates the q-channel ac bus voltage to be zero using the PLL compensator G_{cPLL} in order to track the grid.

$$K = \frac{\max \Delta V_{PCC}}{2\left|\max Q\right|} \tag{2.1}$$

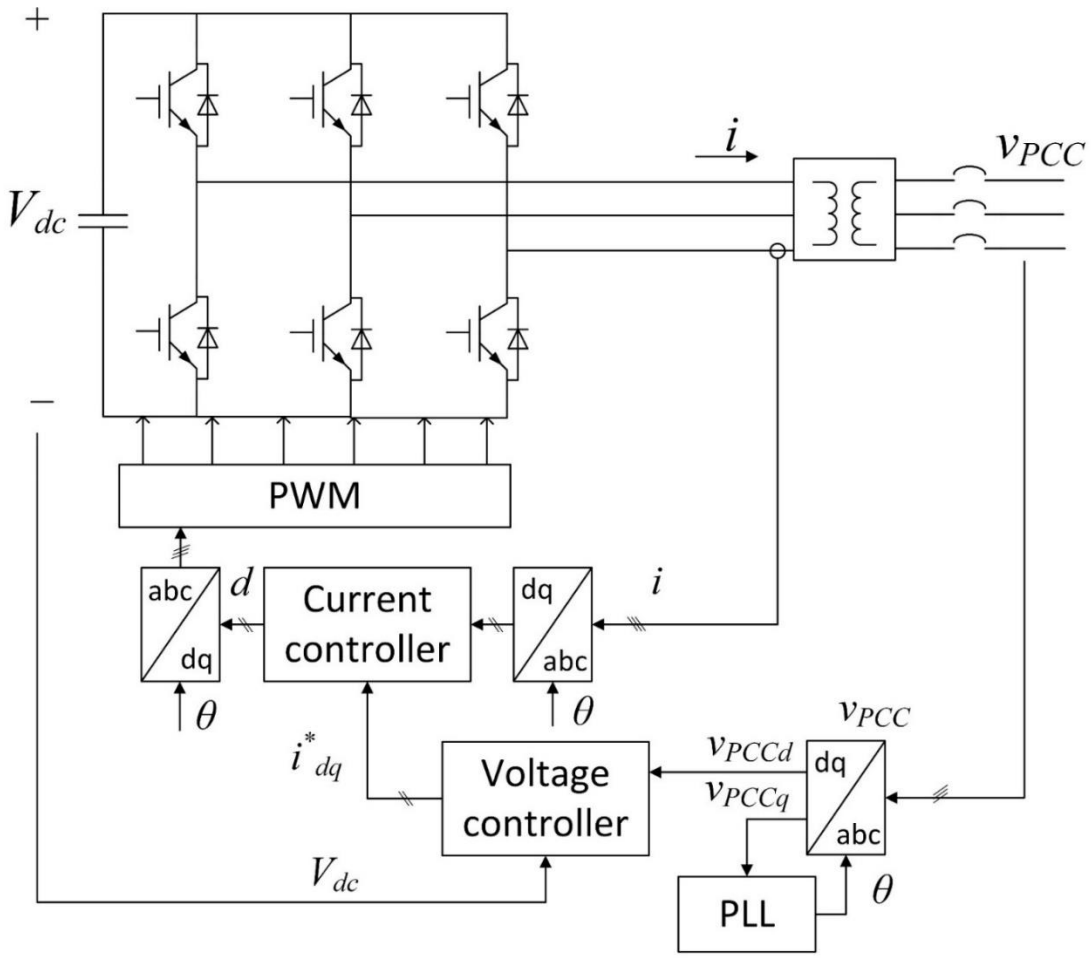

Figure 2-3 STATCOM topology simplified as 2-level converter and its control

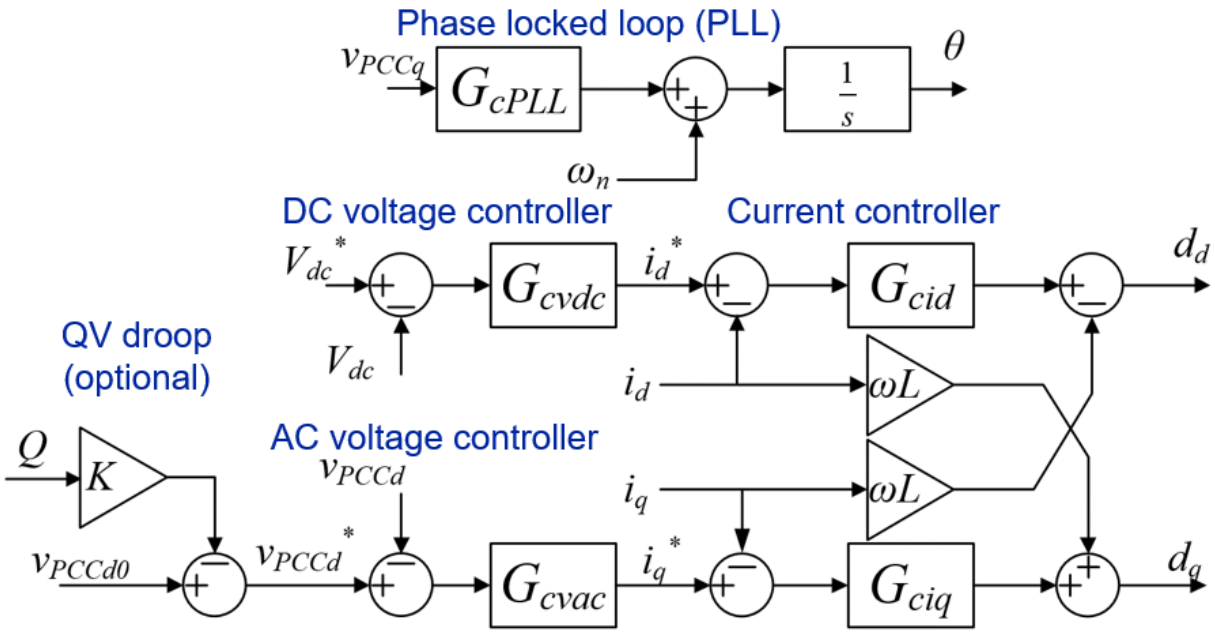

Figure 2-4 Details of STATCOM control

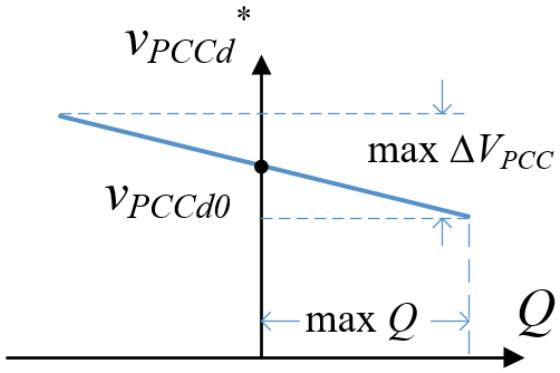

Figure 2-5 QV droop for STATCOM control

A simple design for compensators are as follows:

$$G_{cid} = G_{ciq} = k_{pi} + \frac{k_{ii}}{s}, \text{where } k_{pi} = \frac{\omega_{ci} L}{V_{dc}}, k_{ii} = \frac{\omega_{ci} R}{V_{dc}} \tag{2.2}$$

$$G_{cvac} = k_{pvac} + \frac{k_{ivac}}{s}, \text{where } k_{pvac} = \frac{\omega_{cv}}{\omega_{ci}\omega_n L_g}, k_{ivac} = \frac{\omega_{cv}}{\omega_n L_g} \tag{2.3}$$

$$G_{cPLL} = k_{pPLL} + \frac{k_{iPLL}}{s}, \text{where } k_{pPLL} = \frac{\omega_{cPLL}}{V_{PCCd}}, k_{iPLL} = 0 \tag{2.4}$$

where ω_{ci} is the bandwidth of current loop, ω_{cv} is the bandwidth of ac voltage loop, ω_{cPLL} is the bandwidth of PLL, L is the transformer inductor, R is the parasitic resistor, V_{dc} is the dc bus voltage, ω_n is the line frequency, L_g is the Thevenin grid inductor without any other STATCOM connected, V_{pccd} is the d-channel grid voltage at PCC.

2.3 Evaluation of possible factors affecting stability

Since there is no such power system with multiple STATCOMs reported for small-signal stability, it is important to assess this scenario to discover what factors are significant in affecting stability. Factors that could affect stability come from two aspects: one from the system itself and the other from STATCOM control introduced in the previous section. There are three control loops: PLL, current loop and voltage loop. What matters the closed-loop dynamics most is at which bandwidth the control loop is closed. Thus, in the following assessment, three different compensators with bandwidths for each control loop –factor from STATCOM control– were chosen with enough phase margin. On the other hand, parameters in the power system, a.k.a. factors from system, also could play a role in stability, such as loading level, the impedance of transmission line (or called electric distance) and the bandwidth of constant power loads. For every factor, the other factors were kept constant.

Evaluation was done in time domain simulation in MATLAB/Simulink because it provides plentiful functions in frequency domain analysis and the studied system is not too large for a PC to compute. The parameters of each STATCOM were given in and all four STATCOM are the same. The controllers were designed based on the Thevenin equivalent grid impedance at their terminal as a benchmark individually. The PLL was designed with 5 Hz bandwidth and 85° phase margin for 60 Hz grid frequency to attenuate detected frequency. A current loop with 200 Hz

bandwidth and 90° phase margin, assuming the equivalent switching frequency to be 2 kHz, was designed to ensure a good current waveform. The ac voltage loop was tuned to be at 6 Hz bandwidth with 45° phase margin and the dc voltage loop was adjusted to be at 0.1 Hz bandwidth with 60° phase margin. Every STATCOM was stable by itself connecting to the power system with enough phase margins. The four STATCOMs were connected online successively at the moments of 1, 3, 5 and 7 second in the marked order in Figure 2-1. All the four STATCOMs were identical in terms of power ratings and control parameters.

Table 2.1 Parameters of STATCOMs

Parameter	**Value**
Nominal voltage	30 kV
Nominal power	125 MVar
Transformer inductance	0.38 pu
DC bus voltage	3.3 pu
DC capacitance	1.39 pu

The transient responses in PCC bus voltage in d-channel V_{1d} at the first STATCOM were plotted in Figure 2-6, showing the evaluation of ac voltage loop, current loop and PLL respectively from top to bottom, with the other factors in the boxes on the right. It can be seen that all the three control loops showed significant impacts. The effects of the ac voltage loop are shown on the top of Figure 2-6. High bandwidth at 20 Hz indicated instability after the second STATCOM was connected. When the third STATCOM was connected, the system oscillated so much that STATCOMs were out of their power ratings and tripped at about 5.3 second and the system began being damped. However, when the fourth STATCOM was connected, the system started oscillating again and another STATCOM tripped at about 7.7 second. The lower bandwidth at 7 Hz presented diverged oscillations when all the four STATCOMs were online and only the case with the lowest bandwidth was stable. As for current loop effects in the middle of Figure 2-6, low

bandwidth at 100 Hz in yellow showed instability when the second STATCOM was connected and at bandwidth of 200 Hz the system became unstable with the fourth STATCOM. When the bandwidth further rose to 500 Hz, all STATCOMs could coordinate. With increased PLL bandwidth in the bottom of Figure 2-6, the system became stable as at 10 Hz in blue and all the four STATCOM could work together while at 5 Hz in yellow and 8 Hz in red the connection of the fourth STATCOM triggered instability. Actually, it is worthwhile to mention that the connection sequence of STATCOMs did not matter in terms of stability, no matter which STATCOM was connected first or last, and this is true for all the evaluation. To summarize, higher PLL bandwidth, higher current loop bandwidth and lower ac voltage loop bandwidth tend to stabilize the system.

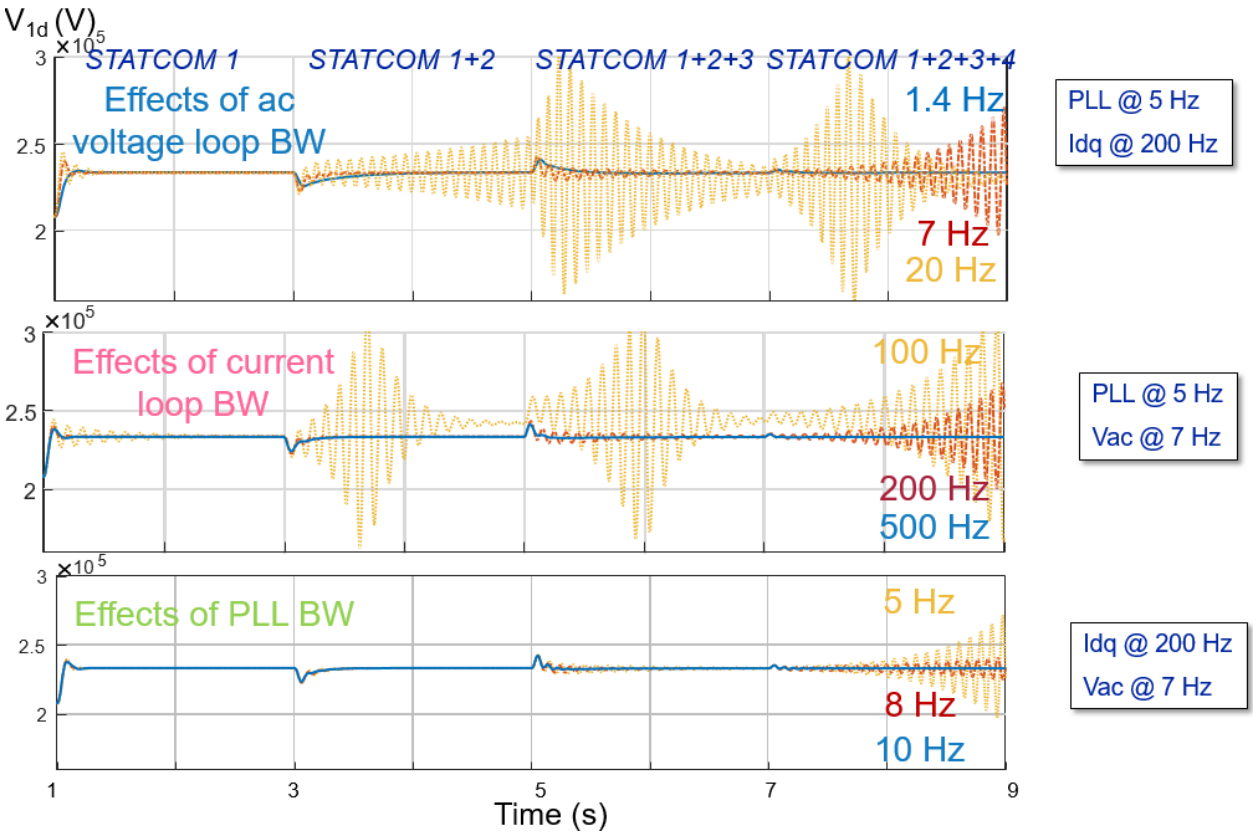

Figure 2-6 Evaluation of impacts of STATCOM control

Figure 2-7 shows the simulation results when all the STATCOMs were working in voltage regulation mode in blue and in QV droop mode in red. The coefficient of the QV droop $K = 1\% V_{PCC}^{*} / \max Q \approx 0.0002$, where V_{PCC}^{*} is the nominal value of PCC bus voltage 233.27 kV and max Q is the nominal output reactive power 125 MVar. By activating the QV droop, the STATCOMs generated less reactive power, but they were unstable when the fourth STATCOM was connected.

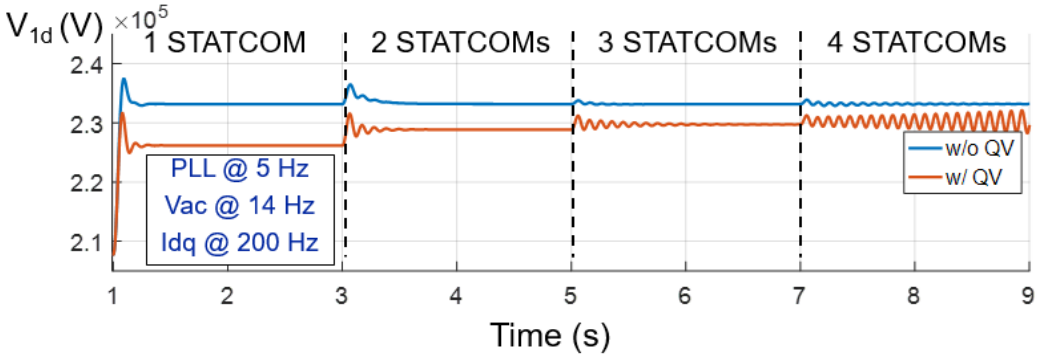

Figure 2-7 Evaluation of impacts of STATCOM operation modes

Two aspects of the effects of loads, load composition and loading level, were evaluated and the results are shown in Figure 2-8. Load composition, was assumed to be typical constant power loads (CPL) and constant impedance load (CZL), also given in Dominion Energy's data. On the top, the loads all over the system were changed in the proportion and showed negligible influences. The loading level was also varied from 0.5 per unit to 1.5 per unit and presented insignificant changes in transients as well. These two tests actually indicate that the loads in the system are not dominant factors causing instability.

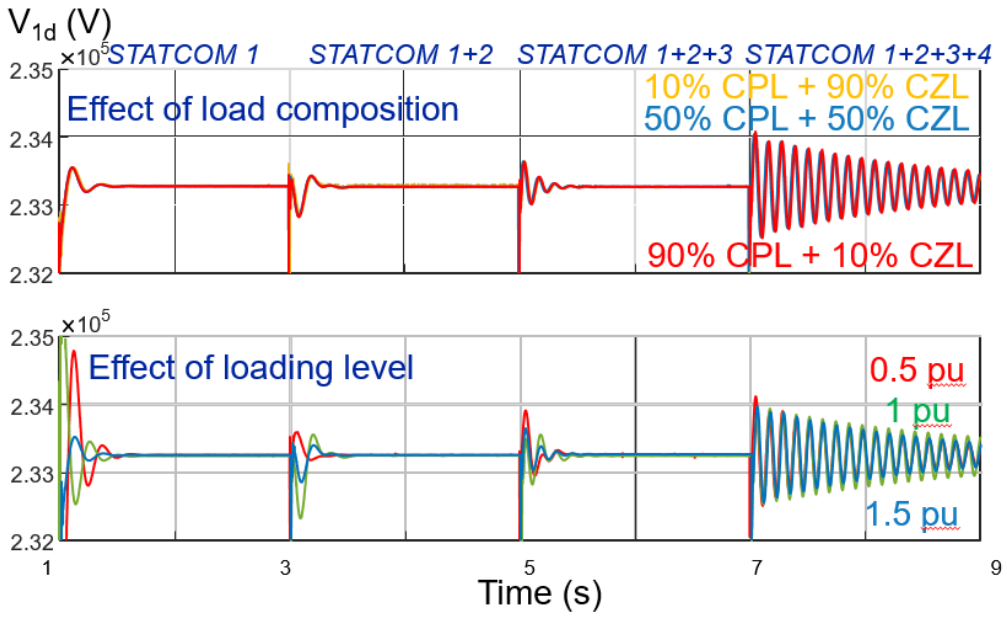

Figure 2-8 Evaluation of impacts of loads

The power ratings of STATCOMs should also be taken into consideration when assessing the system stability. Intuitively, if the STATCOMs are very small, they cannot have significant influences on the grid, as confirmed by Figure 2-9 where only the power ratings were changed and control parameters of STATCOMs remained. When the STATCOMs were designed with smaller power ratings, for example 0.25 and 0.5 per unit, the voltage at the PCC bus could not be compensated to the reference value with enough reactive power. However, under these scenarios, the system was stable, since the diverging currents were limited and clamped by the small power ratings. When the reactive power rating was 1 per unit, one can observe the system instability, as found previously. If the power rating was further increased to 2 per unit, the system was still unstable, because 1 per unit was already enough to cause instability. Therefore, as long as the STATCOMs are properly sized for voltage compensation, the previously found instability due to STATCOM control could happen.

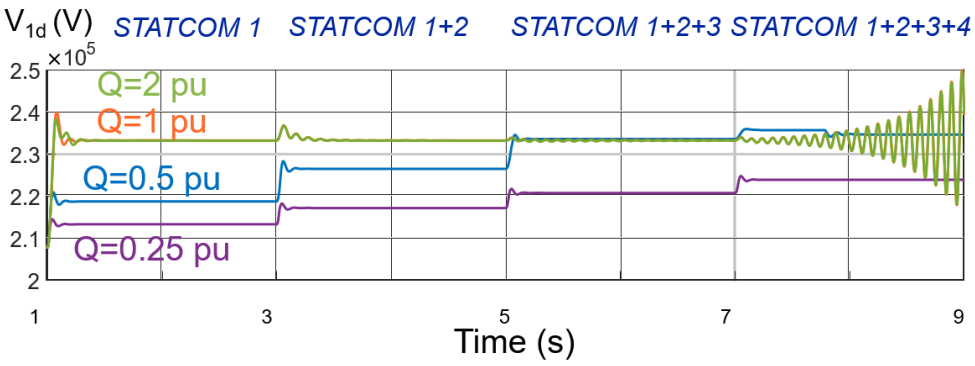

Figure 2-9 Evaluation of impacts of STATCOM power ratings

For the power systems under assessment, the line impedances are in the range of 0.0002 to 0.2 per unit under the base value for a 230-kV 2-GW system, which can be translated to 1~100 miles using typical values for 230-kV lines. For different voltage ratings, the physical length will be different, but what really matters is the electric length, and to be more specific, the impedance values of the lines in per unit. Regarding those transmission lines, their impacts must be categorized into two parts: the lines that connect to infinite buses or large synchronous generators and the other lines that only connect STATCOMs. The first type of lines determines how stiff the power system is – the stiffer the system, the less possible it becomes unstable and the smaller the impedances of the lines, the stiffer the grid. It is shown in Figure 2-10 where the 1x impedance case is the benchmark as shown before. If the impedance was doubled, the system was more unstable as the connection of the third STATCOM caused instability followed by tripping of a STATCOM due to tremendous currents. On the other hand, if the impedance was half, the system was stable with all the four STATCOMs. This shows the stiffness of the power system strongly affected its stability, which is not new but still applies to the previously found instability phenomenon.

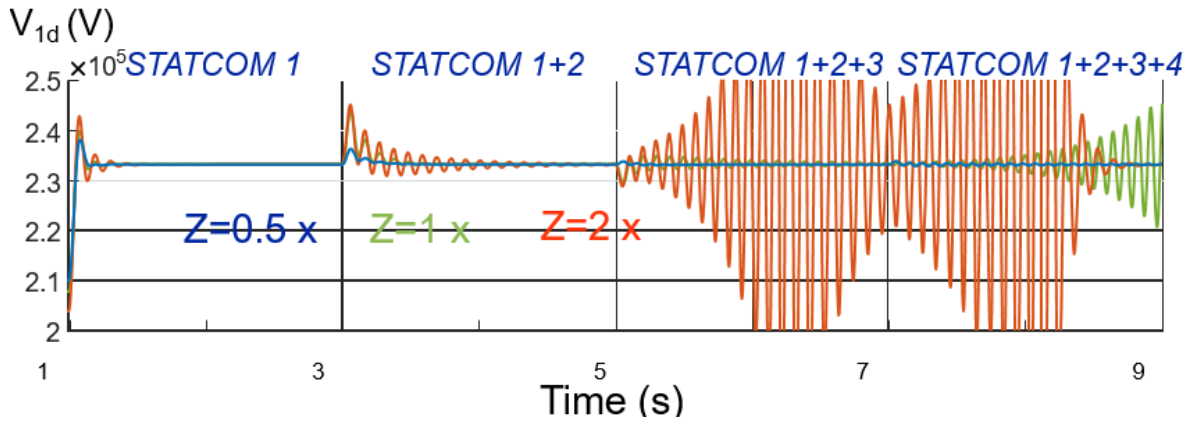

Figure 2-10 Evaluation of impacts of transmission lines connecting to infinite buses

However, the transmission lines that link STATCOMs showed different impacts, depicted in Figure 2-11 with the 1x impedance case being the benchmark too. When the transmission line had impedance values within 2 decades, a.k.a., 0.1 time to 10 times, similar instability happened still, due to STATCOM control. The instability disappeared until the impedance of the connecting line increased to 100 times larger. In this case, STATCOMs would be too far away and they could not interact with each other, as in an extreme case with two STATCOMs not connected electrically. In conclusion, if STATCOMs are installed in the range of 100 miles (that is the proximity), the transmission lines showed minor effects and the instability are mainly because of STATCOM control.

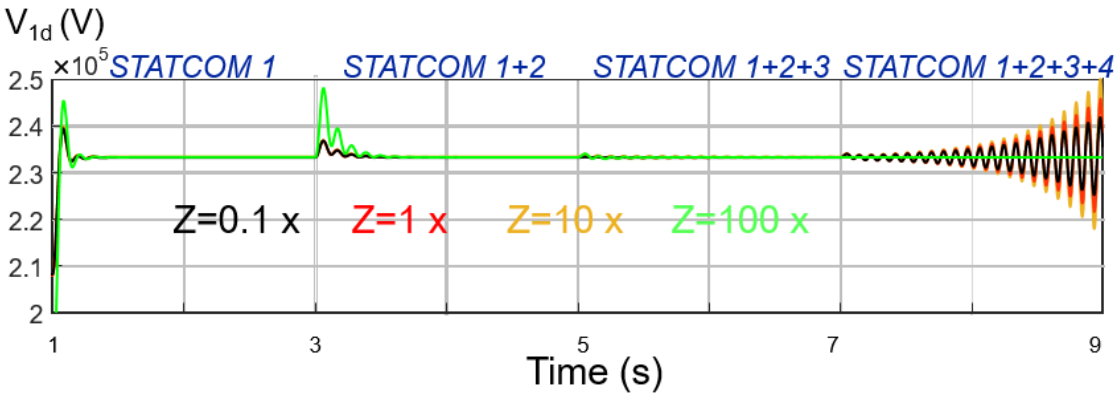

Figure 2-11 Evaluation of impacts of transmission lines between STATCOMs

In summary, for power system under the following assumptions: 1) the load composition is constant power load plus constant impedance load; 2) the STATCOMs are properly sized for compensation; 3) the line impedances are 0.0002~0.2 per unit, the simulation results suggested that STATCOMs could fight each other and fall into instability. In addition, we can conclude that the instability was mainly because of the interactions between STATCOMs and the corresponding control played a very important role. This strengthens the importance of this work and careful design should be performed when adding multiple STATCOMs in proximity to a transmission grid.

2.4 A simplified 2-STATCOM system

To simplify the system and facilitate analysis in the following chapters and sections, a 2-STATCOM system was considered in Figure 2-12 as it is the simplest network where STATCOM could interact with each other. From Section 2.3, we have discovered that the STATCOM control is the main factor of instability. Therefore, the same evaluation was conducted in this section to show that the simplification is meaningful as a testbed in terms of small-signal stability analysis.

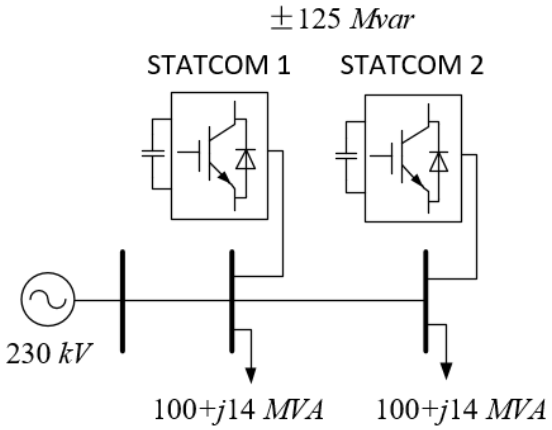

Figure 2-12 A simplified 2-STATCOM system

Similarly, STATCOM 1 and 2 were connected at 0.5 and 1.5 second respectively and the PCC bus voltage in d-channel V_{1d} at the first STATCOM was shown in Figure 2-13. Three factors found significant from STATCOM control - PLL, current loop and ac voltage loop - were evaluated from top to bottom. For PLL on the top of Figure 2-13, the highest bandwidth at 10 Hz in green made the system unstable while the lower bandwidths at 2.5 Hz in blue and 5 Hz in yellow showed a marginal stability. In the middle of Figure 2-13, low current loop bandwidth at 100 Hz in blue showed instability and bandwidth at 200 Hz presented a marginally stable case. Further increased current loop bandwidth at 500 Hz stabilized the system. As for the ac voltage loop in the bottom of Figure 2-13, the scenario with the highest bandwidth at 20 Hz was unstable while the system became stable if the bandwidth was decreased to 1.4 Hz or 6 Hz.

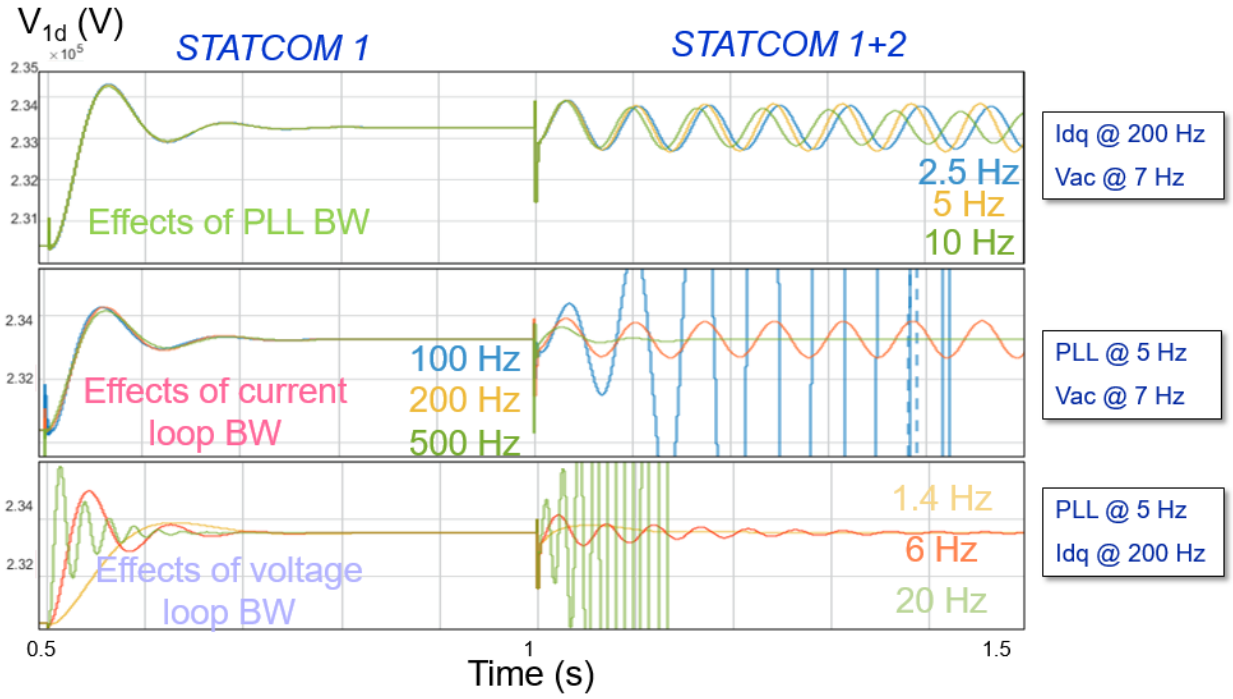

Figure 2-13 Evaluation of impacts of STATCOM control in the 2-STATCOM system

Figure 2-14 shows the impacts of STATCOM operation modes, with the ac voltage regulation mode in blue and the QV droop mode in red. The same conclusions can be drawn here that the QV droop made STATCOMs produce less reactive power and the system tended to be unstable.

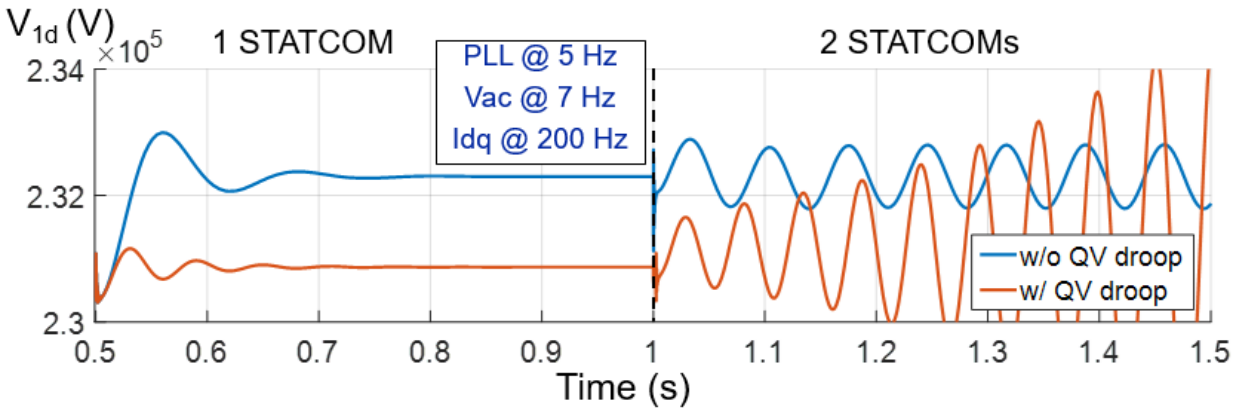

Figure 2-14 Evaluation of impacts of STATCOM operation modes in the 2-STATCOM system

As such, similar oscillatory phenomena were observed in the simplified 2-STATCOM system with the same conclusions that higher PLL bandwidth, higher current loop bandwidth and lower ac voltage loop bandwidth tend to stabilize the system. Thus, the previous found instability problem not only happened in Dominion Energy's system but also the simplified 2-STATCOM radial system, and the stability assessment applies to power systems under the aforementioned assumptions. Also, the 2-STATCOM system is a good simplification to start with

2.5 Scaled-down testbed and experimental verifications

Due to laboratory limitations, only scaled-down experiments can be conducted and also the simplified 2-STATCOM system can be constructed. Two 2-level 3-phase voltage source converters working as STATCOMs were built, one using 50 A, 600 V Si-based IGBT module PM50CL1A060 from Mitsubishi and the other using 120 A, 1200 V SiC-based MOSFET module CAS120M12BM2 from Cree. In order to filter out the harmonics from the switching behaviors,

LCL filters were implemented instead of L filters. The resonant frequency of the LCL filter is about 1.7 kHz, much higher than the fastest current bandwidth, and thus not affecting the stability under study. The converter systems are both controlled by DSP TMS320F28343 from Texas Instruments and CPLD LCMXO2-4000HC-4TG144C from Lattice integrated into one motherboard with sensing, protection and self-startup capabilities. The gate driver boards were separately designed in order to achieve better switching performances. The parameters of passive components of both STATCOMs were chosen to be the same as well as the control parameters, listed in Table 2.2. STATCOM 1 is shown in Figure 2-15 and STATCOM 2 is shown in Figure 2-16, with fully functional converter systems including all passive components, digital control systems and auxiliary components. The details of the scaled-down testbed are further described in Appendix in the end of this Chapter.

Table 2.2 Parameters of scaled-down STATCOMs

Parameter	**Symbol**	**Value**
DC bus voltage	V_{dc}	300 V
Switching frequency of the STACOMs	f_{sw}	20 kHz
Inductance of inverter side inductor of LCL filter	L_1	250 μH
Resistance of inverter side inductor of LCL filter	R_1	20 mΩ
Inductance of grid side inductor of LCL filter	L_2	250 μH
Resistance of grid side inductor of LCL filter	R_2	33 mΩ
Capacitance of capacitor of LCL filter	C	35 μF
Damping resistor in LCL filter	R_c	1 Ω
Capacitance of the dc capacitor	C_{dc}	600 μF
Discharging resistor in dc side	R_{dc}	20 kΩ
Current controller $k_{pi} + k_{ii}/s$	k_{pi}	0.0055
	k_{ii}	2.75
PLL controller $k_{pPLL} + k_{iPLL}/s$	k_{pPLL}	0.549
	k_{iPLL}	5.49
AC voltage controller $k_{pac} + k_{iac}/s$	k_{pac}	0.034
	k_{iac}	334

DC voltage controller $k_{pdc} + k_{idc}/s$	k_{pdc}	0.043
	k_{idc}	0.144

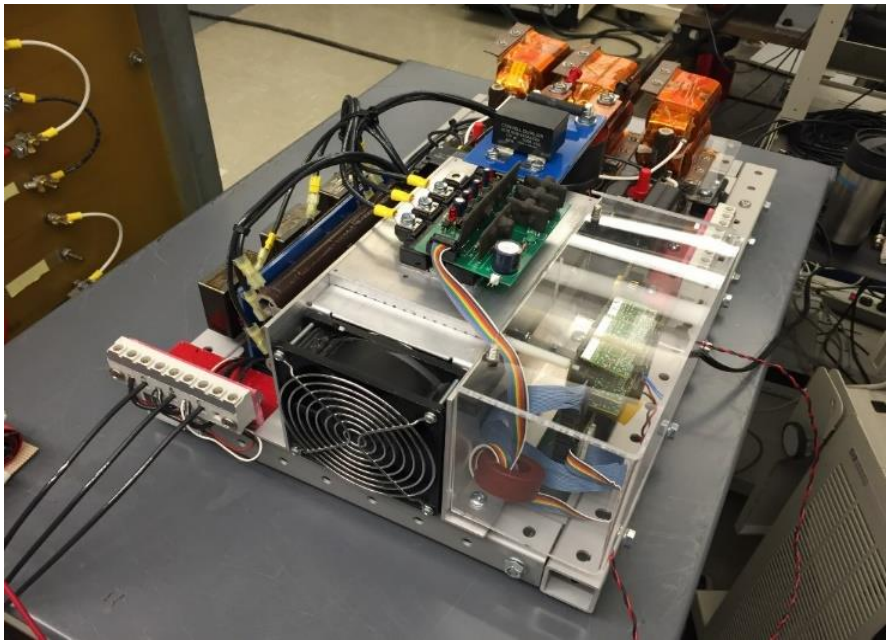

Figure 2-15 Scaled-down STATCOM 1

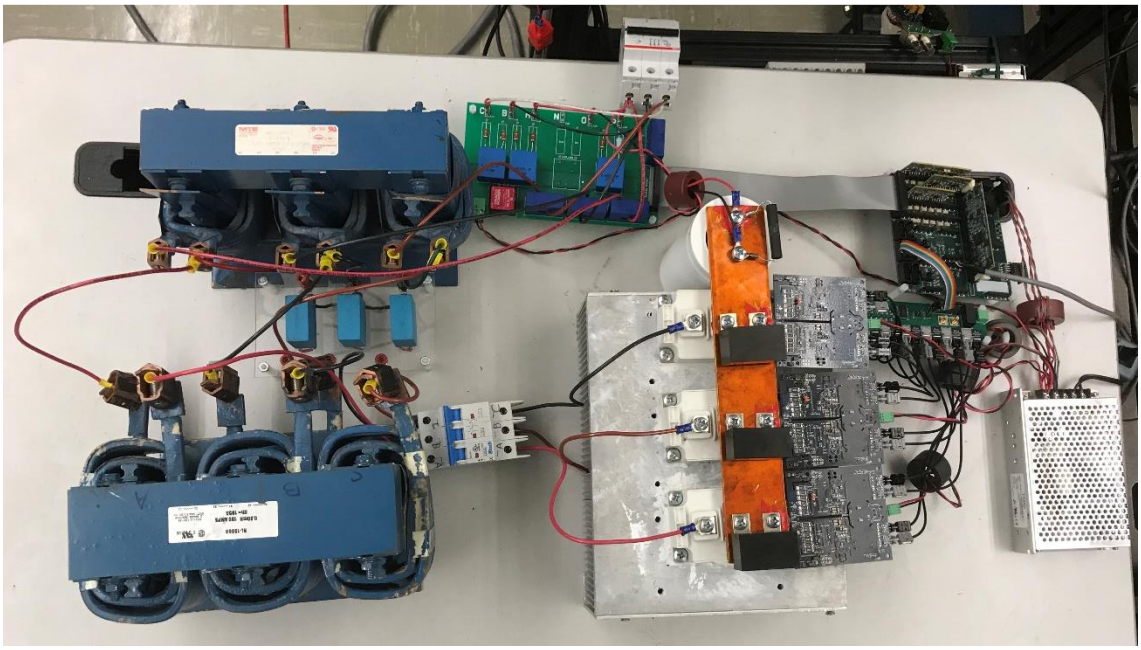

Figure 2-16 Scaled-down STATCOM 2

With the two STATCOMs working, Figure 2-17 shows the schematics of the scaled-down 2-STATCOM system and Figure 2-18 is the picture of it. A voltage source 6814b from HP was used as the infinite bus and resistive loads were selected with line impedances in between. The loads and lines were selected with similar per unit values with those in simulation, as Table 2.3 shows.

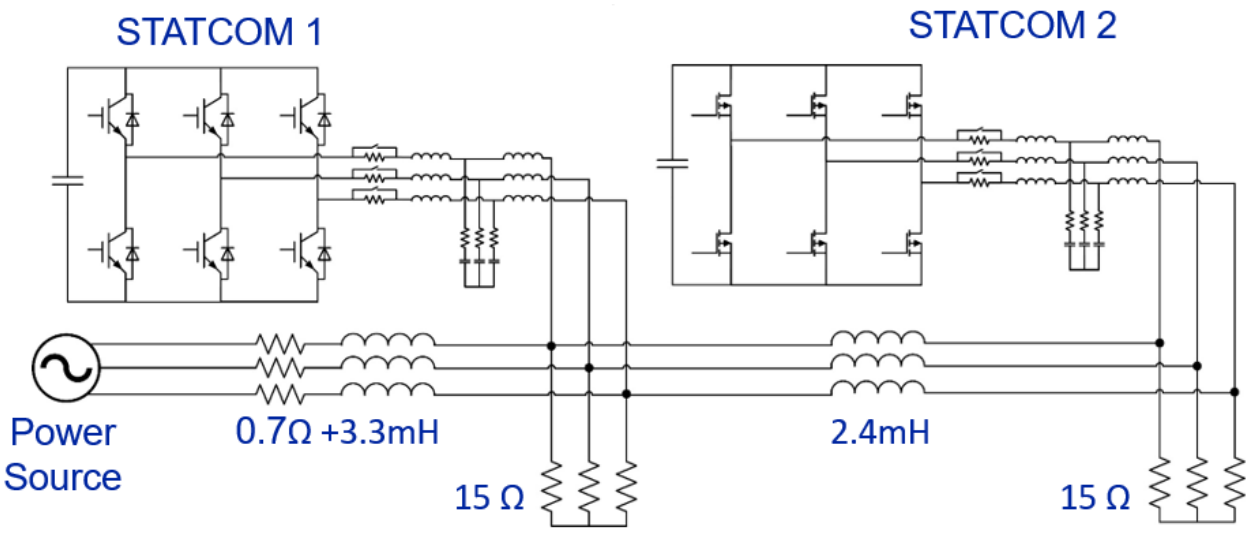

Figure 2-17 Scaled-down 2-STATCOM system schematics

Table 2.3 Impedances comparison between simulation and experiment

	Simulink		**Experiment**	
Z_{base}	529 Ω		7.26 Ω	
Z_{linedd} (X_L)	0.003~0.09 p.u.	@ 60 Hz	0.06 p.u.	@ 60 Hz
Z_{STATdd}	0.004 p.u.	@ 0 Hz	0.11 p.u.	@ 0 Hz
	0.13 p.u.	@ ~20 Hz	0.45 p.u.	@ ~20 Hz
Z_{load}	1~3 p.u.	@ ~20 Hz	2 p.u.	@ ~20 Hz

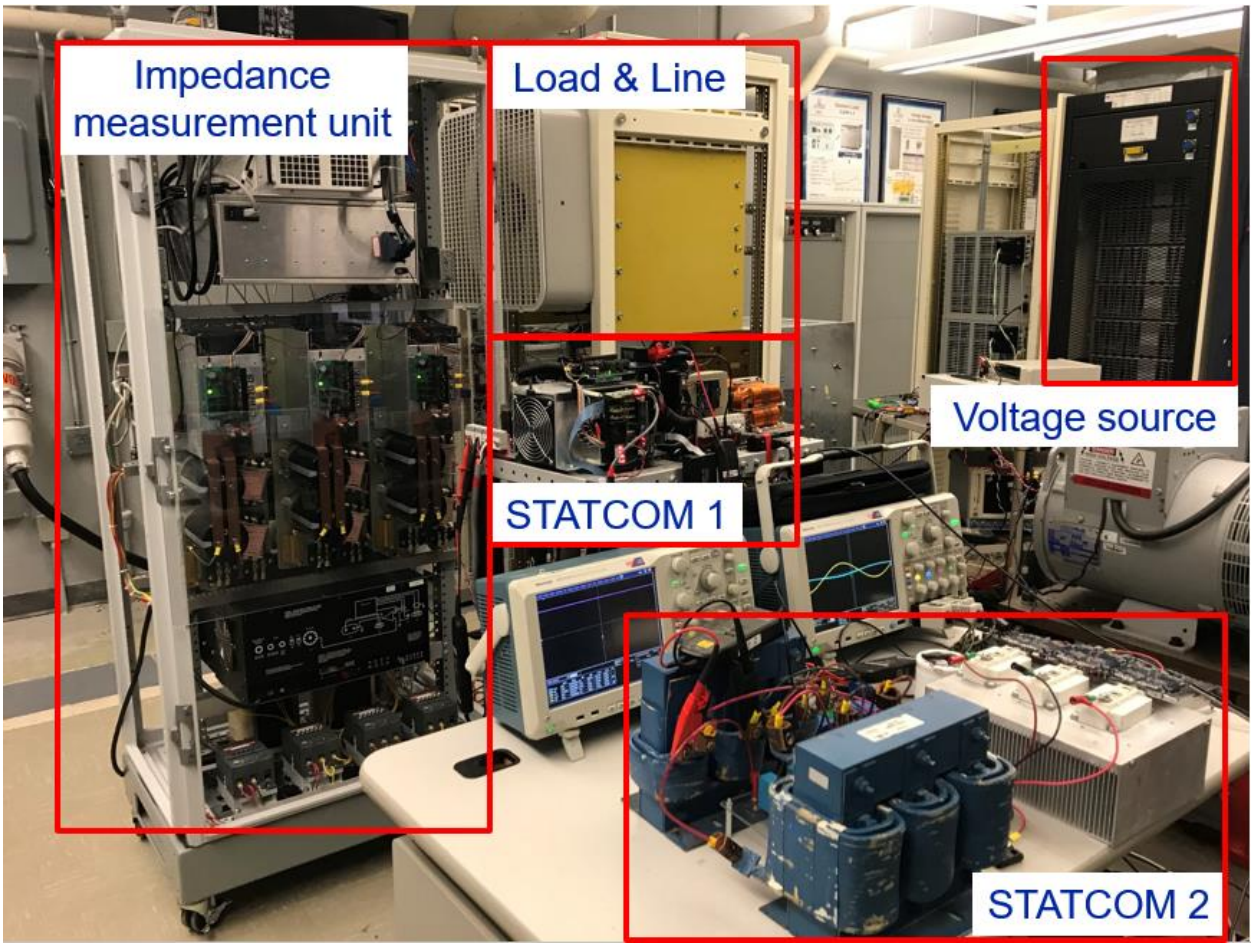

Figure 2-18 Scaled-down 2-STATCOM system

Two STATCOMs started up with the voltage source powering the loads and their dc capacitors were charged via anti-parallel diodes of the power electronics devices. Their dc bus voltages were charged further more to the nominal values after their controllers were synchronized with the system and started sending PWM signals for switching. After this, they stood by, waiting for commands of reactive power compensation from PC consoles. Figure 2-19 shows the PCC bus line to line voltages at the terminals of the two STATCOMs, v_{ab1} and v_{ab2}, and injecting current in phase a of the two STATCOMs i_{a1} and i_{a2} from top to bottom. At first, neither of the STATCOMs was exchanging reactive power with the grid and only a small amount of current was drawn from the grid to balance the losses in the converters. Then STATCOM 1 started to compensate reactive

power, followed by the additional compensation of STATCOM 2, marked on the figure. This case was a stable case as a benchmark with two STATCOMs running where the control loop bandwidths were listed in the figure.

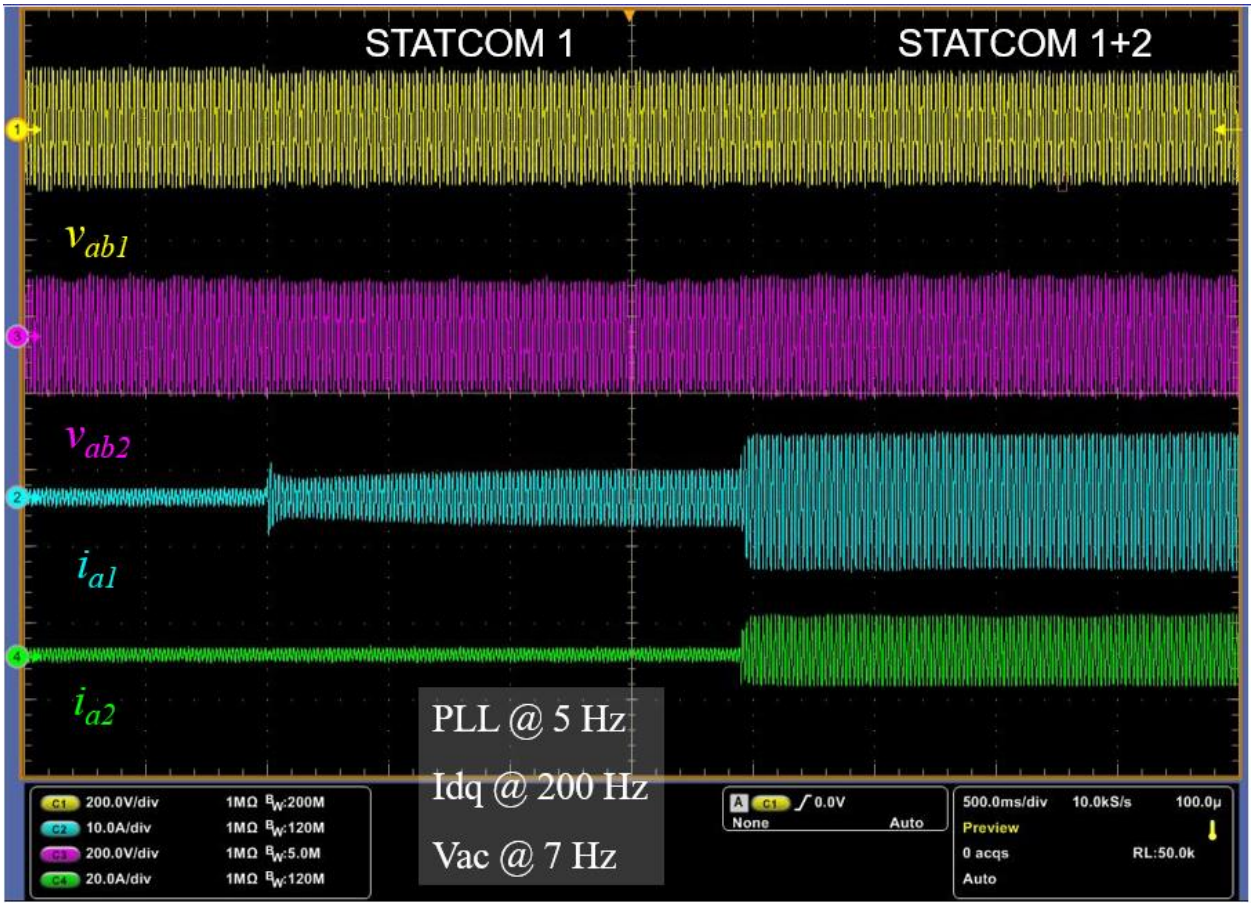

Figure 2-19 Experimental waveforms of 2 STATCOMs: stable case

If the ac voltage loop bandwidth was increased from 7 Hz to 12 Hz, one can see in Figure 2-20 that the system was unstable and the injecting current oscillated, triggering the over-current protection in the end. This phenomenon verified the previous simulation that a higher ac voltage loop bandwidth tends to destabilize the system. Figure 2-21 plots the normalized power spectrum of injecting current in Figure 2-20. The line frequency component in 60 Hz has the magnitude of 1 and the second largest components showed at 102 Hz. If transformed into d-q frame, this 102 Hz component became as 42 Hz oscillation since the line frequency was 60 Hz.

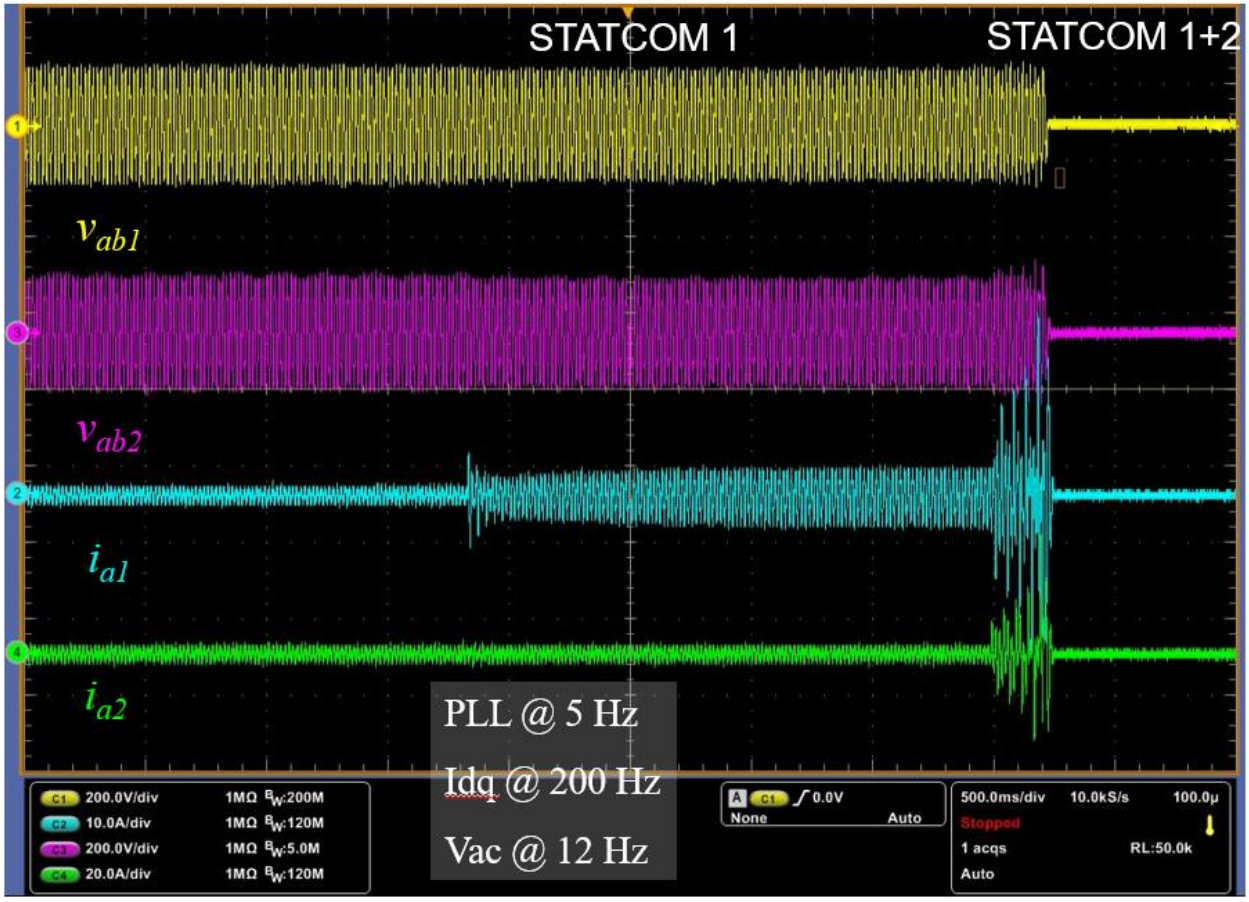

Figure 2-20 Experimental waveforms of 2 STATCOMs: unstable case due to ac voltage loop

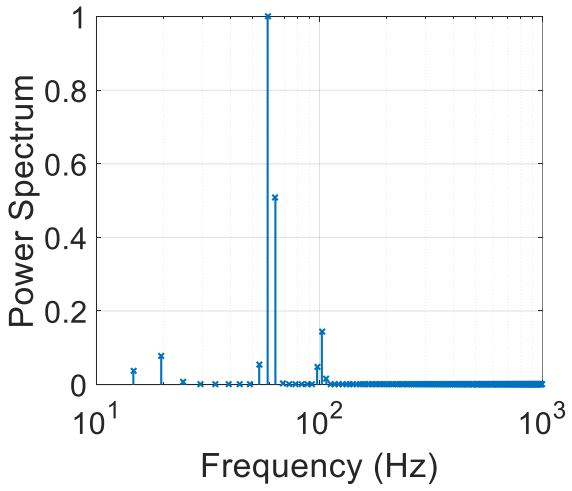

Figure 2-21 Spectrum of current waveforms in unstable case due to ac voltage loop

Figure 2-22 shows how the system behaved if the current loop bandwidth was decreased. The same process of tests was conducted but with a lower current loop bandwidth at 150 Hz. When STATCOM 2 started to compensate, the system oscillated again and triggered the over-current protection. Figure 2-23 analyzed the normalized power spectrum of the injecting current too, showing the second largest component at 92 Hz, which was 32 Hz in d-q frame.

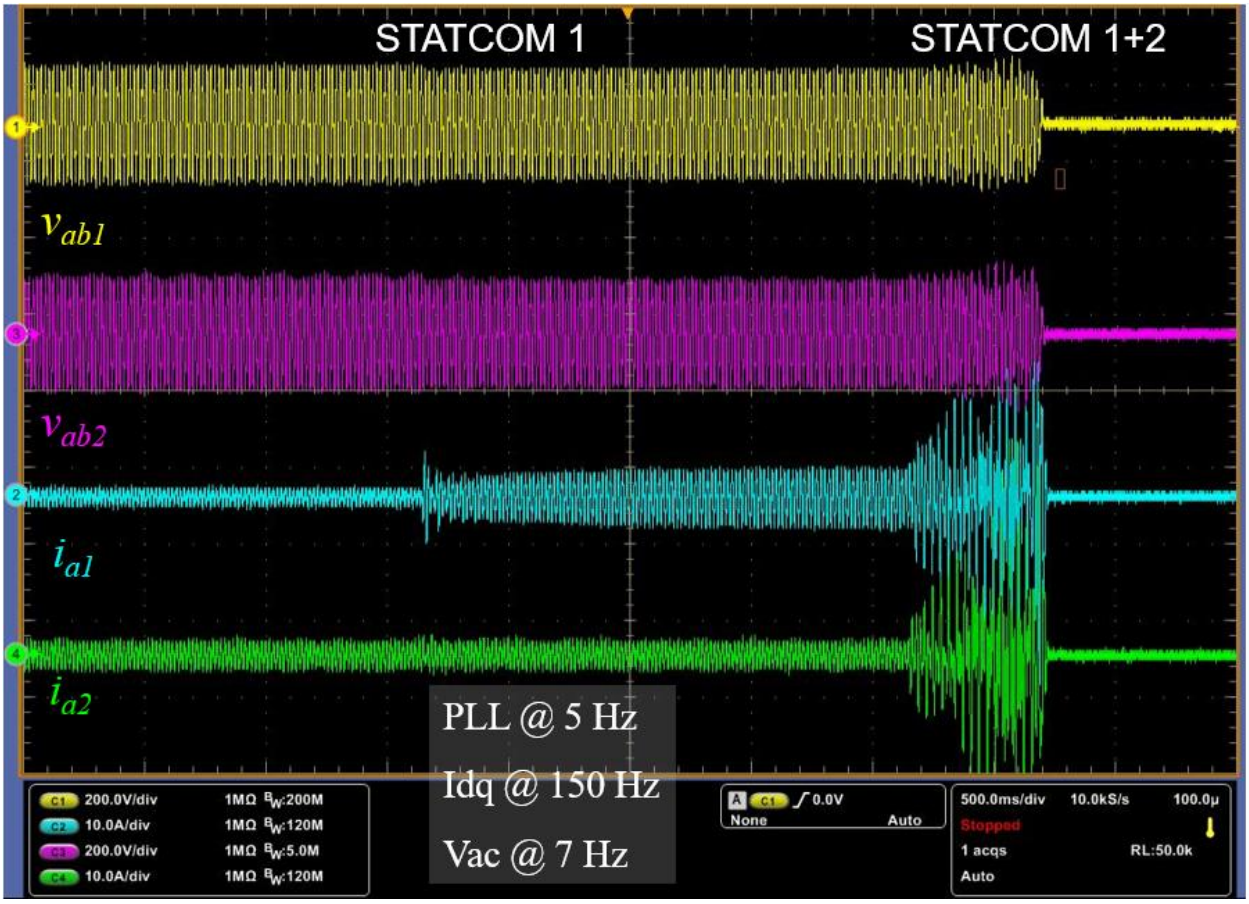

Figure 2-22 Experimental waveforms of 2 STATCOMs: unstable case due to current loop

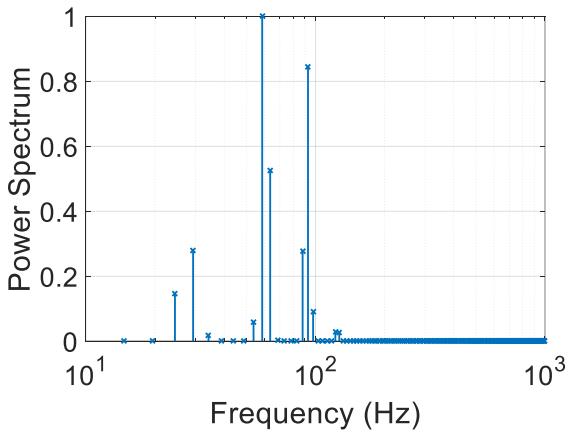

Figure 2-23 Spectrum of current waveforms in unstable case due to current loop

To find a case where the effects of PLL bandwidth were easier to observe, a marginally stable case were identified by increasing the ac voltage loop a little bit from 7 Hz to 10 Hz and increasing the PLL bandwidth from 5 Hz to 10 Hz compared to the benchmark case in Figure 2-19. The marginally stable case is shown in Figure 2-24 where the system was much less damped when STATCOM 2 began compensating reactive power.

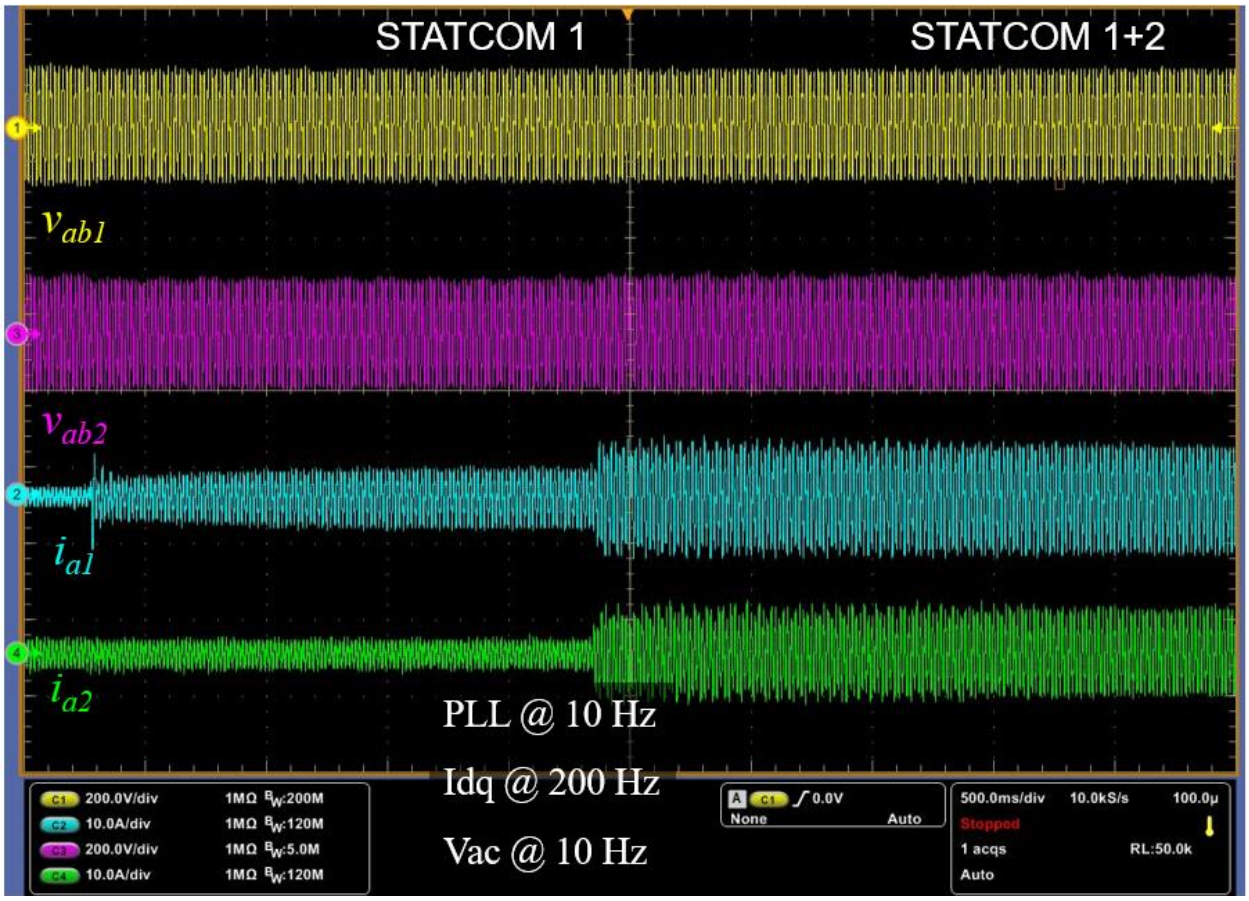

Figure 2-24 Experimental waveforms of 2 STATCOMs: marginally stable case

From the marginally stable case, the PLL bandwidth was reduced from 10 Hz to 5 Hz and the experimental results are shown in Figure 2-25. The system then fell into instability with the over-current protection triggered. Figure 2-26 plotted the normalized power spectrum of the injecting current in Figure 2-25 and the second largest component at 102 Hz in abc frame or 42 Hz in d-q frame were identified.

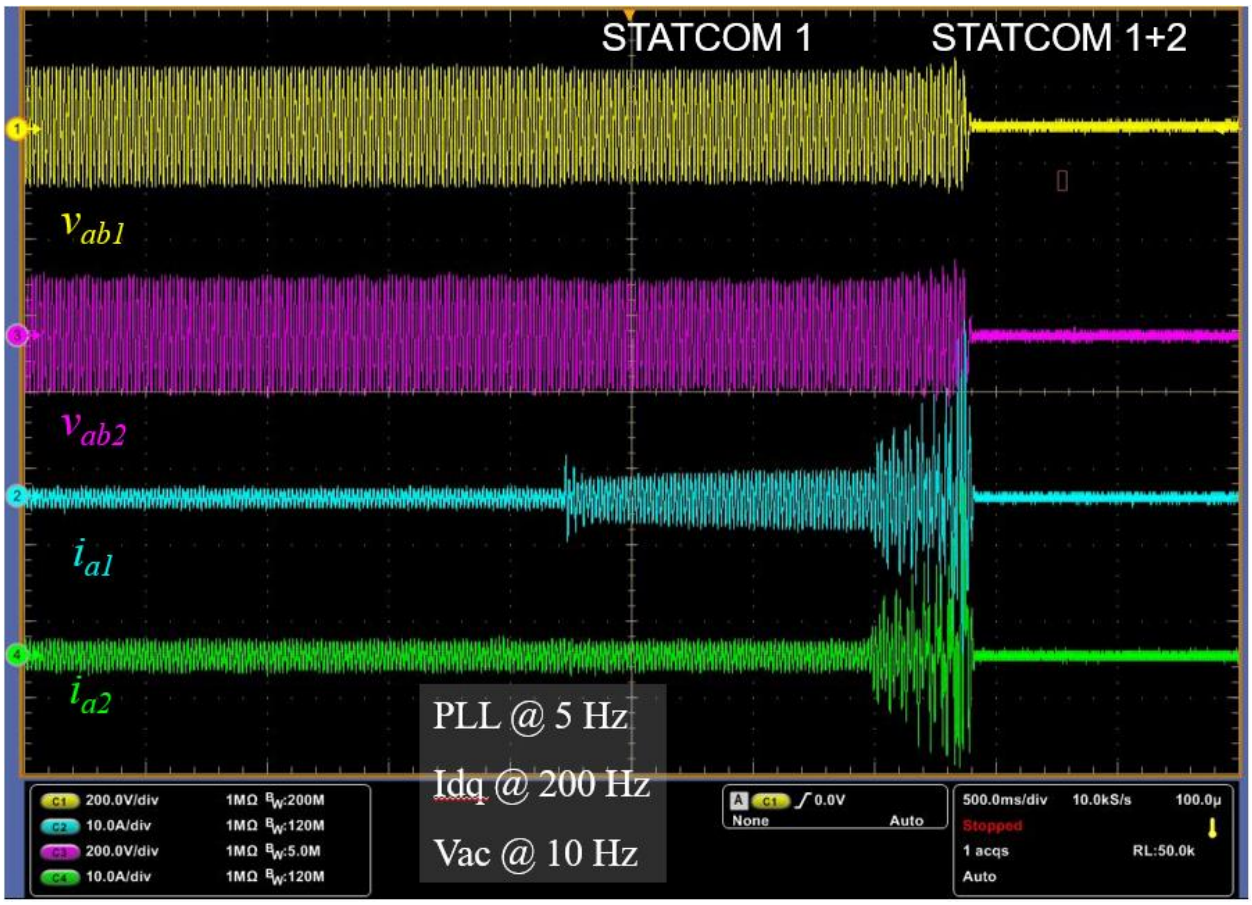

Figure 2-25 Experimental waveforms of 2 STATCOMs: unstable case due to PLL

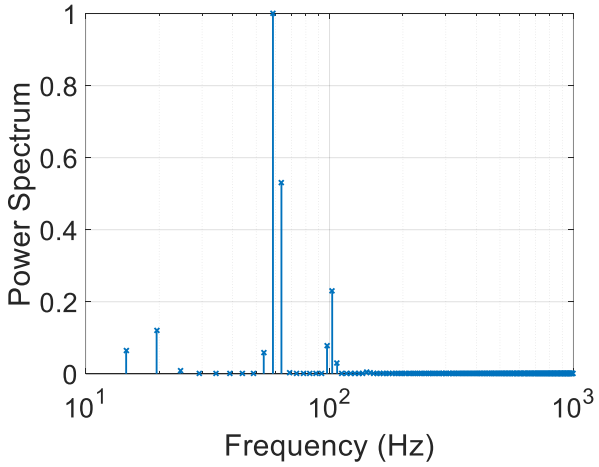

Figure 2-26 Spectrum of current waveforms in unstable case due to PLL

Lastly, when the QV droop was activated compared to the benchmark case, the system was unstable too and the experimental results are shown in Figure 2-27. The power spectrum of the

current is depicted in Figure 2-28 and the oscillatory frequency was 19 and 101 Hz in abc frame, which corresponded to 41 Hz in the dq frame.

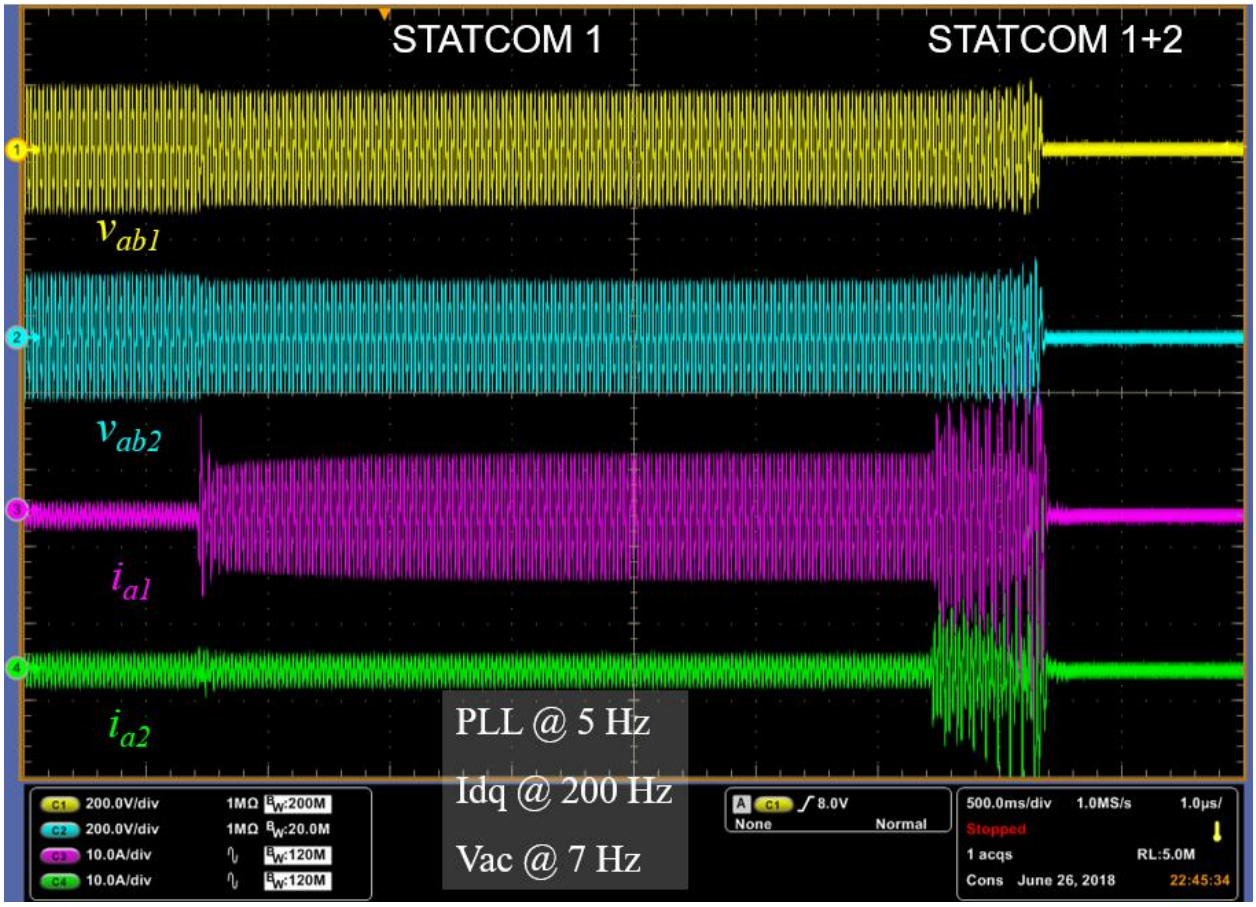

Figure 2-27 Experimental waveforms of 2 STATCOMs: unstable case due to QV droop

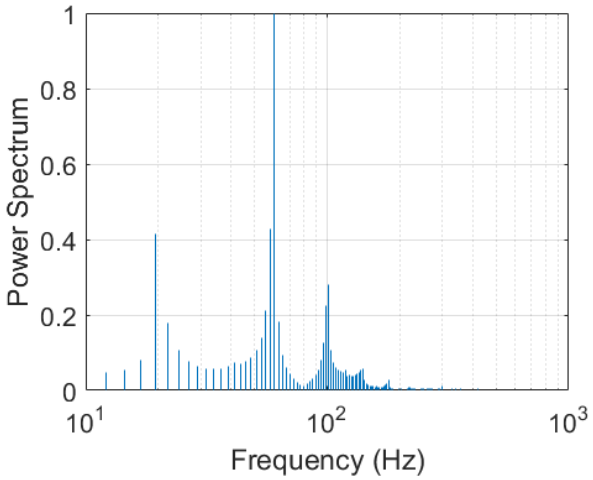

Figure 2-28 Spectrum of current waveforms in unstable case due to QV droop

To summarize, the above experimental results validated the simulation with the same conclusions that higher PLL bandwidth, higher current loop bandwidth, lower ac voltage loop bandwidth and no QV droop tend to stabilize the system.

2.6 Conclusions

In this chapter, the operation of power systems with multiple STATCOMs in proximity was introduced and evaluated. The power system under study has typical load composition (constant power load and constant impedance load) with properly-sized STATCOMs for voltage regulation. The line impedances are within the range of 0.0002 per unit to 0.2 per unit for a 230-kV 2-GW system, which can be physically translated into line lengths between 1 to 100 miles. With the detailed modeling of STATCOMs and the power system, simulation was conducted to assess the small-signal stability using MATLAB/Simulink and possible voltage instability could happen.

It was found out that voltage oscillations were primarily dependent on the STATCOM control while the loads and the transmission lines between STATCOMs had negligible impacts, because the impedance of STATCOMs were significantly larger than that of lines and smaller than that of

loads. This would be further explained in details in Chapter IV and V. The grid stiffness that is determined by the transmission lines connecting to the infinite buses strongly affected the stability. Therefore, the observed voltage instability problem was induced by STATCOMs, specifically the interactions between them. For the STATCOM control, slower ac voltage loop bandwidth, higher current loop bandwidth, higher PLL bandwidth and no QV droop improved the stability conditions.

In order to simplify analytical analysis and start researching from a simple case, a 2-STATCOM system was then introduced. The same conclusions were found in the simulation of the simplified system, making it a good candidate for further analysis. This 2-STATCOM system was also validated experimentally in a scaled-down system with two STATCOM prototypes and the same conclusions were reached.

2.7 Appendix

2.7.1 Converter configuration and digital control

The two converters have the same configuration and the differences are the selection of power electronics devices and corresponding gate driver boards. One converter is based on a Mitsubishi silicon IGBT module PM50CL1A060 and the other is using 3 SiC-based MOSFET modules CAS120M12BM2 from Cree. The gate driver board of the Si-based converter was modified from the BP7B gate driver board from Powerex, with only inputs rearranged for compatibility of the control mother board. The gate driver board of the SiC-based converter was specifically designed by Jun Wang [142], with protection and turn-on/off speed adjustment.

The mother boards and sensing boards for both converters are the same. The motherboards include a DSP, TMS320F28343 from Texas Instruments, and a CPLD, LCMXO2-4000HC-

4TG144C, from Lattice, designed by Zhiyu Shen [143]. The sensing boards are using LEM 25-P for voltage sensing and LEM 55-P for current sensing.

The sensed voltages and currents are sent to the mother board to its DSP through signal conditioning boards and offset for A/D for the DSP. Another path for sensed voltages and currents goes to the CPLD via a set of analog comparators, which simply judge if they are out of pre-set ranges by users for over-voltage/current protections. The DSP receives commands from the PC, including references for the PCC voltage and operation mode. The controllers of the STATCOMs are implemented digitally in DSP using C codes, given the sensed currents and voltages and commands from the PC, and send PWM signals to the CPLD. A manual switch is connected to an I/O port of the DSP to start the STATCOM operation and for emergency stop as well. The CPLD acts like a buffer for PWM signals and sends signals to the gate driver board if it receives no fault signal. When there is a fault signal, from either the gate driver board, or pre-set over-current/voltage protections by users or emergency stop from users, the CPLD will send blocking PWM signals to the gate drive board immediately and return a fault signal to the DSP to stop the codes. The reason for the additional layer of CPLD is to provide fast and robust protection, because it is implemented via logic gates in CPLD instead of codes in DSP, which are influenced by missing communication to the emulator or crashed PC program.

2.7.2 Start-up process

Referring to synchronous condensers, there are typically two kinds of starting methods [144]. The first method is to connect a synchronous condenser to the grid via its transformer tapping down the voltage to speed up the torque, and then increase the secondary side voltage gradually to accelerate to the grid frequency. The second method is to use an additional motor to drive its torque

to the grid frequency approximately, and then use a synchronizer to synchronize before closing the main circuit breaker.

With these ideas, there are also two corresponding methods for a STATCOM. The first one is to connect the converter to the grid and use the anti-parallel diodes of switching devices to charge the dc capacitor while in the meantime the controller begins to synchronize. When the dc bus voltage reaches the steady-state and the synchronization completes, the converter starts switching with the current loop and the dc voltage loop running to charge the dc capacitor further to the nominal value before starting the ac voltage loop to compensate. The second one is to use a separate dc source to charge the dc bus voltage to its nominal value through a pre-charging circuit without connection to the grid and mimic a synchronizer to synchronize. After the dc bus is charged and synchronization is finished, a main circuit breaker is closed and all the loops except the ac voltage loop start working to ensure smooth connection. Finally, the ac voltage loop is turned on to begin compensation. Comparing these two method for a STATCOM, the first one is preferable because it is easier to implement without addition of an extra dc power source and potential danger due to failure mimicking synchronizer.

Chapter 3. D-Q FRAME IMPEDANCE MODEL OF STATCOM

3.1 State of the art: an overview

A first attempt to describe their behavior deriving the small-signal model of a STATCOM was presented in [22, 29, 37], nonetheless neglecting both the current loop and the phase-locked loop (PLL) used to synchronize its operation with the grid, in what is a reduced order model used to understand the basic operating principles of such units. A full-order model of a STATCOM, including the details of the controller, was then presented in [28]. These were formulated, however, in state-space form for analytical and simulation purposes, which requires to have full knowledge of the STATCOM physical and control system structure, and also of the system, in order to use the models for stability studies. This is usually difficult given the various origin of equipment and proprietary constraints that limit information flow between vendors [51].

A more promising and practical alternative is the use of impedance-based stability analysis, which has been proven of great success in dc systems for a long time [55], and has since then become attractive too in power electronics based three-phase ac systems [56-60, 62, 63, 70, 78, 90, 145-149]. Such analysis uses the measureable terminal characteristics of power converters, that is, their small-signal input and output impedances, to analyze the small-signal stability at a given ac-bus or interface at a given operating point. As such, this approach can assess the small-signal stability of systems without knowing the internal details of power converters and other system components, representing a significant advantage for system integrators.

Along these lines, this chapter derives first the d-q frame terminal impedance of a three-phase STATCOM providing insight into the different physical and control system components that compound it, and hence facilitates the use of impedance-based stability analysis in power systems supported by STATCOM units. Such analysis has not been reported so far to the best knowledge of the authors. It represents nonetheless an extension to several small-signal models of power converters that have been analyzed in the past, including [61, 62, 83, 145, 150, 151]. Among these, some models were built in the abc-frame [61, 62, 70, 79, 150, 152], while others are in the d-q frame, both of which have been proven to be equivalent in recently published work [66, 67]. Accordingly, the study of stability at given ac interfaces can be conducted using small-signal impedances in both abc-[62] and d-q frames [56, 57]. In this chapter, the latter approach is pursued given that STATCOM controllers are primarily designed in the d-q frame—seeking to control independently their active and reactive power flow, thereby gaining more insight into the shaping of their impedance by modeling them in the d-q frame too. The d-q frame impedance model derived is finally validated against the measured d-q frame impedance of a 10 kVA STATCOM prototype unit, obtained with an impedance measurement unit (IMU) capable of measuring impedances in the 0.1 Hz to 1 kHz range [153].

From the model, several key features of STATCOM units are identified, which ultimately determine the possibility of a STATCOM to induce dynamic interactions with other system components. The first one is that the impedance of a STATCOM, working at nearly zero power factor, has strong coupling between its d-q channels, which renders all d-q frame impedance elements of similar magnitude. The second feature is that the negative-incremental input impedance of a STATCOM can be reflected either on its d- or q-axis channel depending on its reactive power operating mode, where reactive power is generated to support the grid voltage, and

absorbed under high voltage conditions [59]. This unique characteristic represents a challenge from a stability standpoint as previous findings had shown that instability could be triggered either in the d-channel due to constant power load (CPL) dynamics [56], or in the q-channel as a result of active power being injected synchronously into the grid [57]. STATCOMs, with their dual behavior, and hence double-challenge, embody in consequence a new instability pattern in power system. The third feature is that STATCOMs, by nature, compensate the voltage at the point of common coupling (PCC), which is also where they synchronize their operation. As a result, their synchronization and ac voltage compensation loops are inherently and strongly coupled from a control standpoint, as they do not simply track the grid voltages, but regulate them. All these dynamic characteristics differ significantly from those of grid-tied inverters and rectifiers, which renders previous stability-related findings for these converters nonapplicable directly. The d-q frame impedance model derived will consequently provide aid in this direction seeking to avoid interactions between STATCOMs and with other system components.

3.2 Open-loop power stage model

The schematics and control systme of the STATCOM is shown in Figure II-2. To start with, the averaged small-signal circuit of one STATCOM was plotted in Figure III-1 with v_g to be the ideal grid voltage source at the infinite bus as a reference, v_{PCC} to be the voltage at PCC, i to be the injected current and duty cycle d multiplied by STATCOM's dc voltage V_{dc} to be the output voltage of it. Note that this is based on STATCOM averge model which ignores the switching behaviors but contains every details of the controller in the frequency domain. The d-q frame is aligned with the infinite bus for integration of impedance models in a grid at different buses. That is to say, the derived d-q frame impedance model is based on a common voltage v_g in a given grid.

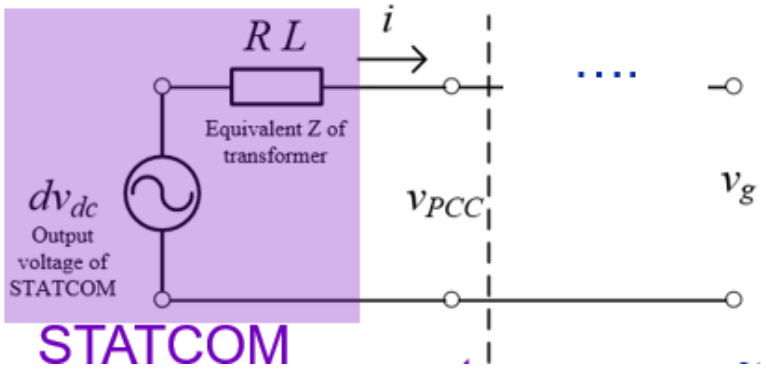

Figure 3-1 Small-signal circuit of STATCOM and grid

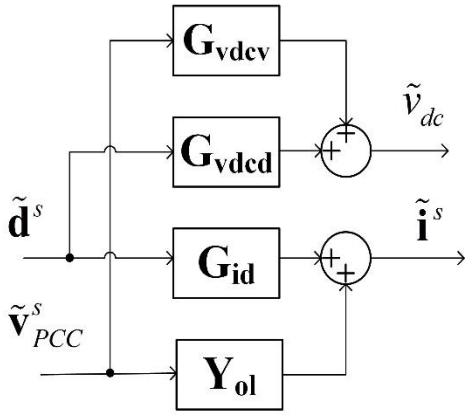

Figure 3-2 Small-signal model of open-loop STATCOM and grid

From the small-signal circuit, the small-signal model of STATCOM and grid without any control can be plotted in a control block diagram form as in Figure III-2 where $\mathbf{G_{vdcv}}$ is the transfer function matrix from the grid voltage in the system frame $\tilde{\mathbf{v}}^s_{PCC}$ to the dc voltage $\tilde{v}_{dc}$; $\mathbf{G_{vdcd}}$ is the transfer function matrix from the duty cycle in the system frame $\tilde{\mathbf{d}}^s$ to the dc voltage $\tilde{v}_{dc}$; $\mathbf{G_{id}}$ is the transfer function matrix from $\tilde{\mathbf{d}}^s$ to the injected current in the system frame $\tilde{\mathbf{i}}^s$; $\mathbf{Y_{ol}}$ is the transfer function matrix from the grid voltage in the system frame $\tilde{\mathbf{v}}^s_g$ to $\tilde{\mathbf{i}}^s$, which is also known as the open-loop admittance matrix and is the inverse of the open-loop impedance $\mathbf{Z_{ol}}$. The open loop transfer functions can be found in the appendix of this chapter. The bold variables are 2-by-1 vectors or 2-by-2 matrices and the tilde indicates that they are in the small-signal sense. The

impedance of the STATCOM is defined as the ratio between $\tilde{\mathbf{v}}^s_{PCC}$ and $\tilde{\mathbf{i}}^s$ (although the notation is not mathematically rigour):

$$\mathbf{Z}_{STAT} = \frac{\tilde{\mathbf{v}}^s_{PCC}}{\tilde{\mathbf{i}}^s} \tag{3.1}$$

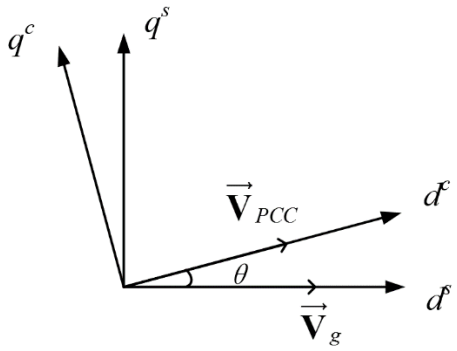

Figure 3-3 System and controller dq-frames

To further illustrate, there are two d-q frames defined – one called the system d-q frame whose d-axis is aligned with the infinite bus grid voltage phasor $\vec{\mathbf{V}}_g$ which can be considered as stiff and the other called the controller d-q frame whose d-axis is aligned with PCC bus voltage phasor $\vec{\mathbf{V}}_{PCC}$, with which the STATCOM's controller is synchronizing. By separating those two frames, the dynamics from the synchronization process can be included and the steady-state positions of these two voltages are not the same. Figure III-3 illustrates these two frames with the controller one (superscript "*c*") aligned with v_{PCC} and the system one (superscript "*s*") aligned with v_g where the steady-state phase difference is θ, which is introduced by the line impedance and power transfer between the PCC bus and infinite bus, without loss of generality. Thus any variables in one d-q-frame can be translated to the other by multiplying a transition matrix **T** or its inverse, which is:

$$\begin{aligned} \mathbf{v}^c_{PCC} &= \mathbf{T}\mathbf{v}^s_{PCC} \\ \mathbf{i}^c &= \mathbf{T}\mathbf{i}^s \\ \mathbf{d}^s &= \mathbf{T}^{-1}\mathbf{d}^c \end{aligned} \tag{3.2}$$

$$\mathbf{T} = \begin{bmatrix} \cos\theta & \sin\theta \\ -\sin\theta & \cos\theta \end{bmatrix} \tag{3.3}$$

With this transition matrix **T** defined, d-q frame impedances in two frames have the following relationship:

$$\mathbf{Z}^c = \mathbf{T}\mathbf{Z}^s\mathbf{T}^{-1} \tag{3.4}$$

In fact, since there is only phase difference in the transformation (3.3), (3.4) is general when transforming d-q frame impedances between different frames. It should be noted that by doing the transformation, impedances defined in different d-q frames can be integrated to a globally common d-q frame, for example a given reference frame, as long as the phase differences to the reference frame are known. Usually this assumption can be satisfied because the steady-state values are solved before doing the small-signal analysis and therefore the phase angles at each terminal are accessible. If analysis of multiple STATCOMs in a given grid is needed, impedances of all STATOMs can be transformed into a same d-q frame for further investigation. Inclusion of the phase angle difference in the impedance model facilitates the extension to multiple STATCOMs cases.

Table 3.1 Parameters of STATCOM in simulation

Parameter	**Symbol**	**Value**
DC bus voltage	V_{dc}	100 kV
D-channel PCC bus voltage in system d-q frame	V^s_{PCCd}	30.35 kV
Q-channel PCC bus voltage in system d-q frame	V^s_{PCCq}	-465.2 V
D-channel grid side current in system d-q frame	I^s_d	-9.12 A
Q-channel grid side current in system d-q frame	I^s_q	-1.78 kA
Inductance of step-up transformer	L	7.3 mH
Resistance of step-up transformer	R	21 mΩ
Capacitance of the dc capacitor	C_{dc}	100 mF

Discharging resistor in dc side	R_{dc}	20 kΩ
Current controller $k_{pi} + k_{ii}/s$	k_{pi}	0.00017
	k_{ii}	0.015
Current loop bandwidth	f_{ci}	500 Hz
PLL controller $k_{pPLL} + k_{iPLL}/s$	k_{pPLL}	0.002
	k_{iPLL}	0.02
PLL bandwidth	f_{cPLL}	5 Hz
AC voltage controller $k_{pac} + k_{iac}/s$	k_{pac}	0.445
	k_{iac}	222.5
AC voltage loop bandwidth	f_{cvac}	20 Hz
DC voltage controller $k_{pdc} + k_{idc}/s$	k_{pdc}	1.25
	k_{idc}	0.225
DC voltage loop bandwidth	f_{cvdc}	0.1 Hz

The parameters of studied STATCOM are shown in Table III-I in analytical derivation and simulation. Note that all the variables are transformed to the low-voltage side of the transformer.

3.3 Derivation of d-q frame impedance model of STATCOM

3.3.1 Effect of PLL

Like any other grid-tied converters, STATCOMs need to synchronize with its terminal ac bus voltage to operate, where a PLL is the most commonly implemented method, among which a simple stationary reference frame (SRF) PLL was chosen for the STATCOM. Other kinds of PLL are out of the scope of this chapter but the same modeling concept can be applied to analyze as well. As mentioned before, the STATCOM detects and synchronizes its own terminal voltage $\vec{\mathbf{V}}_{PCC}$ and there is a phase difference between $\vec{\mathbf{V}}_{PCC}$ and $\vec{\mathbf{V}}_{g}$ which makes the steady-state d-q values of one variables in two frames different. To identify the small-signal perturbation propagated via PLL path from the sensed voltage $\vec{\mathbf{V}}_{PCC}$, transfer function matrices $\mathbf{G}_{\mathbf{PLL}}^{\mathbf{v}}$, $\mathbf{G}_{\mathbf{PLL}}^{\mathbf{i}}$ and $\mathbf{G}_{\mathbf{PLL}}^{\mathbf{d}}$ are defined to represent the small-signal perturbation from the PCC bus voltage in the system

d-q frame $\tilde{\mathbf{v}}_{PCC}^{s}$ to the PCC voltage in the controller d-q frame $\tilde{\mathbf{v}}_{PCC}^{c}$, to the current in the controller d-q frame $\tilde{\mathbf{i}}^{c}$, and to the duty cycle in the controller d-q frame $\tilde{\mathbf{d}}^{c}$ respectively. After applying small-signal perturbation to (3.2) with the PCC voltage, current and duty cycle substituted, we can get:

$$\begin{bmatrix} V_{PCCd}^{s}+\tilde{v}_{PCCd}^{s} \\ V_{PCCq}^{s}+\tilde{v}_{PCCq}^{s} \end{bmatrix} = \begin{bmatrix} \cos\left(\theta+\tilde{\theta}\right) & \sin\left(\theta+\tilde{\theta}\right) \\ -\sin\left(\theta+\tilde{\theta}\right) & \cos\left(\theta+\tilde{\theta}\right) \end{bmatrix} \begin{bmatrix} V_{PCCd}^{c}+\tilde{v}_{PCCd}^{c} \\ V_{PCCq}^{c}+\tilde{v}_{PCCq}^{c} \end{bmatrix}$$
$$\begin{bmatrix} I_{d}^{s}+\tilde{i}_{d}^{s} \\ I_{q}^{s}+\tilde{i}_{q}^{s} \end{bmatrix} = \begin{bmatrix} \cos\left(\theta+\tilde{\theta}\right) & \sin\left(\theta+\tilde{\theta}\right) \\ -\sin\left(\theta+\tilde{\theta}\right) & \cos\left(\theta+\tilde{\theta}\right) \end{bmatrix} \begin{bmatrix} I_{d}^{c}+\tilde{i}_{d}^{c} \\ I_{q}^{c}+\tilde{i}_{q}^{c} \end{bmatrix} \tag{3.5}$$
$$\begin{bmatrix} D_{d}^{c}+\tilde{d}_{d}^{c} \\ D_{q}^{c}+\tilde{d}_{q}^{c} \end{bmatrix} = \begin{bmatrix} \cos\left(\theta+\tilde{\theta}\right) & -\sin\left(\theta+\tilde{\theta}\right) \\ \sin\left(\theta+\tilde{\theta}\right) & \cos\left(\theta+\tilde{\theta}\right) \end{bmatrix} \begin{bmatrix} D_{d}^{s}+\tilde{d}_{d}^{s} \\ D_{q}^{s}+\tilde{d}_{q}^{s} \end{bmatrix}$$

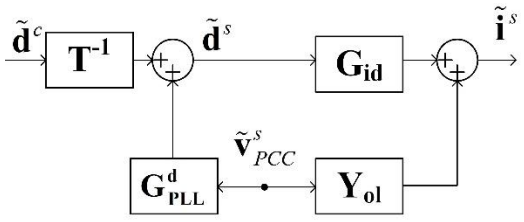

Figure 3-4 Small-signal model of the STATCOM with PLL

According to [14], the output angle in small-signal sense of the SRF-PLL is

$$\tilde{\theta} = \tilde{v}_{PCCq}^{c} \cdot tf_{PLL}\frac{1}{s} \tag{3.6}$$

where

$$f_{PLL} = k_{pPLL} + k_{iPLL}\frac{1}{s} \tag{3.7}$$

Substituting (3.7) into (3.2) and (3.5), and removing the steady-state values, we can get:

$$\begin{bmatrix} \tilde{v}^c_{PCCd} \\ \tilde{v}^c_{PCCq} \end{bmatrix} = \begin{bmatrix} \cos\theta & \sin\theta + \left(V^s_{PCCq}\cos\theta - V^s_{PCCd}\sin\theta\right)G_{PLL} \\ -\sin\theta & \cos\theta - \left(V^s_{PCCd}\cos\theta + V^s_{PCCq}\sin\theta\right)G_{PLL} \end{bmatrix} \begin{bmatrix} \tilde{v}^s_{PCCd} \\ \tilde{v}^s_{PCCq} \end{bmatrix}$$

$$\begin{bmatrix} \tilde{i}^c_d \\ \tilde{i}^c_q \end{bmatrix} = \begin{bmatrix} 0 & \left(I^s_q\cos\theta - I^s_d\sin\theta\right)G_{PLL} \\ 0 & -\left(I^s_d\cos\theta + I^s_q sin\theta\right)G_{PLL} \end{bmatrix} \begin{bmatrix} \tilde{v}^s_{PCCd} \\ \tilde{v}^s_{PCCq} \end{bmatrix} + \mathbf{T}\begin{bmatrix} \tilde{i}^s_d \\ \tilde{i}^s_q \end{bmatrix} \tag{3.8}$$

$$\begin{bmatrix} \tilde{d}^s_d \\ \tilde{d}^s_q \end{bmatrix} = \begin{bmatrix} 0 & -\left(D^s_q\cos\theta + D^s_d\sin\theta\right)G_{PLL} \\ 0 & \left(D^s_d\cos\theta - D^s_q sin\theta\right)G_{PLL} \end{bmatrix} \begin{bmatrix} \tilde{v}^s_{PCCd} \\ \tilde{v}^s_{PCCq} \end{bmatrix} + \mathbf{T}^{-1}\begin{bmatrix} \tilde{d}^c_d \\ \tilde{d}^c_q \end{bmatrix}$$

where

$$G_{PLL} = \frac{tf_{PLL}}{s + V^s_{PCCd}tf_{PLL}} \tag{3.9}$$

Thus according to the previous definitions,

$$\mathbf{G^v_{PLL}} = \begin{bmatrix} \cos\theta & \sin\theta + \left(V^s_{PCCq}\cos\theta - V^s_{PCCd}\sin\theta\right)G_{PLL} \\ -\sin\theta & \cos\theta - \left(V^s_{PCCd}\cos\theta + V^s_{PCCq}\sin\theta\right)G_{PLL} \end{bmatrix} \tag{3.10}$$

$$\mathbf{G^i_{PLL}} = \begin{bmatrix} 0 & \left(I^s_q\cos\theta - I^s_d\sin\theta\right)G_{PLL} \\ 0 & -\left(I^s_d\cos\theta + I^s_q sin\theta\right)G_{PLL} \end{bmatrix} \tag{3.11}$$

$$\mathbf{G^d_{PLL}} = \begin{bmatrix} 0 & -\left(D^s_q\cos\theta + D^s_d\sin\theta\right)G_{PLL} \\ 0 & \left(D^s_d\cos\theta - D^s_q sin\theta\right)G_{PLL} \end{bmatrix} \tag{3.12}$$

If there is no phase difference, which is one of the results of zero grid impedance, these transfer function matrices will devolve to the special case in [Bo]. With all the above transfer function matrices defined and solved, the small-signal model of the STATCOM and PLL in control block form is shown in Figure III-4 and the impedance of STATCOM with PLL implemented can be solved:

$$\mathbf{Z}_{\mathbf{PLL}} = \left(\mathbf{Y}_{\mathbf{ol}} + \mathbf{G}_{\mathbf{id}}\mathbf{G}^{\mathbf{d}}_{\mathbf{PLL}}\right)^{-1} \tag{3.13}$$

Figure III-5 shows the effects of PLL where the blue curve is the open loop impedance of the STATCOM and the red curve is the impedance with PLL. For the open loop impedance, the low frequency part shows the dc capacitor reflected to the ac side and the high frequency part shows the impedance of the transformer. The impedance with PLL shows a resonant peak at 5 Hz, which is its bandwidth and regulates the low frequency part to be resistive while keeping the high frequency part the same.

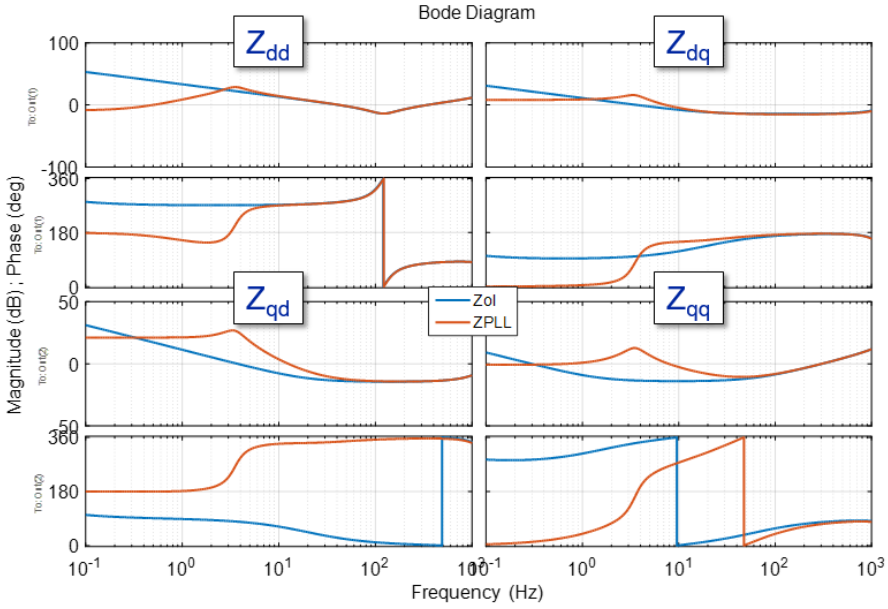

Figure 3-5 STATCOM impedances: open loop (Zol) and with PLL (ZPLL)

3.3.2 Effects of current control loops

With the STATCOM synchronized with the grid using PLL, the current controller and voltage controller can be applied to enhance the operation. The small-signal model of the STATCOM with PLL and current loop is shown in Figure III-6 where the PI current controller is implemented in the controller d-q frame as (3.14) with its reference $\tilde{\mathbf{i}}^{c*}$.

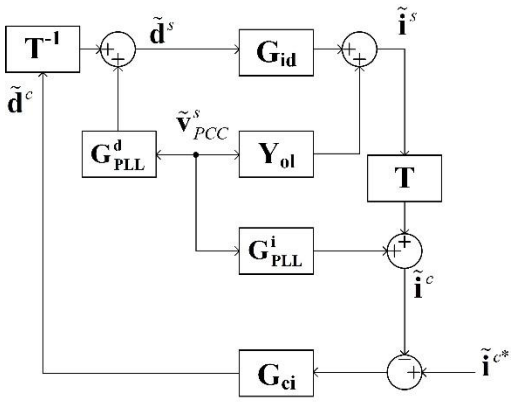

Figure 3-6 Small-signal model of STATCOM with PLL and current loop

$$\mathbf{G}_{\mathbf{ci}} = \begin{bmatrix} k_{pi} + \dfrac{k_{ii}}{s} & 0 \\ 0 & k_{pi} + \dfrac{k_{ii}}{s} \end{bmatrix} \tag{3.14}$$

From Figure 3-6, we can list the following equations for each nodes:

Substituting equations to eliminate duty cycles and setting the current reference to be zero yields:

$$\mathbf{Z}_{\mathbf{PLL,i}} = \left[\mathbf{Y}_{\mathbf{ol}} + \mathbf{G}_{\mathbf{id}} \left(\mathbf{G}^{\mathbf{d}}_{\mathbf{PLL}} - \mathbf{T}^{-1}\mathbf{G}_{\mathbf{ci}}\mathbf{G}^{\mathbf{i}}_{\mathbf{PLL}} \right) \right]^{-1} \left(\mathbf{I} + \mathbf{G}_{\mathbf{id}}\mathbf{T}^{-1}\mathbf{G}_{\mathbf{ci}}\mathbf{T} \right) \tag{3.15}$$

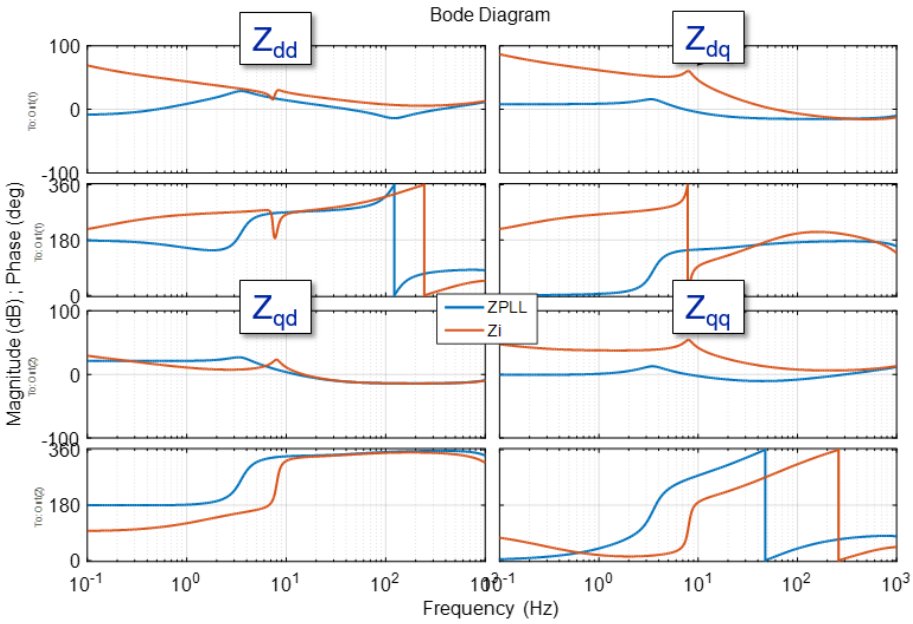

Figure 3-7 STATCOM impedances: with PLL only (ZPLL) and with current loop and PLL (Zi)

The influence of the current control is shown in Figure III-7. The current loop bandwidth is 500 Hz and thus there is no significant discrepancy beyond 200 Hz between the impedances with only PLL in blue and that with PLL and current loop in red, leaving the impedance showing the passive components' impedance characteristic. In the low frequency range, the current controller makes the impedances behave like current source, which is exactly what the current controller regulates. Due to nearly zero power factor, the impedance matrix is no longer diagonal-dominant as in unity-power-factor cases and furthermore Z_{qq} does not appear as a negative resistance.

3.3.3 Effects of voltage control loops

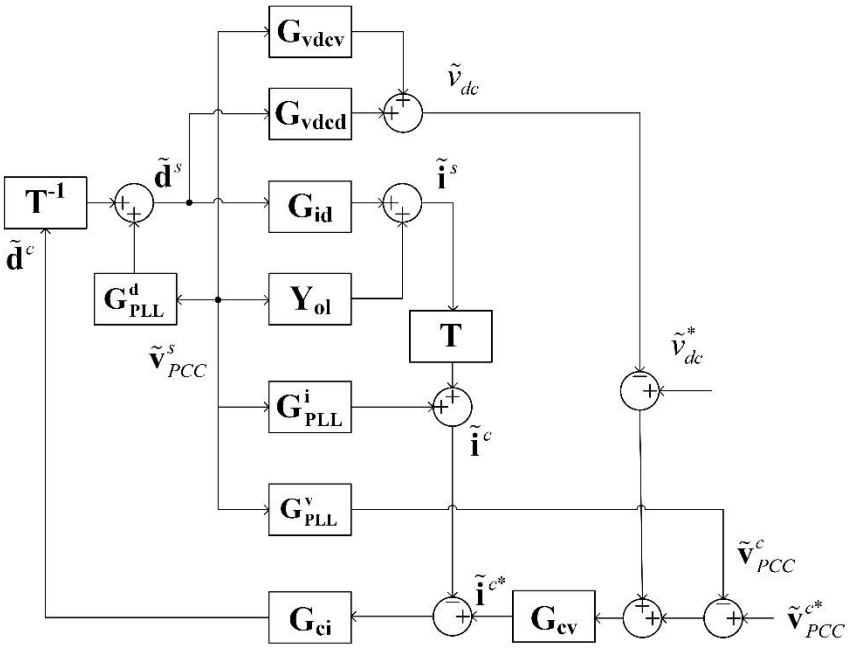

Figure 3-8 Small-signal model of STATCOM with PLL, current and voltage loop

On top of the current loops, the ac voltage loop and the dc voltage loop can be applied. The small-signal model of the STATCOM with all the loops is shown in Figure III-8 where the voltage controllers are

$$\mathbf{G}_{\mathbf{cvac}}=\begin{bmatrix}0 & 0\\ k_{pac}+\dfrac{k_{iac}}{s} & 0\end{bmatrix},\mathbf{G}_{\mathbf{cvdc}}=\begin{bmatrix}k_{pdc}+\dfrac{k_{idc}}{s}\\ 0\end{bmatrix} \tag{3.16}$$

Therefore the impedance of a STATCOM with all loops can be solved:

$$\mathbf{Z}_{\mathbf{PLL,i,v}}=\left\{\begin{matrix}\mathbf{Y}_{\mathbf{ol}}+\mathbf{G}_{\mathbf{id}}\left(\mathbf{I}+\mathbf{T}^{-1}\mathbf{G}_{\mathbf{ci}}\mathbf{G}_{\mathbf{cvdc}}\mathbf{G}_{\mathbf{vdcd}}\right)^{-1}\cdot\\ \left[\mathbf{G}^{\mathbf{d}}_{\mathbf{PLL}}-\mathbf{T}^{-1}\mathbf{G}_{\mathbf{ci}}\left(\mathbf{G}^{\mathbf{i}}_{\mathbf{PLL}}+\mathbf{G}_{\mathbf{cvac}}\mathbf{G}^{\mathbf{v}}_{\mathbf{PLL}}+\mathbf{G}_{\mathbf{cvdc}}\mathbf{G}_{\mathbf{vdcv}}\right)\right]\end{matrix}\right\}^{-1}\cdot \tag{3.17}$$
$$\left[\mathbf{I}+\mathbf{G}_{\mathbf{id}}\left(\mathbf{I}+\mathbf{T}^{-1}\mathbf{G}_{\mathbf{ci}}\mathbf{G}_{\mathbf{cvdc}}\mathbf{G}_{\mathbf{vdcd}}\right)^{-1}\mathbf{T}^{-1}\mathbf{G}_{\mathbf{ci}}\mathbf{T}\right]$$

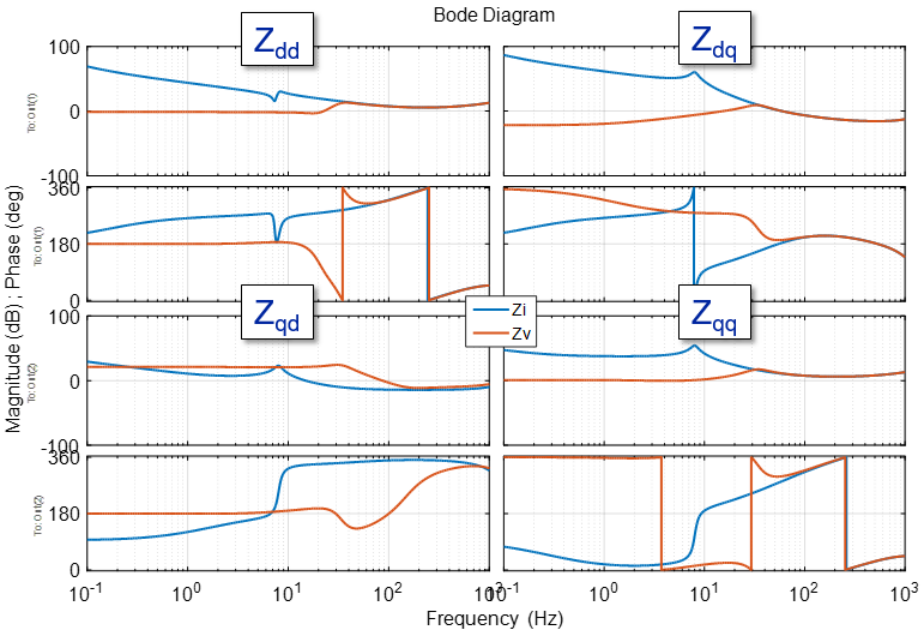

Figure 3-9 STATCOM impedances: with current loop (Zi) and with all loops (Zv)

The influence of the voltage loops can be observed in Figure III-9. The ac voltage loop bandwidth is 20 Hz, within which the impedances are shaped as resistors, either positive or negative depending on the operating point. Above that, the impedances stay the same with those under PLL and current loop only.

3.3.4 Effects of QV droop

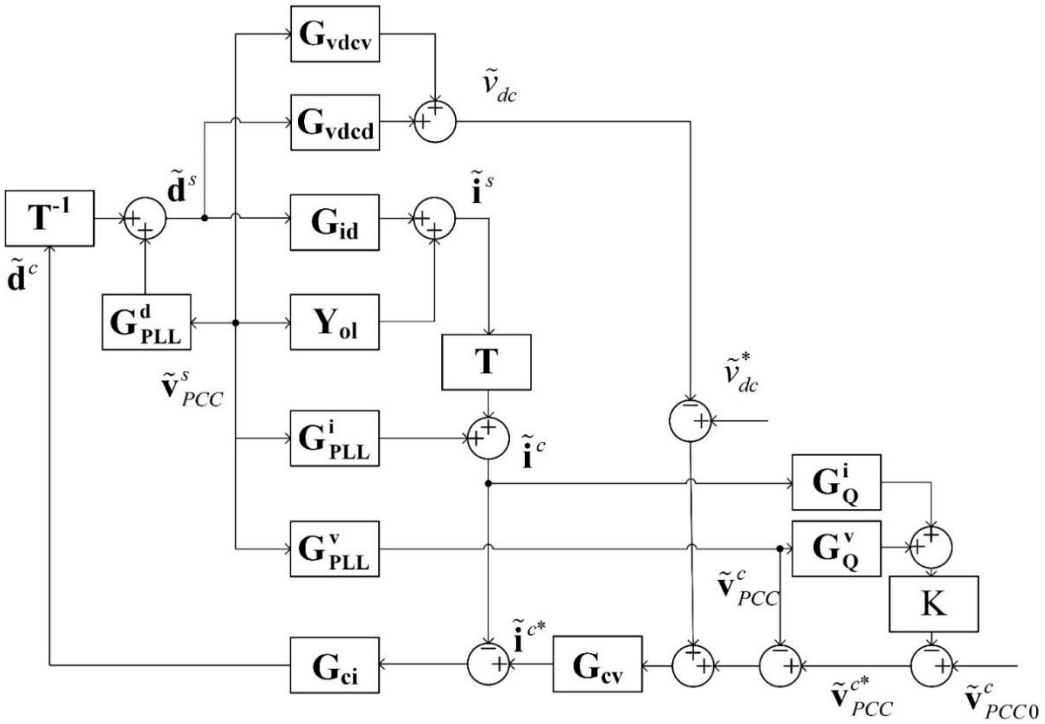

Figure 3-10 Small-signal model of STATCOM with PLL, current and voltage loop with QV droop

Since the grid voltage is allowed to vary in a reasonable range, there is another operation mode for STATCOMs to lessen the burden by activating the QV droop. The QV droop detects the output reactive power of STATCOMs to modify the ac voltage reference. The small-signal model of the STATCOM in addition of the QV droop is shown in Figure III-10, where K is the droop coefficient; $\mathbf{v}^c_{PCC0}$ is the reference voltage without any reactive power compensation and

$$\mathbf{G_Q^v}=\begin{bmatrix} I_q^s & -I_d^s \\ 0 & 0 \end{bmatrix}, \mathbf{G_Q^i}=\begin{bmatrix} -V_q^s & V_d^s \\ 0 & 0 \end{bmatrix} \tag{3.18}$$

The impedance of a STATCOM with all loops and QV droop can be solved:

$$\mathbf{Z}_{\mathbf{PLL,i,v,droop}} = \left\{ \begin{array}{l} \mathbf{Y}_{\mathbf{ol}} + \mathbf{G}_{\mathbf{id}} \left(\mathbf{T} + \mathbf{G}_{\mathbf{ci}} \mathbf{G}_{\mathbf{cvdc}} \mathbf{G}_{\mathbf{vdcd}} \right)^{-1} \cdot \\ \left[\mathbf{T}\mathbf{G}^{\mathbf{d}}_{\mathbf{PLL}} - \mathbf{G}_{\mathbf{ci}} \left(\mathbf{G}^{\mathbf{i}}_{\mathbf{PLL}} + \mathbf{G}_{\mathbf{cvac}} \left(K\mathbf{G}^{\mathbf{v}}_{\mathbf{Q}} + \mathbf{G}^{\mathbf{v}}_{\mathbf{PLL}} \right) + \mathbf{G}_{\mathbf{cvdc}} \mathbf{G}_{\mathbf{vdcv}} \right) \right] \end{array} \right\}^{-1} \cdot \left[\mathbf{I} + \mathbf{G}_{\mathbf{id}} \left(\mathbf{T} + \mathbf{G}_{\mathbf{ci}} \mathbf{G}_{\mathbf{cvdc}} \mathbf{G}_{\mathbf{vdcd}} \right)^{-1} \mathbf{G}_{\mathbf{ci}} \left(\mathbf{G}_{\mathbf{cvac}} K\mathbf{G}^{\mathbf{i}}_{\mathbf{Q}} + \mathbf{T} \right) \right] \tag{3.19}$$

The effects of QV droop is shown in Figure III-11. There is a significant increase in the magnitude of the dq-channel impedance and other channels remain almost the same because the reactive power is mainly dependent on q-channel current and the d-channel PCC voltage is the controlled variable of the QV droop. By activating the droop, q-channel current has equivalently more influence on the d-channel PCC voltage, which indicates larger impedance in the dq-channel.

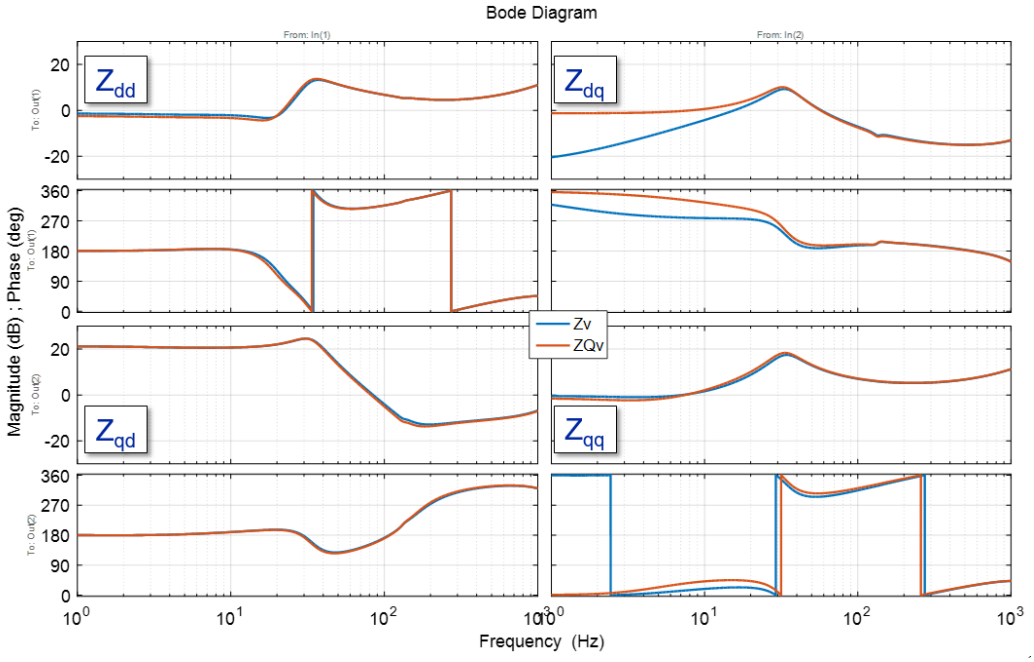

Figure 3-11 STATCOM impedances: without QV droop (Zv) and with QV droop (ZQv)

3.4 Features of STATCOM impedance

3.4.1 Low frequency characteristics

To illustrate the low frequency resistive behavior, the following equations (3.20) are considered. The first equation represents the power balance in the steady-state for the STATCOM, considering the active power absorption in the ac side and all the losses including the parasitic losses in the transformer and an approximate estimation of the losses of the converter, which is basically what the dc voltage loop does to maintain the dc bus voltage. The second equation shows how the ac voltage loop works in the steady state. In all, these two equations (3.20) describe the behaviors of the STATCOM within voltage loops bandwidth under the assumption that all the loops are working perfectly.

$$\begin{cases} \dfrac{V_{dc}^2}{R_{dc}} + V_{PCCd}^s I_d^s + V_{PCCq}^s I_q^s + R\left(\left(I_d^s\right)^2 + \left(I_q^s\right)^2\right) = 0 \\ \left(V_{PCCd}^s\right)^2 + \left(V_{PCCq}^s\right)^2 - V_{PCC}^2 = 0 \end{cases} \tag{3.20}$$

Consider (3.20) as implicit functions of $\mathbf{v}_{PCC}^s$ and $\mathbf{i}^s$ as (3.21) and do the derivative (3.22), we can get the ratio between $\mathbf{v}_{PCC}^s$ and $\mathbf{i}^s$, which is exactly what the STATCOM impedances are defined. Therefore the low frequency values of the STATCOM impedances can be solved as (3.23).

$$\mathbf{f}\left(\mathbf{v}_{PCC}^s, \mathbf{i}^s\right)\Big|_{j\omega=0} = \mathbf{0} \tag{3.21}$$

$$\left.\frac{d\mathbf{v}_{PCC}^s}{d\mathbf{i}^s}\right|_{j\omega=0} = -\left.\frac{\partial \mathbf{f} / \partial \mathbf{i}^s}{\partial \mathbf{f} / \partial \mathbf{v}_{PCC}^s}\right|_{j\omega=0} \tag{3.22}$$

$$\mathbf{Z}_{STAT}\Big|_{j\omega=0}=\begin{bmatrix}\dfrac{V_{PCCd}^{s}V_{PCCq}^{s}+2RI_{d}^{s}V_{PCCq}^{s}}{Q} & \dfrac{\left(V_{PCCq}^{s}\right)^{2}+2RI_{d}^{s}V_{PCCd}^{s}}{Q}\\ -\dfrac{\left(V_{PCCd}^{s}\right)^{2}+2RI_{q}^{s}V_{PCCq}^{s}}{Q} & -\dfrac{V_{PCCd}^{s}V_{PCCq}^{s}+2RI_{q}^{s}V_{PCCd}^{s}}{Q}\end{bmatrix} \tag{3.23}$$

As seen in (3.23), the four elements are all resistive with their polarities depending on the operating point. Roughly speaking if any losses are neglected (3.24), when the STATCOM is generating reactive power to the grid, which means it is in the capacitive mode, Z_{dd} is positive and Z_{qq} is negative, making it behave like a constant power load [56]; when the STATCOM is aborbing reactive power from the grid, meaning that it is in the inductive mode, Z_{dd} is negative and Z_{qq} is postive, making it more as a voltage source inverter with PLL [57], as shown in Figure III-12. For the same amount of reactive power, positive or negative, the magnitude of the impedances are the same but the phase is 180 degree different. The main causes of instability with the presense of constant power loads and voltage source inverters are different, indicating different channels, d-d or q-q, to check primarily. Yet STATCOMs could behave in either way, complicating the cases with the existing knowledge.

$$\mathbf{Z}_{STAT}\Big|_{j\omega=0}\approx\begin{bmatrix}\dfrac{V_{PCCq}^{s}}{I_{q}^{s}} & \dfrac{\left(V_{PCCq}^{s}\right)^{2}}{V_{PCCd}^{s}I_{q}^{s}}\\ -\dfrac{V_{PCCd}^{s}}{I_{q}^{s}} & -\dfrac{V_{PCCq}^{s}}{I_{q}^{s}}\end{bmatrix} \tag{3.24}$$

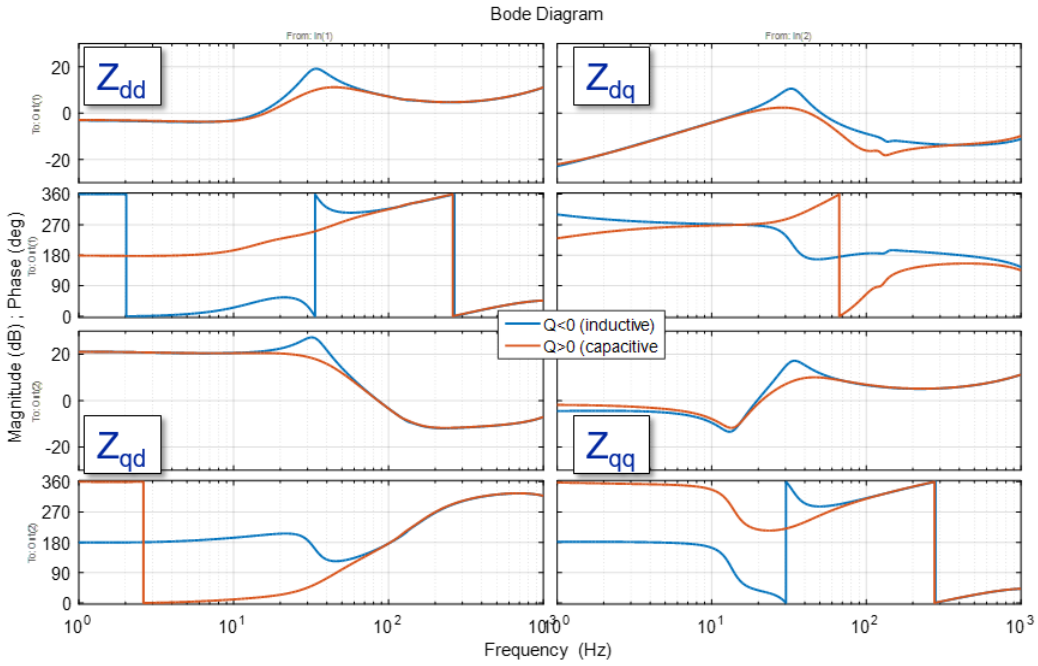

Figure 3-12 STATCOM impedances under different operating points

However, note that in some rare and extreme cases and above conclusions are not true. Figure III-13 shows the extreme cases on the left and normal case on the right where the phasors are plotted where the difference is how the reference dq-frame is selected or practically where the infinite bus voltage is. In the figure, $\vec{\mathbf{V}}_{PCC}^{Q=0}$ is the uncompensated PCC voltage phasor, $\vec{\mathbf{V}}_{PCC}^{Q<0}$ is the PCC voltage phasor when the STATCOM is absorbing reactive current $\vec{\mathbf{I}}_{PCC}^{Q<0}$ and $\vec{\mathbf{V}}_{PCC}^{Q>0}$ is the PCC voltage phasor when the STATCOM is providing reactive current $\vec{\mathbf{I}}_{PCC}^{Q>0}$. Due to the small resistive part in the equivalent grid impedance, there are small phase differences between the compensated and uncompensated voltages, which are drawn exaggeratedly in the figure. Take the dd-channel element in the impedance expression (3.24) as an example. In the extreme case, when the STATCOM is outputting reactive power, V_{PCCq} is negative and I_q is negative and thus Z_{dd} is positive; on the other hand, when the STATCOM is receiving reactive power, V_{PCCq} is positive and I_q is positive and therefore Z_{dd} is still positive. However, because the resistive part in the

transmission systems is trivial, the extreme cases are very rare. Furthermore, note that these cases appear only when the PCC bus is very close to reference frame, which is often selected to be aligned with the infinite bus. The possibility of the extreme cases is diminished further by the fact that STATCOMs are usually installed far away from the infinite bus to help reactive power compensation. In all, the conclusion that the STATCOM impedance polarity changes along with reactive power directions holds true for almost all the situations.

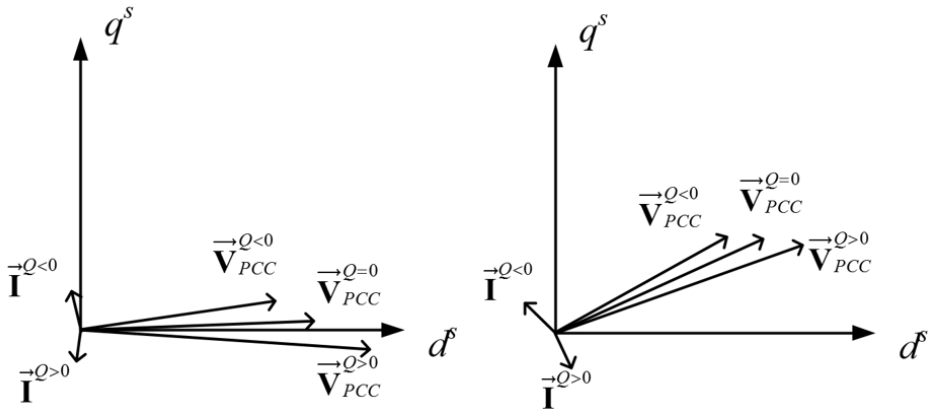

Figure 3-13 Impacts of position of PCC voltage on STATCOM impedance

Another aspect of the STATCOM impedances is that the impedance matrix is not diagonal dominant as in the unity power factor case. In the unity power case, the magnitude of Z_{dd} and Z_{qq} elements are much larger than the other two, Z_{dq} and Z_{qd}, which renders decoupling of the d-channel and q-channel and facilitates the assessment of the stability because the stability can be dertermined by checking the dd-channel and qq-channel individually. However in the STATCOM case, the magnitude of the q-d channel was much larger than the other three channels, indicating that the d and q channels are highly coupled, which is mainly because of the ac voltage loop control that is controlling I_q based on V_{pccd}. This feature makes the STATCOM impedance complicated to analyze in the sense of impedance-based stabilty criterion intuitively and in the most cases characteristic loci must be calculated for stability analysis, which is out of the scope of this chapter.

For impedances like STATCOM or any other converter working under low power factor conditions, the full expression of the return ratio needs to be examined to apply the general Nyquist stability criterion (GNC).

3.4.2 High frequency characteristics: impacts of control loops on the impedances

3.4.2.1 AC voltage loop

Figure III-14 shows the impedances of a STATCOM with increasing voltage loop bandwidths indicated by the arrow and other control parameters unchanged. Specifically, the bandwidth was increased from 2.5 Hz to 20 Hz in this figure. As discussed in Section 3.3.3, the resonant peaks in each channel at the bandwidth frequencies are created by the ac voltage loop because within its bandwidth, the loop regulates the magnitude to be certain values in Section 3.4.1 and above the bandwidth the current loop takes over regulating the impedances to be of a current source. Thus, the resonant peaks move to the high frequency as the bandwidth increases.

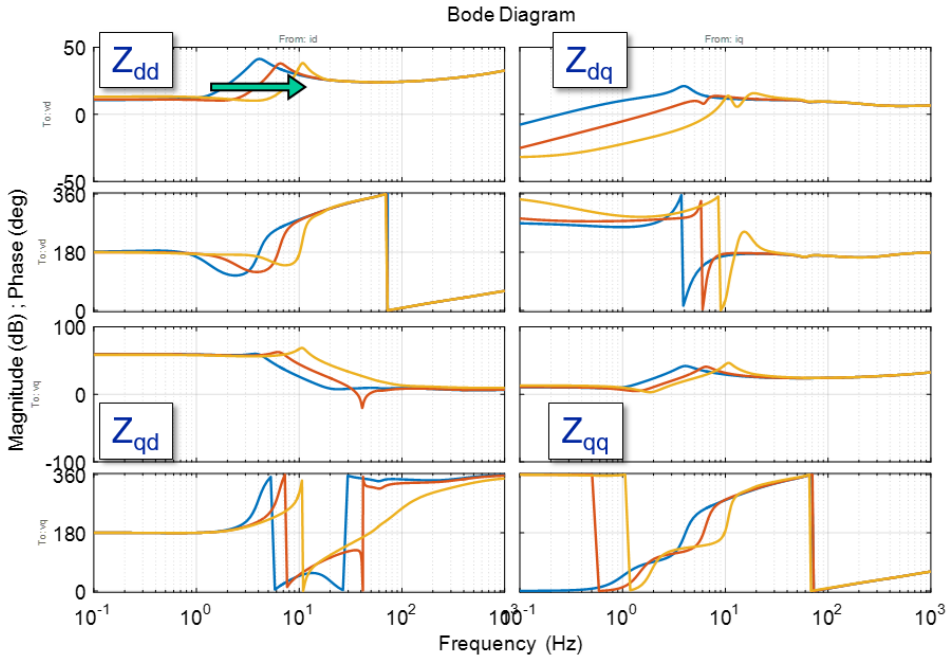

Figure 3-14 AC voltage loop effects on the impedances

3.4.2.2 PLL

The PLL's effects are greatly masked by those from the ac voltage loop. Figure 3-15 shows how the impedances of a STATCOM change with different PLL bandwidths with other control parameters staying as the same, evincing the small effect of the PLL. In effect the resonant peak is changed ever so lightly when changing the PLL bandwidth from 5 Hz to 20 Hz.

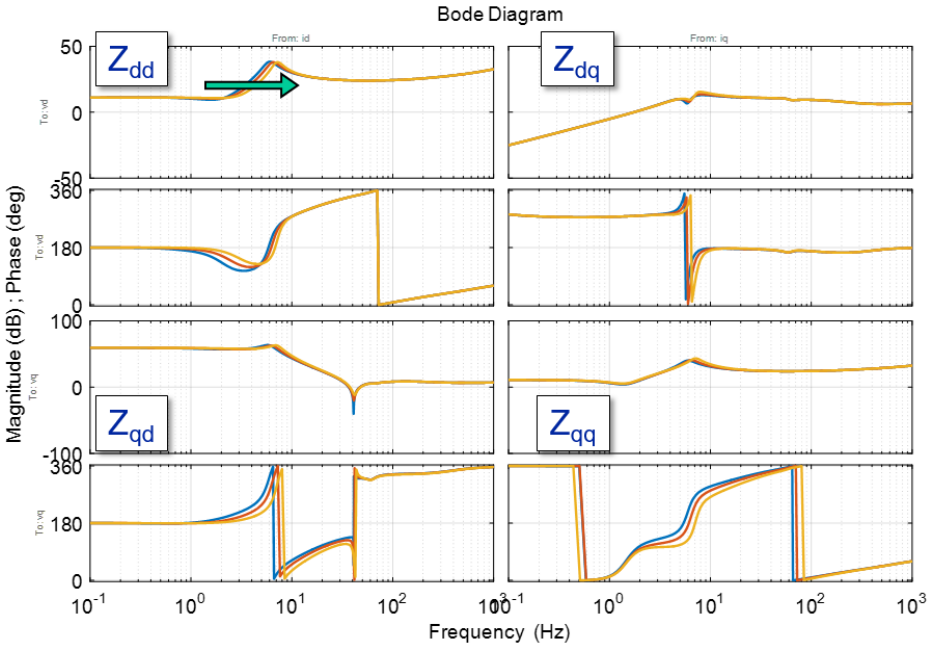

Figure 3-15 PLL effects on the impedances

If only the related terms with PLL and ac voltage loop in (3.17) are taken out, we can get:

$$\mathbf{G}_{\mathbf{PLL}}^{\mathbf{d}} - \mathbf{G}_{\mathbf{ci}}\left(\mathbf{G}_{\mathbf{PLL}}^{\mathbf{i}} + \mathbf{G}_{\mathbf{cvac}}\mathbf{G}_{\mathbf{PLL}}^{\mathbf{v}}\right) \approx \begin{bmatrix} 0 & 0 \\ \left(k_{pi} + \dfrac{k_{ii}}{s}\right)\left(k_{pvac} + \dfrac{k_{ivac}}{s}\right) & \left[D_d^s - \left(k_{pi} + \dfrac{k_{ii}}{s}\right)\left(k_{pvac} + \dfrac{k_{ivac}}{s}\right)V_{PCCq}^s\right]G_{PLL} \end{bmatrix} \tag{3.25}$$

where D_d^s is the duty cycle in the system d-channel. In (3.25), the first element is only related to the current loop compensator and ac voltage loop compensator while the second element is also with operating point and PLL. it is apparent that the left element is only related to the current loop

and ac voltage loop compensators, while the second element is also function of the operating point and the PLL. Given that the duty cycle and operating point do not vary significantly, less than 20 % of the nominal values, and that the compensator gains can change several times as their respective bandwidths change, it can be concluded that it is the left element that reflects how the current and ac voltage loops change the STATCOM impedance, and the right element that reflects the impact of the PLL. Figure III-16 shows the comparison of the two elements, namely effect from ac voltage loop and effect from PLL, showing how the effect of the ac voltage loop is much larger across the frequency range of interest, masking any impact of the PLL. Although this masking effect is dependent on operating points, especially on grid voltage level and STATCOM power ratings, the conclusion still holds for transmission level, because the PLL compensator gain is in inverse proportion to the grid voltage while the ac voltage loop compensator gain is inversely proportional to the grid inductance. For the parameters used in this section, the effects from ac voltage loop are about 100 times larger than that of the PLL. Their magnitudes would only be comparable if the grid voltage drops to 10 times smaller and the grid impedance increases to 10 times larger, showing how the ac voltage loop has a much greater influence than the PLL on the stability of a STATCOM unit. However, in low voltage applications e.g. distribution systems or micro-grids, this conclusion may need to be rechecked.

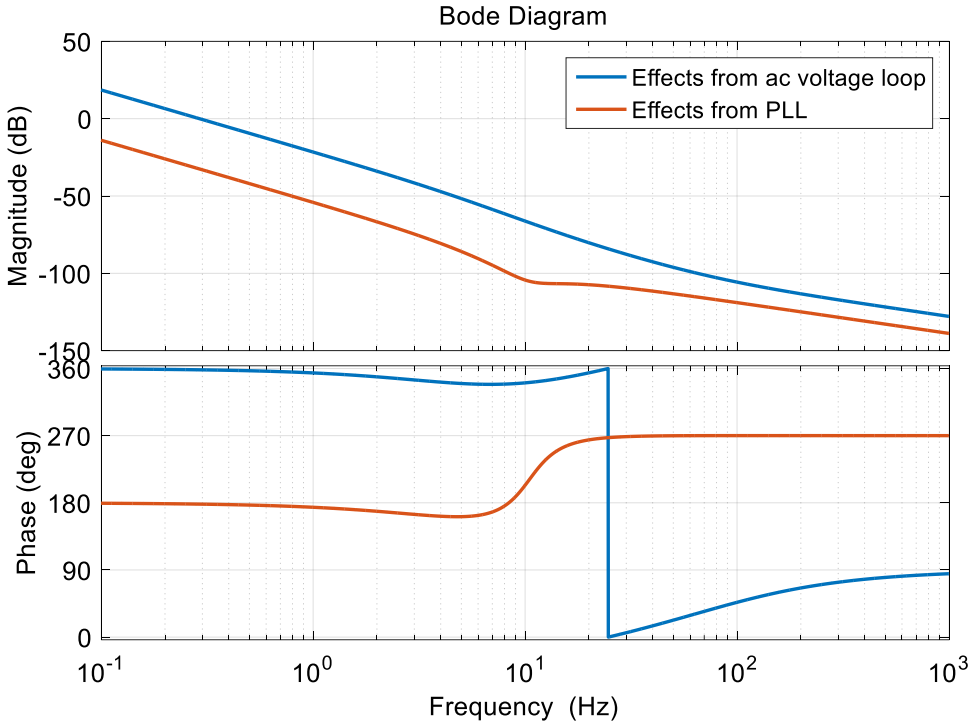

Figure 3-16 Comparison of PLL and ac voltage loop effects on impedances

3.4.2.3 Current loop

Figure III-17 shows the effects of current loop's bandwidths on the impedance of a STATCOM. Because the current loop regulates the impedance to be a current source within its bandwidth, the higher the current loop bandwidth, the wider range of current source behaviors in the impedance. Beyond the current loop bandwidth, the impedances increase in magnitude as the filter inductor appears. In all, from the bandwidth of the ac voltage loop to current loop, the impedances' magnitude drops and rises above the current loop's bandwidth due to the passive inductor. Therefore, as the current loop bandwidth increases, the impedances increase in magnitude.

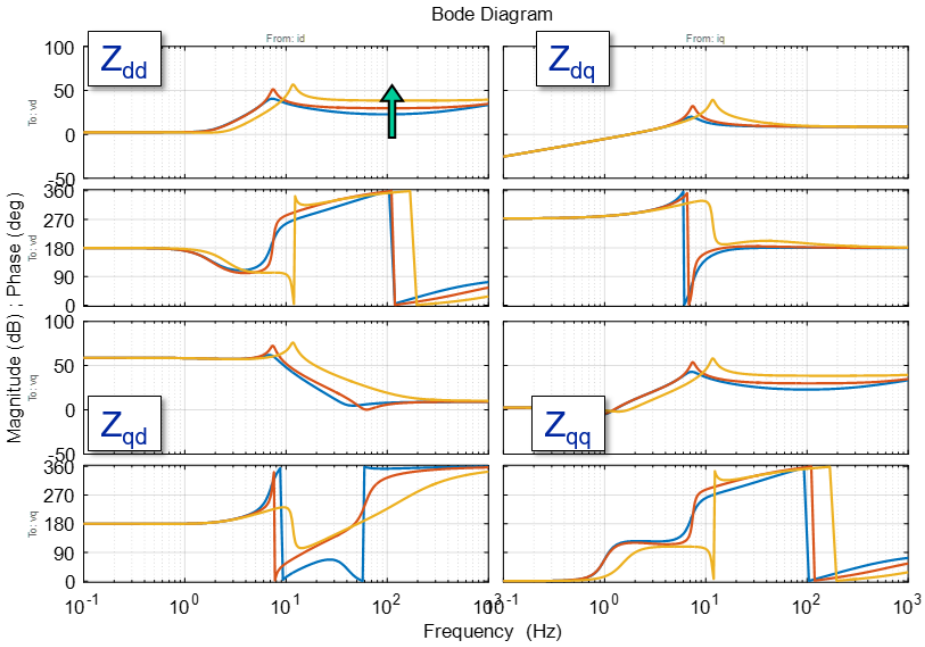

Figure 3-17 Current loop effects on the impedances

3.4.2.4 Droop coefficient

As mentioned, activation of droop increased the impedance magnitude in d-q channel. The larger the droop coefficient, the larger the impedance, with the case without the QV droop being a special case when the droop coefficient is zero. This is shown in Figure III-18.

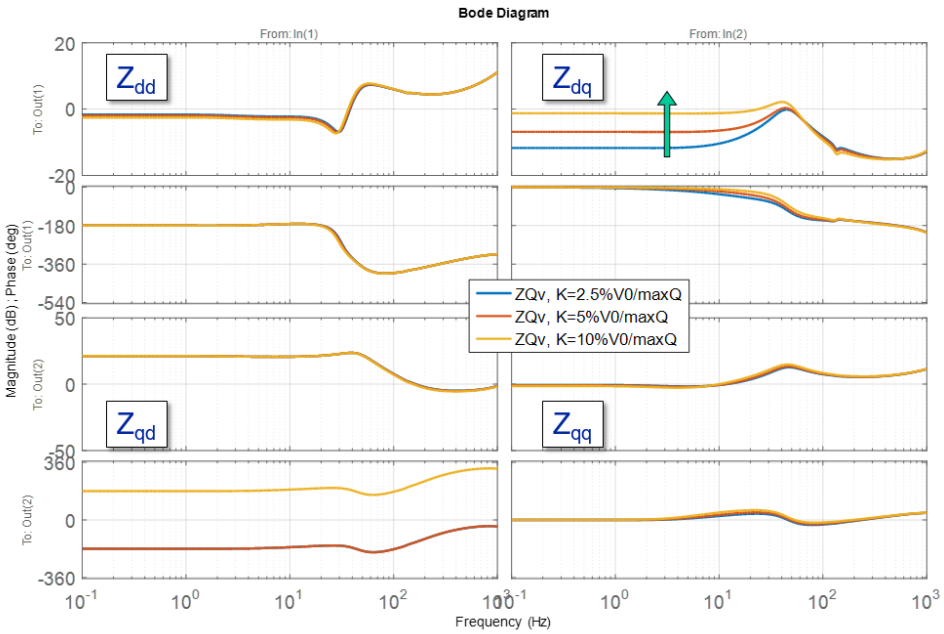

Figure 3-18 Droop coefficient effects on the impedances

With all the above modeling and analysis, this chapter presented the d-q frame impedance model of a STATCOM in the small-signal sense with all control loops including PLL, current loop and voltage loops for frequencies below control loop bandwidths. Actually this impedance model is a generic impedance model which can be applied to other grid-tied converters. For example, if the converter is a front-end for a PV system which only regulates the dc bus voltage and synchornizes with PCC bus voltage, then the model can be revised by removing the ac voltage loop; if the grid impedance is zero, the model can be further reduced by letting the phase difference θ to be zero. If a different PLL or different controller is used, then the corresponding block should be updated for the new controller. By manipulating the control blocks, impedance models can be extended for different control schemes and different topologies.

3.5 Experimental verification of impedance model

In order to validate the proposed impedance model, scaled-down STATCOMs were built as shown in Figure II-9 and Figure II-10. The parameters are listed in Table II-II. The impedances were measured using an impedance measurement unit (IMU) in Figure III-19 from 0.1 Hz to 1 kHz and the measurement circuit were shown in Figure III-20. The series-injection mode of the IMU is better suited for the characterization of the ac side having higher voltage bandwidth, the STATCOM, whereas a shunt-injection mode would be better to characterize the low impedance side, namely the grid impedance. When the STATCOM under test reached its given operating point, IMU started to perturb and measure responses, which could take tens of minutes depending on the number of injection frequencies and the type of injecting signals. Actually, the IMU could measure impedances of both sides but here only impedances of the STATCOM were of interest. More details about the IMU operation can be found in the Appendix in the end of this Chapter.

Figure 3-19 Impedance measurement unit

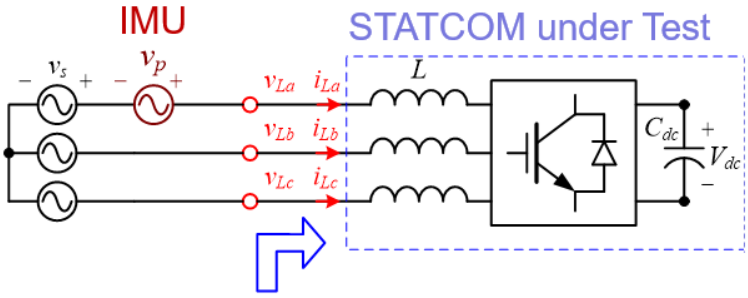

Figure 3-20 Impedance measurement circuit

Because there was possibly no neutral point in the system, the IMU was design to sense line to line voltages and the measured impedances were under line-to-line base. The impedances in d-q frame from line-to-line variables are always three times those from line-to-neutral variables at all frequencies. This can be proven as follows:

Let the subscript "*l-l*" to be variables in line-to-line base and subscript "*l-n*" to be variables in line-to-neutral base. Doing Park transformation from abc variables in line-to-line:

$$\begin{bmatrix} v_{dl-l} \\ v_{ql-l} \end{bmatrix} = \sqrt{\frac{2}{3}} \begin{bmatrix} \cos\theta_{ab} & \cos\left(\theta_{ab} - \frac{2}{3}\pi\right) & \cos\left(\theta_{ab} + \frac{2}{3}\pi\right) \\ -\sin\theta_{ab} & -\sin\left(\theta_{ab} - \frac{2}{3}\pi\right) & -\sin\left(\theta_{ab} + \frac{2}{3}\pi\right) \end{bmatrix} \begin{bmatrix} v_{ab} \\ v_{bc} \\ v_{ca} \end{bmatrix} \tag{3.26}$$

where θ_{ab} is the phase of v_{ab}. To transform variables in line-to-line base to line-to-neutral,

$$\begin{aligned} \begin{bmatrix} v_{dl-l} \\ v_{ql-l} \end{bmatrix} &= \sqrt{\frac{2}{3}} \begin{bmatrix} \cos\theta_{ab} & \cos\left(\theta_{ab} - \frac{2}{3}\pi\right) & \cos\left(\theta_{ab} + \frac{2}{3}\pi\right) \\ -\sin\theta_{ab} & -\sin\left(\theta_{ab} - \frac{2}{3}\pi\right) & -\sin\left(\theta_{ab} + \frac{2}{3}\pi\right) \end{bmatrix} \begin{bmatrix} 1 & -1 & 0 \\ 0 & 1 & -1 \\ -1 & 0 & 1 \end{bmatrix} \begin{bmatrix} v_a \\ v_b \\ v_c \end{bmatrix} \\ &= -\sqrt{3}\sqrt{\frac{2}{3}} \begin{bmatrix} \sin\left(\theta_{ab} - \frac{2}{3}\pi\right) & \sin\left(\theta_{ab} + \frac{2}{3}\pi\right) & \sin\theta_{ab} \\ \cos\left(\theta_{ab} - \frac{2}{3}\pi\right) & \cos\left(\theta_{ab} + \frac{2}{3}\pi\right) & \cos\theta_{ab} \end{bmatrix} \begin{bmatrix} v_a \\ v_b \\ v_c \end{bmatrix} \end{aligned} \tag{3.27}$$

Doing inverse Park transformation for abc variables in line-to-neutral:

$$\begin{aligned} \begin{bmatrix} v_{dl-l} \\ v_{ql-l} \end{bmatrix} &= -\sqrt{3}\sqrt{\frac{2}{3}} \begin{bmatrix} \sin\left(\theta_a - \frac{1}{2}\pi\right) & \sin\left(\theta_a + \frac{5}{6}\pi\right) & \sin\left(\theta_a + \frac{1}{6}\pi\right) \\ \cos\left(\theta_a - \frac{1}{2}\pi\right) & \cos\left(\theta_a + \frac{5}{6}\pi\right) & \cos\left(\theta_a + \frac{1}{6}\pi\right) \end{bmatrix}. \\ &\sqrt{\frac{2}{3}} \begin{bmatrix} \cos\theta_a & -\sin\theta_a \\ \cos\left(\theta_a - \frac{2}{3}\pi\right) & -\sin\left(\theta_a - \frac{2}{3}\pi\right) \\ \cos\left(\theta_a + \frac{2}{3}\pi\right) & -\sin\left(\theta_a + \frac{2}{3}\pi\right) \end{bmatrix} \begin{bmatrix} v_{dl-n} \\ v_{ql-n} \end{bmatrix} \\ &= \sqrt{3} \begin{bmatrix} v_{dl-n} \\ v_{ql-n} \end{bmatrix} \end{aligned} \tag{3.28}$$

Similarly, for current variables,

$$\begin{bmatrix} i_{dl-l} \\ i_{ql-l} \end{bmatrix} = \frac{\sqrt{3}}{3} \begin{bmatrix} i_{dl-n} \\ i_{ql-n} \end{bmatrix} \tag{3.29}$$

Thus, it can be proven by combing (3.28) and (3.29) that

$$\begin{bmatrix} Z_{ddl-l} & Z_{dql-l} \\ Z_{qdl-l} & Z_{qql-l} \end{bmatrix} = 3 \begin{bmatrix} Z_{ddl-n} & Z_{dql-n} \\ Z_{qdl-n} & Z_{qql-n} \end{bmatrix} \tag{3.30}$$

Because nothing has been assumed, (3.30) is generic and applies to any frequency.

The impedance measurement results are shown in Figure 3-21, where the derived impedance model is plotted in blue, and the measurement results are drawn in red corresponding to the case with all control loops closed. The biggest discrepancy is observed in the phase of the Z_{dq} and Z_{qd} elements above 100 Hz, which results from the delay of the voltage sensors in the IMU. Compared to other d-q frame impedance measurements conducted by IMUs, these measurements are very clean and nearly noise-free. This is a result of the non-diagonal nature of the STATCOM impedance that keeps a high signal-to-noise ratio in all d-q frame channels, as opposed to PWM rectifiers where the measurement of the d-q frame cross-channel impedances is always troublesome [56, 57]. Figure 3-22 depicts the STATCOM impedances with and without the QV droop. The impedance element Z_{dq} was increased in magnitude a lot in the low frequency with the QV droop, corresponding to the impedance model analysis above.

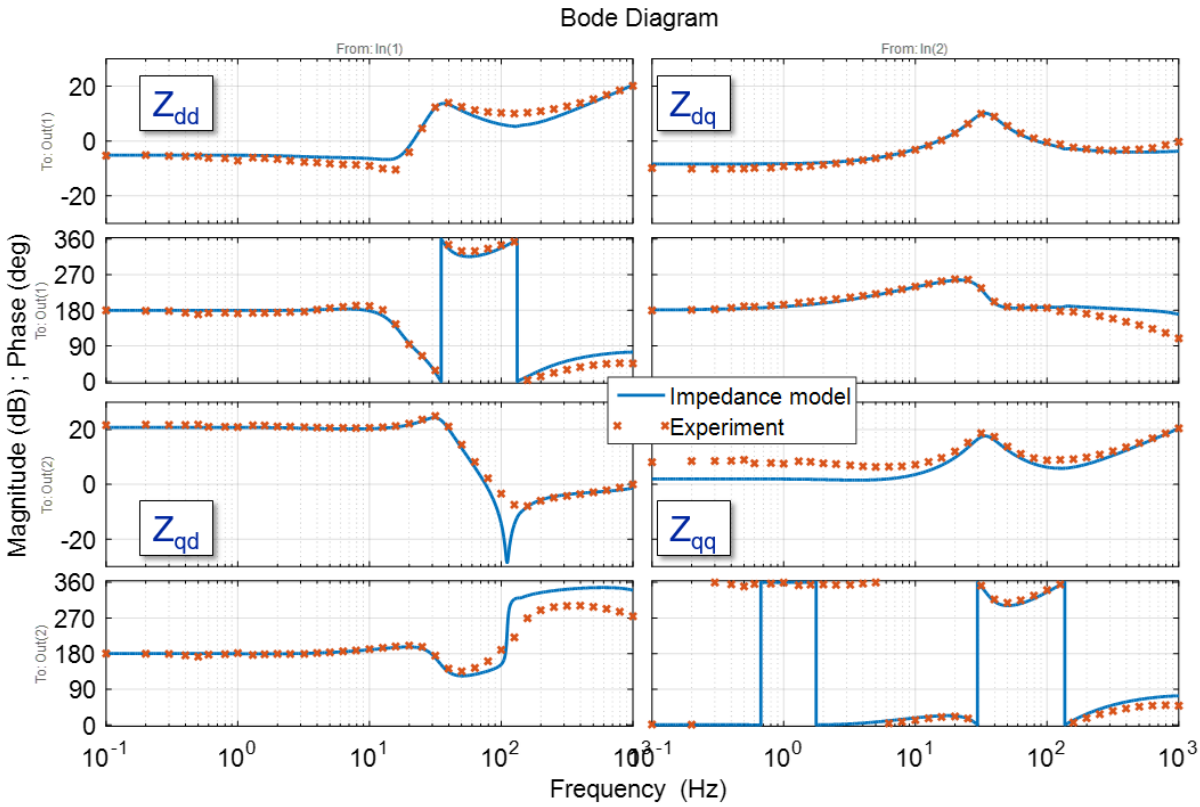

Figure 3-21 STATCOM impedance measurements with all loops

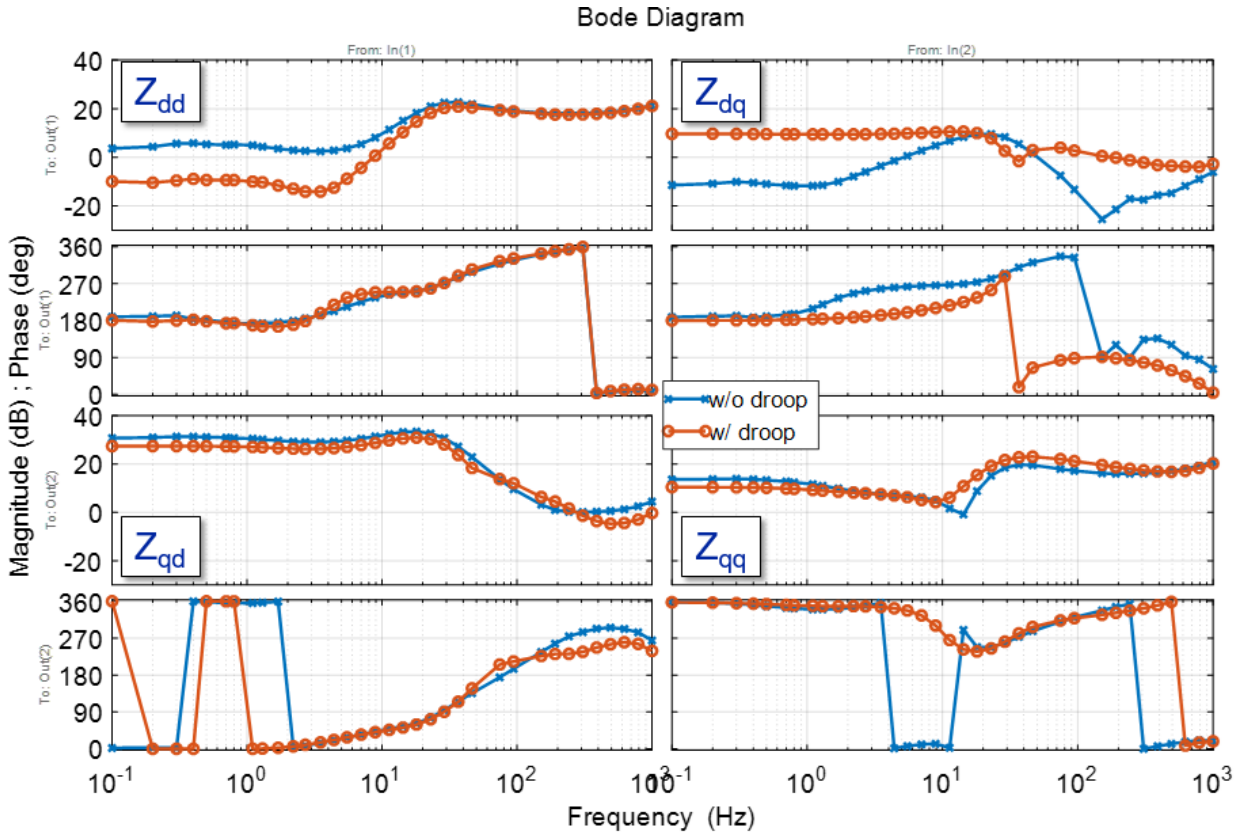

Figure 3-22 STATCOM impedances with and without QV droop

Figure 3-23 shows the STATCOM impedances under different reactive power output, evincing how the polarity of its negative impedance characteristic flips depending on its reactive power flow.

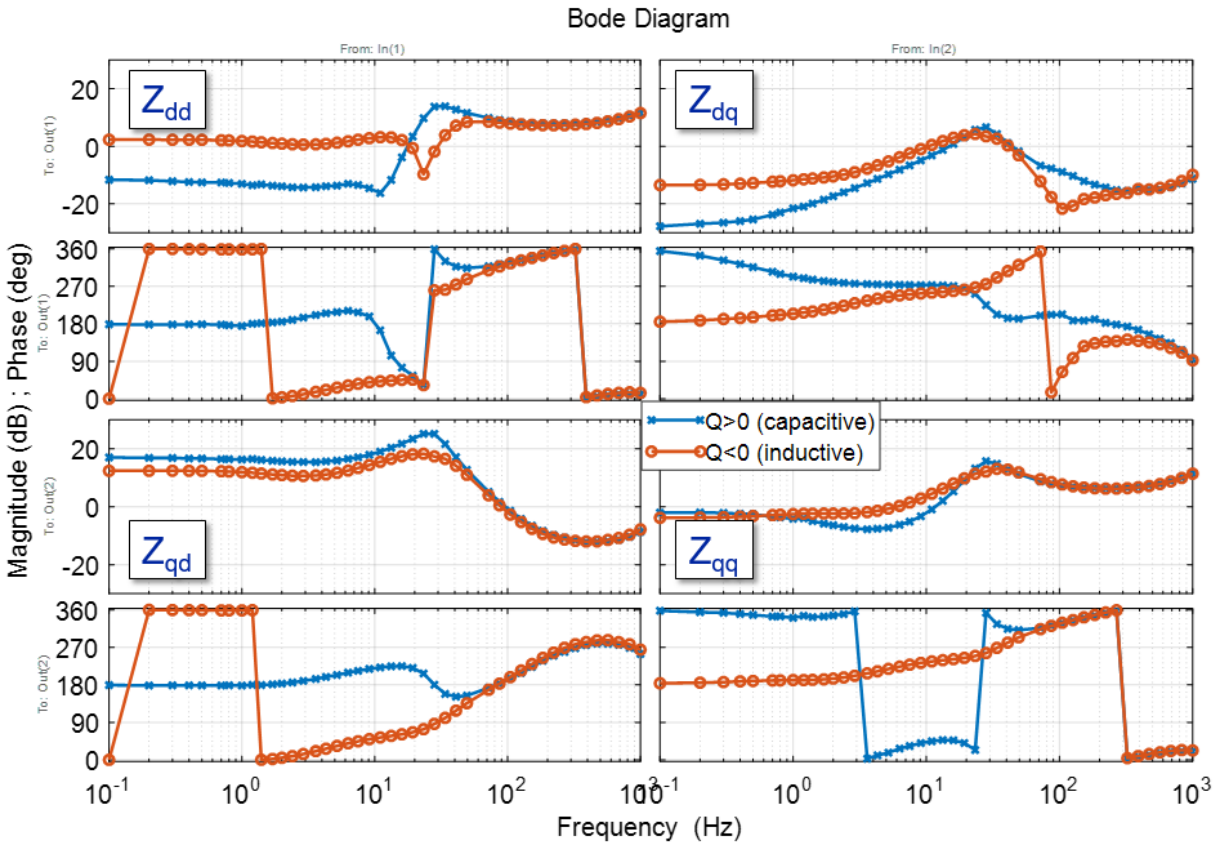

Figure 3-23 STATCOM impedance measurements with different reactive power directions

3.6 Conclusions

This chapter proposed and analyzed in detail the small-signal d-q frame input-impedance model of a STATCOM taking into consideration its PLL, current loop, voltage loop, and QV droop, that can be readily used to study the small-signal stability at three-phase ac system interfaces in the presence of STATCOM units. From the model, the following conclusions were extracted. First, because of the inherent operating conditions of a STATCOM, the stability assessment directly from the d-q frame impedances is very difficult—as opposed to unity power factor rectifiers and inverters, for which a multivariable stability theorem using the return-ratio matrix, product of the upstream and downstream impedances at a given ac interface must be used; for instance, the GNC. Second, the ac voltage loop of the STATCOM was found to be the strongest contributor to its

terminal impedance and in consequence to its small-signal stability conditions. This loop was shown to effectively mask the PLL dynamics, especially for system parameters proper of transmission grids, previously shown to be critical in grid-tied power converters. And third, very importantly, the STATCOM impedance was shown to be able to behave both as a CPL rectifier and as a grid-tied inverter injecting power into the grid, from a dynamic standpoint, featuring a negative incremental input-impedance in its Z_{dd} or Z_{qq} impedance elements respectively, as a function of its reactive power injection mode (capacitive or inductive), and as a function of the relative phase between the d-q frame in question and the voltage at the PCC. These are all unique impedance characteristics that make the stability analysis in the presence of STATCOMs more involved than other unity power factor converters. Lastly, the model was verified experimentally using an IMU to measure the input-impedance of a 10 kVAR STATCOM prototype, which was shown to match very well with the impedance obtained using the model developed.

3.7 Appendix

3.7.1 Open loop transfer functions of a STATCOM

The open loop transfer functions are follows:

$$Z_{dc} = R_{dc} \,||\, \frac{1}{sC} = \frac{R_{dc}}{R_{dc}Cs+1} \tag{3.31}$$

$$\mathbf{Z}_{ol} = \begin{bmatrix} Z_{dc}D_d^{s2} + R + Ls & Z_{dc}D_d^s D_q^s - \omega L \\ Z_{dc}D_d^s D_q^s + \omega L & Z_{dc}D_q^{s2} + R + Ls \end{bmatrix} \tag{3.32}$$

$$\mathbf{G_{id}} = \begin{bmatrix} \frac{num_{11}}{den} & \frac{num_{12}}{den} \\ \frac{num_{21}}{den} & \frac{num_{22}}{den} \end{bmatrix} \tag{3.33}$$

where

$$
\begin{aligned}
num_{11} &= -(-Z_{dc}I_dD_d - V_{dc})(-Z_{dc}D_q^2 - Ls - R) + (-Z_{dc}I_dD_q)(\omega L - Z_{dc}D_dD_q) \\
num_{12} &= -(-Z_{dc}I_qD_d)(-Z_{dc}D_q^2 - Ls - R) + (-Z_{dc}I_qD_q - V_{dc})(\omega L - Z_{dc}D_dD_q) \\
num_{21} &= (-Z_{dc}I_dD_d - V_{dc})(-\omega L - Z_{dc}D_dD_q) - (-Z_{dc}I_dD_q)(-Z_{dc}D_d^2 - Ls - R) \\
num_{22} &= (-Z_{dc}I_qD_d)(-\omega L - Z_{dc}D_dD_q) - (-Z_{dc}I_qD_q - V_{dc})(-Z_{dc}D_d^2 - Ls - R) \\
den &= (-Z_{dc}D_d^2 - Ls - R)(-Z_{dc}D_q^2 - Ls - R) - (-\omega L - Z_{dc}D_dD_q)(\omega L - Z_{dc}D_dD_q)
\end{aligned}
\tag{3.34}
$$

$$
\mathbf{G}_{\mathbf{vdcd}} = Z_{dc}\left(\begin{bmatrix} D_d^s & D_q^s \end{bmatrix}\mathbf{G}_{\mathbf{id}} + \begin{bmatrix} I_d^s & I_q^s \end{bmatrix}\right) \tag{3.35}
$$

$$
\mathbf{G}_{\mathbf{vdcv}} = Z_{dc}\begin{bmatrix} D_d^s & D_q^s \end{bmatrix}\mathbf{Y}_{ol} \tag{3.36}
$$

3.7.2 The operation of the impedance measurement unit

The impedance measurement unit (IMU) is conceptually an impedance analyzer with large power ratings, which can generate small-signal perturbations on top of normal operation points. However, in this scenario the small-signal perturbations are practically 1~3% of the power of the whole system under test, probably several kVA to tens of kVA. The overall architecture of the IMU is plotted in Figure 3-24.

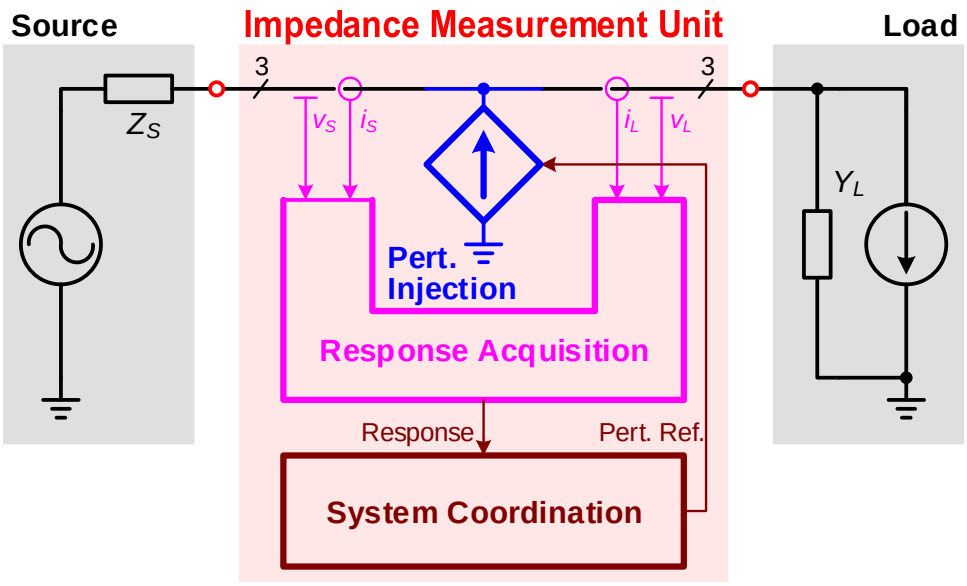

Figure 3-24 Overall architecture of IMU

To achieve this power rating and wide frequency range of measurements, the IMU is composed of 3 H-bridges using silicon modules and a power amplifier, as in the "Pert. Injection" part in Figure 3-24. The 3 H-bridges are for low frequency measurements from 0.1 Hz to 1 kHz as their switching frequency limits the control bandwidths and therefore the frequency range of perturbations. The power amplifier is for high frequency measurements from 10 Hz to 10 kHz because the ferrite core of its step-up transformer will be saturated under low frequency perturbations. The IMU can inject either voltage or current perturbations, called series or shunt mode respectively, because the IMU is series connected in the system to inject small-signal voltages and is parallel connected to inject small-signal currents. The pros and cons of these two modes have been discussed previously. In the series mode, the IMU bares the system current, and therefore the 3 H-bridges will be connected in parallel to increase current capability. On the other hand in the shunt mode, the IMU bares the system voltage and the 3 H-bridges will be connected in series to withstand higher voltages. This configuration change is achieved by manipulating switches, controlled by a PC "System Coordination".

Once the configuration of the IMU is decided, one can start the system under test and operate it under desired operating points. The IMU can automatically charge its dc capacitors to prepare perturbation injection. The injected signals can be sinusoidal waveforms at a single frequency, multi-tone signals at several frequencies and a chirp signal. To obtain the most accurate measurements, sinusoidal waveforms are preferable but most time-consuming. For example, measurements from 0.1 Hz to 1 kHz for 40 frequency points take about 50 minutes. Details about how the injection waveforms are generated are in [154]. All the responses are acquired by a specific computer from National Instruments, marked as “Response Acquisition”. After all the injections are done, the PC will calculate the impedances, both the grid and load sides, and store under a specific folder. The procedure of impedance measurements using IMU is drawn in Figure 3-25.

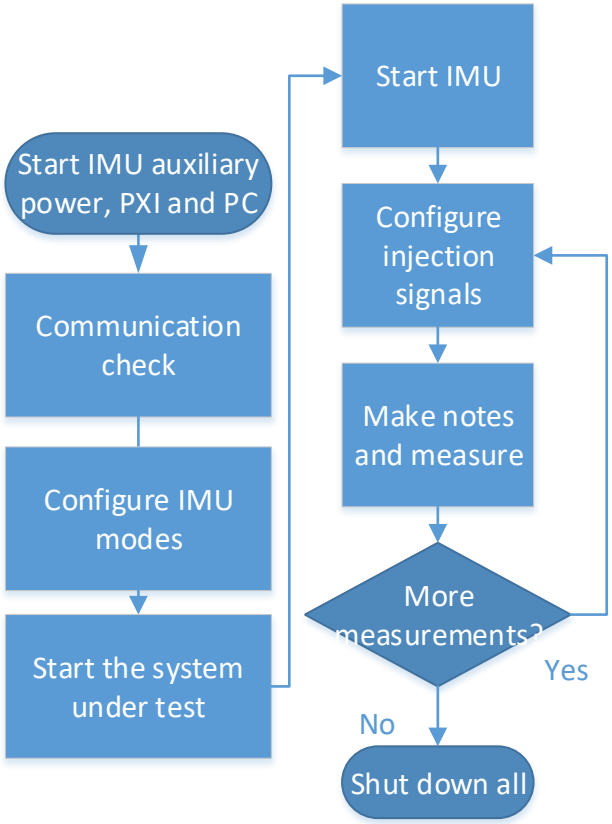

Figure 3-25 Procedure of impedance measurements using IMU

Chapter 4. IMPEDANCE-BASED STABILITY ANALYSIS ON 2-STATCOM SYSTEM

4.1 Impedance-based analysis on significant factors on 2-STATCOM system

With the previously developed STATCOM impedance model, the stability issue in the 2-STATCOM system can be analyzed from the impedance point of view. The 2-STATCOM system is drawn again in Figure 4-1, with two impedances defined at STATCOM 1 terminal: $\mathbf{Z_{vsi}}$ to be the d-q frame impedances of STATCOM 1 and $\mathbf{Z_{grid}}$ to be the impedances of the equivalent impedances of everything else in the system, including STATCOM 2, transmission lines and loads. The selection of terminal is arbitrary, as division of the system at any terminal should give the same stability conclusions when applying generalized Nyquist stability criterion (GNC). However, it is better to choose a STATCOM terminal because it will offer the impedances of the converter and the rest of the grid, which are more intuitive and easier to understand.

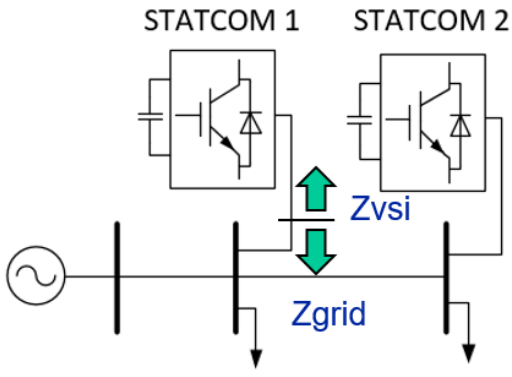

Figure 4-1 The 2-STATCOM system with two impedances defined

Figure 4-2 shows how the grid impedance at the terminal of STATCOM 1 was formulated. The blue curve shows the impedance of STATCOM 2, which is the impedance derived in Chapter III. The red lines shows the equivalent impedance of STATCOM 2 in parallel with the load at its

bus and it was very similar to the blue curve, the impedance of STATCOM 2. This is because a properly sized STATCOM had a much smaller impedance than the load. Then the impedance in yellow is the one in red in series with a transmission line, which did not vary much from the red, as the line impedances were small because of close physical proximity. The impedance in green is the grid impedance seen by STATCOM 1, which equals to the equivalent impedance of the yellow, a load and the transmission line connecting to the infinite bus in parallel. Although the grid impedance in green was dominant by the impedance of the transmission line connecting to the infinite bus, one could still see impacts from the impedance of STATCOM 2, especially around 10 Hz. This shows that STATCOMs could see each other through the transmission lines due to the higher relative magnitude of their impedances with respect to that of the lines.

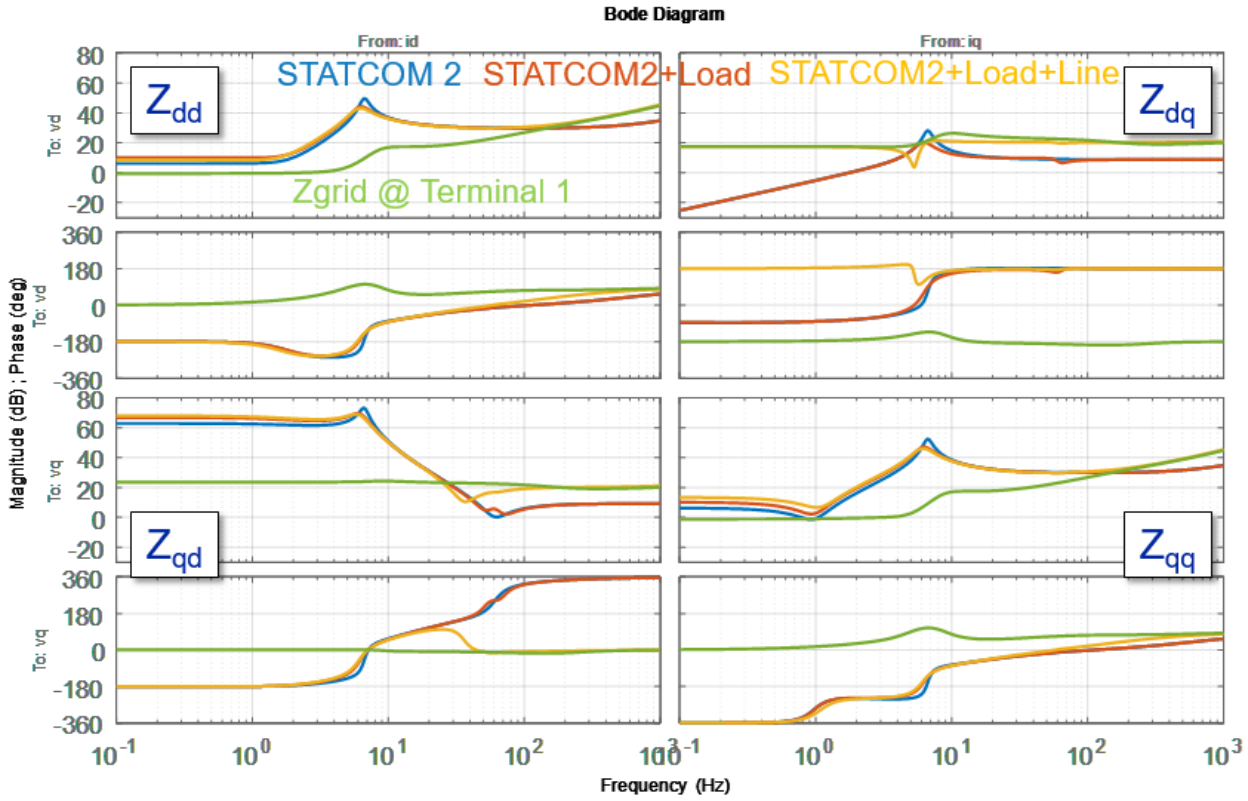

Figure 4-2 Dynamic propagation from one STATCOM to the other in impedances

The transmission lines connecting to the infinite bus had different and strong effects on the stability, as mentioned in Chapter II. In the 2-STATCOM system, this specific line determined the grid stiffness. The smaller the line impedance, the stiffer the system. One extreme case is that when the line impedance is zero, STATCOM 1 will see nothing from STATCOM 2 because now the infinite bus clamps the voltage at the PCC of STATCOM 1 and the grid impedance at the terminal of STATCOM 1 is zero. Figure 4-3 shows the grid impedances under two cases with typical values of the line impedances, where the blue lines show the cases with double the line impedances than that of the red. If the specific line decreased in impedance magnitude, the grid impedance observed by STATCOM 1 would be smaller and thus there would be fewer interactions from STATCOM 2.

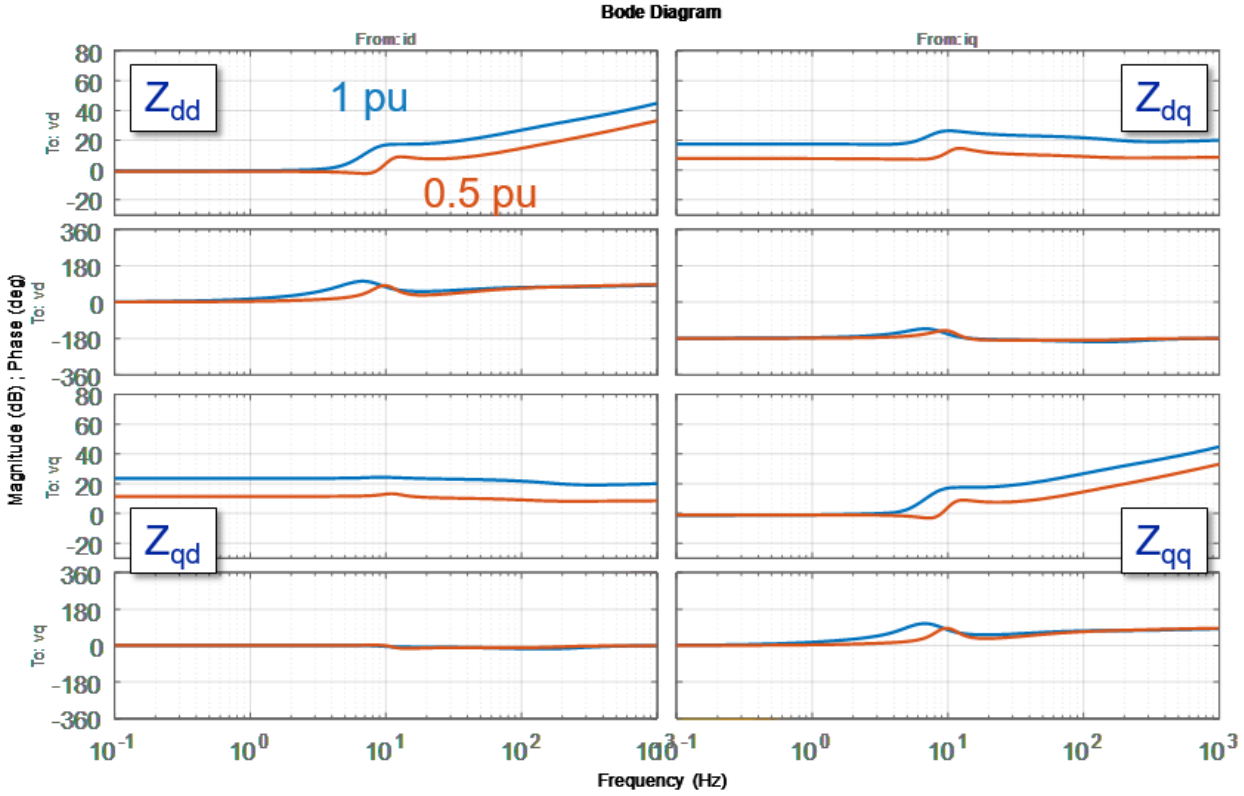

Figure 4-3 Grid impedance at terminal of STATCOM 1 regarding the transmission lines connecting to the infinite bus

The following sub-sections will give detailed analysis on the previously discussed instability issues in the 2-STATCOM system.

4.1.1 Impacts of ac voltage loop

The d-q frame impedances measured as defined in the simulation are shown in Figure 4-4. Three cases, 1 Hz, 7 Hz and 20 Hz, were considered and measured. The STATCOM 1 impedances are in dashed lines and those of the rest of the grid are in solid lines. Looking at the STATCOM impedances in solid lines, as analyzed in 3.4.2.1, the increase in the bandwidth of the ac voltage loop resulted in the increase of the resonant peak in $\mathbf{Z}_{\mathbf{vsi}}$ (from blue to red to green), because this peak was created by the exact loop. On the other hand, this change also reflected in the equivalent grid impedance $\mathbf{Z}_{\mathbf{grid}}$ (from blue to red to green) because STATCOM 2 also presented the same change and $\mathbf{Z}_{\mathbf{grid}}$ was a combination of the impedances of STATCOM 2, loads and transmission lines. Of course, the impedances of loads or transmission lines were not too large to mask those of STATCOM 2 as in this system, which can be often guaranteed in transmission systems and ensured by the fact that STATCOMs are in near proximity. In the end, the impacts on d-q frame impedances from the ac voltage loop could be observed in both $\mathbf{Z}_{\mathbf{vsi}}$ and $\mathbf{Z}_{\mathbf{grid}}$.

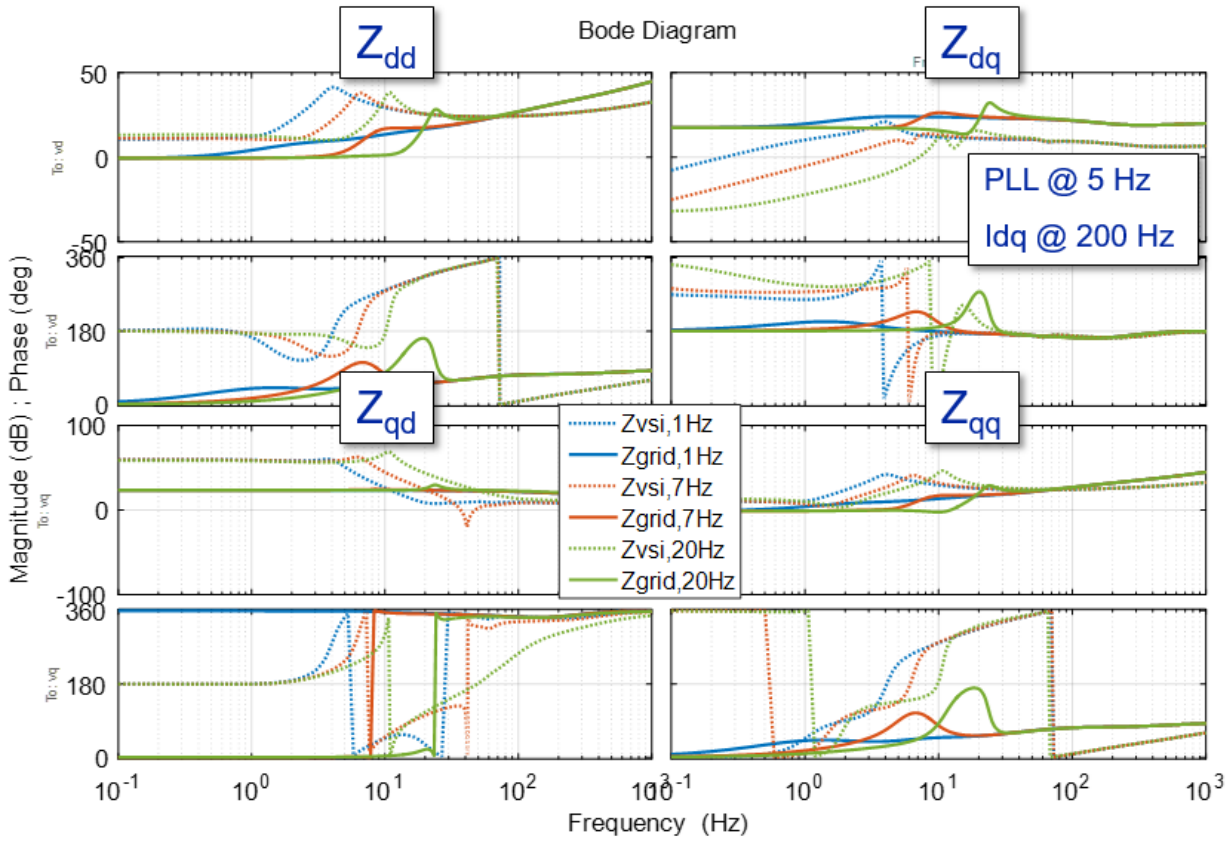

Figure 4-4 Impacts of ac voltage loop on d-q frame impedances at terminal of STATCOM 1 in simulation

To analyze small-signal stability, it is necessary to calculate the eigenvalues $\lambda_1(s)$ and $\lambda_2(s)$ of the return ratio $\mathbf{L}(s)=\mathbf{Z}_{\mathbf{grid}}(s)\mathbf{Y}_{\mathbf{vsi}}(s)$ because the impedance matrices and the return ratio were not diagonal-dominant and no direct indications of stability could be obtained. Figure 4-5 shows the eigenvalue $\lambda_1(s)$ in three cases and zoomed-in part around $(-1+j0)$ in Nyquist plot. The other eigenvalue $\lambda_2(s)$ were too small and away from the critical point and thus not plotted in the figure. It is clear that the eigenvalue encircled the critical point counter-clockwise zero times for 1 Hz bandwidth and twice for 20 Hz bandwidth while the eigenvalue for 7 Hz just intersected at the critical point. Because both $\mathbf{Z}_{\mathbf{grid}}(s)$ and $\mathbf{Y}_{\mathbf{vsi}}(s)$ contained no right half plane (RHP) poles, one can deduce that the case with 1 Hz bandwidth was stable and that with 20 Hz bandwidth was unstable and the case with 7 Hz bandwidth was marginally stable. This corresponded to the time-domain

simulation results in Section 2.4. Moreover, for the unstable case the eigenvalue intersected the negative real axis at the frequency of about 30 Hz, which is the exactly the oscillatory frequency in the time-domain simulation. As such, the use of d-q frame impedances predicted not only whether the system was stable or not but also the oscillatory frequency.

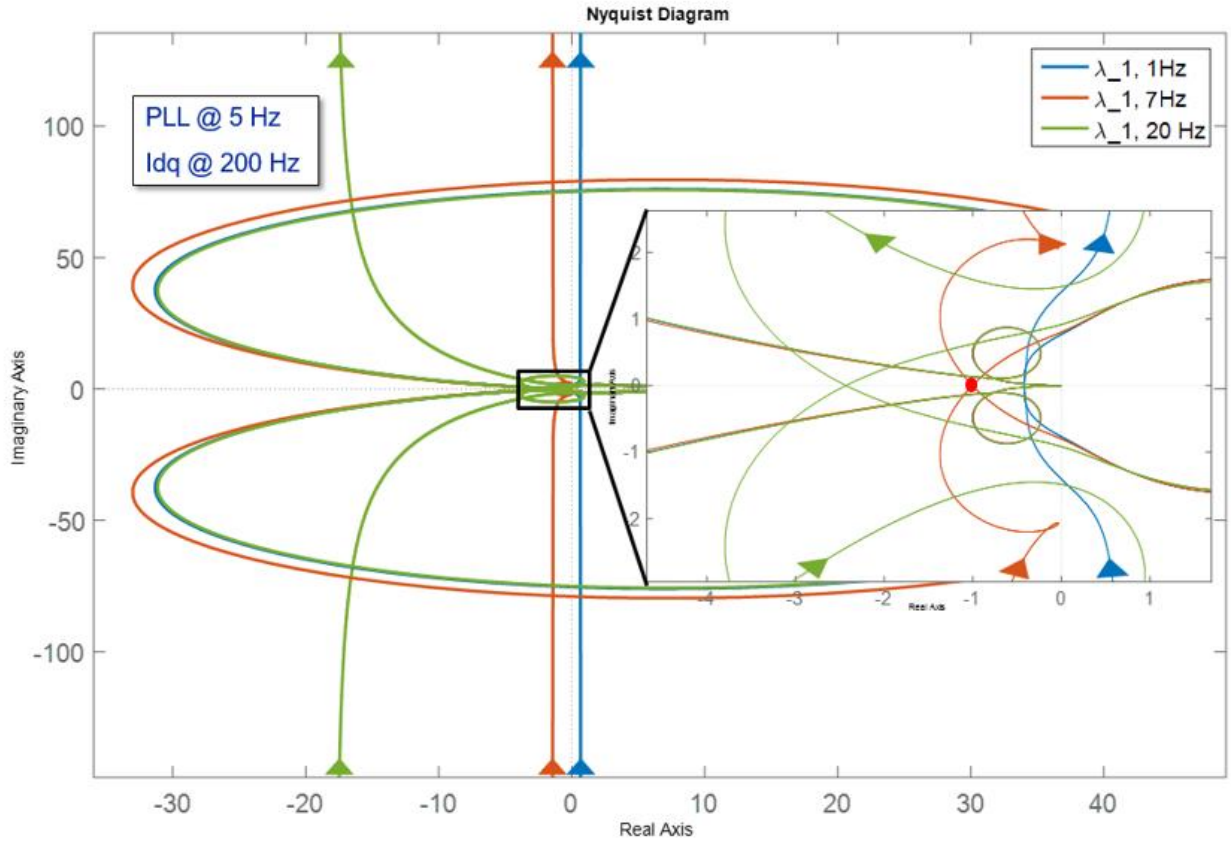

Figure 4-5 Impacts of ac voltage loop on characteristic loci in simulation

To pinpoint the reason of possible instability, Figure 4-6 plots the eigenvalues from Figure 4-5 in Bode plot. When the characteristic loci reach 180 degrees in Bode plot, they cross the negative real axis in Nyquist plot; if at this frequency the magnitude is greater than 0 dB, then they intersect the negative real axis outside the unity circle. According to the low and high frequency behaviors, this means encirclement of the critical point. With the increased bandwidth of the ac voltage loop, a resonant peak showed up and moved to high frequency, as the change in $\mathbf{Z}_{\mathbf{grid}}$. This made the

magnitude of the characteristic loci rise in magnitude and eventually encircle the critical point at 30 Hz, the oscillatory frequency. Sensitivity check of characteristic loci also indicated that $\mathbf{Z_{grid}}$ contributed much more than $\mathbf{Z_{vsi}}$. Therefore, one can conclude that the increment of the ac voltage loop enlarged the impedance of STATCOM and reflected to the terminal of the other STATCOM and finally escalated the possibility that two STATCOMs could interact with each other. This clearly showed how the ac voltage loop control influenced the small-signal stability, from the d-q frame impedance point of view.

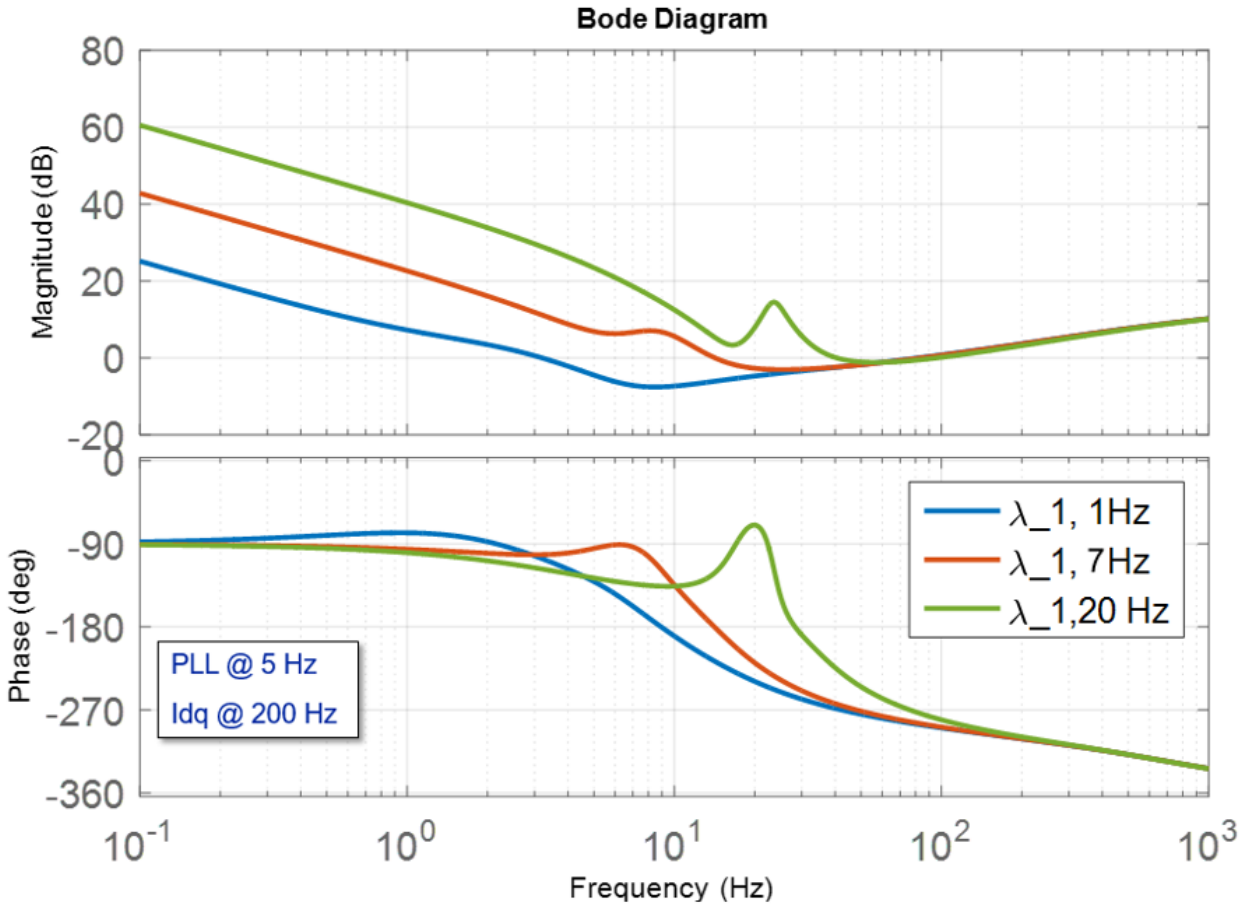

Figure 4-6 Impacts of ac voltage loop on characteristic loci in simulation (Bode plot)

4.1.2 Impacts of PLL

Figure 4-7 shows the measured impedances of $\mathbf{Z_{vsi}}$ in dashed lines and $\mathbf{Z_{grid}}$ in solid lines at the same terminal with respect to changes in PLL. Three cases, 2.5 Hz in blue, 5 Hz in red and 10 Hz in green, were measured. The resonant peaks in $\mathbf{Z_{vsi}}$ moved to high frequency as the bandwidth rose as shown in the analysis in 3.4.2.2. $\mathbf{Z_{grid}}$ showed corresponding move in the resonant peaks too for the same reason in the previous subsection. However, the changes were smaller, compared to the ac voltage loop case, which was already discussed in 3.4.2.2 that in transmission systems the ac voltage loop affected the d-q frame impedances much more than PLL. Due to this, PLL had small but nonetheless negligible impacts on small-signal stability and in order to show the impacts a marginally stable case was tested in Figure 4-7.

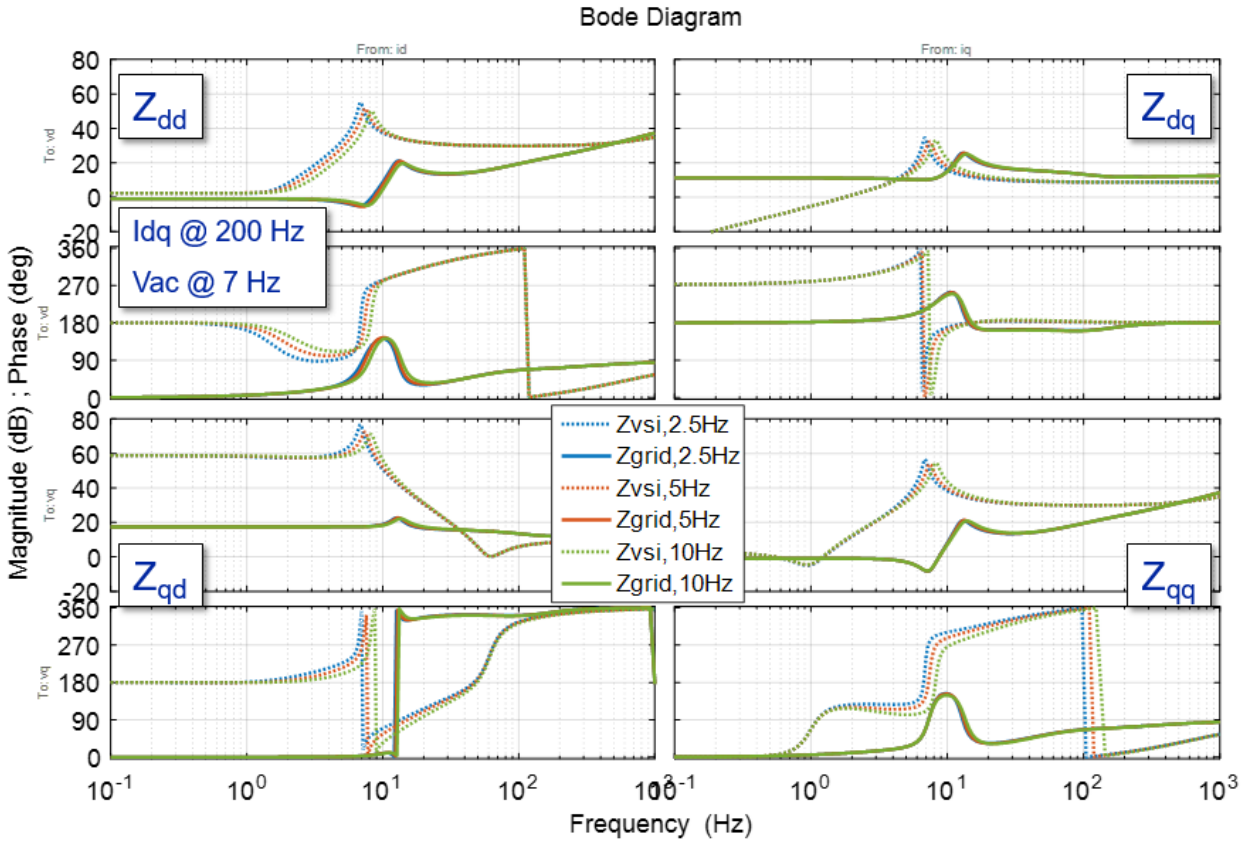

Figure 4-7 Impacts of PLL on d-q frame impedances at terminal of STATCOM 1 in simulation

The impedance matrices and return ratio were still not diagonal-dominant and eigenvalues are plotted in Figure 4-8. The change in eigenvalues were still very small but still showed some impacts on small-signal stability. Why the effect of PLL was masked by that of the ac voltage loop was explained in Section 3.4.2.2.

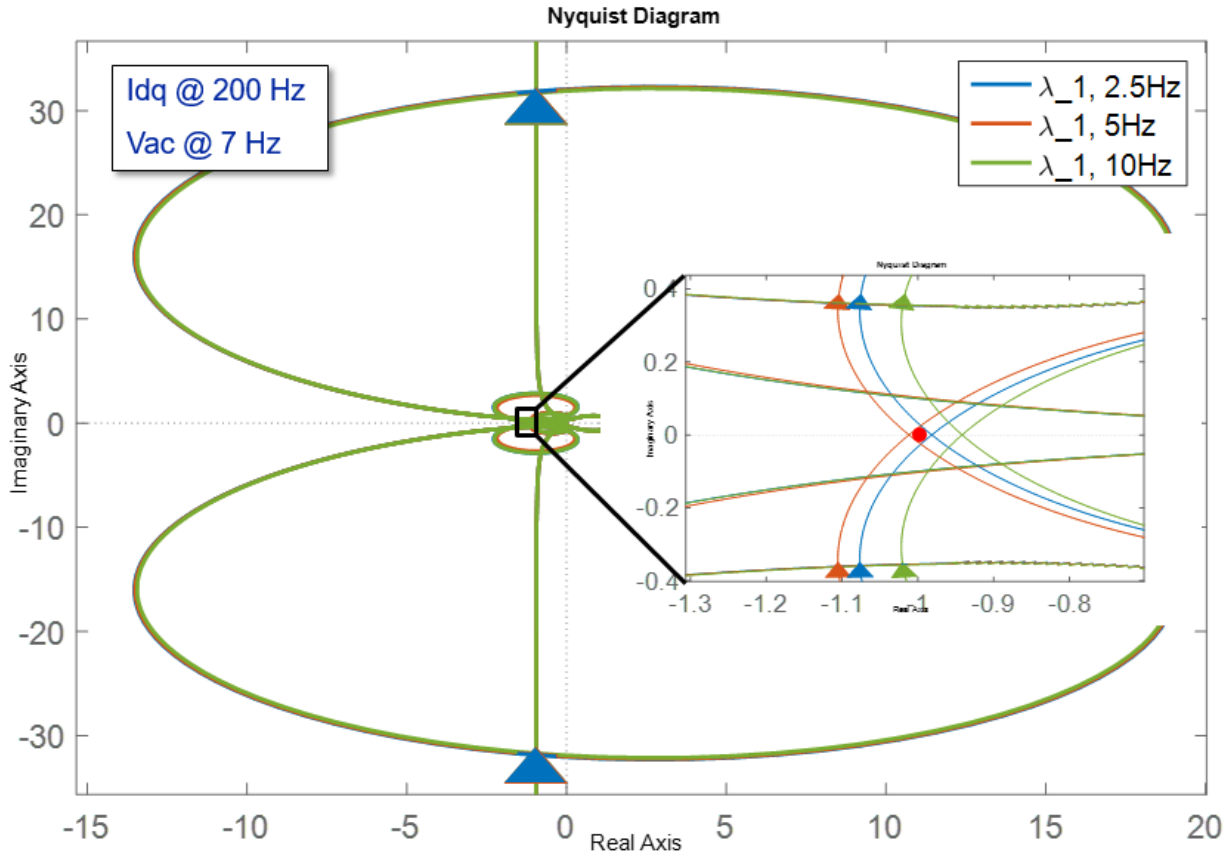

Figure 4-8 Impacts of PLL on characteristic loci in simulation

4.1.3 Impacts of current loop

Similar analysis was done with respect to the current loop and impedances were measured at the same terminal as plotted in Figure 4-9. $\mathbf{Z}_{\mathbf{vsi}}$ are in dashed lines and $\mathbf{Z}_{\mathbf{grid}}$ are in solid lines under three circumstances: 100 Hz in blue, 200 Hz in red and 500 Hz in green. As discussed, the increase in the current loop bandwidth resulted in the increase in the magnitude of $\mathbf{Z}_{\mathbf{vsi}}$ within its bandwidth.

However, the change in this frequency range (from several hundreds of Hertz to 1 kHz) in $\mathbf{Z}_{vsi}$ had relatively smaller influences in $\mathbf{Z}_{grid}$, because the impedances of STATCOM 2 were not significantly greater than those of other components in the grid in that frequency range. Therefore, the return ratio with respect to the current loop depended on $\mathbf{Z}_{vsi}$ mostly, unlike the occasions with respect to the ac voltage loop.

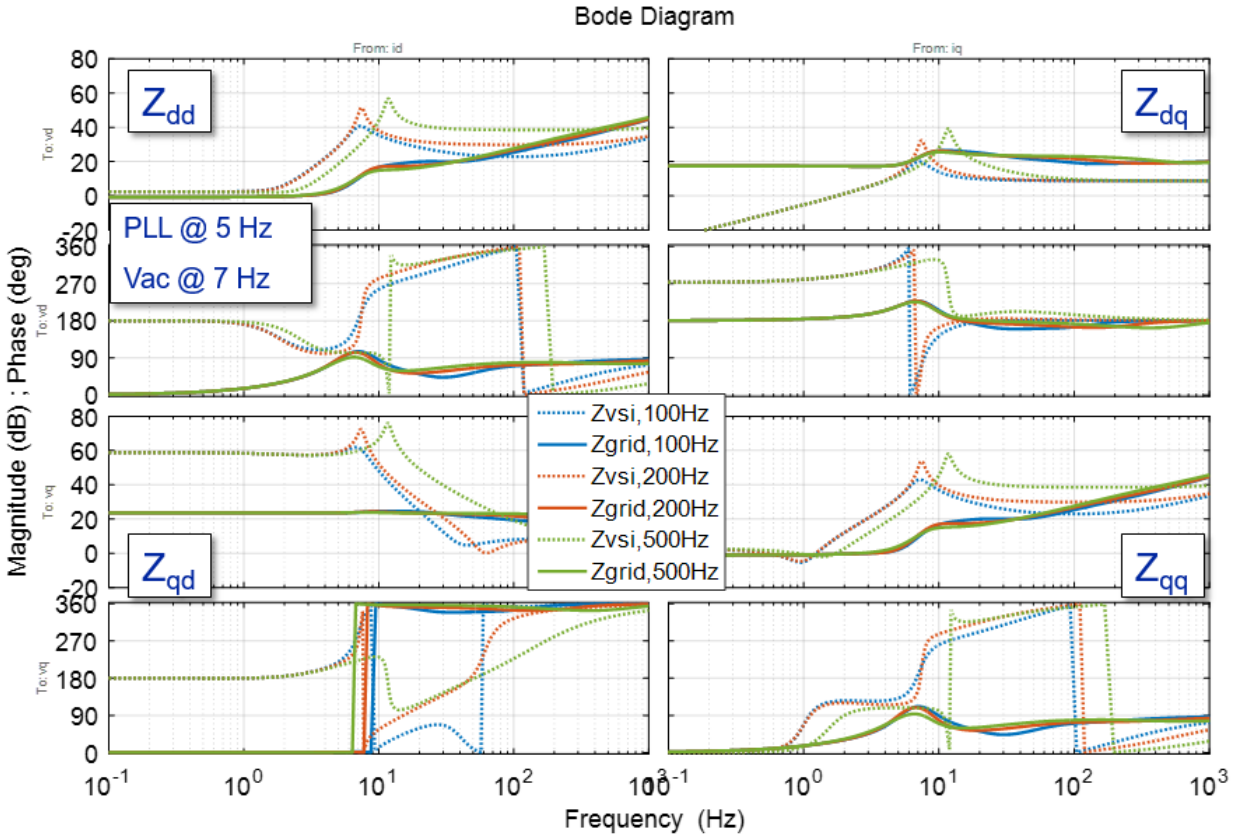

Figure 4-9 Impacts of current loop on d-q frame impedances at terminal of STATCOM 1 in simulation

The eigenvalues of the return ratio were calculated and plotted in Nyquist plot in Figure 4-10. It is clear that in the 100 Hz bandwidth case the characteristic locus encircled the critical point and in the 500 Hz bandwidth case it did not. Because there was no RHP pole in either $\mathbf{Z}_{grid}(s)$ or $\mathbf{Y}_{vsi}(s)$, one can conclude that the 100 Hz bandwidth case was unstable and the 500 Hz bandwidth case was stable. Additionally, the 200 Hz bandwidth case was marginally stable because the intersection

point was right at the critical point. This d-q frame impedance based stability analysis also validated the simulation results shown in Section 2.4.

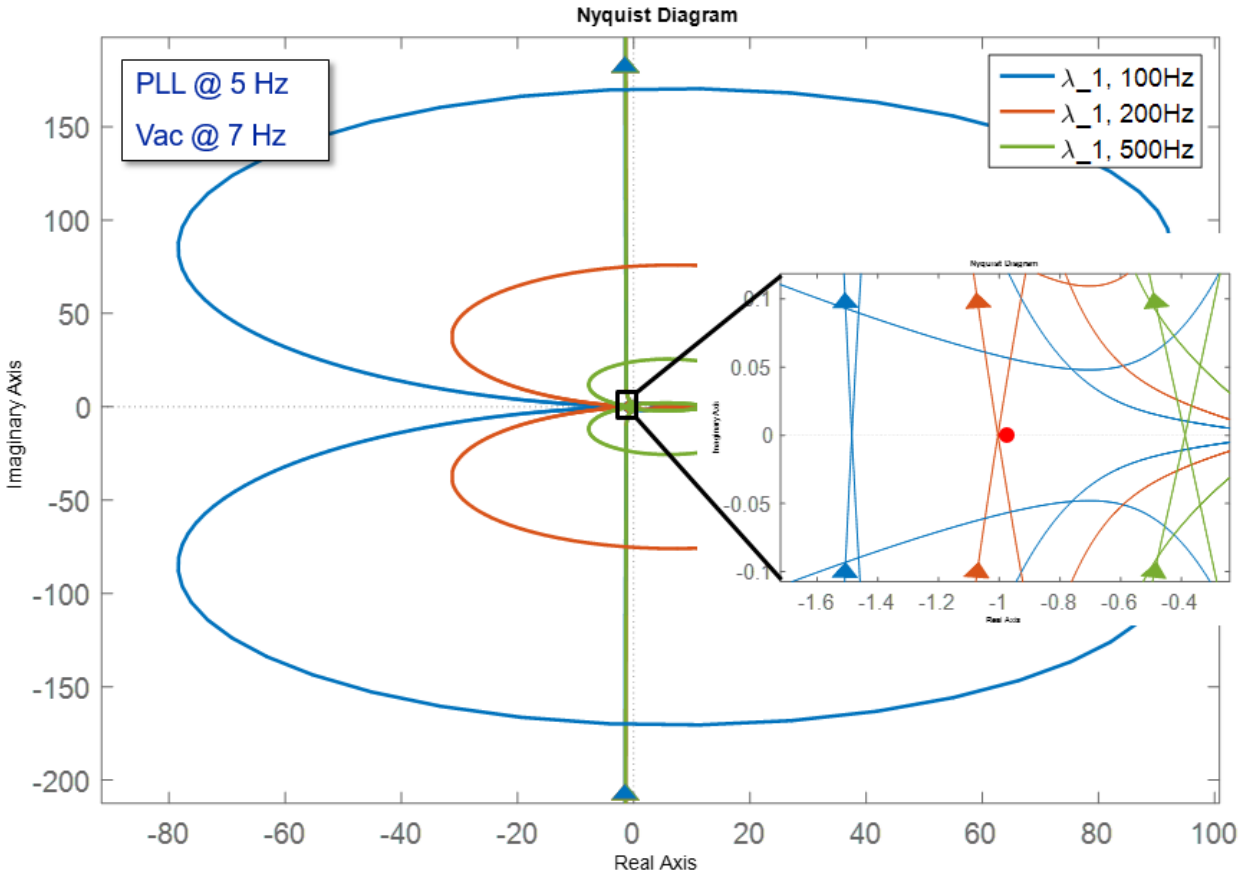

Figure 4-10 Impacts of current loop on characteristic loci in simulation

The characteristic loci are plotted in Bode plot in Figure 4-11. When the current loop bandwidth increased, the magnitude of $\mathbf{Z}_{vsi}$ in high frequency increased and hence the return ratio dropped in magnitude as well as eigenvalues. Recall that when the phase reached 180 degrees, the characteristic loci intersected with the negative real axis and the magnitude at this particular frequency showed where the intersection point was. In Figure 4-11, as the magnitude of eigenvalues decreased, it was more possible that the intersection point of the negative real axis

moved within the unity circle, thus making the characteristic locus not encircling the critical point in Nyquist plot, which means more stable.

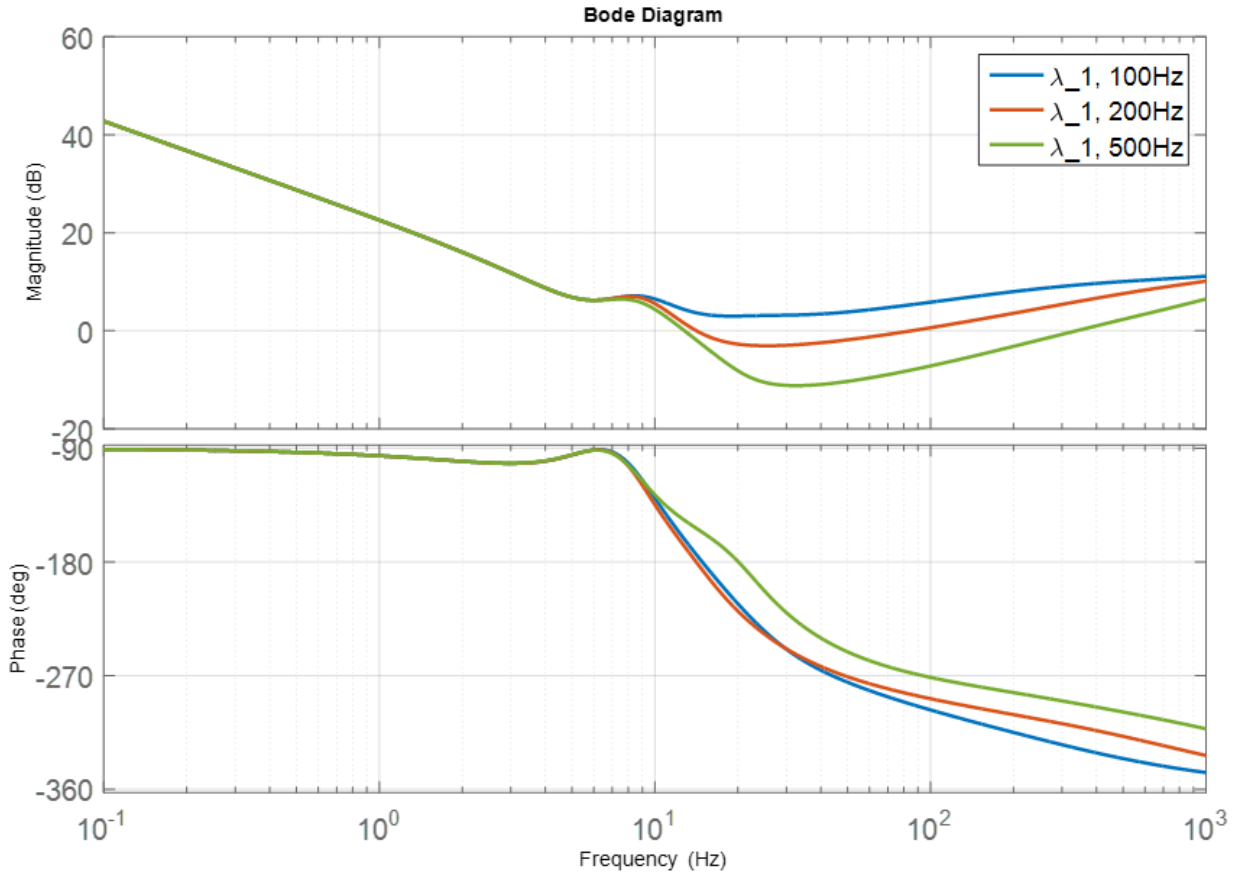

Figure 4-11 Impacts of current loop on characteristic loci in simulation (Bode plot)

4.1.4 Impacts of QV droop

Lastly, the impacts of STATCOM operation modes: the ac voltage regulation mode (without the QV droop) and the QV droop mode were analyzed in this sub-section. The impedances of STATCOM 1 and the grid without the QV droop are in blue and those with the QV droop are in red, in Figure 4-12. Not only did the QV droop change the operating point, it greatly increased the STATCOM impedance magnitude in the dq channel.

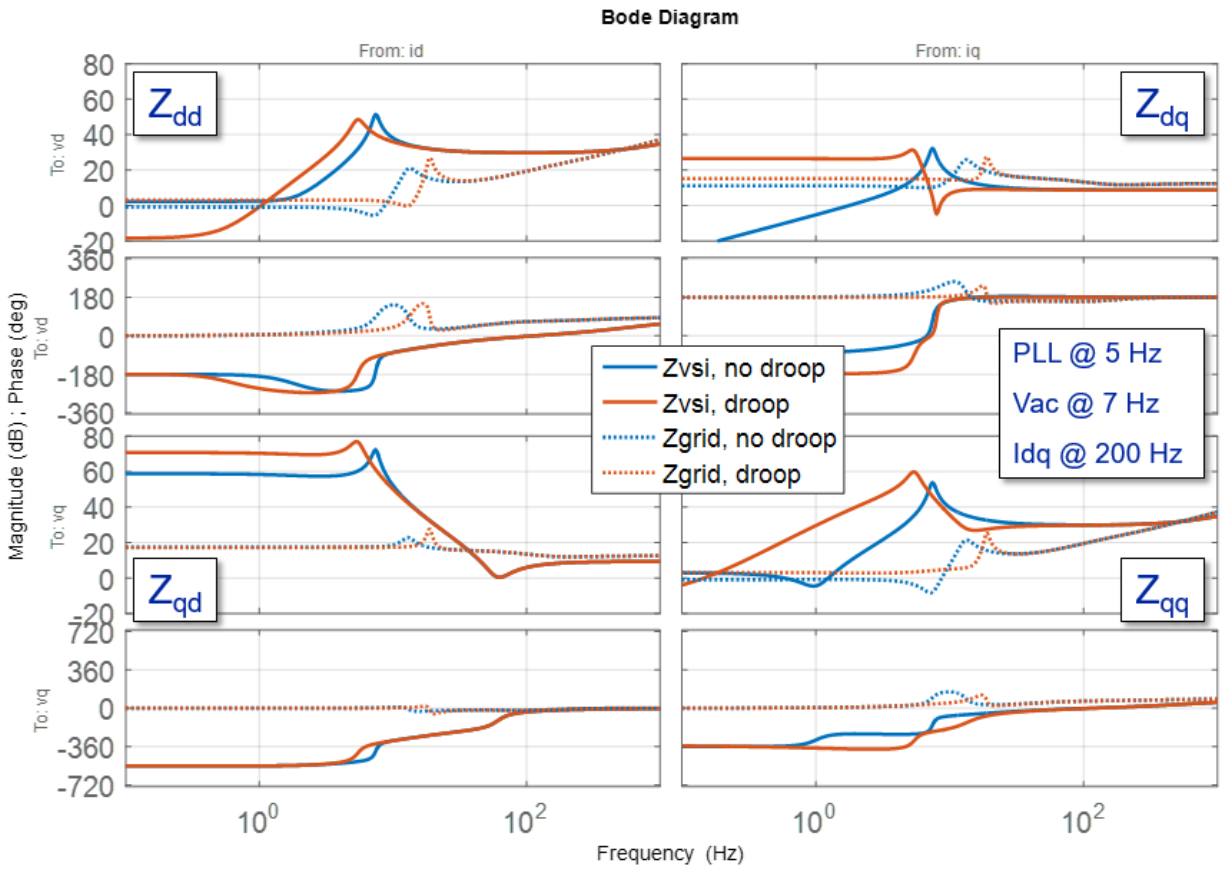

Figure 4-12 Impacts of QV droop on d-q frame impedances at terminal of STATCOM 1 in simulation

The corresponding calculated eigenvalues are plotted in Figure 4-13 with the one without the QV droop in blue and the one with the QV droop in red. When the STATCOMs were working without the QV droop, the system was marginally stable, as in Figure 2-14. This can be inferred from the characteristic locus because it crossed the negative real axis just at the critical point (-1+*j*0). On the contrary, if the STATCOMs were working under the QV droop mode, the system was unstable as the characteristic locus encircled the critical point.

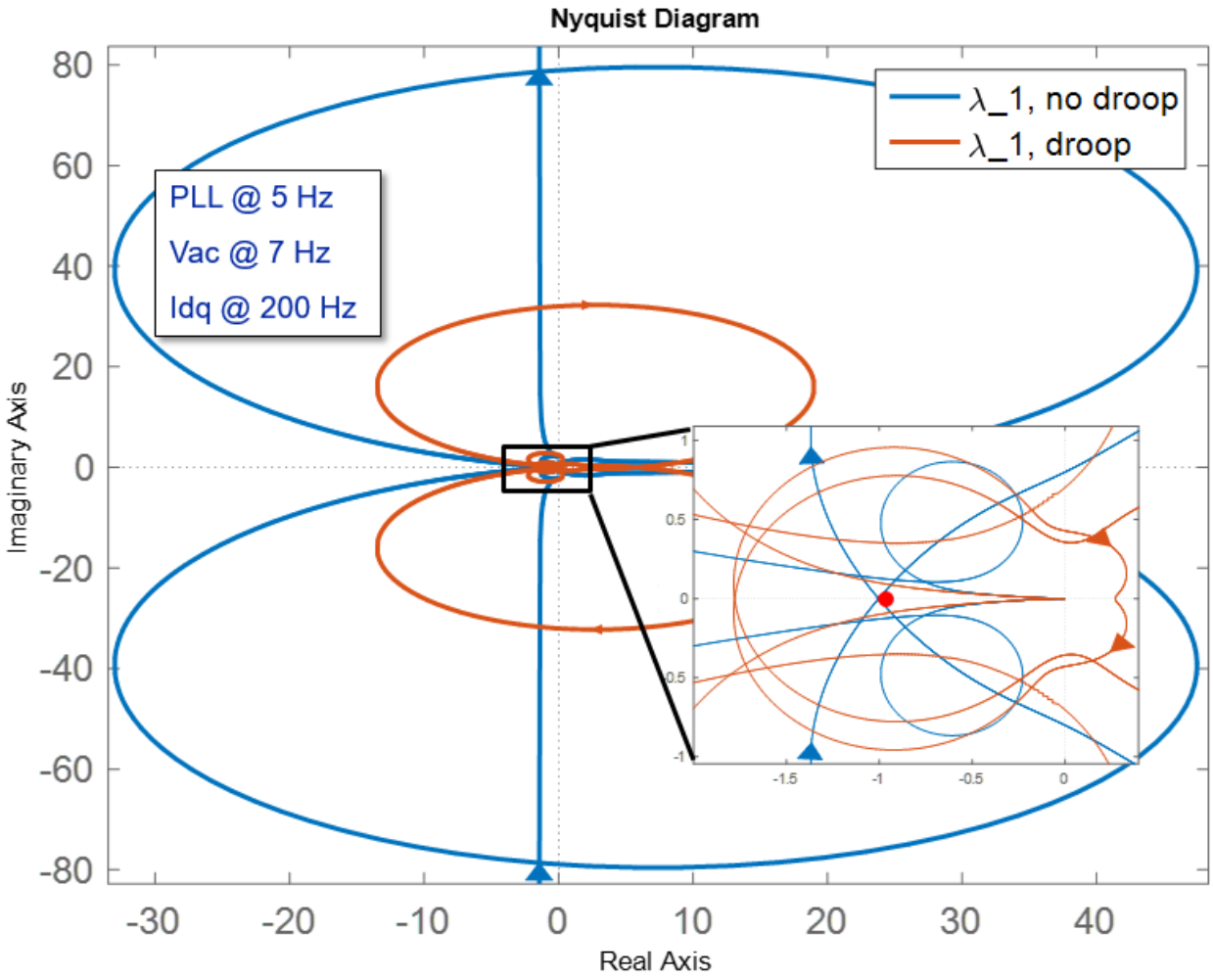

Figure 4-13 Impacts of QV droop on characteristic loci in simulation

From the above analysis based on d-q frame impedances, we can know that in the 2-STATCOM power system, one STATCOM could see the other one in terms of impedances through transmission lines and thus interact in a possibly negative way. This is mainly because the line impedances of transmission systems are relatively low with respect to those of STATCOMs.

The use of d-q frame impedances identified the frequency range of interaction and investigated how control loops influenced the stability. AC voltage regulation was the main reason of stability and STATCOMs strongly disrupt each other's operation. The PLL was masked in this system to

some extent. Low current loop bandwidth also caused instability because of the decreasing impedance magnitude of STATCOMs.

4.2 Discussions on instability patterns

4.2.1 Instability due to ac voltage loop and PLL

In these two scenarios, the change in impedance with respect to ac voltage loop and PLL was in the frequency range of the observed oscillations, about 10 to 50 Hz. In this frequency range, the STATCOM impedance was much larger than the impedance of other units in the power system. As a result, there were significant changes in $\mathbf{Z_{grid}}$ when the control parameters of the further STATCOM varied, especially the resonant peak which caused instability. As the bandwidths of the ac voltage loop and PLL increased, the resonant peak moved accordingly. Therefore, it would be a good remedy to move the peak to low frequencies to stabilize the system. As long as the transient responses of the ac voltage loop regulation meet the grid code, a slower ac voltage loop bandwidth is preferred to avoid interactions, which is also a practical method in merchandised products.

4.2.2 Instability due to current loop

Unlike the other two scenarios, the current loop bandwidth showed less influences on $\mathbf{Z_{grid}}$ because at higher frequencies the magnitude of the line impedances started to increase due to its inductive part. Due to this, small impedance of STATCOM was not preferred because it would increase the possibility of interacting with the grid impedance. A high current loop bandwidth would enlarge the magnitude of the STATCOM impedance and is thus recommended for small-

signal stability. Meanwhile, a high current loop bandwidth as high as possible is always preferable in order to obtain better control over a larger frequency range.

4.2.3 Instability channels

Additionally, the fact that only $\lambda_1(s)$ had the potential to cause instability indicated that the discussed instability happened only in d-channel of the given system d-q frame, introduced by the ac voltage regulation instead of synchronization [57]. To explain this in detail, two system d-q frames with respect to the position of PCC voltage were selected in Figure 4-14, where in the left $\vec{\mathbf{V}}_{\mathbf{PCC}}$ voltage vector was close to the d-channel of the system d-q frame and in the right it was the far away from the d-channel. Again, remember that the selection of the system d-q frame is arbitrary and the position of $\vec{\mathbf{V}}_{\mathbf{PCC}}$ stayed the same.

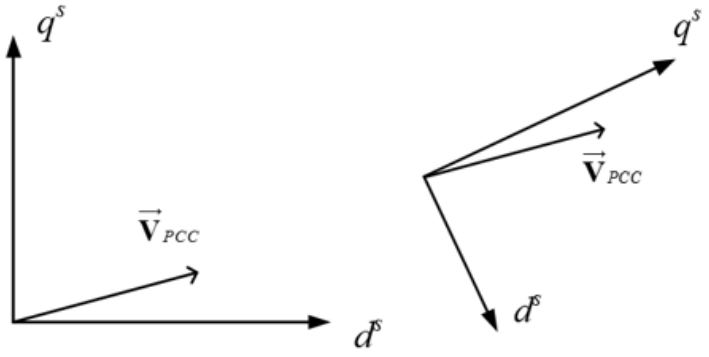

Figure 4-14 Different positions of system d-q frame

Let us first look at the first case where $\vec{\mathbf{V}}_{\mathbf{PCC}}$ is close to the d-channel of the system d-q frame. Figure 4-15 shows the STATCOM impedance and the equivalent grid impedance including the other STATCOM in an unstable case. Figure 4-16 plots the corresponding characteristic loci. In this case, $\lambda_1(s)$ encircled the critical point and $\lambda_2(s)$ was far away from it, which is exactly what we

saw in the previous sections. This is because the previously chosen system d-q frame was close to $\vec{\mathbf{V}}_{\mathbf{PCC}}$, since the STATCOM 1 was only one line impedance away from $\vec{\mathbf{V}}_{\mathbf{g}}$ in Figure 4-1.

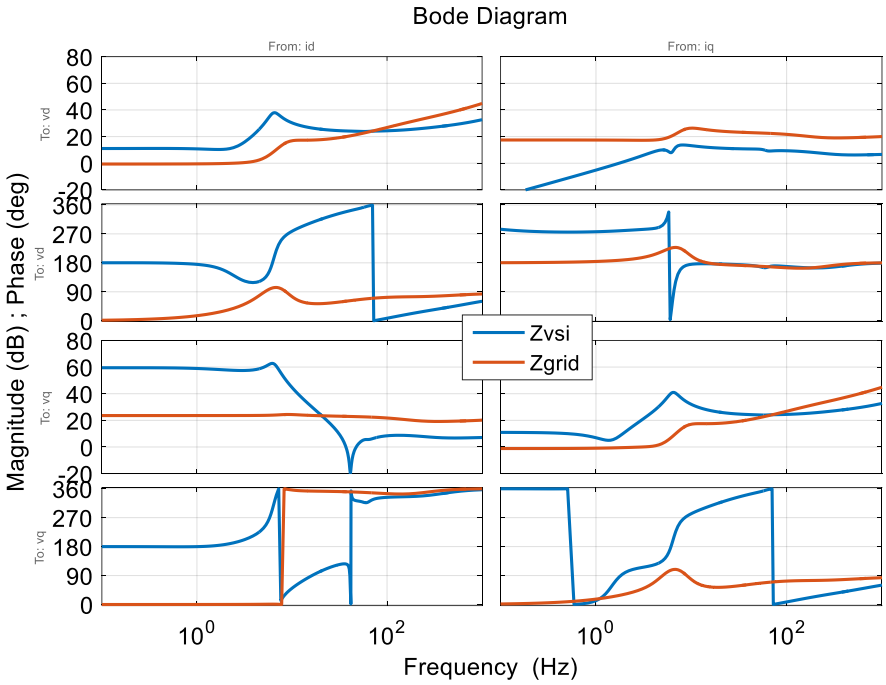

Figure 4-15 Impedances of an unstable case with V_{pcc} close to V_g

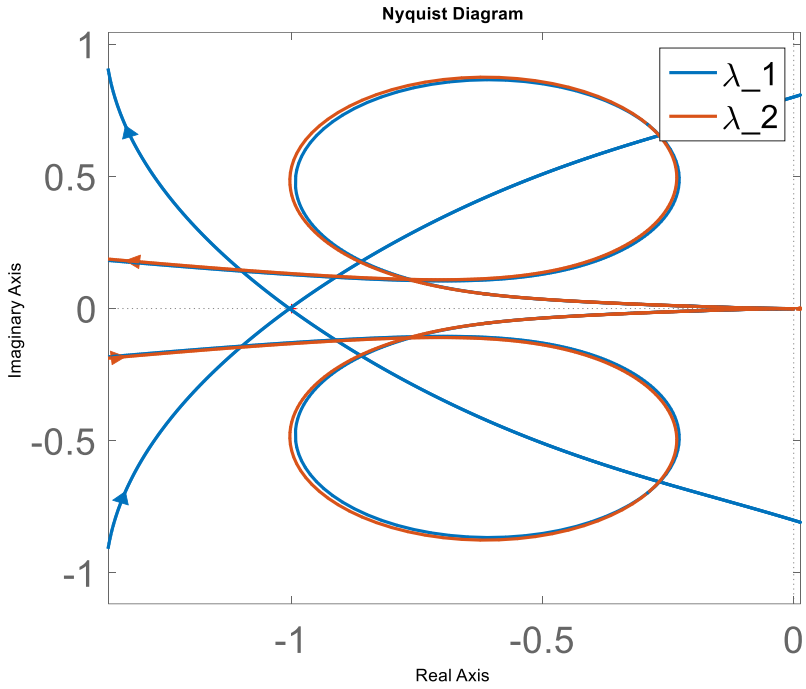

Figure 4-16 Characteristic loci of an unstable case with V_{pcc} close to V_g

However, if the system d-q frame was chosen to be away from $\vec{\mathbf{V}}_{\mathbf{PCC}}$, for the same control parameters and operating point, the impedances were measured again in Figure 4-17. Nothing changed here except the selection of the system d-q frame. These impedances can also be obtained via the transformation matrix in (3.4). Figure 4-18 shows the corresponding characteristic loci under the new system d-q frame. In this case, $\lambda_2(s)$ encircled the critical point instead of $\lambda_1(s)$. This difference was just because of the change in the system d-q frame as the reference.

Therefore, the channel where the instability happened depended on the relative position difference between $\vec{\mathbf{V}}_{\mathbf{PCC}}$ and $\vec{\mathbf{V}}_{\mathbf{g}}$, which is essentially the selection of the system d-q frame. The instability was always associated with $\vec{\mathbf{V}}_{\mathbf{PCC}}$ instead of its perpendicular direction, and thus was actually a problem introduced by the ac voltage regulation instead of synchronization which happened at the perpendicular direction of $\vec{\mathbf{V}}_{\mathbf{PCC}}$. That is to say, one cannot simply say that the

instability found here always happened at the d-channel. Precisely speaking, the instability occurred at the same direction of $\vec{\mathbf{V}}_{\mathbf{PCC}}$ observed for multiple STATCOMs. It is worthwhile to point it out because in a more complexed power grid, the phase difference between $\vec{\mathbf{V}}_{\mathbf{PCC}}$ and $\vec{\mathbf{V}}_{\mathbf{g}}$ may be large and a simple statement about stability at either d- or q-channel is not an accurate description.

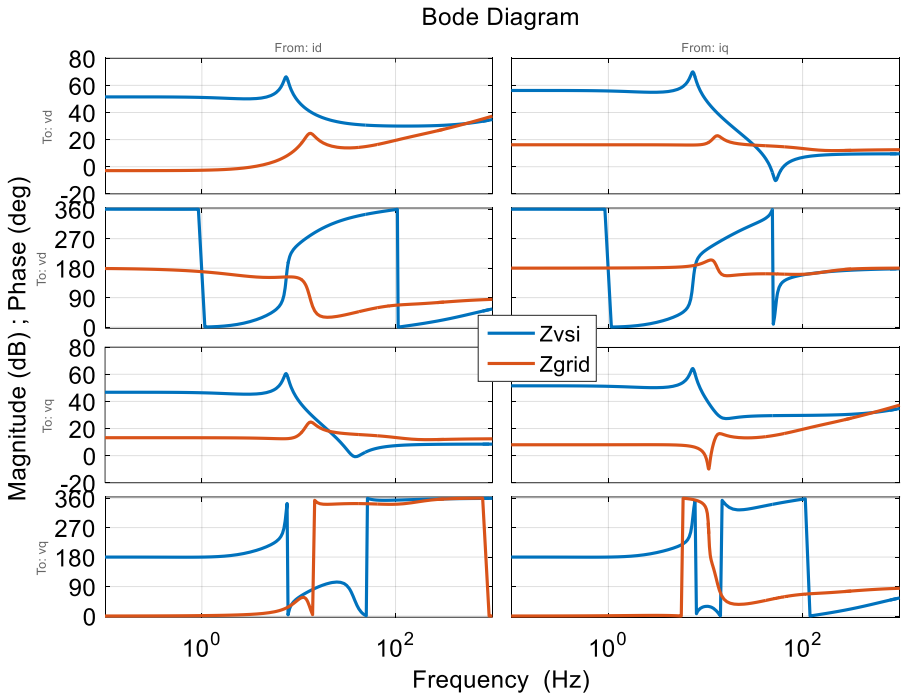

Figure 4-17 Impedances of an unstable case with Vpcc away from Vg

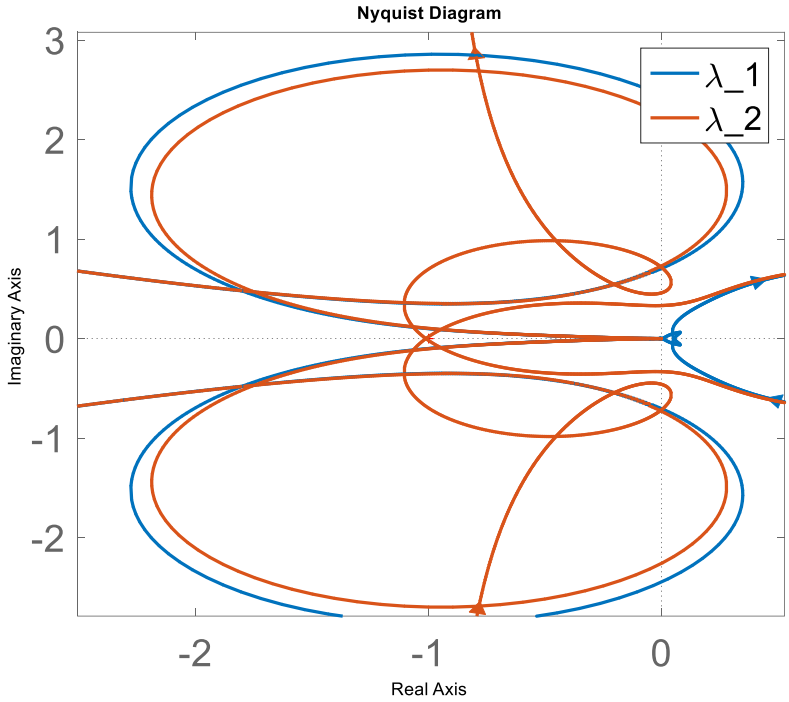

Figure 4-18 Characteristic loci of an unstable case with Vpcc away from Vg

4.3 Effects of alternative controls

4.3.1 Proportional controller for inner current loop

As discussed in Section 3.4, the inner current loop tries to regulate the converter to behave as a current source that has ideally infinite magnitude of impedance at low frequencies, which is actually fulfilled by the integrator in the current controller. If we remove the integrator, there will be no large impedance at the frequency of the ac voltage loop bandwidth and the resonant peak will be greatly damped. Figure 4-19 shows the impedances of STATCOM with a proportional control in the current loop plotted in blue, in comparison with the PI control plotted in red. As predicted, the resonant peak almost disappeared and left the sections in low and high frequencies stay the same.

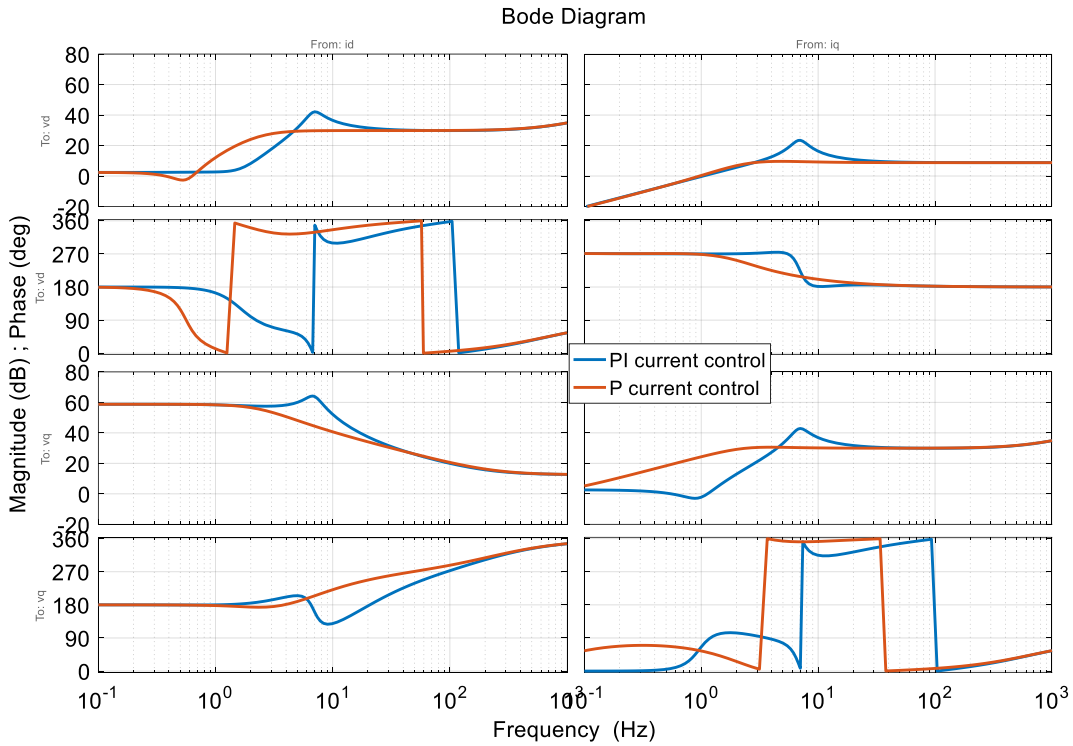

Figure 4-19 STATCOM impedance with P and PI controllers for current loop

Figure 4-20 shows that with the bandwidths of all control loops in the legend, the proportional controller for the current loop helped to stabilize the system as expected.

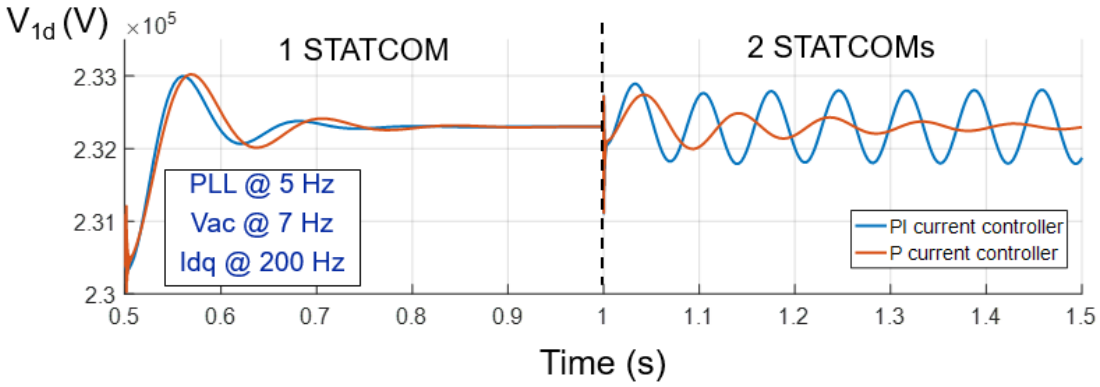

Figure 4-20 Simulation waveforms with PI and P controllers for current loop

However, without the integrator in the current controller, we lost a lot of regulation capability of currents within the current loop bandwidth, as the closed-loop loop gains of current loop were

much smaller than unity, meaning that the currents could not follow their references well, especially for low-frequency disturbances. In the low frequencies, the integrator in the PI controller increased the magnitude of the open-loop transfer function from $\tilde{\mathbf{i}}^{ref}$ to $\tilde{\mathbf{i}}$, such that the controlled current could resist perturbations and track the corresponding references accurately. Without the integrator, the only regulation of currents falls into indirect control by the outer voltage loops, which is not preferable to handle complex grid conditions. Especially, the overshoot or undershoot of the current to grid transients may be very large without the integral term.

4.3.2 Alternative controllers for ac voltage loop

Another way to tune the STATCOM impedance is to change the ac voltage loop controller. Because a sharp resonant peak indicates insufficient damping and a small phase margin, alternative controllers can replace the PI controller in order to boost the phase margin to provide additional damping.

Figure 4-21 shows open loop gains for the ac voltage loop, $\tilde{v}_d \big/ \tilde{v}_d^{ref}$, with different compensators tuned at the same bandwidth. The PI controller could achieve an 86-degree phase margin, which was used for evaluation previously, as plotted in red marked as “PM 86”. A type II controller was designed in order to place a zero before the bandwidth to boost the phase and get a 135-degree phase margin, drawn in yellow marked as “PM 135”. Another controller was designed representing a low-pass filter below the bandwidth and a high-frequency zero, decreasing the phase margin to 40 degree, depicted in blue and marked as “PM 40”. With no additional zero before the bandwidth, the most phase margin was only a little bit less than 90 degree. The lower the frequency of the additional zero before the bandwidth, the more phase margin for the open-loop gain. As a result, STATCOM impedance was changed accordingly shown in Figure 4-22, showing in blue,

red and yellow as 40-, 86- and 135-degree phase margins. The larger the phase margin, the more damping for the resonant peak, indicating smaller possibility to interact with the other STATCOMs.

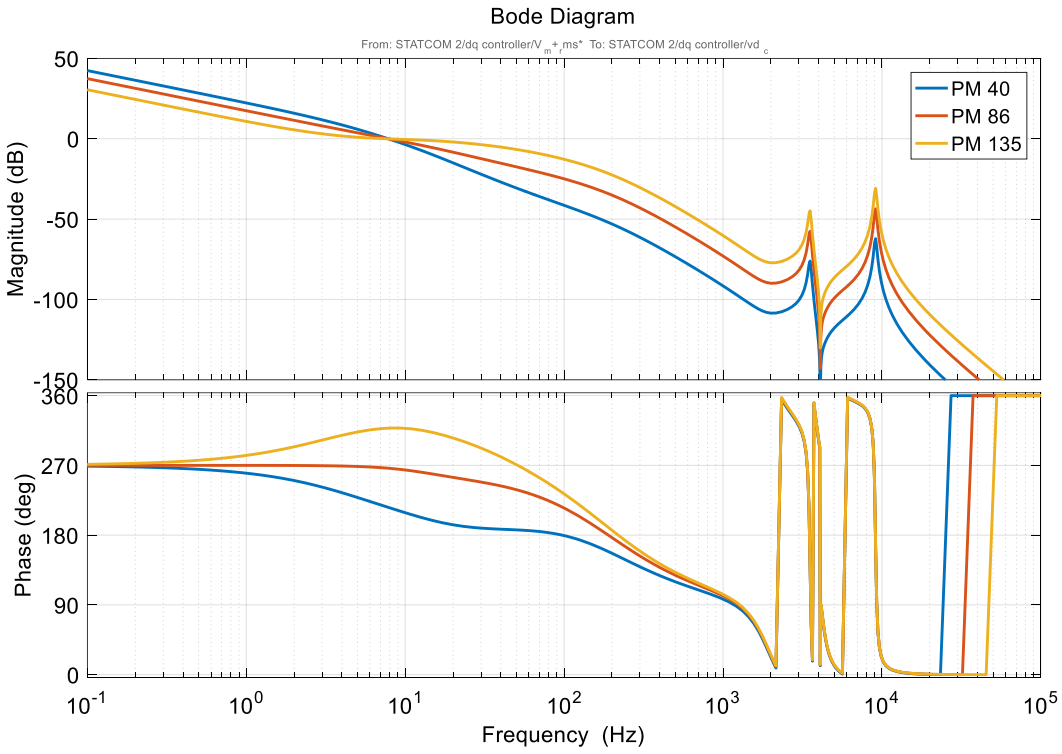

Figure 4-21 AC voltage open loop gains with different controllers

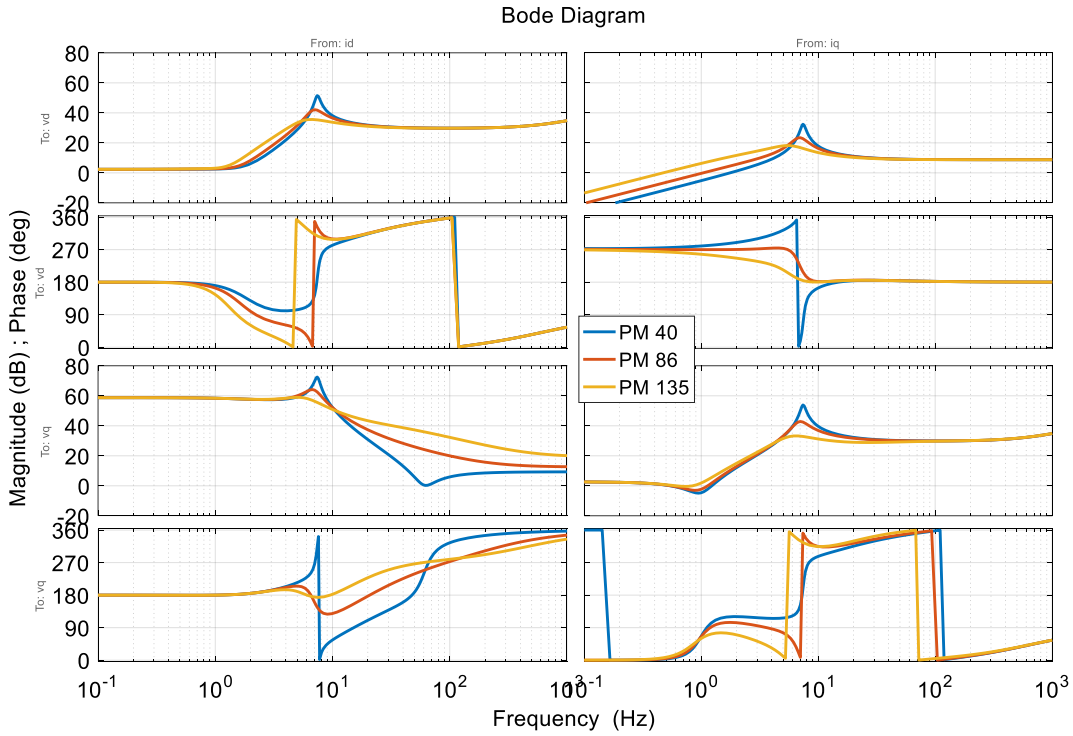

Figure 4-22 STATCOM impedance with different controllers for ac voltage loop

Figure 4-23 shows the time-domain simulation waveforms with different controllers. With increasing phase margin, the system tended to be more stable. However, note that although the additional zero before the bandwidth increased the phase margin, it also slowed down the settling time because the transient responses were mainly dependent on the zero with the lowest frequency.

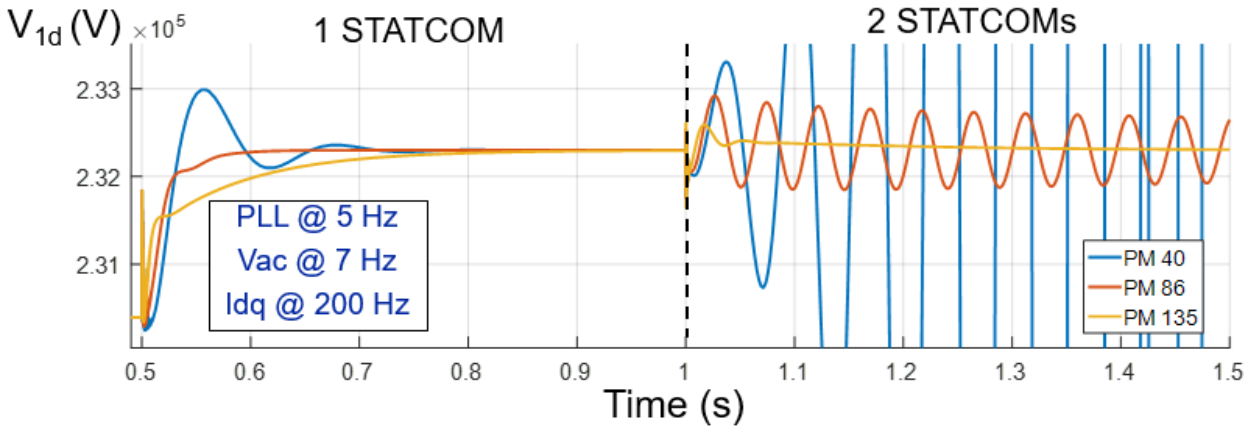

Figure 4-23 Simulation waveforms with different controllers for ac voltage loop

However, these two alternative controls cannot solve the instability problem fundamentally, and in other words, the problem will appear again if the ac voltage loop bandwidth is to be pushed higher. This can be seen in Figure 4-24 and Figure 4-25, where the ac voltage loop bandwidth was further increased and the system fell in to instability again, shown in red compared to stable cases in blue, using either the proportional current control or the ac voltage controller with increased phase margin.

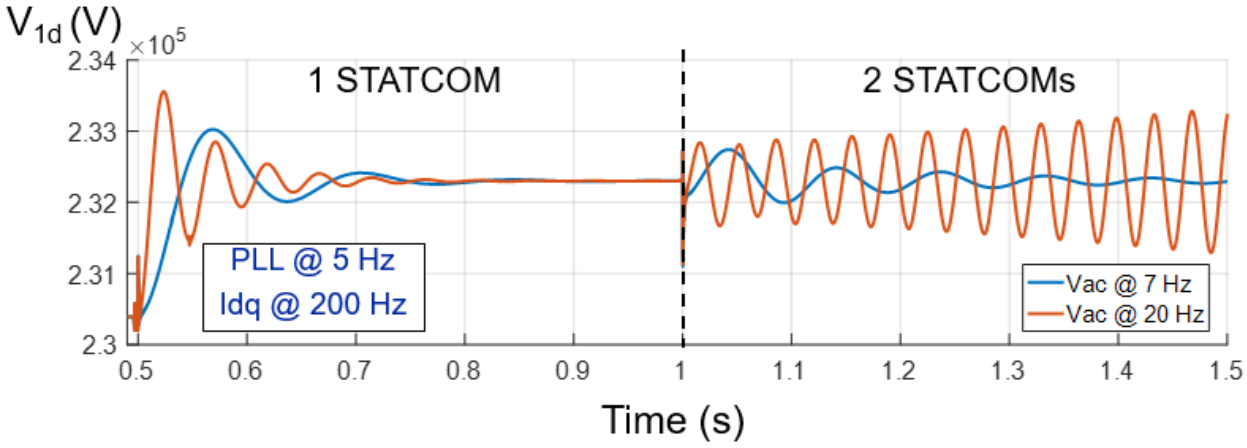

Figure 4-24 Instability with increased AC voltage loop bandwidth, using proportional current controller

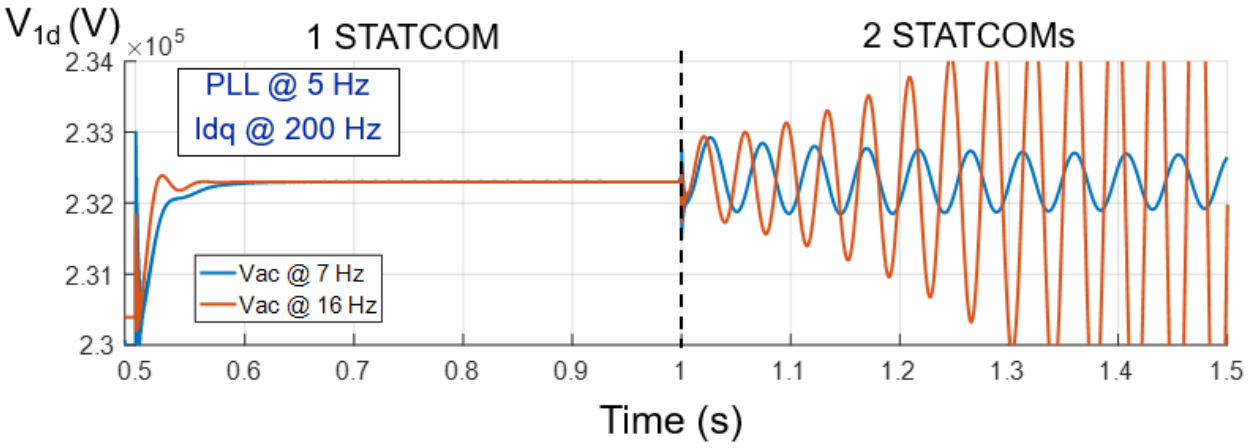

Figure 4-25 Instability with increased AC voltage loop bandwidth, using alternative ac voltage controller

4.4 Experimental verification of impedance-based stability analysis

To verify the analysis above, impedances were measured at the terminal of STATCOM 1 in the constructed scaled-down 2-STATCOM system as shown in Figure 2-18 using the impedance measurement unit (IMU) in Figure 3-19. The IMU was inserted in series at the terminal of STATCOM 1 and was able to measure the impedances on both sides at the same time after the system reached steady state. For stable cases, the measurements were done only once to achieve both the impedances $\mathbf{Z_{vsi}}$ and $\mathbf{Z_{grid}}$. For unstable cases, the process was different because it took ten to thirty minutes for the IMU to finish the measurements but oscillations would trigger over-current protection in seconds. In order to tackle this, the measurements were done twice to obtain the impedances on both sides individually. For example, to measure $\mathbf{Z_{vsi}}$, the parameters of STATCOM 1 were set to be in the unstable case while the parameters of STATCOM 2 were tuned so that it could work stably with STATCOM 1. Because only control parameters were changed, the steady-state operating point stayed the same as long as the same references were given. In this way, STATCOM 1 was working in the same situation as the previous unstable case with every small-signal behavior preserved for the IMU to catch for in the meantime the system was running without any oscillations. Since the parameters of STATCOM 2 were searched to ensure stable operation, $\mathbf{Z_{grid}}$ was not correct when measuring $\mathbf{Z_{vsi}}$, which required the second test. Therefore, for the second measurements, the parameters of STATCOM 2 were set to be in the unstable case and those of STATCOM 1 were found to make the system stable. As such, $\mathbf{Z_{grid}}$ was measured and the two impedances were ready for further analysis.

4.4.1 Impacts of ac voltage loop

Using the methods mentioned before, the impedances of both sides under two different ac voltage loop bandwidth cases (7 Hz and 12 Hz) in the evaluation in Section 2.5 were measured and shown in Figure 4-26. The impedances of STATCOM 1 are in circles and those of the rest of the grid are in crosses. With the increasing ac voltage loop bandwidth, the resonant peak in both $\mathbf{Z}_{vsi}$ and $\mathbf{Z}_{grid}$ moved to high frequency.

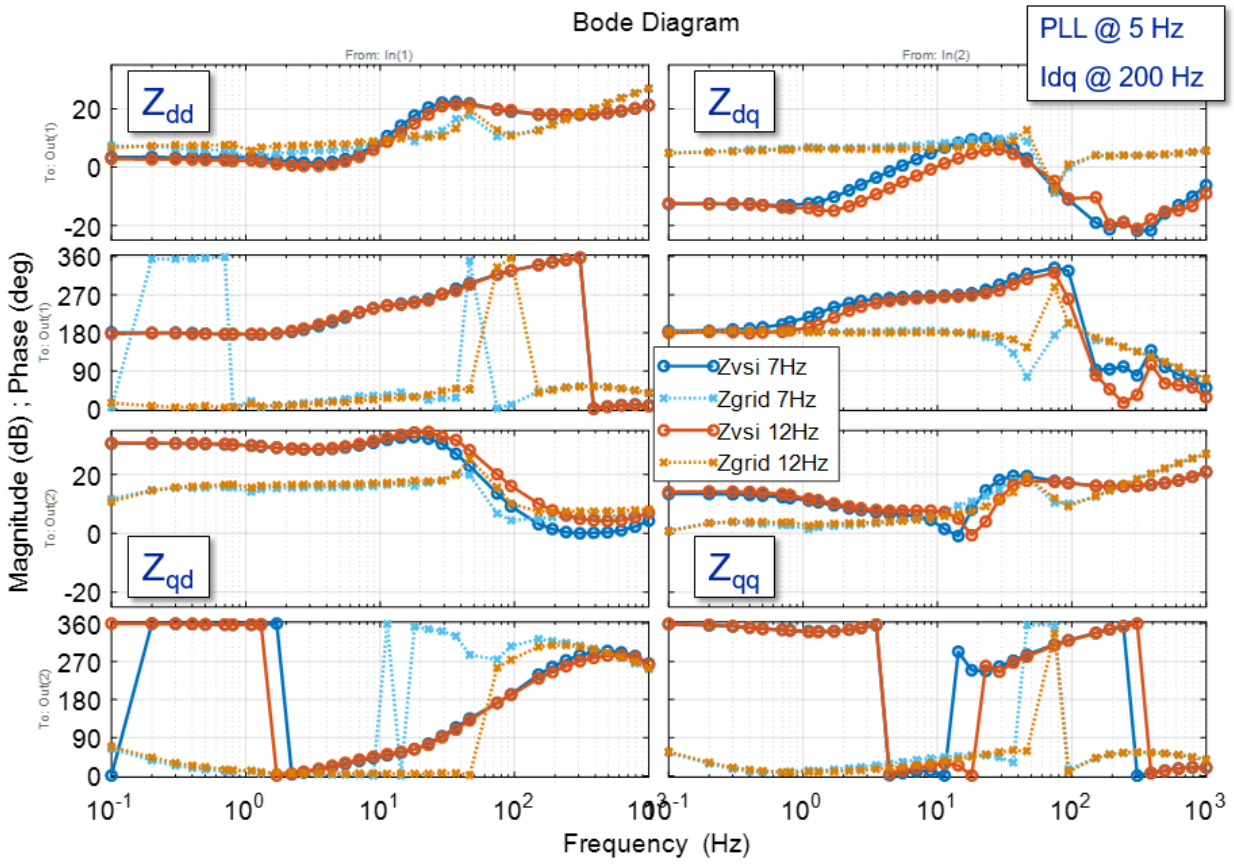

Figure 4-26 Impacts of ac voltage loop on d-q frame impedances at terminal of STATCOM 1 in experiment

The eigenvalues in both cases were computed and plotted in Figure 4-27. $\lambda_2(s)$ was always far away from the critical point while $\lambda_1(s)$ encircled it when the ac voltage loop was 12 Hz. Because there was no RHP pole in either $\mathbf{Z}_{grid}(s)$ or $\mathbf{Y}_{vsi}(s)$, the system was unstable for the 12 Hz case.

When $\lambda_1(s)$ encircled the critical point, it intersected with the negative real axis at the frequency of about 43 Hz. This oscillatory frequency was in d-q frame and can be translated to a 103-Hz oscillation in abc frame. Recall the experimental results in Section 2.5, the system was unstable when the ac voltage loop was 12 Hz and the oscillatory frequency was 102 Hz, matching well with the d-q frame based impedance stability analysis.

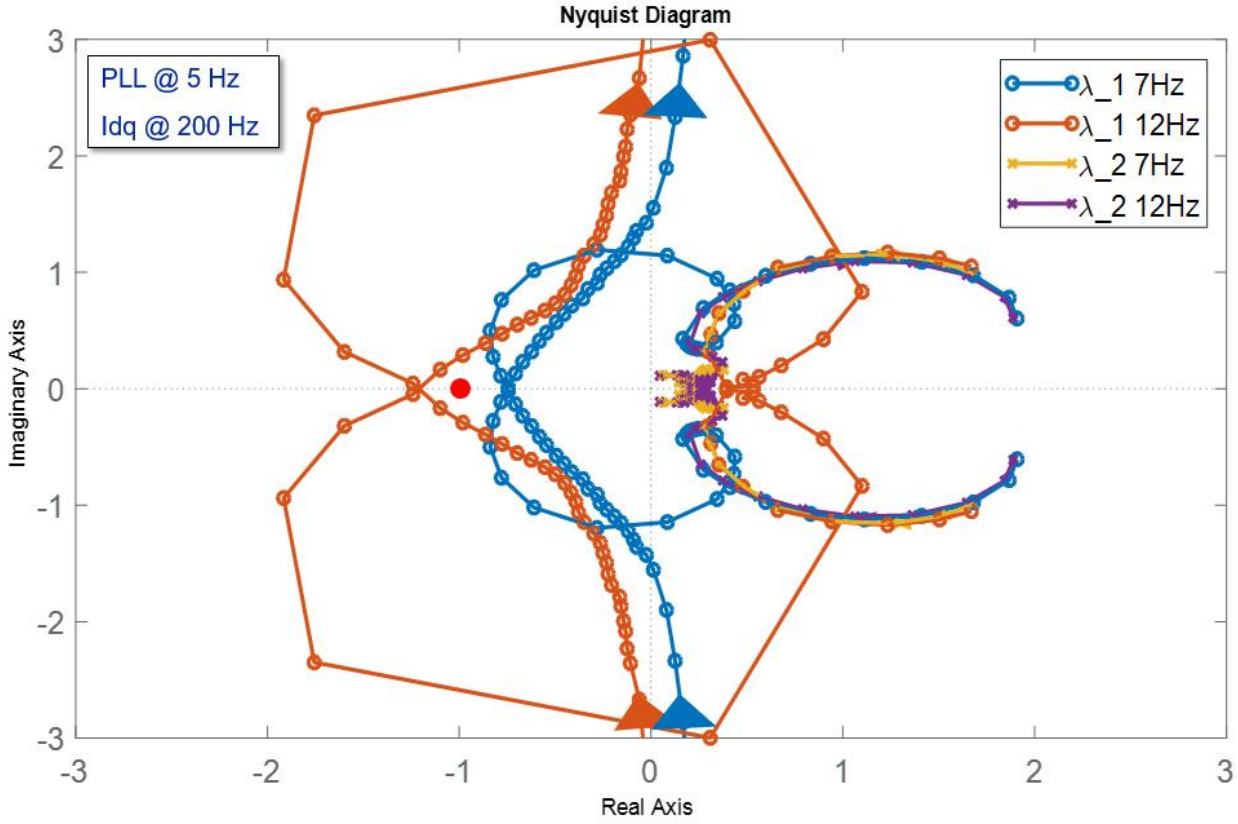

Figure 4-27 Impacts of ac voltage loop on characteristic loci in experiment

4.4.2 Impacts of PLL

The impedances of $\mathbf{Z_{vsi}}$ and $\mathbf{Z_{grid}}$ were measured in the same way with respect to PLL. Two cases, 5 Hz and 10 Hz, were evaluated. Also as discussed, the resonant peak moved with the increase of the bandwidth of PLL, which can be seen in Figure 4-28.

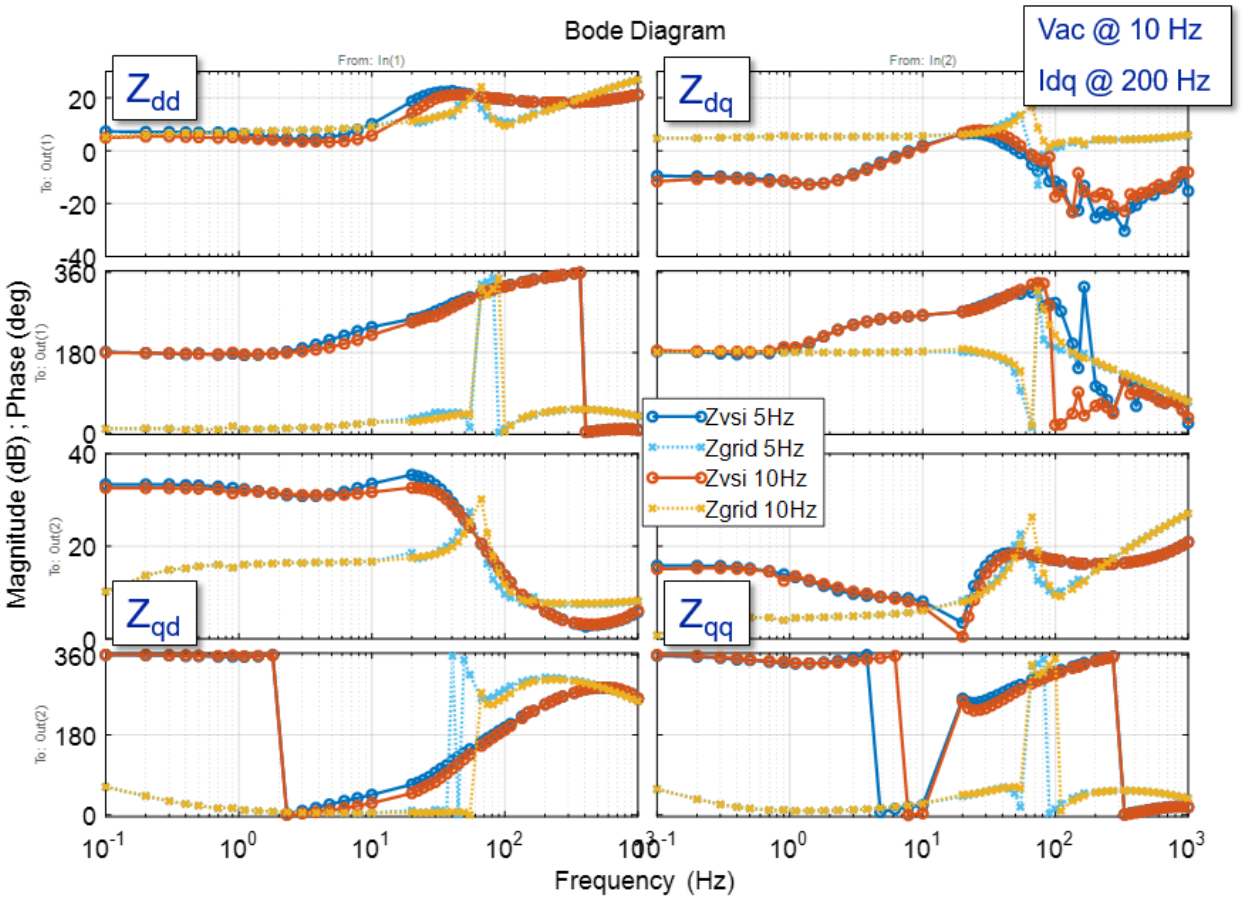

Figure 4-28 Impacts of PLL on d-q frame impedances at terminal of STATCOM 1 in experiment

Figure 4-29 shows the eigenvalues in the two cases. Still, $\lambda_1(s)$ was potential to encircle the critical point when the PLL bandwidth was low as 5 Hz, while $\lambda_2(s)$ was far way. Because there was no RHP pole in either $\mathbf{Z}_{\mathbf{grid}}(s)$ or $\mathbf{Y}_{\mathbf{vsi}}(s)$, the system was unstable for the 5 Hz case. The intersection point with the negative real axis was at the frequency of about 42 Hz, corresponding to a 102-Hz oscillation in abc frame. As in the experimental results in Section 2.5, the system was unstable when the PLL was 5 Hz and the oscillatory frequency was 102 Hz, evincing that the impedance-based stability criterion worked.

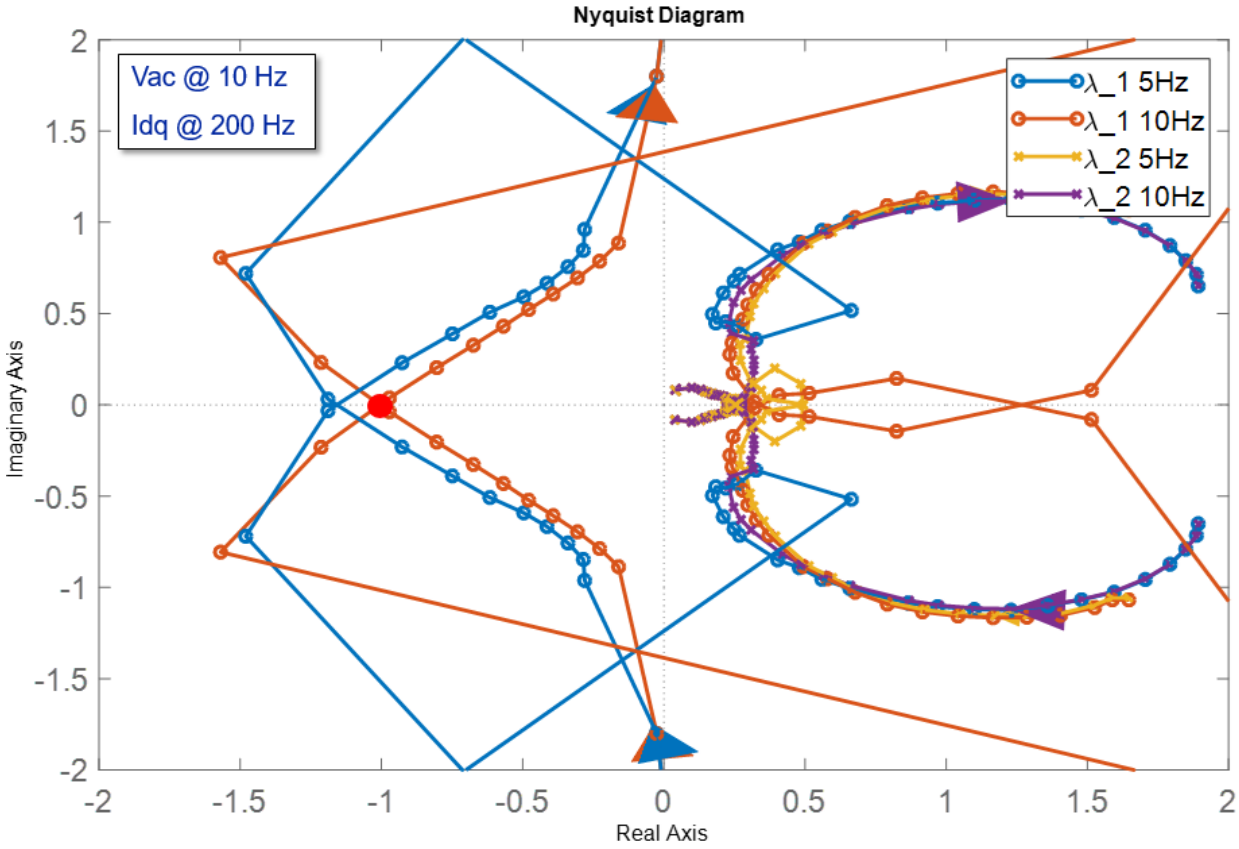

Figure 4-29 Impacts of PLL on characteristic loci in experiment

4.4.3 Impacts of current loop

Figure 4-30 depicts the impedances of $\mathbf{Z_{vsi}}$ and $\mathbf{Z_{grid}}$ with respect to changes in current loop bandwidth. The impedance of STATCOM grew in magnitude as the bandwidth increased.

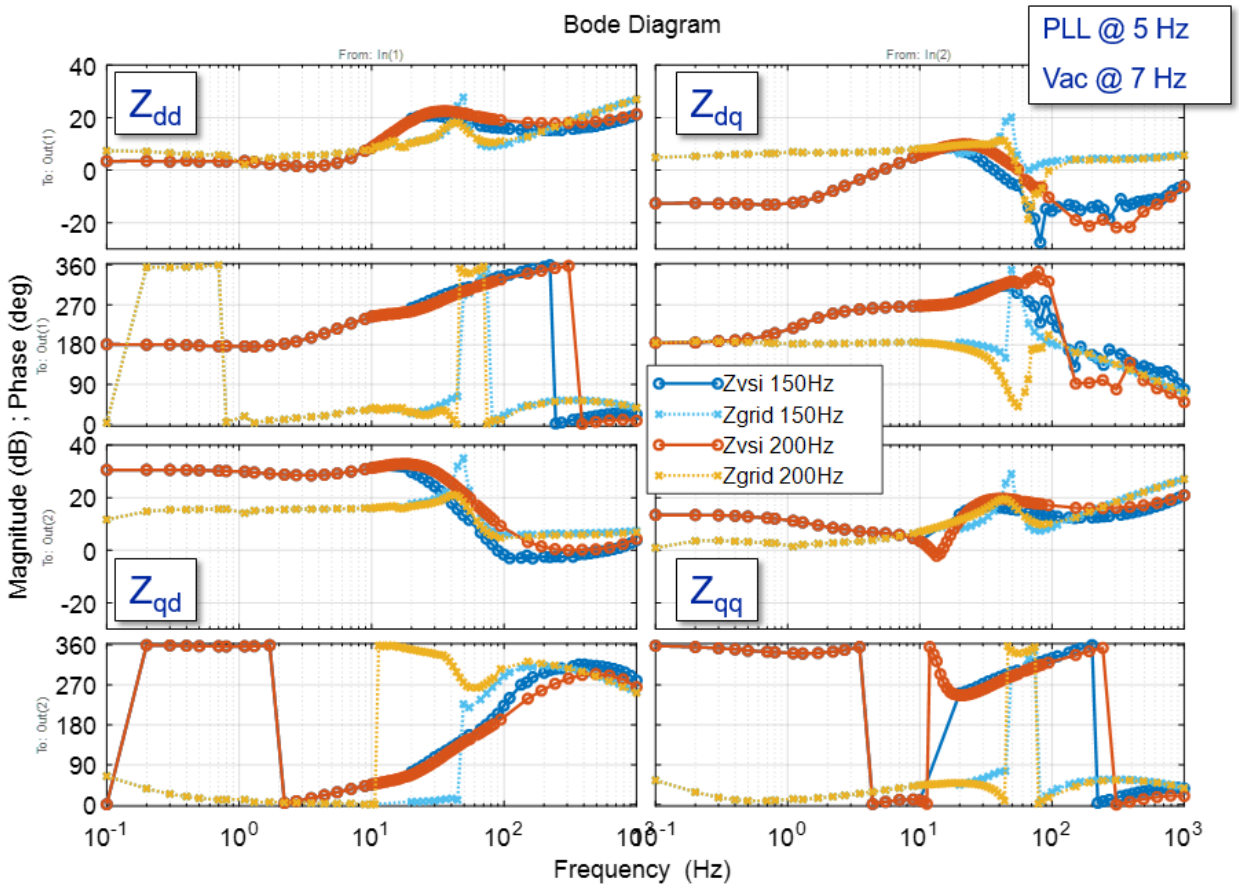

Figure 4-30 Impacts of current loop on d-q frame impedances at terminal of STATCOM 1 in experiment

Figure 4-31 shows the eigenvalues in two cases. $\lambda_2(s)$ was also far away from the critical point while $\lambda_1(s)$ encircled it when the current loop was 150 Hz and hence the system was unstable for the 150 Hz case. The intersection point of $\lambda_1(s)$ and the negative real axis was at the frequency of about 31 Hz. This oscillatory frequency was in d-q frame and can be translated to a 92-Hz oscillation in abc frame. This corresponded to the experimental results too.

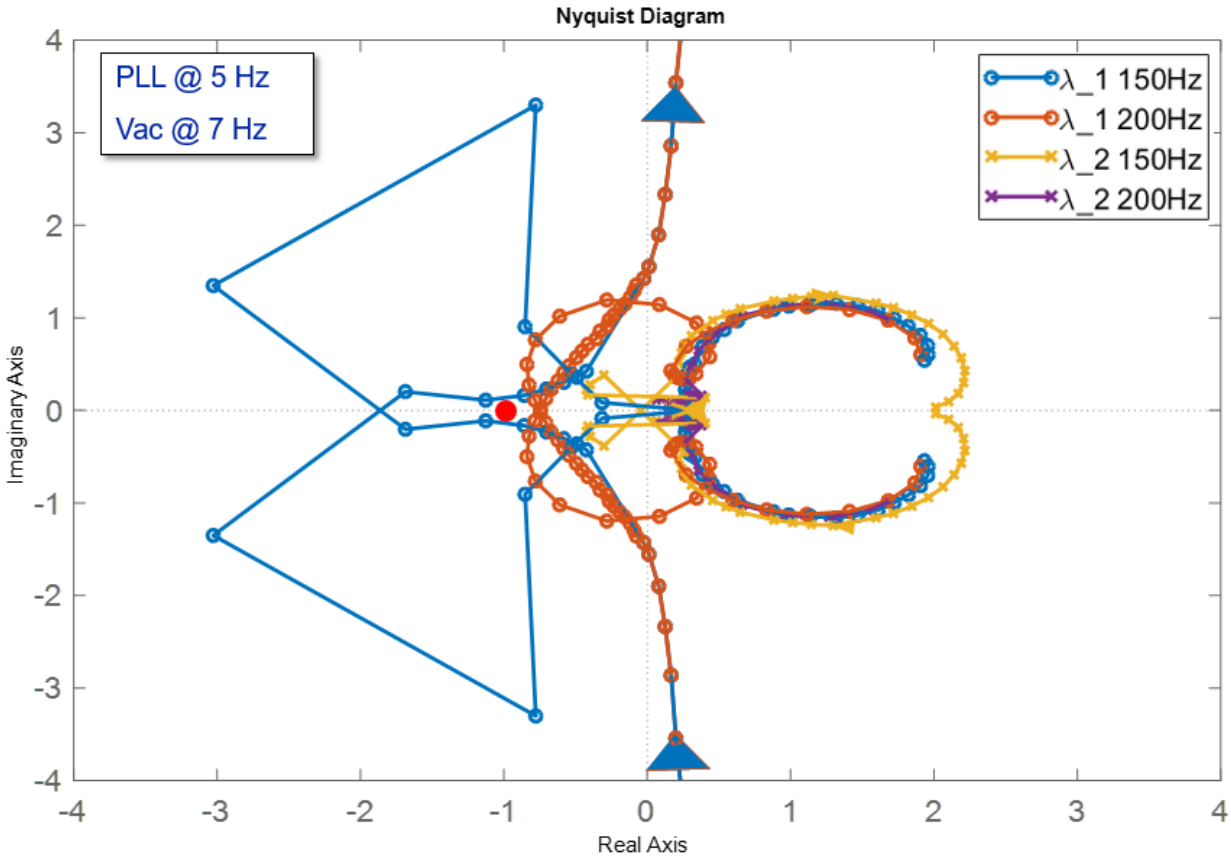

Figure 4-31 Impacts of current loop on characteristic loci in experiment

4.4.4 Impacts of QV droop

Figure 4-32 shows the impedances of STATCOM 1 and the grid, with and without the QV droop. When the QV droop was activated, the impedance element in dq channel increased significantly in magnitude in the low frequency below 10 Hz, just as in Figure 3-22. However, it did not change the grid impedance much, because in the low frequency the grid impedance was relatively larger and thus dominant.

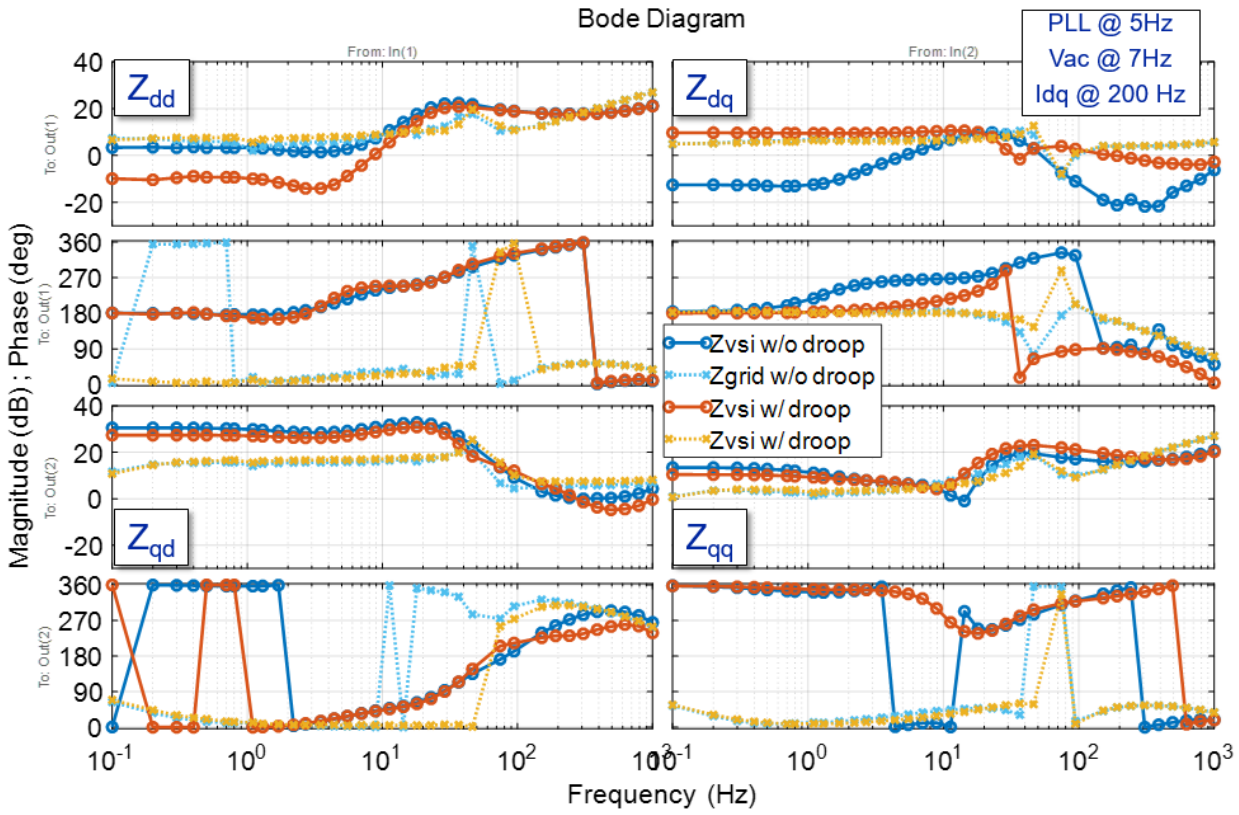

Figure 4-32 Impacts of QV droop on d-q frame impedances at terminal of STATCOM 1 in experiment

The corresponding eigenvalues are plotted in Figure 4-33. The case with the QV droop had $\lambda_1(s)$ encircling the critical point, indicating instability, which matched the experimental results in Figure 2-27. Additionally, the intersection point was at about 41 Hz and it was close to the unity circle, which indicated 19 and 101 Hz oscillation modes in the abc frame with a little damping.

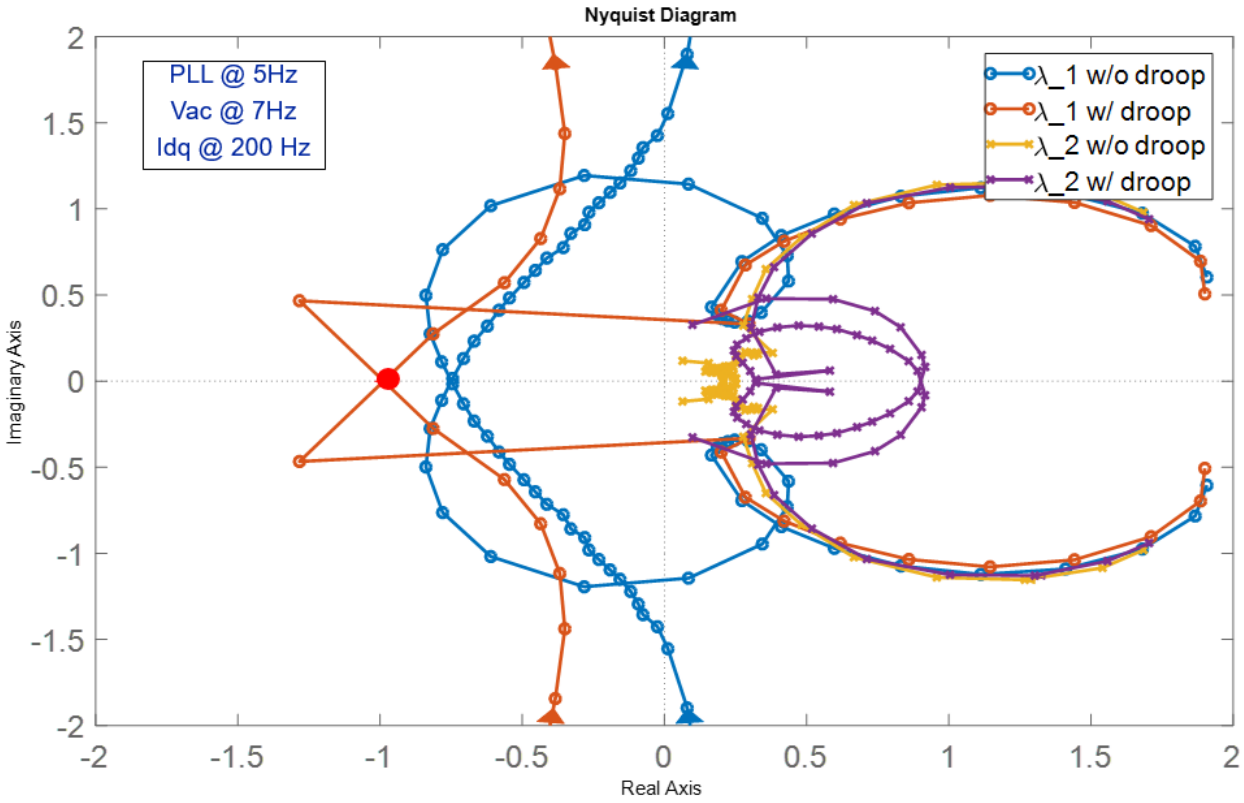

Figure 4-33 Impacts of QV droop on characteristic loci in experiment

4.5 Experimental verification of the alternative controls

To verify the alternative controls in Section 4.3, corresponding experiments were conducted with different types of controllers -- proportional current control and alternative ac voltage control in this chapter. One specific unstable case, where the ac voltage loop bandwidth was at 12 Hz, the PLL bandwidth was at 5 Hz and the current loop bandwidth was at 200 Hz in Section 2.5 and 4.4, was selected, to show that the proposed solutions could solve the instability issue.

4.5.1 Proportional current control

By simply removing the integral term in the current compensator and retuning the proportional term, the same bandwidth of current loop could be achieved. Figure 4-34 shows the improved stability condition by proportional current control as opposed to the previously unstable system in

Figure 2-20, where both cases have the same bandwidths for all control loops. Yet, a large current spike appeared when STATCOM 1 was connected and started to compensate.

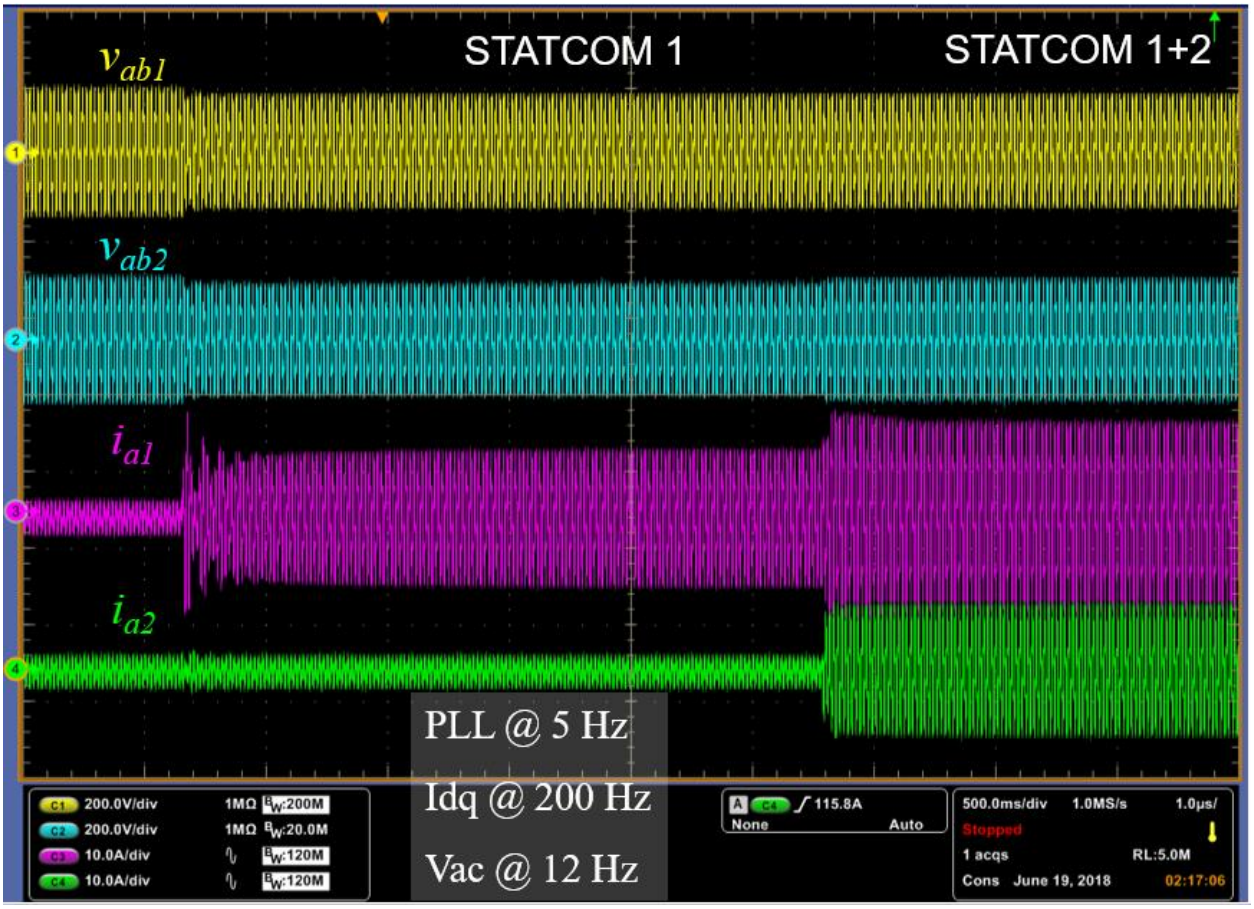

Figure 4-34 Stability improvements by proportional current control in experiment

Figure 4-35 depicts the STATCOM impedances with proportional and PI current control respectively and corresponding characteristic loci are shown in Figure 4-36. It can be observed that the characteristic locus did not encircle the critical point (-1+*j*0) under proportional current control. As neither the grid impedance nor the STATCOM admittance had RHP poles, the characteristic locus under proportional current control indicated that the system was stable. Therefore, it was verified experimentally that proportional current control helped the stability conditions.

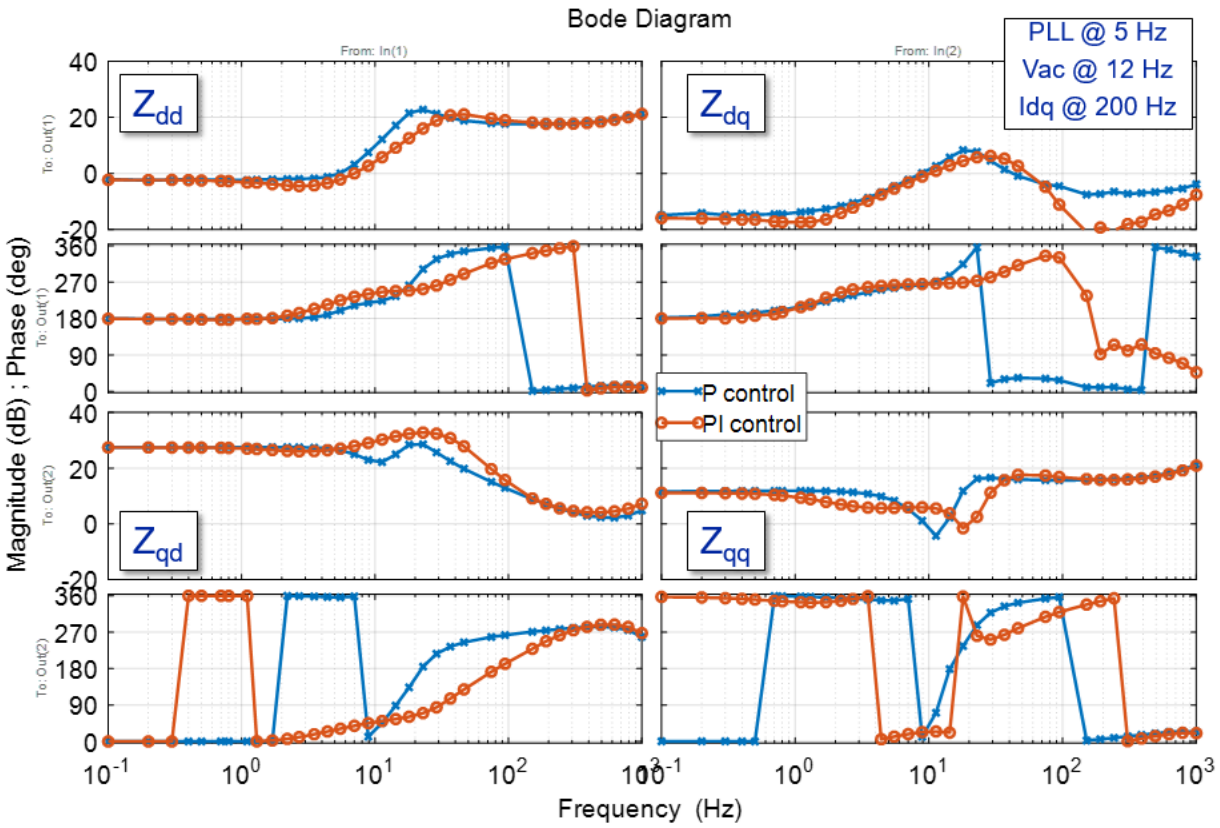

Figure 4-35 STATCOM impedance with P and PI control for current loop in experiment

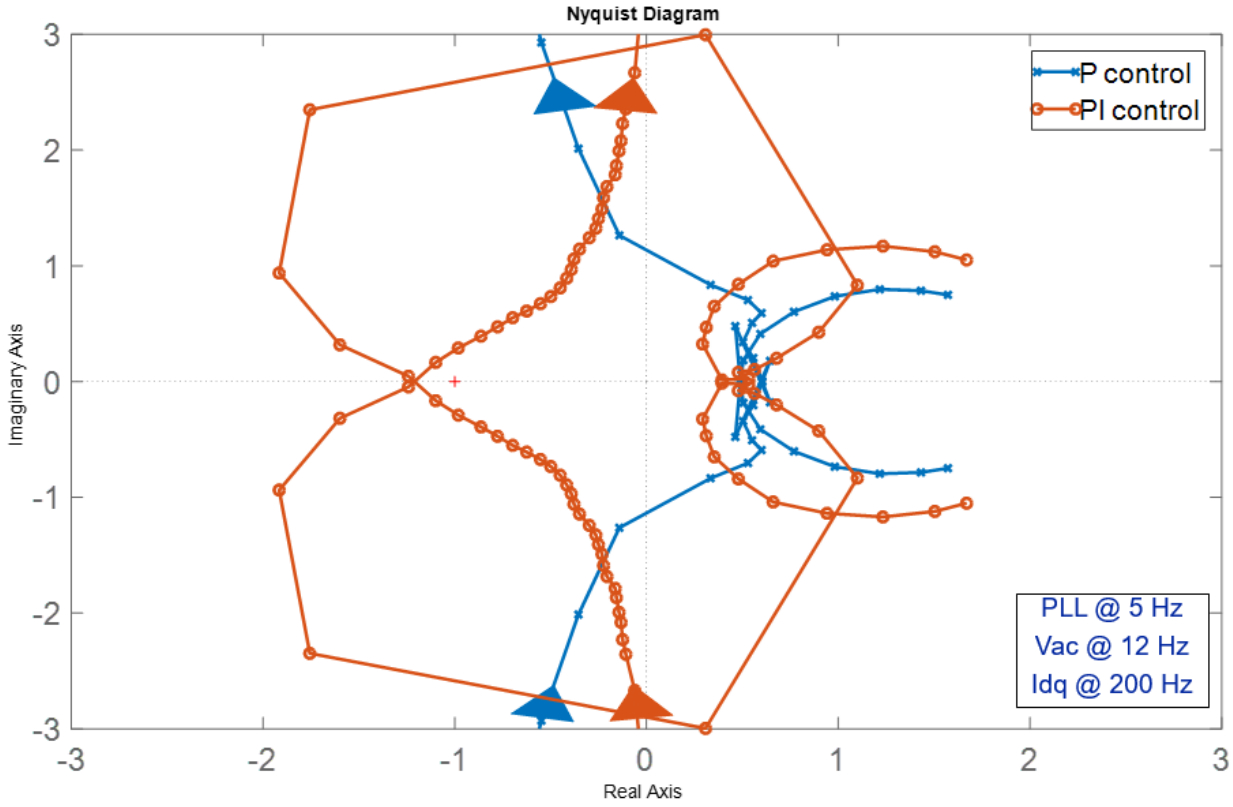

Figure 4-36 Characteristic loci λ_1 with P and PI control for current loop in experiment

However, when the ac voltage loop bandwidth was further pushed to 30 Hz, the system would be unstable again, plotted in Figure 4-37 where the current oscillated and triggered the over-current protection.

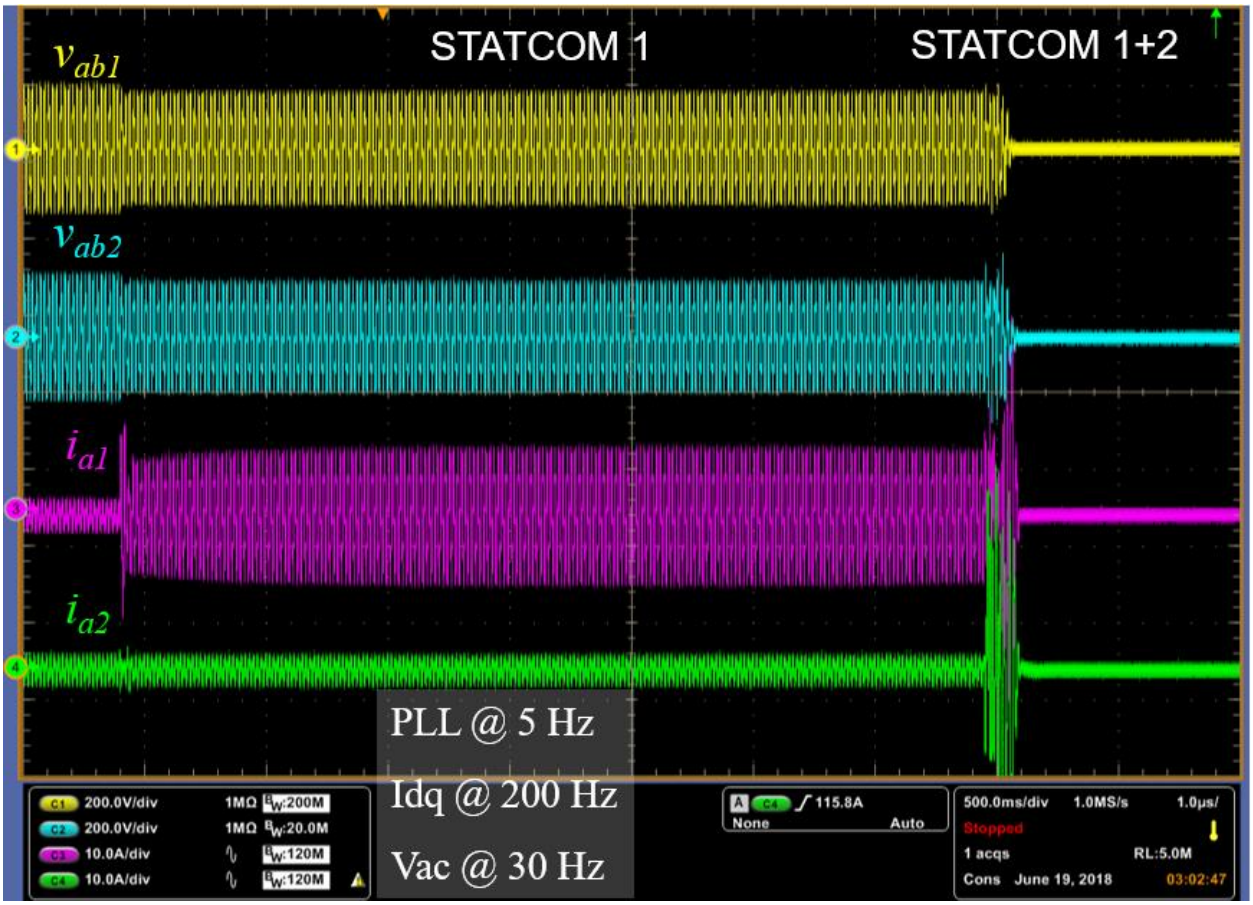

Figure 4-37 Instability with increased ac voltage loop bandwidth using proportional current control

4.5.2 Alternative ac voltage control

By moving the zero below the crossover frequency and adding one more pole after, a larger phase margin could be achieved using a type-II compensator in the ac voltage loop. Compared to the previously used PI compensator, the phase margin was increased from almost 90 degree to 140 degree. Using a type-II compensator helped the system stability, as shown in Figure 4-38, while the system was unstable with the PI compensator for the ac voltage loop in Figure 2-20. Although the system was stable with the type-II compensator, the settling time increased too compared to Figure 2-20. This was because the zero before its bandwidth determined the time constant the most and it was at about 3 Hertz, which indicated about a setting time of a second.

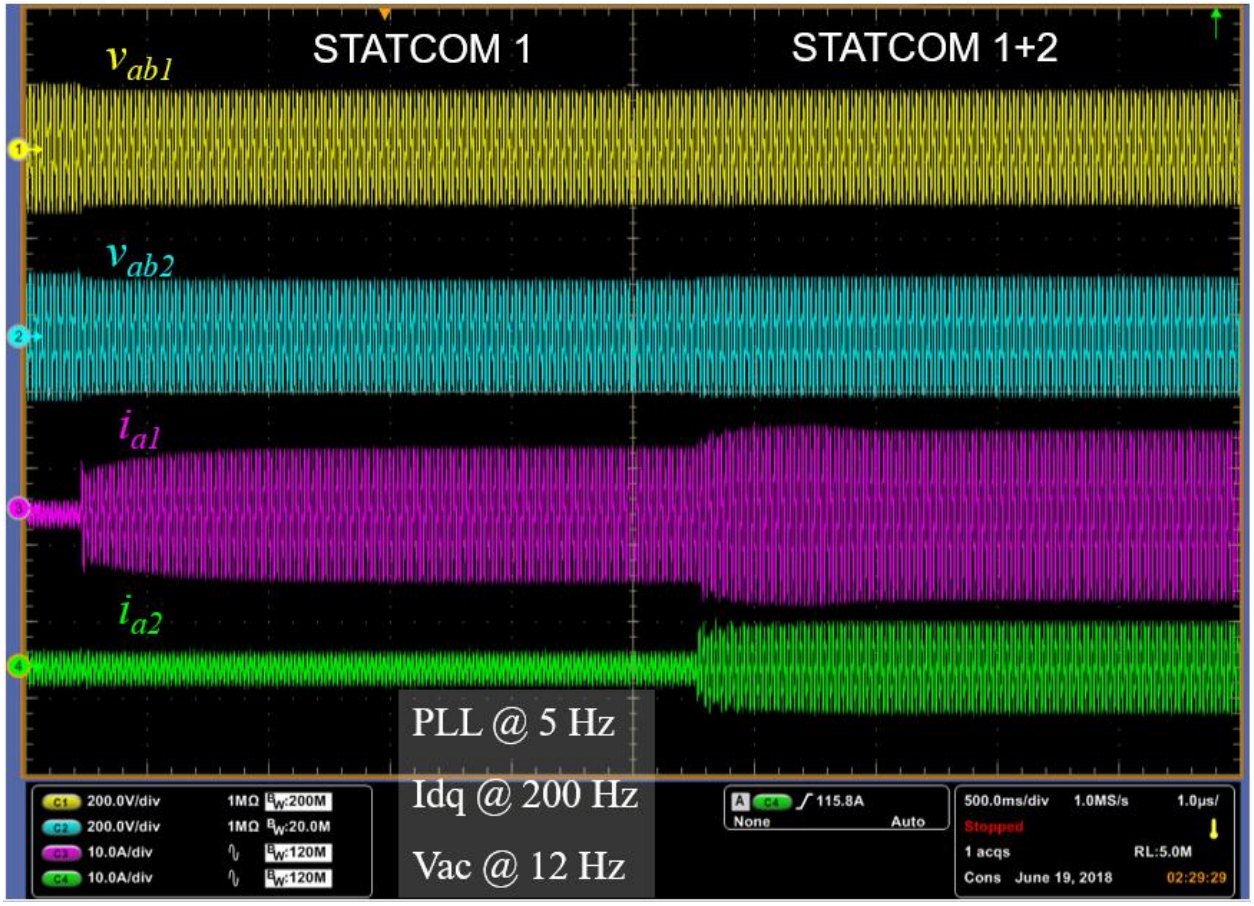

Figure 4-38 Stability improvements by alternative ac voltage control in experiment

Figure 4-39 depicts the STATCOM impedances with type-II and PI control for the ac voltage loop respectively and corresponding characteristic loci are shown in Figure 4-40. It can be observed that the characteristic locus did not encircle the critical point (-1+*j*0) under the type-II ac voltage loop control. Similarly, neither the grid impedance nor the STATCOM admittance had RHP poles, the characteristic locus with type-II ac voltage control showed that the system was stable.

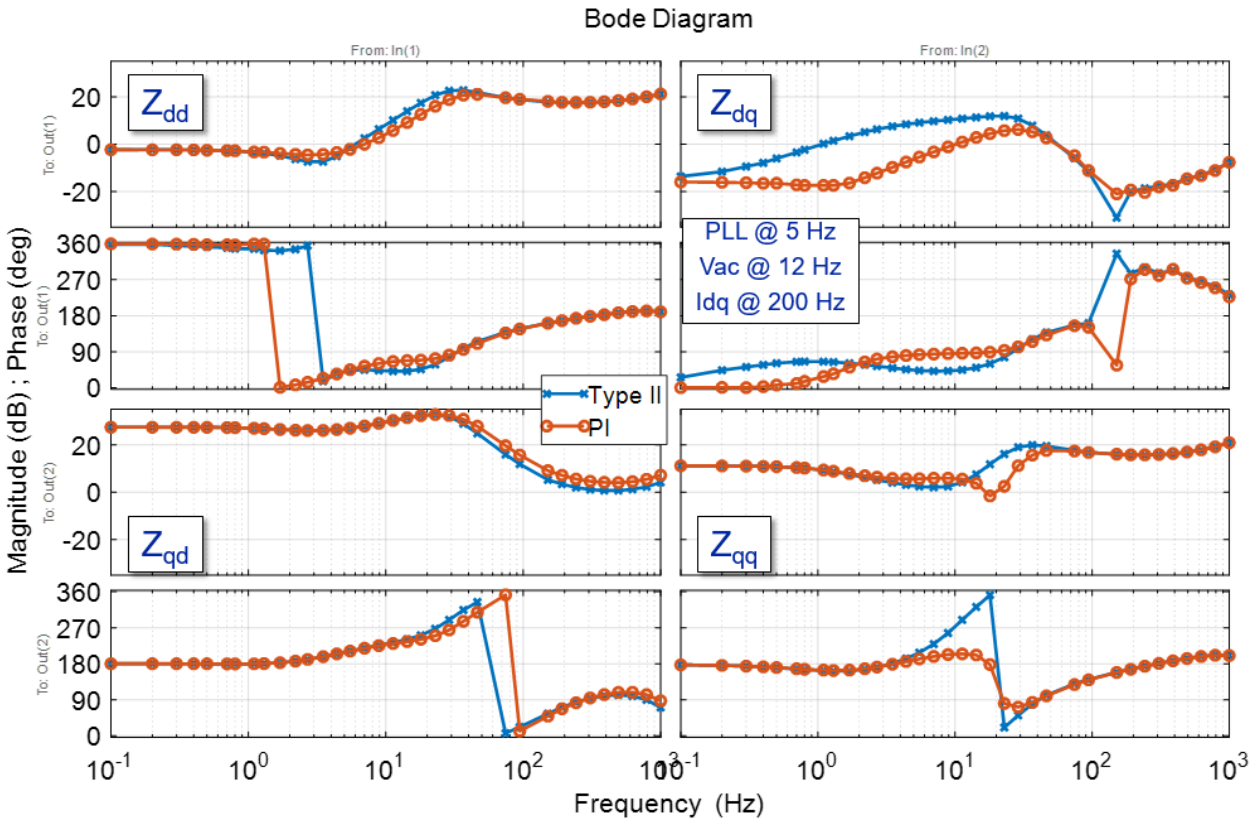

Figure 4-39 STATCOM impedance with different ac voltage loop control in experiment

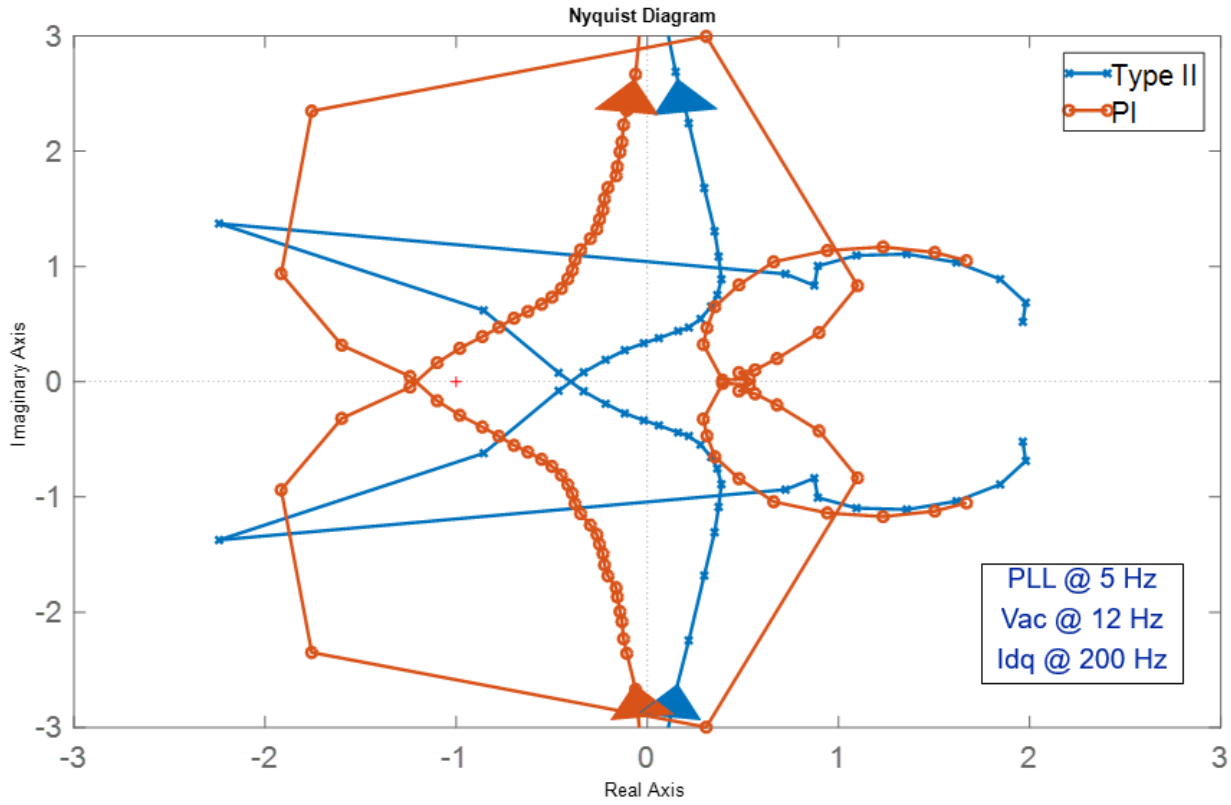

Figure 4-40 Characteristic loci λ_1 with different ac voltage loop control in experiment

Nonetheless, as the ac voltage loop bandwidth was further pushed to 20 Hz, the system became unstable again, as shown in Figure 4-41 where the current oscillated and triggered the over-current protection.

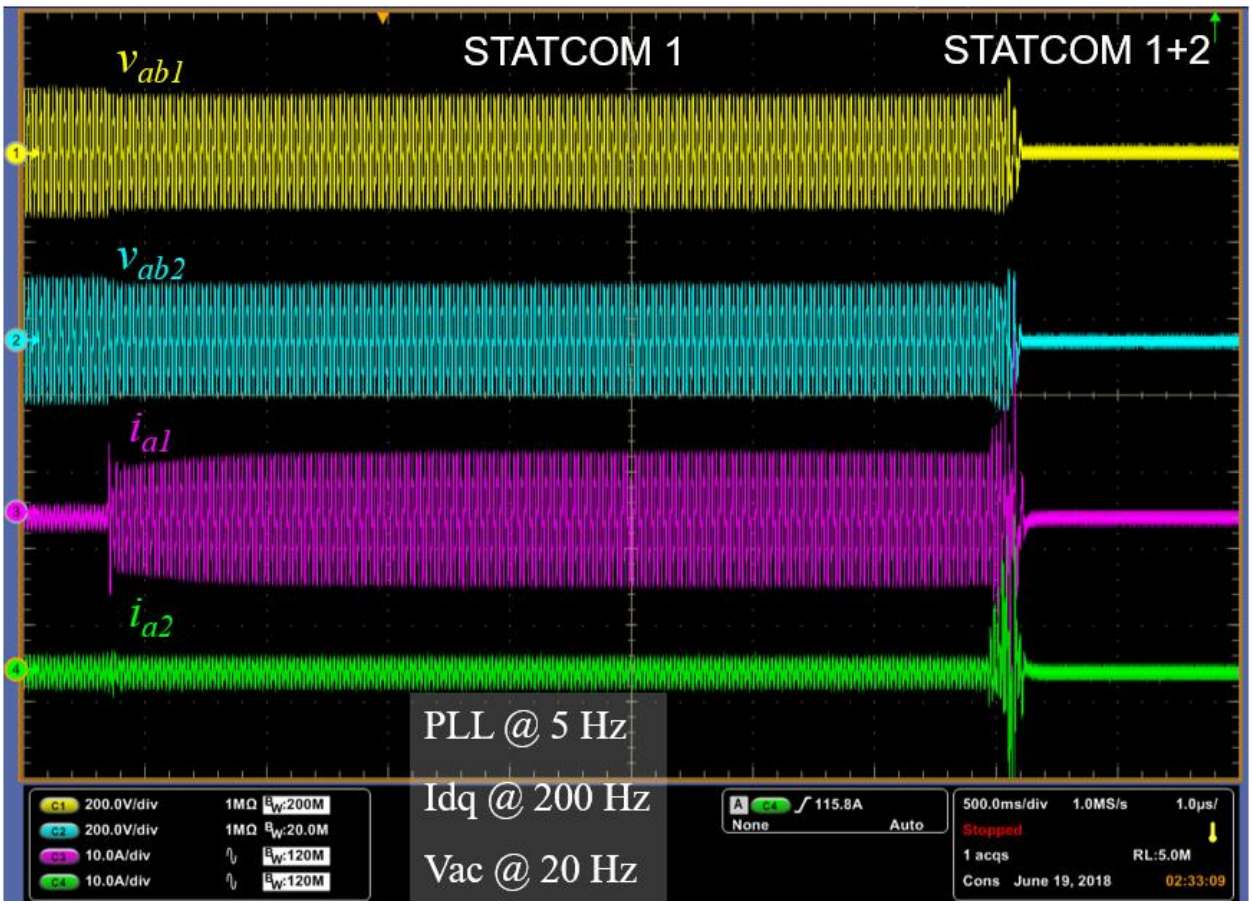

Figure 4-41 Instability with increased ac voltage loop bandwidth using alternative ac voltage control

4.6 Conclusions

In this chapter, potential instability in power systems with multiple STATCOMs in proximity was found due to STATCOM control: ac voltage loop, PLL and QV droop. D-Q frame impedance-based stability analysis was used to explore the instability. From the analysis, the following conclusions were obtained. First, STATCOMs were seen to interact with each other through the transmission lines due to the relatively high magnitude of their impedances with respect to that of the lines. As such, STATCOM control could lead to the instability of power systems because of limited information flow between vendors. Second, the use of d-q frame impedances identified the frequency range of interactions. The ac voltage regulation was the main reason of instability among

STATCOM control and masked the effects of PLL in transmission systems. This kind of instability adds new knowledge to three-phase ac systems besides constant power load dynamics and synchronization, with presence of STATCOMs. Although STATCOMs synchronize with the power grid, the instability is nonetheless due to ac voltage regulation. Third, alternative controllers were proposed to mitigate stability problems and trade-offs were discussed. Lastly, the scaled-down 2-STATCOM power grid shown in Chapter II was used to verify the conclusions experimentally.

Chapter 5. IMPEDANCE-BASED STABILITY ANALYSIS ON THE FULL SYSTEM

5.1 Recall from evaluations in the full system

In Chapter VI, the potential instability was revealed using impedance-based stability analysis for the simplified 2-STATCOM system. This chapter will try to expand the conclusions to the full meshed system with four STATCOMs and explore new issues introduced in the full system.

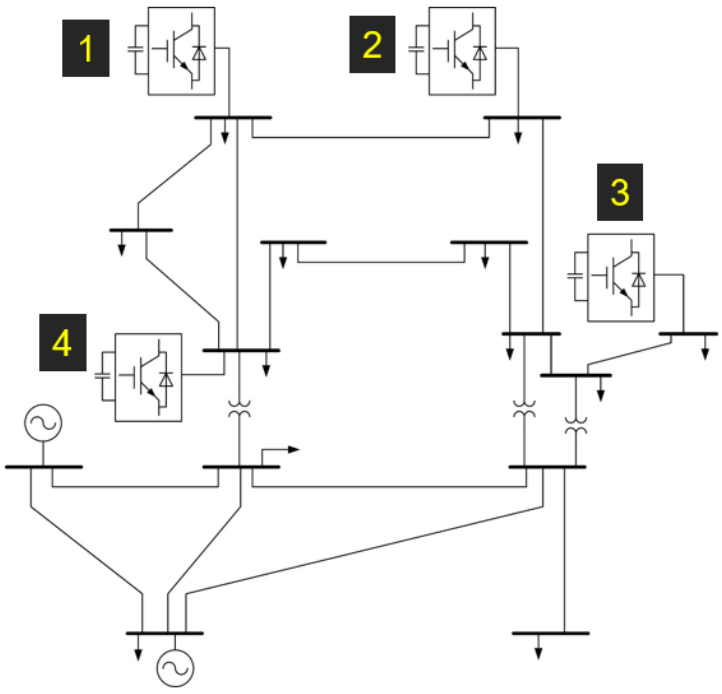

Figure 5-1 IEEE 14-bus system with four STATCOMs

The IEEE 14-bus system with four STATCOMs is redrawn in Figure 5-1 for convenience with simulation waveforms showing potential instability due to STATCOM control. All the four STATCOMs were equipped with the same control and parameters, and their operating points were close with the same voltage and similar reactive power outputs. The four STATCOMs were connected online successively at the moments of 1, 3, 5 and 7 second in the marked order. The

effects of ac voltage loop, PLL, current loop and QV droop were assessed respectively, with the d-channel voltage at the terminal of STATCOM 1 shown as an indicator of stability, as the same in Chapter II. For each control loop, the system was evaluated with only two different control bandwidths selected from the evaluation in Chapter II Section 3, one stable and another unstable, for simplicity. In the following figures, stable cases are plotted in blue and unstable cases are in orange.

Figure 5-2 depicts how the system would behave with two ac voltage loop bandwidths: when its bandwidth was 7 Hz (blue), the system was stable with four STATCOMs connected; when the bandwidth was increased to 16 Hz (orange), the system had faster responses before the fourth STATCOM working and unstable when the fourth connected at the oscillatory frequency of about 10 Hz. With increasing ac voltage loop bandwidth, the system tended to be more unstable. Actually, the connection sequence of STATCOMs did not matter in terms of stability, no matter which STATCOM was connected first or last, and this is true for all the evaluation. This is because in the frequency range of instability, the STATCOM dynamics were dominant in frequency responses, which will be further analyzed from impedance point of view in the following section.

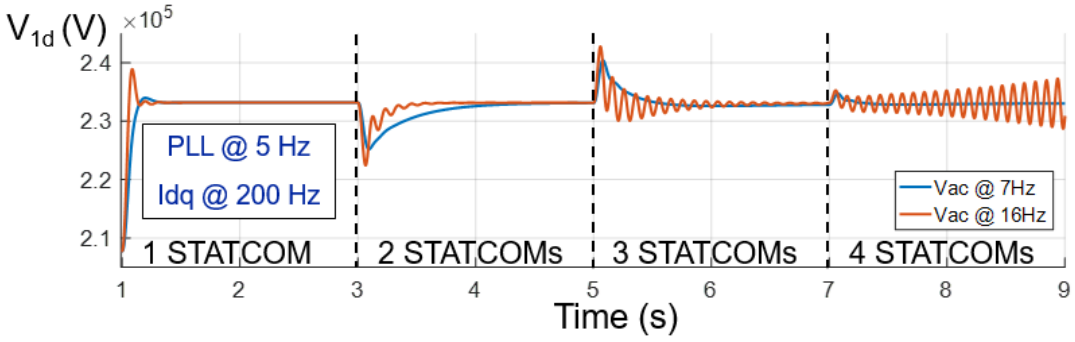

Figure 5-2 Potential instability due to ac voltage loop

The effects of PLL bandwidth are shown in Figure 5-3. The differences in waveform dynamics were smaller compared to the case of ac voltage loop but it still had effects on stability. Still, the

QV droop was not running at this time. When PLL bandwidth was low at 5 Hz in orange, the system was unstable; when the PLL bandwidth was increased to 10 Hz shown in blue, the system became damped and stable. A higher PLL bandwidth tended to stabilize the system.

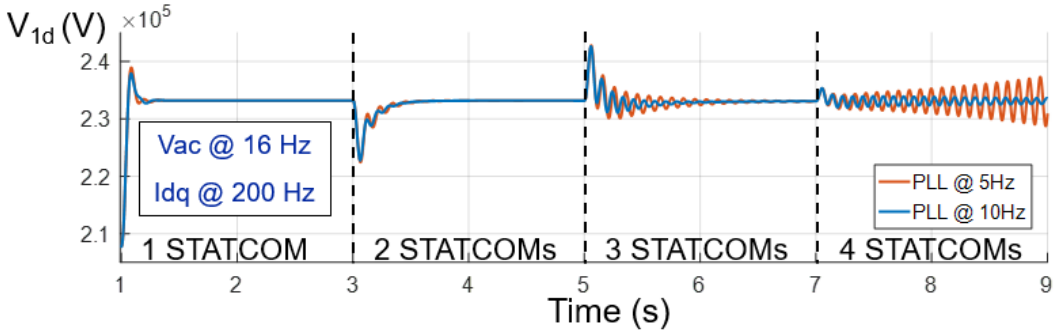

Figure 5-3 Potential instability due to PLL

Figure 5-4 shows how the current loop affected the instability. With a lower current loop bandwidth at 200 Hz in orange, the system oscillated when the fourth STATCOM was connected. If the bandwidth increased to 500 Hz, the system was stable as shown in blue.

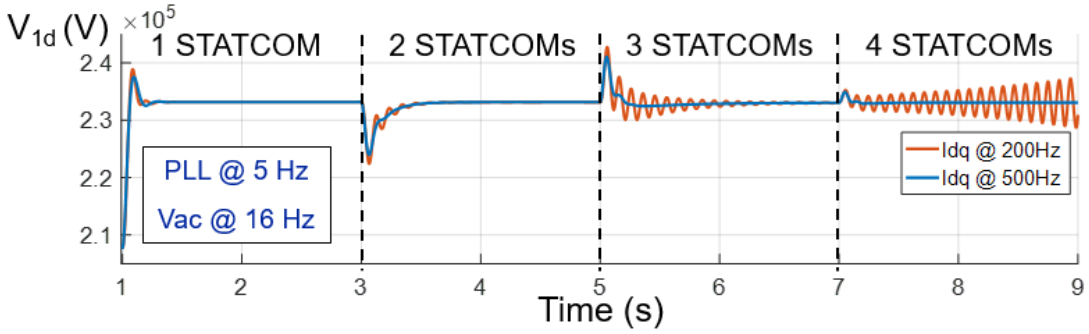

Figure 5-4 Potential instability due to current loop

Figure 5-5 presents how the QV droop influenced the system stability. The ac voltage loop bandwidth was tuned to 14 Hz to make the system stable with 4 STATCOMs running without QV droop activated and the waveform is plotted in blue. The waveform in orange shows the case with QV droop. Clearly, the PCC voltage was smaller in magnitude, thanks to QV droop which allowed the voltage to be within a certain range instead of a fixed value in order to lessen the output reactive

power burden. However, with QV droop when the fourth STATCOM was connected, the systems was unstable. QV droop strengthened the interactions between STATCOMs and there were higher possibility that they could behave in an undesired manner. Actually, no QV droop is equavalent to zero droop coefficient with QV droop. Thus, deactivation of QV droop or a small droop coefficient was preferred in terms of stability.

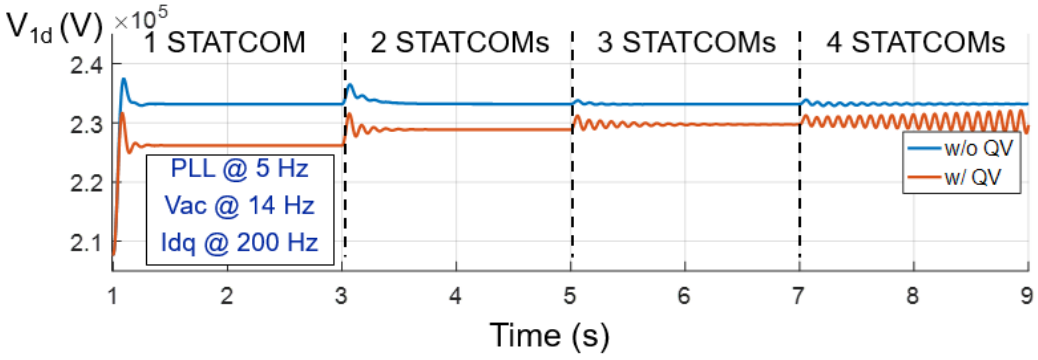

Figure 5-5 Potential instability due to QV droop

5.2 Extension of previous conclusions to the full system

In order to analyze the previously found instability phenomena, d-q frame impedance was used in this section in the same manner of Chapter VI. Separated at the PCC of STATCOM 1, impedances from both sides, named as $\mathbf{Z}_{vsi}(s)$ for STATCOM impedance and $\mathbf{Z}_{grid}(s)$ for the rest of the grid including the other three STATCOMs, were measured in Simulink at the moment of 7 second when the fourth STATCOM were just connected.

5.2.1 Effects of ac voltage loop

Figure 5-6 shows the impedances of STATCOM 1 $\mathbf{Z}_{vsi}(s)$ and the rest of the grid $\mathbf{Z}_{grid}(s)$, with an increasing ac voltage loop bandwidth from 7 to 16 Hz, indicated by arrows. The solid lines are the impedances of STATCOM 1 $\mathbf{Z}_{vsi}(s)$ and relatively larger in the frequency range of several Hertz than the impedances of the rest of the grid $\mathbf{Z}_{grid}(s)$ in dashed lines. Note that there is a

resonant peak in the STATCOM impedance at about 10 Hz and this is created by the ac voltage loop as we have observed in the previous chapter. With the bandwidths increasing, the resonant peak as a result of the ac voltage loop moved to the high frequency in $\mathbf{Z}_{\mathbf{vsi}}(s)$ and the same change happened in the impedance of the second STATCOM due to the identical control for the other three STATCOMs. The grid side impedance $\mathbf{Z}_{\mathbf{grid}}(s)$ hence changed with the similarly moving resonant peak as well, because the impedance change of the other STATCOMs were reflected through transmission lines which were relatively small in impedance magnitude due to close physical distance. As such, in the full meshed power system with four STATCOMs, $\mathbf{Z}_{\mathbf{grid}}(s)$ included the dynamic behaviors of the other STATCOMs and the STATCOMs saw small-signal impacts from each other because of short distance in between, and therefore they could possibly interact with each other, similarly to the 2-STATCOM system in Chapter IV.

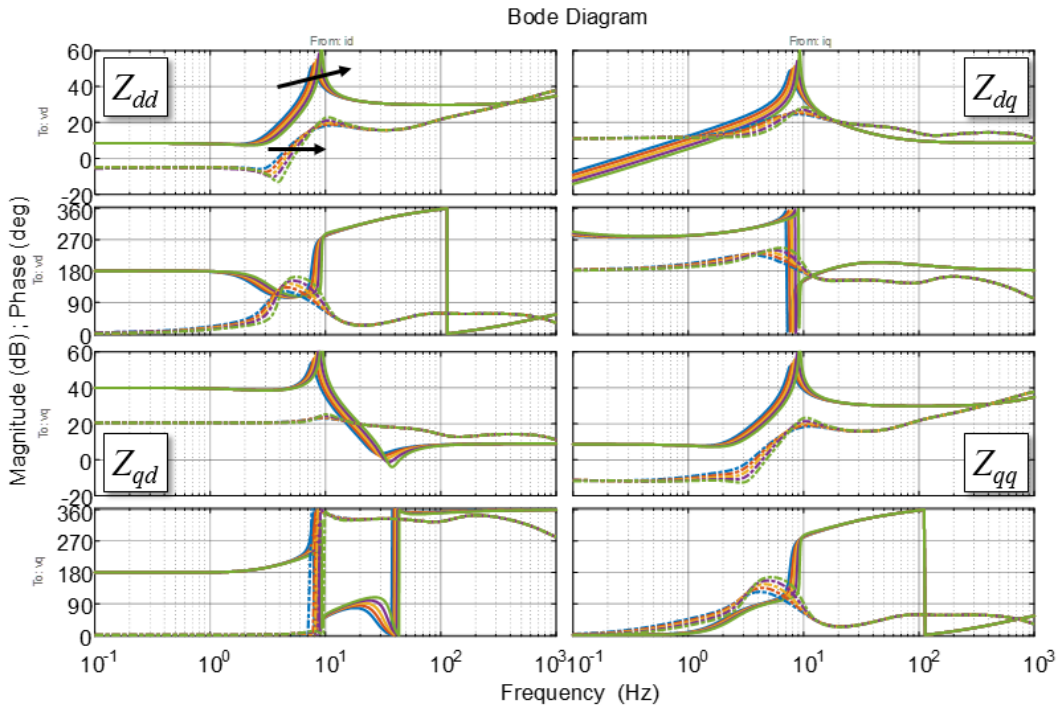

Figure 5-6 Impedances at STATCOM 1 terminal with respect to ac voltage loop - solid: Zvsi; dashed: Zgrid

The eigenvalues $\lambda_1(s)$ and $\lambda_2(s)$ of the return ratio $\mathbf{L}(s)= \mathbf{Z_{grid}}(s)\mathbf{Z_{vsi}}(s)^{-1}$ to plot the characteristic loci in the Nyquist plot in Figure 5-7 and an arrow indicates $\lambda_1(s)$ with the increase of the ac voltage loop bandwidth. One of the loci, $\lambda_1(s)$ was relatively large in magnitude, intersecting the negative real axis and the unity circle while th other one, $\lambda_2(s)$ was far away from the critical point (-1+j0). Neither of the impedance $\mathbf{Z_{grid}}(s)$ and admittance $\mathbf{Y_{vsi}}(s)$ contained right half plane (RHP) poles because the STATCOMs were unable to run only with all the four online. As the bandwidth increased, the characteristic loci moved closer to the critical point from the origin point and eventually encircled it, indicating that the system finally fell into instability with the highest ac voltage loop bandwidth at 16 Hz, which corresponds to the simulation results shown above in Section 5.1. To this end, impedances measured at the terminal of STATCOM 1 have predicted the system stability.

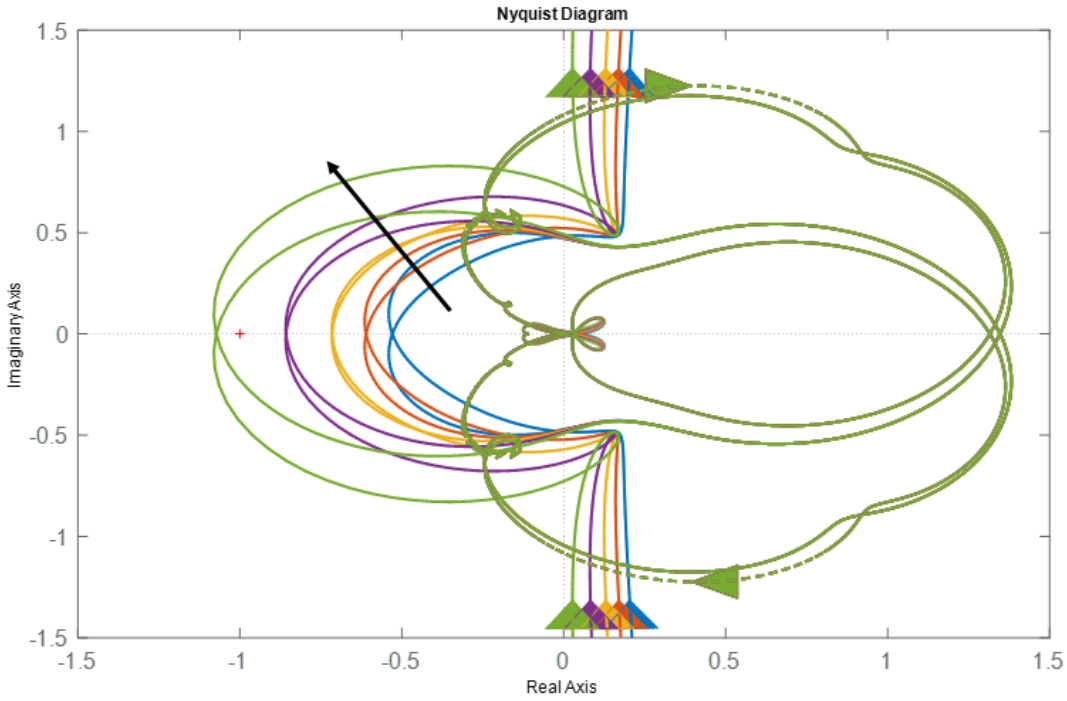

Figure 5-7 Characteristic loci at STATCOM 1 terminal with respect to ac voltage loop: solid - λ1; dashed - λ2

In order to check whether the previous conclusions about the reason of possible instability in Chapter IV still hold, Figure 5-8 plots the eigenvalues $\lambda_1(s)$ from Figure 5-7 in Bode plot. Still, with the increased bandwidth of the ac voltage loop, a resonant peak in the eigenvalues $\lambda_1(s)$ showed up, because of the change in the impedance of both $\mathbf{Z_{vsi}}(s)$ and $\mathbf{Z_{grid}}(s)$. This made the magnitude of the characteristic loci rise in magnitude and eventually above 0 dB. Therefore, for the highest ac voltage loop bandwidth at 16 Hz, the magnitude was larger than 0 dB when it intersected with the negative real axis, causing encirclements and thus instability. Although the impedances alone indicated nothing about reasons of instability, the characteristic loci in Bode plot showed that the resonant peak from the ac voltage loop caused the instability. One can conclude that the increment of the ac voltage loop enlarged the impedance of STATCOMs, especially the resonant peak around the oscillatory frequency, which reflected to the terminal of the other STATCOMs and finally escalated the possibility that STATCOMs could interact with each other. This clearly showed how the ac voltage loop control influenced the small-signal stability, from the d-q frame impedance point of view.

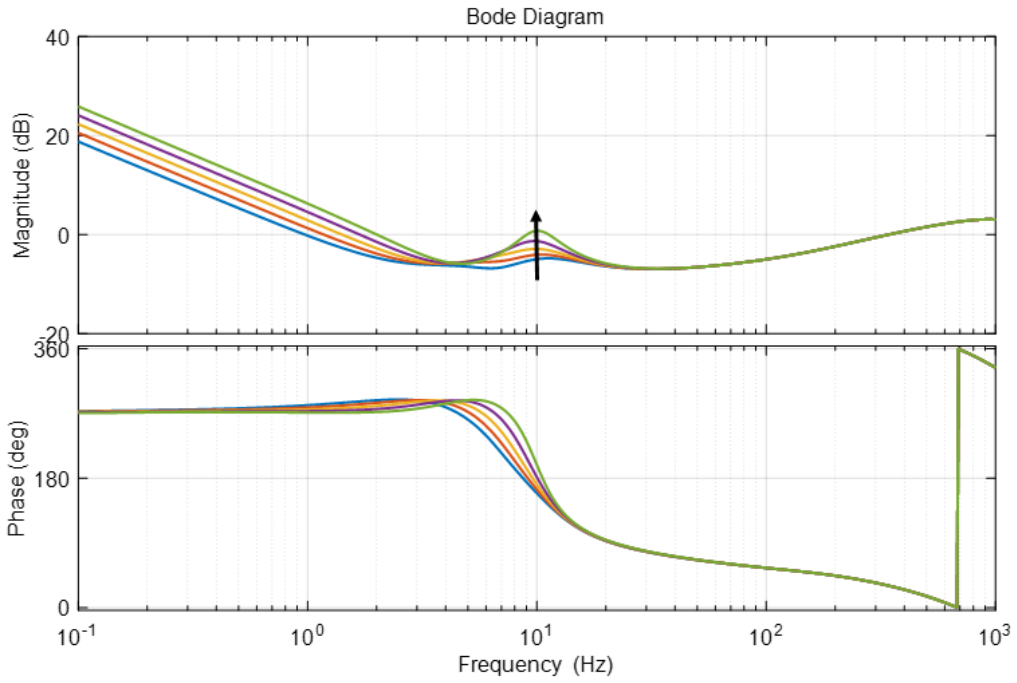

Figure 5-8 Characteristic loci λ1 at STATCOM 1 terminal with respect to ac voltage loop in Bode pot

5.2.2 Effects of PLL

The effects of PLL on impedances are plotted in Figure 5-9 with increasing bandwidth from 5 Hz to 10 Hz. Similarly, the solid lines are the impedances of STATCOM 1 $\mathbf{Z}_{\mathbf{vsi}}(s)$ and relatively larger in the frequency range of several Hertz than the impedances of the rest of the grid $\mathbf{Z}_{\mathbf{grid}}(s)$ in dashed lines. Still, the increase in bandwidth resulted in the resonant peak moving to high frequency in both $\mathbf{Z}_{\mathbf{vsi}}(s)$ and $\mathbf{Z}_{\mathbf{grid}}(s)$ for the same reason as in the previous sub-section. However compared to the ac voltage loop, PLL showed smaller impacts on impedances, implying that the found instability was more dependent on ac voltage loop instead of PLL. Again, we see the previous conclusions that the origin of this instability was mostly ac voltage regulation instead of synchronization, is still valid in the full system. It is because the masking effects happen in the transmission power grids and for the full system, the assumptions are satisfied too.

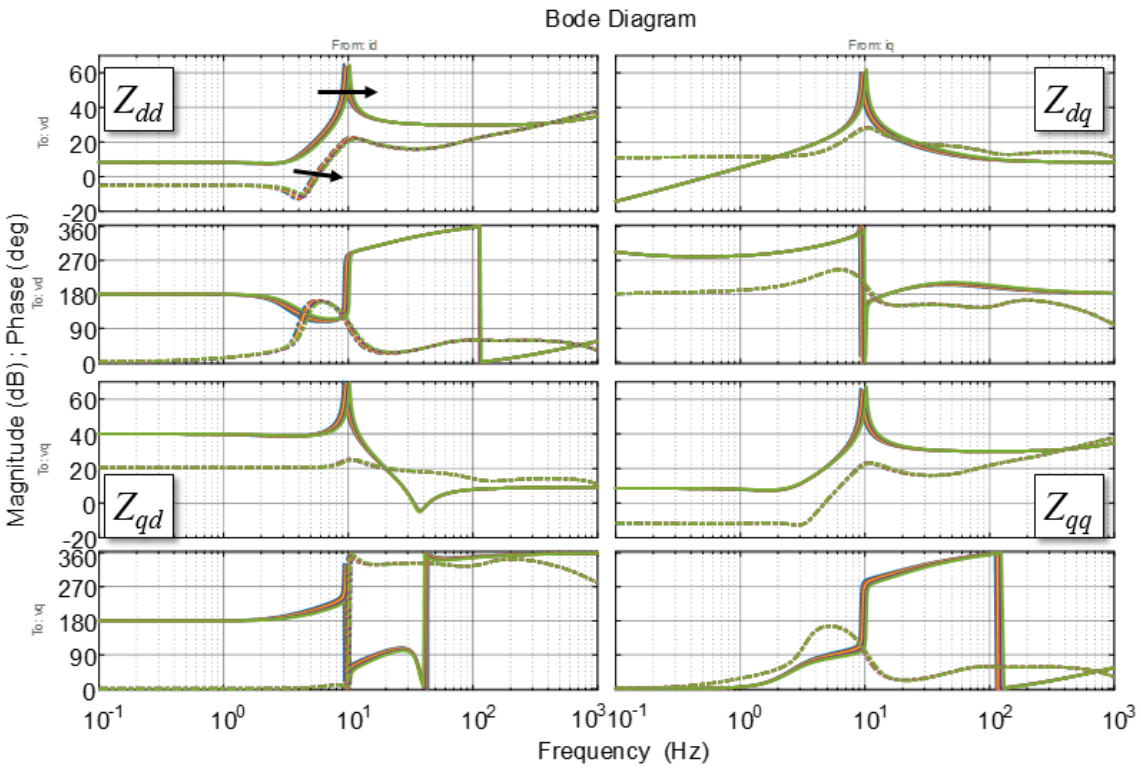

Figure 5-9 Impedances at STATCOM 1 terminal with respect to PLL - solid: Zvsi; dashed: Zgrid

The characteristic loci are drawn in Figure 5-10 from the impedances in Figure 5-9. $\lambda_2(s)$ was in dashed lines and far away from the critical point and $\lambda_1(s)$ was potential to encircle. The arrow indicates that when the bandwidth of PLL increased, the system was inclined to be stable, as the characteristic loci approached to the unity circle from the outside and didn't encircle the critical point in the end with no RHP poles in either $\mathbf{Z}_{\mathbf{grid}}(s)$ or $\mathbf{Y}_{\mathbf{vsi}}(s)$. One can also observe that the change in charateristic loci with different bandwidths of PLL was relatively small, as explained above. This corresponds to the simulation results shown in the previous section 5.1.

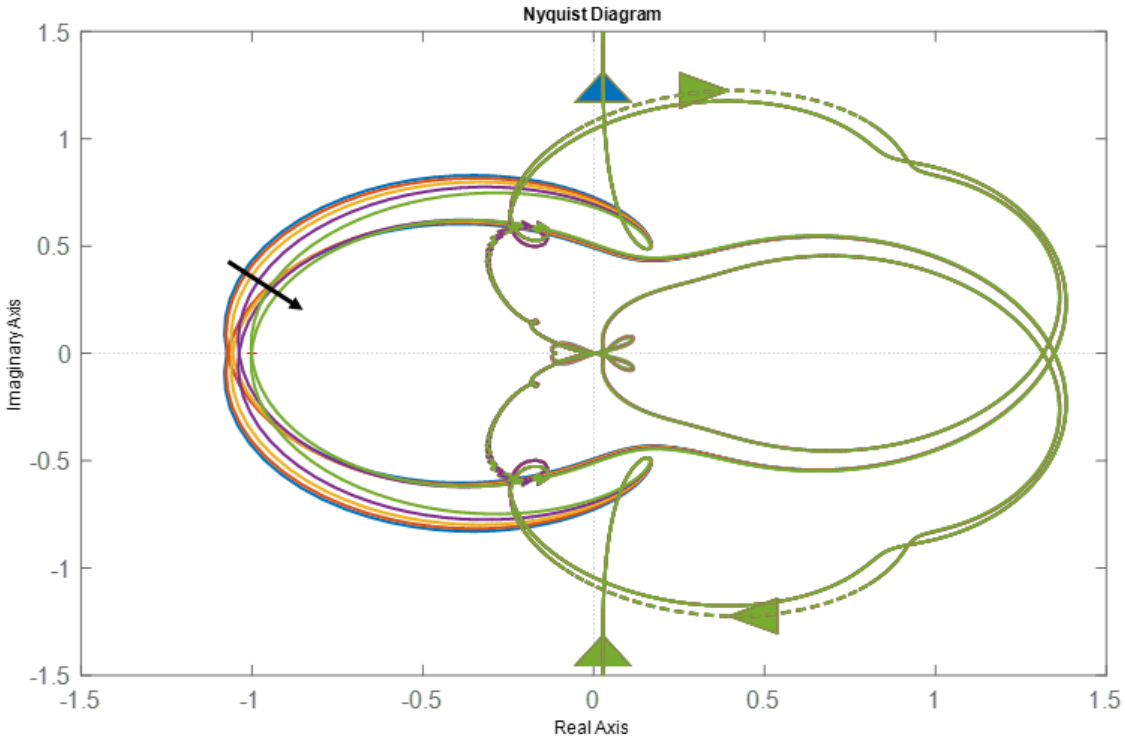

Figure 5-10 Characteristic loci at STATCOM 1 terminal with respect to PLL: solid - λ1; dashed - λ2

Again, the first eigenvalue $\lambda_1(s)$ is plotted in Bode plot in Figure 5-11. The increase in the bandwidth of PLL did not cause a rise of resonance but moved the peak to high frequency. This actually made the characteristic locus intersect with the negative real axis at a higher frequency where its magnitude was smaller. When the magnitude was smaller than 0 dB at the intersection frequency, the locus did not encircle the critical point, indicating a stable operation.

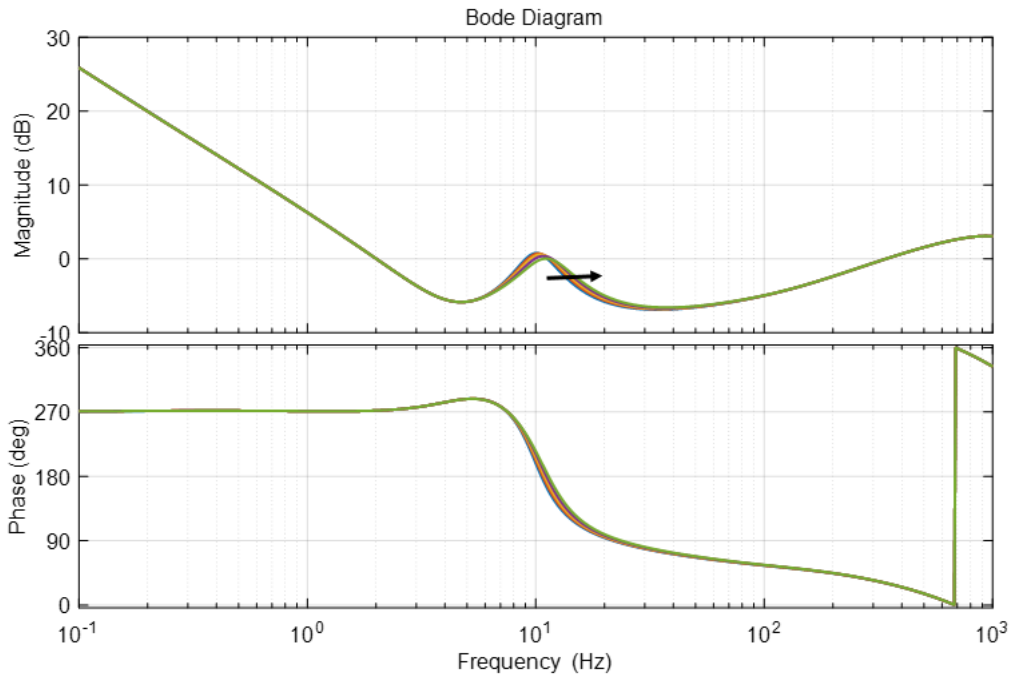

Figure 5-11 Characteristic loci λ1 at STATCOM 1 terminal with respect to PLL in Bode pot

5.2.3 Effects of current loop

The effects of the current loop are shown in Figure 5-12 with increasing bandwidths from 200 to 500 Hz. Still, the impedance of STATCOM 1 $\mathbf{Z}_{\mathbf{vsi}}(s)$ are in solid lines and relatively larger while the impedances of the rest of the grid $\mathbf{Z}_{\mathbf{grid}}(s)$ are in dashed lines. When the current loop bandwidth increased, the impedance of STATCOM 1 was magnified in the frequency range from 10 to 1000 Hz where the resonant peak slightly diminished. On the other hand, the grid impedance $\mathbf{Z}_{\mathbf{grid}}(s)$ showed less magnitude around 10 Hz because of the reduced resonant peak.

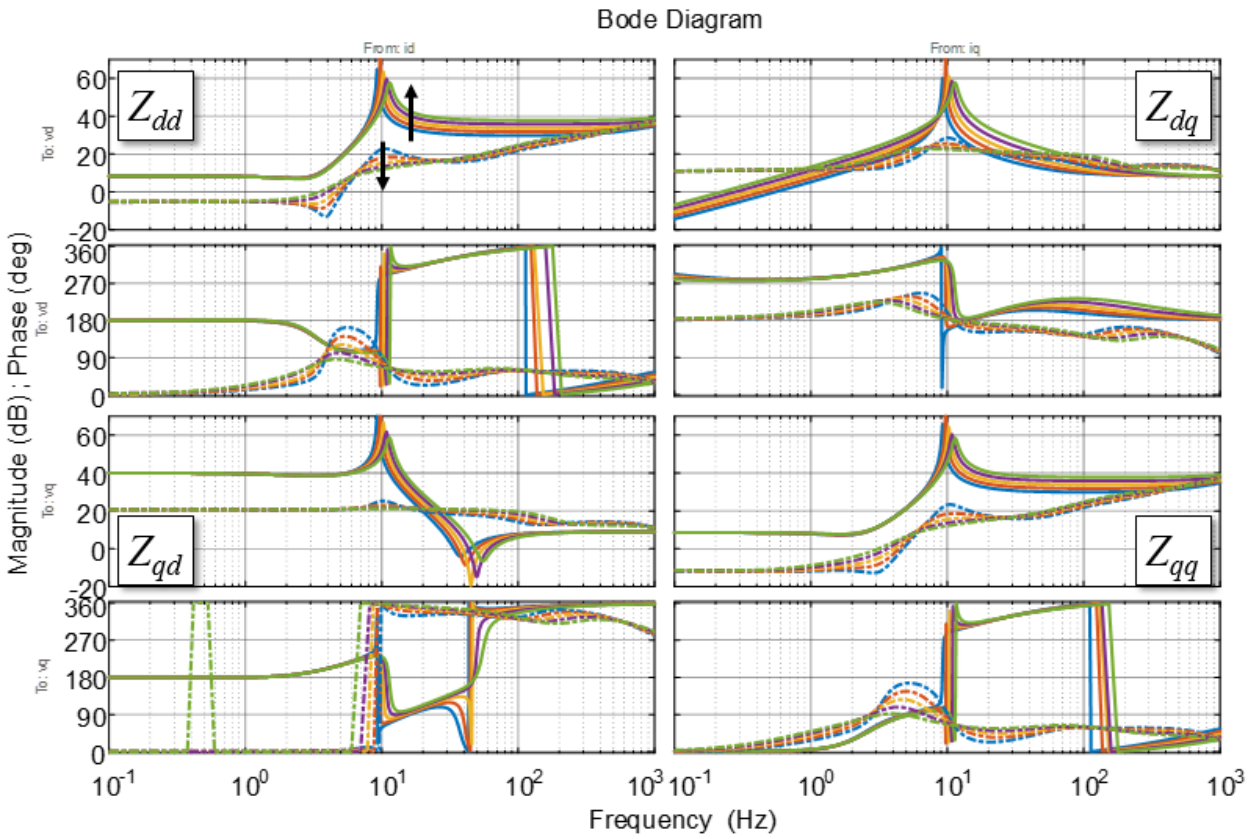

Figure 5-12 Impedances at STATCOM 1 terminal with respect to current loop - solid: Zvsi; dashed: Zgrid

The eigenvalues of the return ratio are plotted in Figure 5-13. $\lambda_2(s)$ was in dashed lines and far away from the critical point and $\lambda_1(s)$ was potential to encircle, with the arrow showing the increase of the bandwidth of current loop. The system tended to be stable with higher current loop bandwidth, since the characteristic loci moved into the unity circle from the outside and didn't encircle the critical point in the end with no RHP poles in either $\mathbf{Z}_{\mathbf{grid}}(s)$ or $\mathbf{Y}_{\mathbf{vsi}}(s)$.

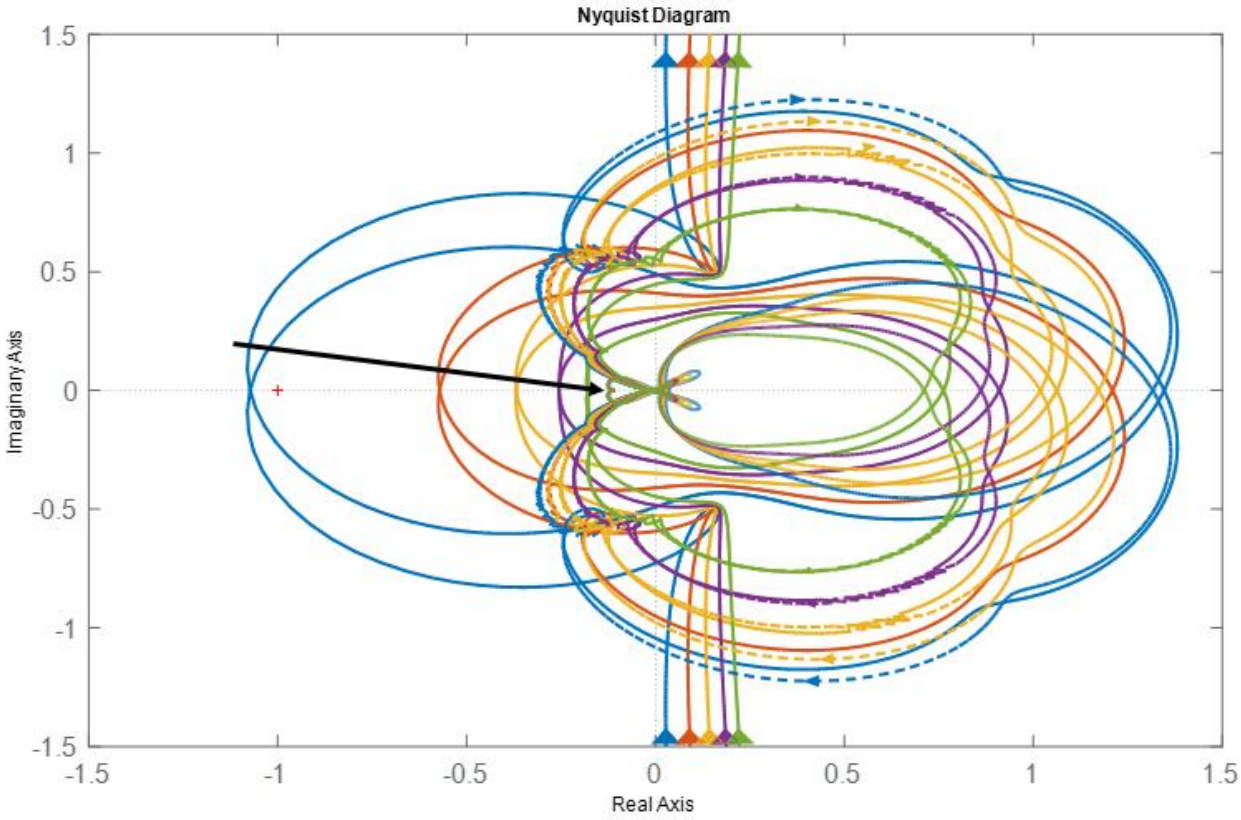

Figure 5-13 Characteristic loci at STATCOM 1 terminal with respect to current loop: solid - λ1; dashed - λ2

Figure 5-14 shows $\lambda_1(s)$ in Bode plot and the arrow shows the increase of the current loop bandwidth. Clearly, with the increase of the current loop bandwidth, the magnitude of $\lambda_1(s)$ dropped a lot because of the increase of STATCOM impedance magnitude. This trend actually pushed the characteristic locus into the unity circle and formed a more stable system.

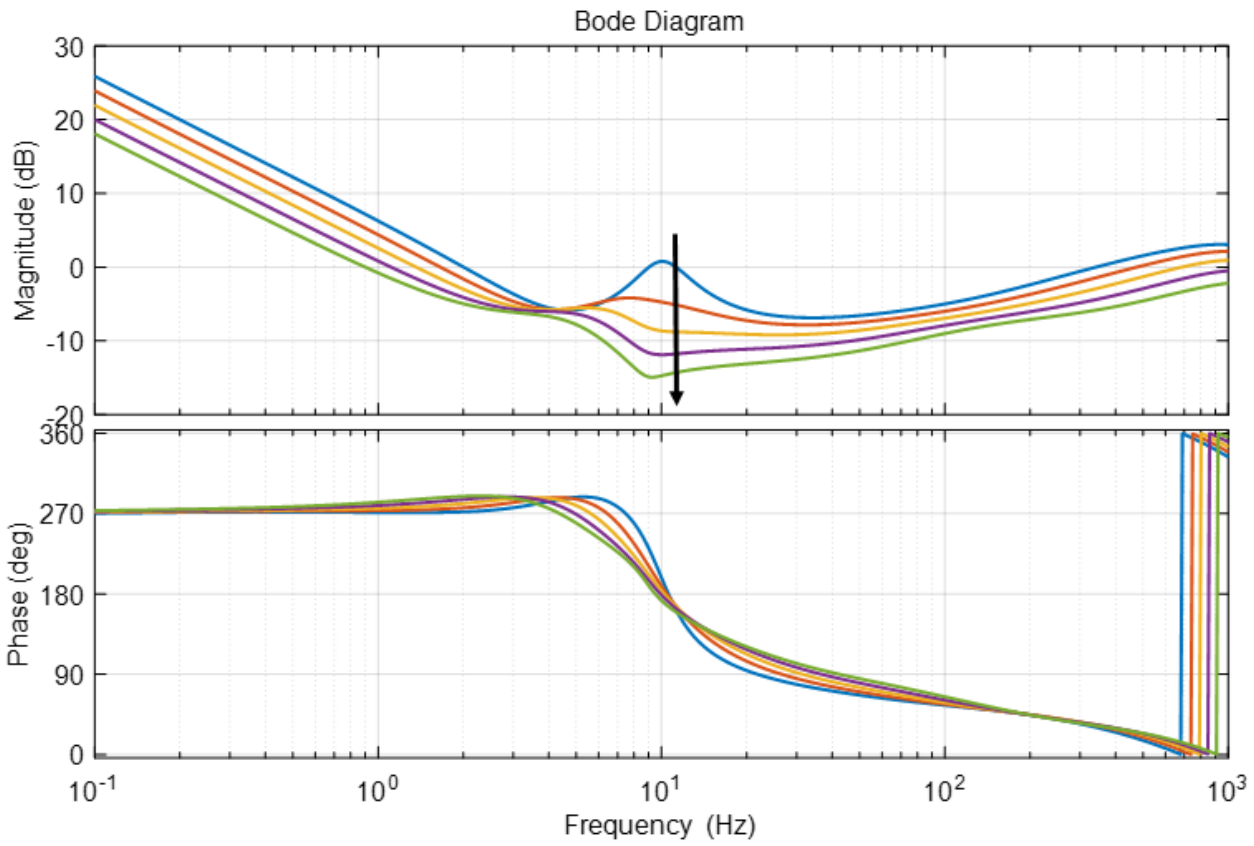

Figure 5-14 Characteristic loci λ1 at STATCOM 1 terminal with respect to current loop in Bode pot

5.2.4 Effects of QV droop

As for QV droop, the impedances of STATCOM 1 and the rest of the grid were measured in Figure 5-15, where the solid lines are STATCOM impedance $\mathbf{Z}_{\mathbf{vsi}}(s)$ and the dashed lines are $\mathbf{Z}_{\mathbf{grid}}(s)$. The case with QV droop in red lines had one significant difference compared to the case without QV droop in blue lines: the STATCOM impedance in dq-channel was much larger at low frequencies. This is because the reactive power is mainly dependent on q-channel current and the d-channel PCC voltage is the controlled variable of the QV droop. By activating the droop, q-channel current has equivalently more influence on the d-channel PCC voltage, which indicates larger impedance in the dq-channel. Intrinsically, QV droop brought about more interactions among STATCOM units in steady state by the means of adding one feedback loop to the ac voltage

loop. The addition not only changed the operating points but the dynamics of the ac voltage loop as well.

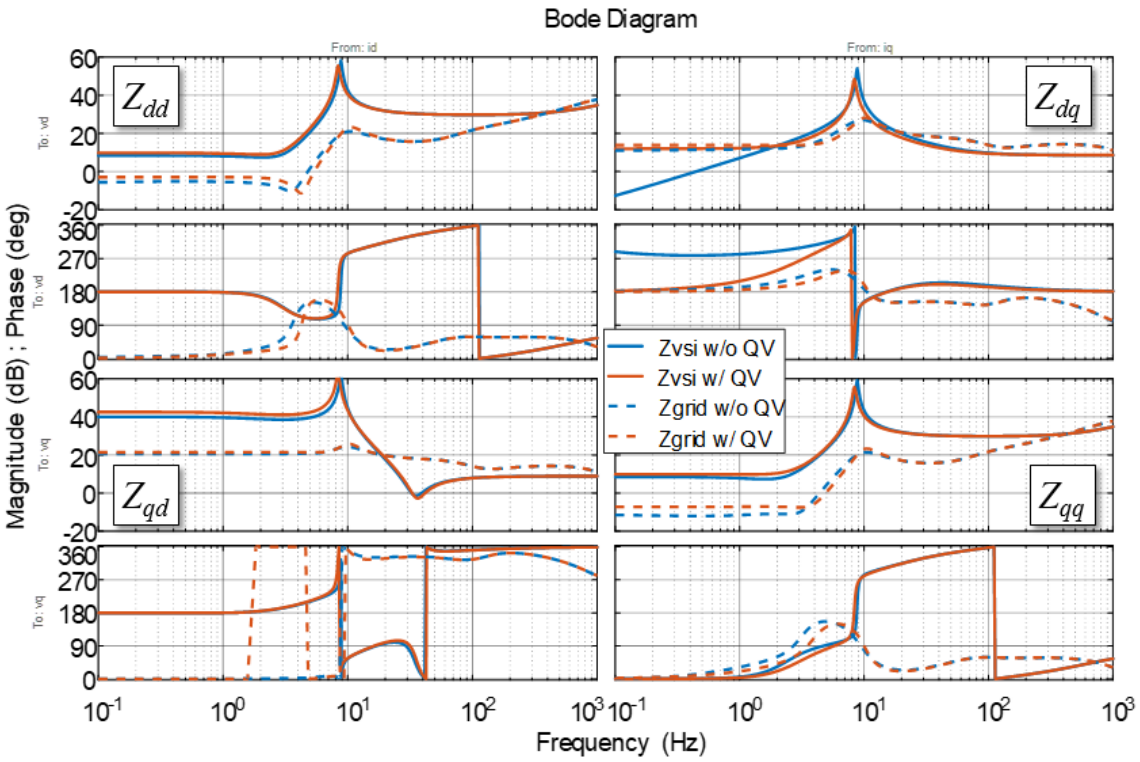

Figure 5-15 Impedances at STATCOM 1 terminal with respect to QV droop - solid: Zvsi; dashed: Zgrid

The characteristic loci are drawn in Figure 5-16 calculated from the impedances in Figure 5-15. The case with QV droop is plotted in red and the case without QV droop is depicted in blue. Similarly, $\lambda_2(s)$ in dashed lines were far way from the critical point and $\lambda_1(s)$ in solid lines were close. Because of the addition feedback loop from the QV droop, characteristic locus $\lambda_1(s)$ with QV droop encircled the critical point and indicated instability, which mathces the simulation results in the previous section.

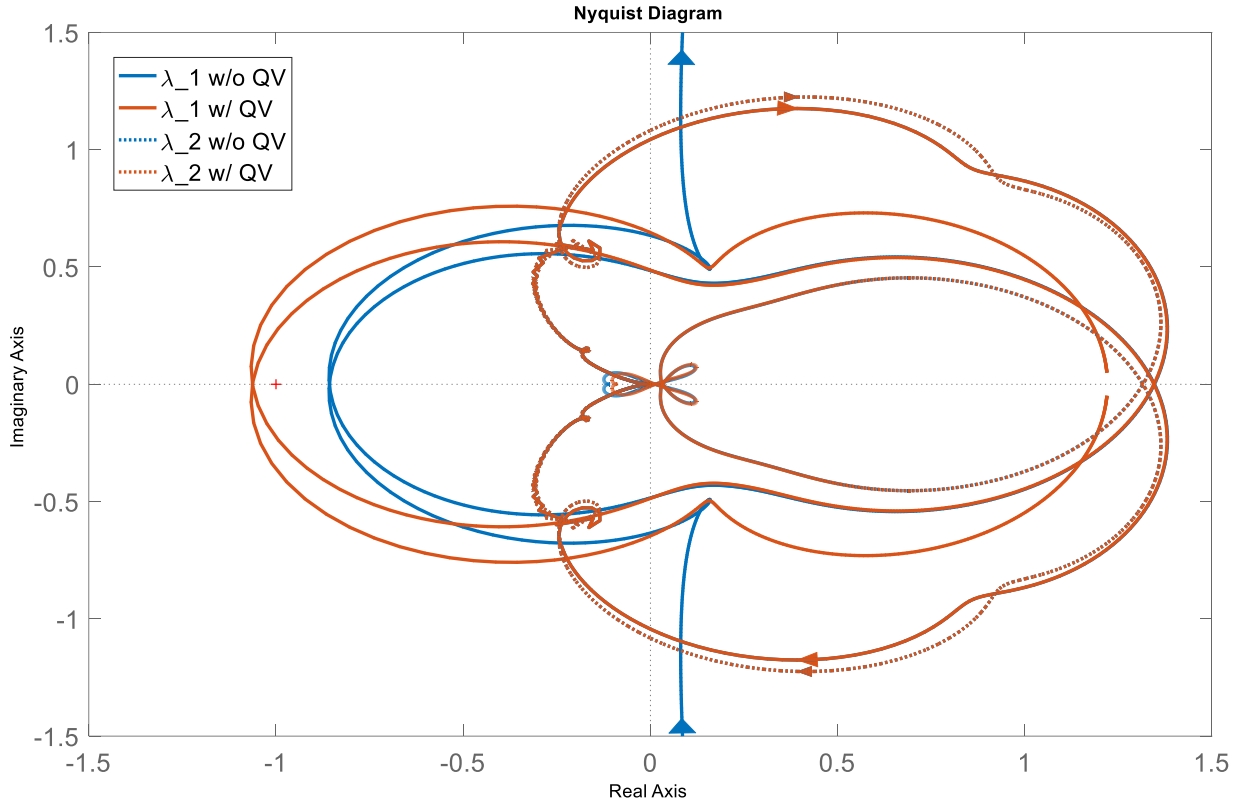

Figure 5-16 Characteristic loci at STATCOM 1 terminal with respect to QV droop: solid - λ1; dashed - λ2

5.3 New issues introduced in the full system

5.3.1 System topology and STATCOM locations

Extending from the simplified 2-STATCOM system to the meshed power system, one could first wonder what effects are from relative locations or distances between STATCOMs, or simply put, power system topology. To explore this from impedance point of view, we can arbitrarily select the terminal of one STATCOM and investigate how the grid impedance is like with respect to any changes in the power system. The reason is that at this terminal if the operating point of this specific STATCOM is kept the same, the stability is solely dependent on the grid impedance that reflects any dynamic behaviors from others.

Different locations of STATCOMs showed negligible effects on impedances, and therefore trivial influences on stability. Figure 5-17 depicts the grid impedance $\mathbf{Z}_{\mathbf{grid}}(s)$ at the terminal of STATCOM 1 with no other STATCOMs, STATCOM 2, STATCOM 3 and STATCOM 4 connected respectively, $\mathbf{Z}_{\mathbf{grid1}}(s)$ in blue solid lines, $\mathbf{Z}_{\mathbf{grid1\_2}}(s)$ in red dashed lines, $\mathbf{Z}_{\mathbf{grid1\_3}}(s)$ in yellow dashed lines and $\mathbf{Z}_{\mathbf{grid1\_4}}(s)$ in purple dashed lines. $\mathbf{Z}_{\mathbf{grid1}}(s)$ shows simply the equivalent impedance of the grid network and loads while the other three contained impedances from other STATCOMs respectively. Clearly, the grid impedance increased in magnitude with other STATCOMs were connected. However, no matter which STATCOM 2, 3 or 4 was connected, the grid impedances $\mathbf{Z}_{\mathbf{grid1\_2}}(s)$, $\mathbf{Z}_{\mathbf{grid1\_3}}(s)$ and $\mathbf{Z}_{\mathbf{grid1\_4}}(s)$ were almost identical with less than 1 dB differences around the oscillatory frequency of 10 Hz.

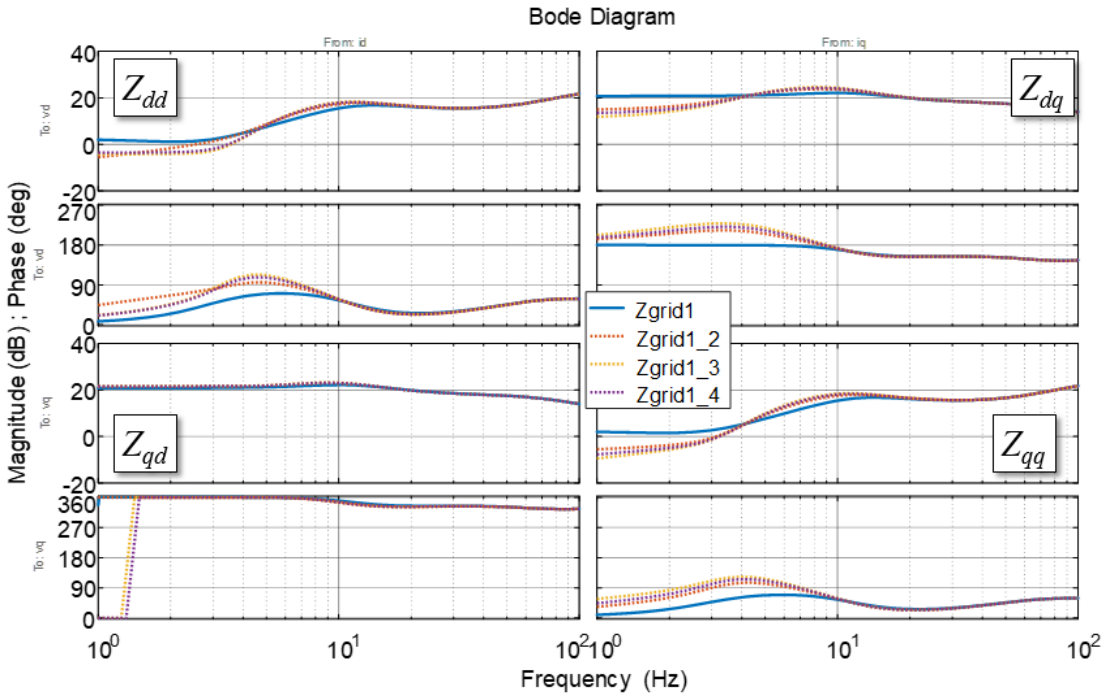

Figure 5-17 Grid impedance with different STATCOMs

This is because at the oscillatory frequency the STATCOM impedance had much larger magnitude (40-50 dB) than the equivalent impedances of the longest transmission line path (less

than 1 dB). Thus, impedance of one STATCOM played a much important role in the grid impedance at the terminal of the other STATCOMs and the line in between was negligible. It leads to the conclusions that the locations of STATOMs did not matter much in the found instability with oscillatory frequency at about 10 Hz. Actually, the magnitude of STATCOM impedance is much larger than that of transmission lines until 100 Hz, for a transmission grid with typical parameters. Therefore, the conclusion that the locations of STATCOMs did not matter much would hold for oscillatory modes up to at least 100 Hz. This conclusion also provides answers to the simulation results in Section 2.3 that the system parameters were negligible in terms of stability.

With the above conclusion, we can further infer that the combination of STATCOMs did not influence the stability for a given connected number, because STATCOM 1 could hardly tell which other STATCOM were connected. This answers why the connection sequence of STATCOMs did not matter in terms of stability in simulation in Section 2.3.

5.3.2 Number of connected STATCOMs

One more step leads to the second conclusion that the found stability highly depended on the number of connected STATCOMs because which STATCOM was connected did not matter much. This is shown in Figure 5-18 where the grid impedance at the terminal of STATCOM 1 with one, two and three STATCOMs are plotted in blue, red and yellow respectively. The arrow indicates the increase of the number of the connected STATCOMs. It is clear that one more STATCOM made the magnitude of the resonant peak increase significantly, because all the STATCOM impedance had the same peak at the same frequency and they added up to the grid impedance. As discussed previously, the rising magnitude of this resonant peak tended to cause instability. Moreover, the increase introduced by an additional STATCOM was dominant. Thus, the more STATCOM connected, the more unstable the system was.

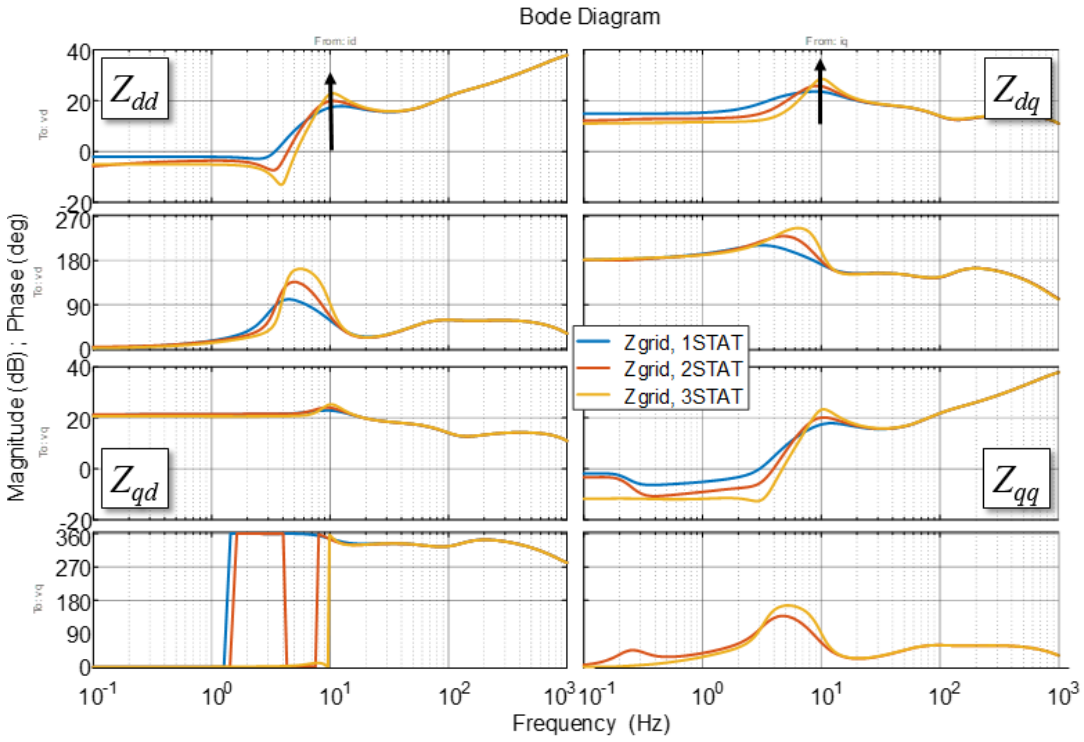

Figure 5-18 Grid impedance with different numbers of STATCOMs

5.4 Alternative controls

The two alternative controls proposed in Section 4.3 were applied to the full system. Figure 5-19 depicts that by removing the integrator in the current controller, the system became stable. Again, it is worthwhile to mention that proportional controller for current loop is not recommended, because the current regulation performance is worse than PI controller, especially resistance to low frequency perturbations from the power grid.

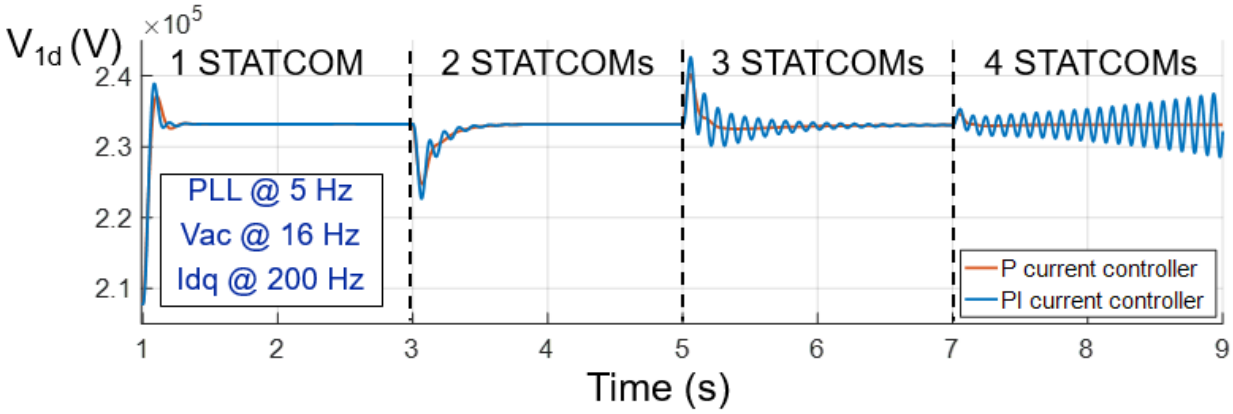

Figure 5-19 Instability mitigation by proportional current controller

Figure 5-20 shows that increasing the phase margin of the ac voltage loop helped stabilize the system. However, the transient responses were slowed down as a result of additional zero before the crossover frequency. In this case, the response time was nearly one second, much longer than typical requirements from the grid side. Therefore, the trade-off between stability margin and settling time must be taken into consideration in design.

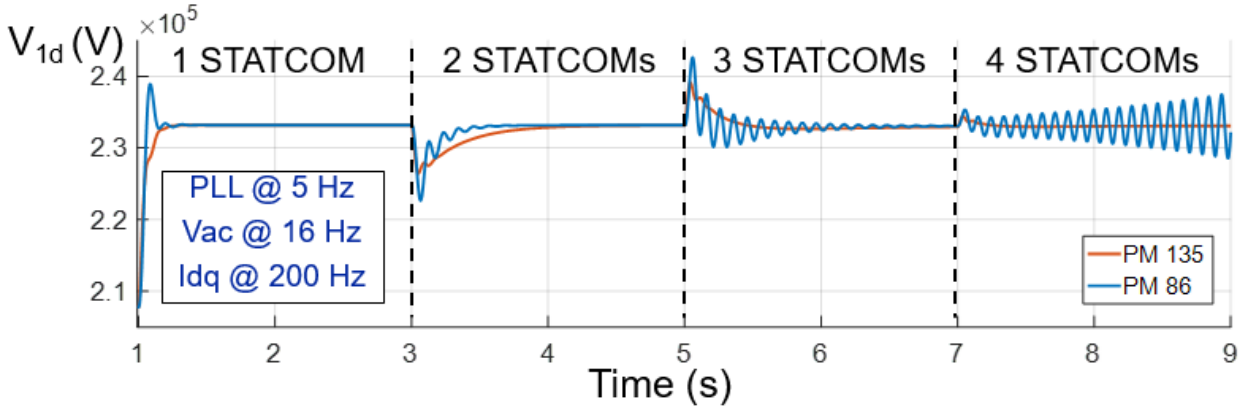

Figure 5-20 Instability mitigation by alternative ac voltage controller with larger phase margin

5.5 Conclusions

In this chapter, the previous conclusions about instability in Chapter IV were extended to the full system with four STATCOMs and they were found to be valid. Besides, new issues regarding

the positions of STATCOMs and topology of the system were discussed with respect to previously found instability, where these two factors turned out to be negligible, because the crucial reason of instability was STATCOM control that showed much higher impacts than grid parameters.

Chapter 6. CONCLUSIONS AND FUTURE WORK

6.1 Conclusions

STATCOMs have been adopted into power systems for decades to enhance power system operations by means of reactive power compensation. There is now a trend to use multiple STATCOMs in proximity to further improve the benefits, especially better voltage profiles and better operation burden share among STATCOMs for an economic purpose. However, the impacts of multiple STATCOMs close to each other have been little studied, specifically in terms of small-signal stability.

This research first studied how a power system with multiple STATCOMs works and what factors influence the small-signal stability. It turned out that control of STATCOMs had the most impacts, while the parameters of the power system did not show significant effects. Among the control of STATCOMs, a higher current bandwidth, a higher PLL bandwidth and a slower ac voltage loop bandwidth helped improve the stability conditions respectively. Besides the full system with four STATCOMs, the same conclusions were also drawn in a simplified 2-STATCOM system, which was used to simplify analysis as a starting point. The conclusions were experimentally verified in a scaled-down 2-STATCOM system in the end of Chapter II.

In order to analyze the aforementioned stability issues, impedance-based stability method was used because of its advantages over the traditional state-space modeling method, especially easier assessment and less a priori knowledge required. To begin with, a D-Q frame impedance model for STATCOMs including all control loops were proposed and derived. From the impedance model, one can see that the STATCOM impedance was highly non-diagonal and changed its polarity in low frequencies with inverse directions of reactive power flow. The first feature makes

the stability assessment directly from the d-q frame impedances is very difficult—as opposed to unity power factor rectifiers and inverters, for which a multivariable stability theorem using the return-ratio matrix, product of the upstream and downstream impedances at a given ac interface must be used; for instance, the GNC. The second feature shows that STATCOMs could behave both as a CPL rectifier and as a grid-tied inverter injecting power into the grid, from a dynamic standpoint, featuring a negative incremental input-impedance in its Z_{dd} or Z_{qq} impedance elements respectively. Furthermore, the ac voltage loop of the STATCOM was found to be the strongest contributor to its terminal impedance and in consequence to its small-signal stability conditions. This loop was shown to effectively mask the PLL dynamics, especially for system parameters proper of transmission grids, previously shown to be critical in grid-tied power converters. The impedance model was validated using an impedance measurement unit (IMU) and showed good correspondence.

With the impedance model ready, the stability issues were studied in the simplified 2-STATCOM system and the full system as well. The following conclusions were obtained. First, STATCOMs were seen to interact with each other through the transmission lines due to the relatively high magnitude of their impedances with respect to that of the lines. As such, STATCOM control could lead to the instability of power systems because of limited information flow between vendors, which explained why the previously found instability happened and why the system parameters had negligible impacts. Second, the use of d-q frame impedances identified the frequency range of interactions. The ac voltage regulation was the main reason of instability among STATCOM control and masked the effects of PLL in transmission systems, which was anticipated from the conclusions in the impedance model part. Third, due to the large impedance of STATCOMs around the frequency range of interactions, the number of connected STATCOMs

was the main contributor to stability instead of the topology of the power system or the locations of the STATCOMs. The high magnitude of STATCOM impedance around oscillatory frequency range makes it the dominant reason of instability and topology of the power systems showed negligible influences. Fourth, alternative controllers were assessed to mitigate stability problems and trade-offs were discussed. Lastly, the scaled-down 2-STATCOM power grid was used to verify the conclusions experimentally.

6.2 Future work

This research mainly focused on evaluation of power system operation with multiple STATCOMs in proximity and analysis from an impedance point of view. Remedies to these instability issues were proposed and could be studied further to improve. Specifically, recent researches on virtual synchronous machine (VSM) control for grid-tied converters presented a lot of progress, and whether the VSM control can help improve the discovered instability is still open to successors.

Another possible direction is to explore the operation of STATCOMs in the sense of large-signal stability, which are essentially faults and large load steps. It is a crucial piece of assessments for power system operators in order to have a practical sense of how they work and it is even more difficult to tackle. Methods based on linear system theory, the traditional state-space modeling and impedance-based method, would fail in this scenario. Tools based on non-linear system theory are either too complicated to implement in industrial applications, e.g. Lyapunov- or energy-based methods or very time-consuming and not economic-effective, for example real-time simulation. There are many challenges in this field.

Finally, it is interesting to see the extension of conclusions to power systems with other types of grid-tied converters, PV farms or HVDC ends for example, where active power is also involved. There are probably different instability patterns and it is meaningful to explore the unknown.

REFERENCES

[1] L. Gyugyi, "Reactive Power Generation and Control by Thyristor Circuits," *Industry Applications, IEEE Transactions on,* vol. IA-15, pp. 521-532, 1979.

[2] Y. Ou and C. Singh, "Improvement of total transfer capability using TCSC and SVC," in *Power Engineering Society Summer Meeting, 2001,* 2001, pp. 944-948 vol.2.

[3] L. Naihu, X. Yan, and C. Heng, "FACTS-based power flow control in interconnected power system," *Power Systems, IEEE Transactions on,* vol. 15, pp. 257-262, 2000.

[4] X. Ying, Y. H. Song, and Y. Z. Sun, "Power flow control approach to power systems with embedded FACTS devices," *Power Systems, IEEE Transactions on,* vol. 17, pp. 943-950, 2002.

[5] X. Ying, Y. H. Song, L. Chen-Ching, and Y. Z. Sun, "Available transfer capability enhancement using FACTS devices," *Power Systems, IEEE Transactions on,* vol. 18, pp. 305-312, 2003.

[6] H. Farahmand, M. Rashidi-nejad, and M. Fotuhi-Firoozabad, "Implementation of FACTS devices for ATC enhancement using RPF technique," in *Power Engineering, 2004. LESCOPE-04. 2004 Large Engineering systems Conference on*, 2004, pp. 30-35.

[7] W. Ongsakul and P. Jirapong, "Optimal allocation of FACTS devices to enhance total transfer capability using evolutionary programming," in *Circuits and Systems, 2005. ISCAS 2005. IEEE International Symposium on*, 2005, pp. 4175-4178 Vol. 5.

[8] E. V. Larsen, J. J. Sanchez-Gasca, and J. H. Chow, "Concepts for design of FACTS controllers to damp power swings," *Power Systems, IEEE Transactions on,* vol. 10, pp. 948-956, 1995.

[9] M. Noroozian, L. Angquist, M. Ghandhari, and G. Andersson, "Improving power system dynamics by series-connected FACTS devices," *Power Delivery, IEEE Transactions on,* vol. 12, pp. 1635-1641, 1997.

[10] H. F. Wang and F. J. Swift, "A unified model for the analysis of FACTS devices in damping power system oscillations. I. Single-machine infinite-bus power systems," *Power Delivery, IEEE Transactions on,* vol. 12, pp. 941-946, 1997.

[11] P. Pourbeik and M. J. Gibbard, "Simultaneous coordination of power system stabilizers and FACTS device stabilizers in a multimachine power system for enhancing dynamic performance," *Power Systems, IEEE Transactions on,* vol. 13, pp. 473-479, 1998.

[12] H. F. Wang, F. J. Swift, and M. Li, "A unified model for the analysis of FACTS devices in damping power system oscillations. II. Multi-machine power systems," *Power Delivery, IEEE Transactions on,* vol. 13, pp. 1355-1362, 1998.

[13] P. K. Dash, S. Mishra, and G. Panda, "Damping multimodal power system oscillation using a hybrid fuzzy controller for series connected FACTS devices," *Power Systems, IEEE Transactions on,* vol. 15, pp. 1360-1366, 2000.

[14] W. HaiFeng, "A unified model for the analysis of FACTS devices in damping power system oscillations. III. Unified power flow controller," *Power Delivery, IEEE Transactions on,* vol. 15, pp. 978-983, 2000.

[15] L. Xianzhang, E. N. Lerch, and D. Povh, "Optimization and coordination of damping controls for improving system dynamic performance," *Power Systems, IEEE Transactions on,* vol. 16, pp. 473-480, 2001.

[16] B. Chaudhuri, B. C. Pal, A. C. Zolotas, I. M. Jaimoukha, and T. C. Green, "Mixed-sensitivity approach to H_∞ control of power system oscillations employing multiple FACTS devices," *Power Systems, IEEE Transactions on,* vol. 18, pp. 1149-1156, 2003.

[17] B. Chaudhuri and B. C. Pal, "Robust damping of multiple swing modes employing global stabilizing signals with a TCSC," *Power Systems, IEEE Transactions on,* vol. 19, pp. 499-506, 2004.

[18] A. B. Arsoy, Y. Liu, P. F. Ribeiro, and F. Wang, "StatCom-SMES," *Industry Applications Magazine, IEEE,* vol. 9, pp. 21-28, 2003.

[19] M. S. El-Moursi, B. Bak-Jensen, and M. H. Abdel-Rahman, "Novel STATCOM Controller for Mitigating SSR and Damping Power System Oscillations in a Series Compensated Wind Park," *Power Electronics, IEEE Transactions on,* vol. 25, pp. 429-441, 2010.

[20] M. H. Haque, "Improvement of first swing stability limit by utilizing full benefit of shunt FACTS devices," *Power Systems, IEEE Transactions on,* vol. 19, pp. 1894-1902, 2004.

[21] N. Mithulananthan, C. A. Canizares, J. Reeve, and G. J. Rogers, "Comparison of PSS, SVC, and STATCOM controllers for damping power system oscillations," *Power Systems, IEEE Transactions on,* vol. 18, pp. 786-792, 2003.

[22] K. R. Padiyar and N. Prabhu, "Design and performance evaluation of subsynchronous damping controller with STATCOM," *Power Delivery, IEEE Transactions on,* vol. 21, pp. 1398-1405, 2006.

[23] T. Shintai, Y. Miura, and T. Ise, "Oscillation Damping of a Distributed Generator Using a Virtual Synchronous Generator," *Power Delivery, IEEE Transactions on,* vol. 29, pp. 668-676, 2014.

[24] H. Chong, A. Q. Huang, M. E. Baran, S. Bhattacharya, W. Litzenberger, L. Anderson, *et al.*, "STATCOM Impact Study on the Integration of a Large Wind Farm into a Weak Loop Power System," *Energy Conversion, IEEE Transactions on,* vol. 23, pp. 226-233, 2008.

[25] D. J. Gotham and G. T. Heydt, "Power flow control and power flow studies for systems with FACTS devices," *Power Systems, IEEE Transactions on,* vol. 13, pp. 60-65, 1998.

[26] M. M. Farsangi, Y. H. Song, and K. Y. Lee, "Choice of FACTS device control inputs for damping interarea oscillations," *Power Systems, IEEE Transactions on,* vol. 19, pp. 1135-1143, 2004.

[27] P. Rao, M. L. Crow, and Y. Zhiping, "STATCOM control for power system voltage control applications," *Power Delivery, IEEE Transactions on,* vol. 15, pp. 1311-1317, 2000.

[28] C. Woei-Luen, L. Wei-Gang, and G. Hrong-Sheng, "Design of a Mode Decoupling STATCOM for Voltage Control of Wind-Driven Induction Generator Systems," *Power Delivery, IEEE Transactions on,* vol. 25, pp. 1758-1767, 2010.

[29] W. Li and H. Chia-Tien, "Dynamic Stability Improvement of an Integrated Grid-Connected Offshore Wind Farm and Marine-Current Farm Using a STATCOM," *Power Systems, IEEE Transactions on,* vol. 26, pp. 690-698, 2011.

[30] W. Li and T. Dinh-Nhon, "Dynamic Stability Improvement of Four Parallel-Operated PMSG-Based Offshore Wind Turbine Generators Fed to a Power System Using a STATCOM," *Power Delivery, IEEE Transactions on,* vol. 28, pp. 111-119, 2013.

[31] S. B. Karanki, M. K. Mishra, and B. K. Kumar, "Particle Swarm Optimization-Based Feedback Controller for Unified Power-Quality Conditioner," *Power Delivery, IEEE Transactions on,* vol. 25, pp. 2814-2824, 2010.

[32] X. Zhang, W. Zhang, Y. Lv, W. Liu, and Q. Wang, "Unified power quality conditioner with model predictive control," in *Computer Science and Education (ICCSE), 2010 5th International Conference on*, 2010, pp. 1239-1244.

[33] V. G. Kinhal, P. Agarwal, and H. O. Gupta, "Performance Investigation of Neural-Network-Based Unified Power-Quality Conditioner," *Power Delivery, IEEE Transactions on,* vol. 26, pp. 431-437, 2011.

[34] A. E. Leon, S. J. Amodeo, I. A. Solsona, and M. I. Valla, "Non-linear optimal controller for unified power quality conditioners," *Power Electronics, IET,* vol. 4, pp. 435-446, 2011.

[35] V. Khadkikar, "Enhancing Electric Power Quality Using UPQC: A Comprehensive Overview," *Power Electronics, IEEE Transactions on,* vol. 27, pp. 2284-2297, 2012.

[36] J. A. Diaz de Leon and C. W. Taylor, "Understanding and solving short-term voltage stability problems," in *Power Engineering Society Summer Meeting, 2002 IEEE*, 2002, pp. 745-752 vol.2.

[37] A. Arulampalam, M. Barnes, N. Jenkins, and J. B. Ekanayake, "Power quality and stability improvement of a wind farm using STATCOM supported with hybrid battery energy storage," *Generation, Transmission and Distribution, IEE Proceedings-,* vol. 153, pp. 701-710, 2006.

[38] Z. Saad-Saoud, M. L. Lisboa, J. B. Ekanayake, N. Jenkins, and G. Strbac, "Application of STATCOMs to wind farms," *Generation, Transmission and Distribution, IEE Proceedings-,* vol. 145, pp. 511-516, 1998.

[39] H. Gaztanaga, I. Etxeberria-Otadui, D. Ocnasu, and S. Bacha, "Real-Time Analysis of the Transient Response Improvement of Fixed-Speed Wind Farms by Using a Reduced-Scale STATCOM Prototype," *Power Systems, IEEE Transactions on,* vol. 22, pp. 658-666, 2007.

[40] M. J. Hossain, H. R. Pota, V. A. Ugrinovskii, and R. A. Ramos, "Simultaneous STATCOM and Pitch Angle Control for Improved LVRT Capability of Fixed-Speed Wind Turbines," *Sustainable Energy, IEEE Transactions on,* vol. 1, pp. 142-151, 2010.

[41] M. Molinas, J. A. Suul, and T. Undeland, "Low Voltage Ride Through of Wind Farms With Cage Generators: STATCOM Versus SVC," *Power Electronics, IEEE Transactions on,* vol. 23, pp. 1104-1117, 2008.

[42] C. Wessels, N. Hoffmann, M. Molinas, and F. W. Fuchs, "StatCom control at wind farms with fixed-speed induction generators under asymmetrical grid faults," *Industrial Electronics, IEEE Transactions on,* vol. 60, pp. 2864-2873, 2013.

[43] P. Kundur, *Power system stability and control*. New York: McGraw-hill, 1994.

[44] Y. Zhuang, R. W. Menzies, O. B. Nayak, and H. M. Turanli, "Dynamic performance of a STATCON at an HVDC inverter feeding a very weak AC system," *Power Delivery, IEEE Transactions on,* vol. 11, pp. 958-964, 1996.

[45] D. Jovcic, N. Pahalawaththa, and M. Zavahir, "Investigation of the use of inverter control strategy instead of synchronous condensers at inverter terminal of an HVDC system," *Power Delivery, IEEE Transactions on,* vol. 15, pp. 704-709, 2000.

[46] A. J. P. Ramos and H. Tyll, "Dynamic performance of a radial weak power system with multiple static VAr compensators," *Power Systems, IEEE Transactions on,* vol. 4, pp. 1316-1325, 1989.

[47] L. Gerin-Lajoie, G. Scott, S. Breault, E. V. Larsen, D. H. Baker, and A. F. Imece, "Hydro-Quebec multiple SVC application control stability study," *Power Delivery, IEEE Transactions on,* vol. 5, pp. 1543-1551, 1990.

[48] N. Martins, N. J. P. Macedo, L. T. G. Lima, and H. J. C. P. Pinto, "Control strategies for multiple static VAr compensators in long distance voltage supported transmission systems," *Power Systems, IEEE Transactions on,* vol. 8, pp. 1107-1117, 1993.

[49] M. Parniani and M. R. Iravani, "Voltage control stability and dynamic interaction phenomena of static VAr compensators," *Power Systems, IEEE Transactions on,* vol. 10, pp. 1592-1597, 1995.

[50] C. d. P. d. E. Eletrica, E. P. R. Institute, and U. o. W.-M. C. D. o. E. P. Development, "Analysis of Control Interactions on FACTS Assisted Power Systems," Electric Power Research Institute1998.

[51] H. F. Wang, "Modelling multiple FACTS devices into multi-machine power systems and applications," *International Journal of Electrical Power & Energy Systems,* vol. 25, pp. 227-237, 3// 2003.

[52] A. R. Messina, O. Begovich, J. H. López, and E. N. Reyes, "Design of multiple FACTS controllers for damping inter-area oscillations: a decentralised control approach," *International Journal of Electrical Power & Energy Systems,* vol. 26, pp. 19-29, 1// 2004.

[53] M. Zarghami and M. L. Crow, "Damping inter-area oscillations in power systems by STATCOMs," in *Power Symposium, 2008. NAPS '08. 40th North American*, 2008, pp. 1-6.

[54] M. A. Furini, A. L. S. Pereira, and P. B. Araujo, "Pole placement by coordinated tuning of Power System Stabilizers and FACTS-POD stabilizers," *International Journal of Electrical Power & Energy Systems,* vol. 33, pp. 615-622, 3// 2011.

[55] R. D. Middlebrook, "Input filter considerations in design and application of switching regulators," in *Proc. IEEE Ind. Appl. Soc. Conf.*, 1976, pp. 94-107.

[56] B. Wen, D. Boroyevich, R. Burgos, P. Mattavelli, and Z. Shen, "Small-Signal Stability Analysis of Three-Phase AC Systems in the Presence of Constant Power Loads Based on Measured <italic>d-q</italic> Frame Impedances," *IEEE Transactions on Power Electronics,* vol. 30, pp. 5952-5963, 2015.

[57] W. Bo, D. Dong, D. Boroyevich, R. Burgos, P. Mattavelli, and S. Zhiyu, "Impedance-Based Analysis of Grid-Synchronization Stability for Three-Phase Paralleled Converters," *IEEE Transactions on Power Electronics,* vol. 31, pp. 26-38, 2016.

[58] M. Belkhayat, "Stability criteria for ac power systems with regulated loads," Ph. D. dissertation, Purdue University, West Lafayette, IN, USA, 1997.

[59] C. Li, R. Burgos, Y. Tang, and D. Boroyevich, "Impedance-based stability analysis of multiple STATCOMs in proximity," in *2016 IEEE 17th Workshop on Control and Modeling for Power Electronics (COMPEL)*, 2016, pp. 1-6.

[60] Z. Liu, J. Liu, W. Bao, and Y. Zhao, "Infinity-norm of Impedance Based Stability Criterion for Three-phase AC Distributed Power Systems with Constant Power Loads," *Power Electronics, IEEE Transactions on,* vol. PP, pp. 1-1, 2014.

[61] M. Cespedes and S. Jian, "Impedance Modeling and Analysis of Grid-Connected Voltage-Source Converters," *Power Electronics, IEEE Transactions on,* vol. 29, pp. 1254-1261, 2014.

[62] S. Jian, "Impedance-Based Stability Criterion for Grid-Connected Inverters," *Power Electronics, IEEE Transactions on,* vol. 26, pp. 3075-3078, 2011.

[63] X. Wang, F. Blaabjerg, and W. Wu, "Modeling and Analysis of Harmonic Stability in an AC Power-Electronics-Based Power System," *IEEE Transactions on Power Electronics,* vol. 29, pp. 6421-6432, 2014.

[64] J. Xiao and A. M. Gole, "A frequency scanning method for the identification of harmonic instabilities in HVDC systems," *IEEE Transactions on Power Delivery,* vol. 10, pp. 1875-1881, 1995.

[65] B. Badrzadeh, M. Sahni, Y. Zhou, D. Muthumuni, and A. Gole, "General Methodology for Analysis of Sub-Synchronous Interaction in Wind Power Plants," *IEEE Transactions on Power Systems,* vol. 28, pp. 1858-1869, 2013.

[66] A. Rygg, M. Molinas, C. Zhang, and X. Cai, "A Modified Sequence-Domain Impedance Definition and Its Equivalence to the dq-Domain Impedance Definition for the Stability Analysis of AC Power Electronic Systems," *IEEE Journal of Emerging and Selected Topics in Power Electronics,* vol. 4, pp. 1383-1396, 2016.

[67] X. Wang, L. Harnefors, and F. Blaabjerg, "Unified Impedance Model of Grid-Connected Voltage-Source Converters," *IEEE Transactions on Power Electronics,* vol. 33, pp. 1775-1787, 2018.

[68] Y. Song and C. Breitholtz, "Nyquist Stability Analysis of an AC-Grid Connected VSC-HVDC System Using a Distributed Parameter DC Cable Model," *IEEE Transactions on Power Delivery,* vol. 31, pp. 898-907, 2016.

[69] M. F. M. Arani and Y. A. R. I. Mohamed, "Analysis and Performance Enhancement of Vector-Controlled VSC in HVDC Links Connected to Very Weak Grids," *IEEE Transactions on Power Systems,* vol. 32, pp. 684-693, 2017.

[70] D. Shu, X. Xie, H. Rao, X. Gao, Q. Jiang, and Y. Huang, "Sub- and Super- Synchronous Interactions between STATCOMs and Weak AC/DC Transmissions with Series Compensations," *IEEE Transactions on Power Electronics,* vol. PP, pp. 1-1, 2017.

[71] L. Xu and L. Fan, "Impedance-Based Resonance Analysis in a VSC-HVDC System," *IEEE Transactions on Power Delivery,* vol. 28, pp. 2209-2216, 2013.

[72] L. Piyasinghe, Z. Miao, J. Khazaei, and L. Fan, "Impedance Model-Based SSR Analysis for TCSC Compensated Type-3 Wind Energy Delivery Systems," *IEEE Transactions on Sustainable Energy,* vol. 6, pp. 179-187, 2015.

[73] J. Lyu, X. Cai, and M. Molinas, "Frequency Domain Stability Analysis of MMC-Based HVdc for Wind Farm Integration," *IEEE Journal of Emerging and Selected Topics in Power Electronics,* vol. 4, pp. 141-151, 2016.

[74] M. Amin and M. Molinas, "Understanding the Origin of Oscillatory Phenomena Observed Between Wind Farms and HVdc Systems," *IEEE Journal of Emerging and Selected Topics in Power Electronics,* vol. 5, pp. 378-392, 2017.

[75] K. M. Alawasa, Y. A. R. I. Mohamed, and W. Xu, "Active Mitigation of Subsynchronous Interactions Between PWM Voltage-Source Converters and Power Networks," *IEEE Transactions on Power Electronics,* vol. 29, pp. 121-134, 2014.

[76] X. Chen, Y. Zhang, S. Wang, J. Chen, and C. Gong, "Impedance-Phased Dynamic Control Method for Grid-Connected Inverters in a Weak Grid," *IEEE Transactions on Power Electronics,* vol. 32, pp. 274-283, 2017.

[77] K. M. Alawasa and Y. A. R. I. Mohamed, "Impedance and Damping Characteristics of Grid-Connected VSCs With Power Synchronization Control Strategy," *Power Systems, IEEE Transactions on,* vol. PP, pp. 1-10, 2014.

[78] Y. Liao, Z. Liu, G. Zhang, and C. Xiang, "Vehicle-Grid System Modeling and Stability Analysis With Forbidden Region-Based Criterion," *IEEE Transactions on Power Electronics,* vol. 32, pp. 3499-3512, 2017.

[79] W. Ren and E. Larsen, "A Refined Frequency Scan Approach to Sub-Synchronous Control Interaction (SSCI) Study of Wind Farms," *IEEE Transactions on Power Systems,* vol. 31, pp. 3904-3912, 2016.

[80] A. Rygg, M. Molinas, C. Zhang, and X. Cai, "On the Equivalence and Impact on Stability of Impedance Modeling of Power Electronic Converters in Different Domains," *IEEE Journal of Emerging and Selected Topics in Power Electronics,* vol. 5, pp. 1444-1454, 2017.

[81] M. Cespedes and J. Sun, "Adaptive Control of Grid-Connected Inverters Based on Online Grid Impedance Measurements," *IEEE Transactions on Sustainable Energy,* vol. 5, pp. 516-523, 2014.

[82] M. Cespedes and J. Sun, "Mitigation of Inverter-Grid Harmonic Resonance by Narrow-Band Damping," *IEEE Journal of Emerging and Selected Topics in Power Electronics,* vol. 2, pp. 1024-1031, 2014.

[83] D. Yang, X. Ruan, and H. Wu, "Impedance Shaping of the Grid-Connected Inverter with LCL Filter to Improve Its Adaptability to the Weak Grid Condition," *Power Electronics, IEEE Transactions on,* vol. PP, pp. 1-1, 2014.

[84] J. Pérez, S. Cobreces, R. Griñó, and F. J. R. Sánchez, "$mathcal {H}_infty$ Current Controller for Input Admittance Shaping of VSC-Based Grid Applications," *IEEE Transactions on Power Electronics,* vol. 32, pp. 3180-3191, 2017.

[85] M. Davari and Y. A. R. I. Mohamed, "Robust Vector Control of a Very Weak-Grid-Connected Voltage-Source Converter Considering the Phase-Locked Loop Dynamics," *IEEE Transactions on Power Electronics,* vol. 32, pp. 977-994, 2017.

[86] A. A. A. Radwan and Y. A. R. I. Mohamed, "Analysis and Active-Impedance-Based Stabilization of Voltage-Source-Rectifier Loads in Grid-Connected and Isolated Microgrid Applications," *IEEE Transactions on Sustainable Energy,* vol. 4, pp. 563-576, 2013.

[87] K. M. Alawasa and Y. A. R. I. Mohamed, "A Simple Approach to Damp SSR in Series-Compensated Systems via Reshaping the Output Admittance of a Nearby VSC-Based System," *IEEE Transactions on Industrial Electronics,* vol. 62, pp. 2673-2682, 2015.

[88] A. Egea-Alvarez, S. Fekriasl, F. Hassan, and O. Gomis-Bellmunt, "Advanced Vector Control for Voltage Source Converters Connected to Weak Grids," *IEEE Transactions on Power Systems,* vol. 30, pp. 3072-3081, 2015.

[89] L. Harnefors, A. G. Yepes, A. Vidal, and J. Doval-Gandoy, "Passivity-Based Controller Design of Grid-Connected VSCs for Prevention of Electrical Resonance Instability," *IEEE Transactions on Industrial Electronics,* vol. 62, pp. 702-710, 2015.

[90] M. Salmani, N. Rahbari-Asr, C. S. Edrington, and M. Y. Chow, "Online and Offline Stability Analysis Methods for the Power Electronic-Based Components in Design and Operational Stages," *IEEE Transactions on Power Electronics,* vol. 31, pp. 3151-3164, 2016.

[91] W. Cao, Y. Ma, and F. Wang, "Sequence Impedance Based Harmonic Stability Analysis and Controller Parameter Design of Three-Phase Inverter-Based Multi-Bus Ac Power Systems," *IEEE Transactions on Power Electronics,* vol. PP, pp. 1-1, 2016.

[92] W. Cao, Y. Ma, L. Yang, F. Wang, and L. Tolbert, "D-Q Impedance Based Stability Analysis and Parameter Design of Three-Phase Inverter-Based Ac Power Systems," *IEEE Transactions on Industrial Electronics,* vol. PP, pp. 1-1, 2017.

[93] R. E. D. Saeks, R. A., *Interconnected dynamical systems*. New York: Marcel Dekker, 1981.

[94] Z. Yao, P. G. Therond, and B. Davat, "Stability analysis of power systems by the generalised Nyquist criterion," in *Control, 1994. Control '94. International Conference on*, 1994, pp. 739-744 vol.1.

[95] F. Liu, J. Liu, H. Zhang, and D. Xue, "Stability Issues of <formula formulatype="inline"> <img src="/images/tex/21485.gif" alt="Z + Z"> </formula> Type Cascade System in Hybrid Energy Storage System (HESS)," *IEEE Transactions on Power Electronics,* vol. 29, pp. 5846-5859, 2014.

[96] Q. Zhu, L. Wang, A. Huang, K. Booth, and L. Zhang, "7.2 kV Single Stage Solid State Transformer Based on Current Fed Series Resonant Converter and 15 kV SiC MOSFETs," *IEEE Transactions on Power Electronics,* pp. 1-1, 2018 2018.

[97] X. Yue, D. Boroyevich, F. C. Lee, F. Chen, R. Burgos, and F. Zhuo, "Beat Frequency Oscillation Analysis for Power Electronic Converters in DC Nanogrid Based on Crossed Frequency Output Impedance Matrix Model," *IEEE Transactions on Power Electronics,* vol. 33, pp. 3052-3064, April 2018 2018.

[98] F. Chen, R. Burgos, and D. Boroyevich, "A Bidirectional High-Efficiency Transformerless Converter with Common-Mode Decoupling for the Interconnection of AC and DC Grids," *IEEE Transactions on Power Electronics,* pp. 1-1, 2018 2018.

[99] Q. Zhu, L. Wang, D. Chen, L. Zhang, and A. Q. Huang, "Design and implementation of a 7.2kV single stage AC-AC solid state transformer based on current source series resonant converter and 15 kV SiC MOSFET," in *2017 IEEE Energy Conversion Congress and Exposition (ECCE)*, 2017, pp. 1288-1295.

[100] L. Wang, Q. Zhu, W. Yu, and A. Q. Huang, "Full ZVS soft-start of a SiC medium voltage series resonant DC-DC converter using variable frequency variable duty cycle control," in *2017 IEEE 3rd International Future Energy Electronics Conference and ECCE Asia (IFEEC 2017 - ECCE Asia)*, 2017, pp. 1855-1860.

[101] L. Wang, Q. Zhu, W. Yu, and A. Q. Huang, "A Medium-Voltage Medium-Frequency Isolated DC–DC Converter Based on 15-kV SiC MOSFETs," *IEEE Journal of Emerging and Selected Topics in Power Electronics,* vol. 5, pp. 100-109, March 2017 2017.

[102] L. Wang, A. Q. Huang, and Q. Zhu, "Multi-objective optimization of medium voltage SiC DC-DC converter based on modular input-series-output-parallel (ISOP) architecture," in *2017 IEEE 3rd International Future Energy Electronics Conference and ECCE Asia (IFEEC 2017 - ECCE Asia)*, 2017, pp. 627-632.

[103] C. Li, F. d. Bosio, F. Chen, S. K. Chaudhary, J. C. Vasquez, and J. M. Guerrero, "Economic Dispatch for Operating Cost Minimization Under Real-Time Pricing in Droop-Controlled DC Microgrid," *IEEE Journal of Emerging and Selected Topics in Power Electronics,* vol. 5, pp. 587-595, March 2017 2017.

[104] M. Jakšić, Z. Shen, I. Cvetković, D. Boroyevich, R. Burgos, C. DiMarino, *et al.*, "Medium-Voltage Impedance Measurement Unit for Assessing the System Stability of Electric Ships," *IEEE Transactions on Energy Conversion,* vol. 32, pp. 829-841, June 2017 2017.

[105] A. Q. Huang, Q. Zhu, L. Wang, and L. Zhang, "15 kV SiC MOSFET: An enabling technology for medium voltage solid state transformers," *CPSS Transactions on Power Electronics and Applications,* vol. 2, pp. 118-130, 2017 2017.

[106] F. Chen, R. Burgos, D. Boroyevich, and X. Zhang, "Low-Frequency Common-Mode Voltage Control for Systems Interconnected With Power Converters," *IEEE Transactions on Industrial Electronics,* vol. 64, pp. 873-882, January 2017 2017.

[107] F. Chen, R. Burgos, and D. Boroyevich, "A high-efficiency interleaved single-phase AC-DC converter with common-mode voltage regulation for 380 V DC microgrids," in *2017 IEEE Energy Conversion Congress and Exposition (ECCE)*, 2017, pp. 4128-4135.

[108] F. Chen, R. Burgos, and D. Boroyevich, "A transformerless single-phase utility interface converter to attenuate common-mode voltage for DC microgrid," in *2017 IEEE 3rd International Future Energy Electronics Conference and ECCE Asia (IFEEC 2017 - ECCE Asia)*, 2017, pp. 157-162.

[109] Q. Zhu, L. Wang, L. Zhang, W. Yu, A. Q. Huang, and X. Ni, "Practical consideration and implementation of a medium voltage SiC AC-DC rectifier," in *2016 IEEE Energy Conversion Congress and Exposition (ECCE)*, 2016, pp. 1-6.

[110] Q. Zhu, L. Wang, L. Zhang, W. Yu, and A. Q. Huang, "Improved medium voltage AC-DC rectifier based on 10kV SiC MOSFET for Solid State Transformer (SST) application," in *2016 IEEE Applied Power Electronics Conference and Exposition (APEC)*, 2016, pp. 2365-2369.

[111] L. Wang, Q. Zhu, W. Yu, and A. Q. Huang, "A study of dynamic high voltage output charge measurement for 15 kV SiC MOSFET," in *2016 IEEE Energy Conversion Congress and Exposition (ECCE)*, 2016, pp. 1-7.

[112] E. Rodriguez-Diaz, F. Chen, J. C. Vasquez, J. M. Guerrero, R. Burgos, and D. Boroyevich, "Voltage-Level Selection of Future Two-Level LVdc Distribution Grids: A Compromise Between Grid Compatibiliy, Safety, and Efficiency," *IEEE Electrification Magazine,* vol. 4, pp. 20-28, June 2016 2016.

[113] J. E. Huber, D. Rothmund, L. Wang, and J. W. Kolar, "Full-ZVS modulation for all-SiC ISOP-type isolated front end (IFE) solid-state transformer," in *2016 IEEE Energy Conversion Congress and Exposition (ECCE)*, 2016, pp. 1-8.

[114] A. Q. Huang, L. Wang, Q. Tian, Q. Zhu, D. Chen, and W. Yu, "Medium voltage solid state transformers based on 15 kV SiC MOSFET and JBS diode," in *IECON 2016 - 42nd Annual Conference of the IEEE Industrial Electronics Society*, 2016, pp. 6996-7002.

[115] F. Chen, R. Burgos, D. Boroyevich, and X. Zhang, "Active control of low frequency common mode voltage to connect AC utility and 380 V DC grid," in *2016 IEEE Applied Power Electronics Conference and Exposition (APEC)*, 2016, pp. 177-184.

[116] F. Chen, R. Burgos, D. Boroyevich, E. Rodriguez-Diaz, L. Meng, J. C. Vasquez, *et al.*, "Analysis and distributed control of power flow in DC microgrids to improve system efficiency," in *2016 4th International Symposium on Environmental Friendly Energies and Applications (EFEA)*, 2016, pp. 1-6.

[117] F. Chen, R. Burgos, and D. Boroyevich, "Output impedance comparison of different droop control realizations in DC systems," in *2016 IEEE 17th Workshop on Control and Modeling for Power Electronics (COMPEL)*, 2016, pp. 1-6.

[118] L. Wang, Q. Zhu, W. Yu, and A. Q. Huang, "A medium voltage bidirectional DC-DC converter combining resonant and dual active bridge converters," in *2015 IEEE Applied Power Electronics Conference and Exposition (APEC)*, 2015, pp. 1104-1111.

[119] F. Chen, R. Burgos, D. Boroyevich, and W. Zhang, "A nonlinear droop method to improve voltage regulation and load sharing in DC systems," 2015, pp. 45–50.

[120] F. Chen, R. Burgos, and D. Boroyevich, "Efficiency comparison of a single-phase grid-interface bidirectional AC/DC converter for DC distribution systems," 2015, pp. 6261–6268.

[121] F. Chen, W. Zhang, R. Burgos, and D. Boroyevich, "Droop voltage range design in DC micro-grids considering cable resistance," 2014, pp. 770–777.

[122] F. Chen, R. Burgos, D. Boroyevich, and D. Dong, "Control loop design of a two-stage bidirectional AC/DC converter for renewable energy systems," in *2014 IEEE Applied Power Electronics Conference and Exposition - APEC 2014*, 2014, pp. 2177-2183.

[123] N. R. Mehrabadi, Q. Wang, R. Burgos, and D. Boroyevich, "Multi-objective design and optimization of a vienna rectifier with parametric uncertainty quantification," in *2017 IEEE 18th Workshop on Control and Modeling for Power Electronics (COMPEL)*, 2017, pp. 1-6.

[124] N. R. Mehrabadi, R. Burgos, C. Roy, J. Yu, and D. Boroyevich, "Study of the predictive capability of modular multilevel converter simulation models under parametric and model form uncertainty," in *2017 IEEE Applied Power Electronics Conference and Exposition (APEC)*, 2017, pp. 1062-1069.

[125] N. R. Mehrabadi, R. Burgos, C. Roy, and D. Boroyevich, "Power Electronics Modeling and Design: Using Parametric and Model-Form Uncertainty Quantification to Assess Predictive Accuracy of Power Converter Models," *IEEE Power Electronics Magazine*, vol. 4, pp. 44-52, 2017.

[126] N. R. Mehrabadi, R. Burgos, D. Boroyevich, and C. Roy, "Modeling and design of the modular multilevel converter with parametric and model-form uncertainty quantification," in *2017 IEEE Energy Conversion Congress and Exposition (ECCE)*, 2017, pp. 1513-1520.

[127] N. R. Mehrabadi, I. Cvetkovic, J. Wang, R. Burgos, and D. Boroyevich, "Busbar design for SiC-based H-bridge PEBB using 1.7 kV, 400 a SiC MOSFETs operating at 100 kHz," in *2016 IEEE Energy Conversion Congress and Exposition (ECCE)*, 2016, pp. 1-7.

[128] N. R. Mehrabadi, R. Burgos, D. Boroyevich, J. Yu, and C. Roy, "Predicting the behavior of a high switching frequency SiC-based modular power converter based on low-power validation experiments," in *2016 IEEE 17th Workshop on Control and Modeling for Power Electronics (COMPEL)*, 2016, pp. 1-7.

[129] N. R. Mehrabadi, R. Burgos, D. Boroyevich, and C. Roy, "Model-based design of a modular multilevel converter with minimized design margins," in *2015 IEEE 16th Workshop on Control and Modeling for Power Electronics (COMPEL)*, 2015, pp. 1-7.

[130] N. R. Mehrabadi, R. Burgos, D. Boroyevich, and C. Roy, "Sensitivity analysis of a modular multilevel converter," in *2015 IEEE Energy Conversion Congress and Exposition (ECCE)*, 2015, pp. 3578-3584.

[131] F. Shahnia, S. Rajakaruna, and A. Ghosh, *Static Compensators (STATCOMs) in Power Systems*: Springer Singapore, 2014.

[132] Y. H. Song and A. Johns, *Flexible Ac Transmission Systems (FACTS)*: Institution of Electrical Engineers, 1999.

[133] E. Ghahremani and I. Kamwa, "Optimal placement of multiple-type FACTS devices to maximize power system loadability using a generic graphical user interface," *Power Systems, IEEE Transactions on*, vol. 28, pp. 764-778, 2013.

[134] R. Sirjani, A. Mohamed, and H. Shareef, "Optimal allocation of shunt Var compensators in power systems using a novel global harmony search algorithm," *International Journal of Electrical Power & Energy Systems*, vol. 43, pp. 562-572, 12// 2012.

[135] Y. Del Valle, J. C. Hernandez, G. K. Venayagamoorthy, and R. G. Harley, "Multiple STATCOM Allocation and Sizing Using Particle Swarm Optimization," in *Power Systems Conference and Exposition, 2006. PSCE '06. 2006 IEEE PES*, 2006, pp. 1884-1891.

[136] A. R. Messina, M. A. Pérez, and E. Hernández, "Co-ordinated application of FACTS devices to enhance steady-state voltage stability," *International Journal of Electrical Power & Energy Systems*, vol. 25, pp. 259-267, 5// 2003.

[137] A. Elmitwally, M. Elsaid, and M. Elgamal, "Multi-agent-based voltage stabilization scheme considering load model effect," *International Journal of Electrical Power & Energy Systems*, vol. 55, pp. 225-237, 2// 2014.

[138] L. B. Perera, G. Ledwich, and A. Ghosh, "Multiple distribution static synchronous compensators for distribution feeder voltage support," *Generation, Transmission & Distribution, IET*, vol. 6, pp. 285-293, 2012.

[139] W. Hai Feng, H. Li, and H. Chen, "Coordinated secondary voltage control to eliminate voltage violations in power system contingencies," *Power Systems, IEEE Transactions on*, vol. 18, pp. 588-595, 2003.

[140] L. A. S. Pilotto, W. F. Long, F. L. Alvarado, and A. Edris, "Determination of needed FACTS controllers that increase asset utilization of power systems," *Power Delivery, IEEE Transactions on*, vol. 12, pp. 364-371, 1997.

[141] A. Yazdani and R. Iravani, *Voltage-Sourced Converters in Power Systems: Modeling, Control, and Applications*: Wiley, 2010.

[142] J. Wang, "Switching-Cycle Control and Sensing Techniques for High-Density SiC-Based Modular Converters," Ph. D. dissertation, Virginia Tech, Blacksburg, 2017.

[143] S. Zhiyu, "Online Measurement of Three-phase AC Power System Impedance in Synchronous Coordinates," Ph. D. dissertation, Virginia Tech, Blacksburg, VA, 2013.

[144] T. J. E. Miller, *Reactive power control in electric systems*. New York: Wiley, 1982.

[145] L. Harnefors, M. Bongiorno, and S. Lundberg, "Input-Admittance Calculation and Shaping for Controlled Voltage-Source Converters," *IEEE Transactions on Industrial Electronics,* vol. 54, pp. 3323-3334, 2007.

[146] D. Dong, B. Wen, D. Boroyevich, P. Mattavelli, and Y. Xue, "Analysis of Phase-Locked Loop Low-Frequency Stability in Three-Phase Grid-Connected Power Converters Considering Impedance Interactions," *IEEE Transactions on Industrial Electronics,* vol. 62, pp. 310-321, 2015.

[147] L. Harnefors, X. Wang, A. G. Yepes, and F. Blaabjerg, "Passivity-Based Stability Assessment of Grid-Connected VSCs—An Overview," *IEEE Journal of Emerging and Selected Topics in Power Electronics,* vol. 4, pp. 116-125, 2016.

[148] C. Yoon, H. Bai, R. N. Beres, X. Wang, C. L. Bak, and F. Blaabjerg, "Harmonic Stability Assessment for Multiparalleled, Grid-Connected Inverters," *IEEE Transactions on Sustainable Energy,* vol. 7, pp. 1388-1397, 2016.

[149] C. Li, R. Burgos, Y. Tang, and D. Boroyevich, "Application of d-q frame impedance-based stability criterion in power systems with multiple STATCOMs in proximity," in *IECON 2017 – 43rd Annual Conference of the IEEE Industrial Electronics Society*, Beijing, 2017, pp. 126-131.

[150] M. Mohaddes, A. M. Gole, and S. Elez, "Steady state frequency response of STATCOM," *IEEE Transactions on Power Delivery,* vol. 16, pp. 18-23, 2001.

[151] W. Bo, D. Boroyevich, R. Burgos, P. Mattavelli, and S. Zhiyu, "Analysis of D-Q Small-Signal Impedance of Grid-Tied Inverters," *IEEE Transactions on Power Electronics,* vol. 31, pp. 675-687, 2016.

[152] M. K. Bakhshizadeh, X. Wang, F. Blaabjerg, J. Hjerrild, K. Ł, C. L. Bak, *et al.*, "Couplings in Phase Domain Impedance Modeling of Grid-Connected Converters," *IEEE Transactions on Power Electronics,* vol. 31, pp. 6792-6796, 2016.

[153] Z. Shen, M. Jaksic, P. Mattavelli, D. Boroyevich, J. Verhulst, and M. Belkhayat, "Three-phase AC system impedance measurement unit (IMU) using chirp signal injection," in *2013 Twenty-Eighth Annual IEEE Applied Power Electronics Conference and Exposition (APEC)*, 2013, pp. 2666-2673.

[154] J. Marko, "Identification of Small-Signal dq Impedances of Power Electronics Converters via Single-Phase Wide-Bandwidth Injection," Ph. D. dissertation, Virginia Tech, Blacksburg, VA, 2014.